Dynamique des grandes échelles dans les jets turbulents avec ou sans effets de rotation

Samuel Davoust

ONERA
Département d'Aérodynamique Fondamentale et Expérimentale

THÈSE DE L'ÉCOLE POLYTECHNIQUE

présentée par

Samuel Davoust

pour obtenir le titre de

Docteur de l'Ecole Polytechnique

Spécialité : Mécanique

Dynamique des grandes échelles dans les jets turbulents avec ou sans effets de rotation

soutenue le 12 Octobre 2011

devant le jury composé de :

M. Bonnet, J-P.
M. Gence, J-N. *Rapporteur*
M. Jacquin, L. *Directeur de thèse*
M. Jiménez, J.
M. Leclaire, B. *Encadrant*
M. Moisy, F. *Rapporteur*
M. Schmid, P. J.

Dynamique des grandes échelles dans les jets turbulents avec ou sans effets de rotation

Résumé : Cette thèse est une contribution à l'étude de la turbulence dans le champ proche de la sortie de jets, avec ou sans effets de rotation. Notre dispositif expérimental permet de générer un jet tournant qui se développe en formant une couche de mélange axisymétrique turbulente et dont le nombre de swirl peut être précisément fixé. L'écoulement est caractérisé par PIV stéréoscopique, avec un recours à des acquisitions à haute cadence de manière à résoudre la dynamique des grandes échelles de la turbulence. Nous avons proposé une méthode qui permet de déterminer la vitesse de convection des structures turbulentes et d'estimer la validité de l'approximation de Taylor. Cette étude démontre qu'il est ici légitime de décrire les structures spatiales de la turbulence à partir de mesures temporelle réalisées dans un plan transverse à l'écoulement.

Dans le coeur du jet non tournant, une POD confirme la prédominance de modes m=0 et m=1 décrite dans de précédentes études. Le mode m=1 prend plus souvent la forme d'un battement que d'une hélice. Dans la couche de mélange, les tourbillons longitudinaux sont les structures dominantes. Une organisation sous forme de paires de signe opposé orientées radialement est mise en évidence par l'analyse des corrélations doubles de vorticité. L'étude des corrélations vorticité-vitesse donne la position préférentielle de ces tourbillons par rapport aux modes m=0 et m=1. Nous avons alors proposé un scénario d'interaction entre les modes m=0 et m=1, les tourbillons longitudinaux et le champ moyen.

Lorsque le nombre de swirl augmente, le taux de croissance et l'énergie cinétique turbulente dans la couche de mélange du jet varient de manière non-monotone. Ceci est dû à des conditions initiales issues du mécanisme de mise en rotation, qui ont un effet contraire à celui de l'alignement du tenseur de Reynolds avec le tenseur des déformations. L'orientation des paires de tourbillons avec le swirl permet d'interpréter dynamiquement l'évolution du tenseur de Reynolds.

Mots-clés : Jet, Turbulence, Ecoulement cisaillé, Ecoulement tournant, Swirl, PIV, POD, Hypothèse de Taylor, Structures cohérentes, Tourbillons longitudinaux, Tenseur de Reynolds.

Dynamics of large scale structures in turbulent jets with or without the effects of swirl

Summary : This thesis is a contribution to the study of turbulence in the near field of a jet exit, with or without swirl. We use an experimental setup which has been validated to generate a thin axisymmetric mixing layer developing into a jet, and where the amount of swirl can be precisely set. The flow is characterized using stereoscopic PIV measurements, including high-speed acquisitions which resolve the dynamics of the large scale turbulent structures. We have proposed and tested a method which allows the estimate the convection velocities of these structures and to determine the validity of Taylor's hypothesis using the experimental dataset. This study shows that in the jet near field, it is legitimate to perform a pseudo spatial reconstruction using temporal PIV data.

In the jet core, without swirl, a POD confirms the predominance of m=0 and m=1 modes, in line with previous studies. A detailed statistical analysis brings to light that the motion of m=1 modes is closer to a flapping than to a helix. In the mixing layer, streamwise vortices are dominant. Radially oriented pairs are shown to be frequent by analyzing spatial correlation of streamwise vorticity. The relative organization of these vortices with m=0 and m=1 modes is quantitatively established using velocity and vorticity correlations. This leads us to propose an interaction scenario between m=0 and m=1 modes, streamwise vortices, and the mean flow.

When swirl is added, the growth rate and turbulent kinetic energy level in the mixing layer do not vary in a monotonous manner. This is due to specific initial conditions obtained from the swirl generation mechanism, which counter the effects arising from the increased alignment between the Reynolds stress and the strain tensor. On this last point, we show that the orientation of the initially radial vortex pair changes with swirl, and this provides a dynamical interpretation of evolution of the Reynolds stress tensor.

Keywords : Jet, Turbulence, Shear flow, Rotating flow, Swirl, PIV, POD, Taylor hypothesis, Coherent structures, Streamwise vortices, Reynolds stress.

Remerciements

Laurent, tout d'abord merci de m'avoir accueilli au Dafe, de m'avoir accordé ta confiance avec une grande liberté expérimentale, des moyens techniques et du soutien. Ce fut un plaisir constant de travailler avec toi pour préparer les expériences, analyser les résultats, puis comprendre et décrire ce que la soufflerie R4 avait à nous dire. Aussi, je te suis reconnaissant d'avoir partagé avec moi une vision scientifique et humaine, qui m'a beaucoup marqué. J'ai beaucoup apprécié les instants que tu m'as accordé pour discuter physique, et parfois aussi d'autres choses, comme de la mer. Merci d'avoir compris mon choix de virer de bord, dans la risée. La régate ne fait que commencer.

Benjamin, merci pour ta disponibilité, tes qualités d'écoute et d'analyse. Ton sens physique, ta rigueur et ta clarté d'esprit ont constamment contribué à faire avancer et à améliorer mes travaux.

Je tiens à remercier avec respect et gratitude messieurs les membres du Jury Jean-Paul Bonnet, Javier Jiménez et Peter Schmid, et en particulier messieurs les rapporteurs Jean-Noël Gence et Frédéric Moisy pour leur travail.

Merci à tous ceux qui ont participé à la réussite des expériences avec la soufflerie R4. Merci à ceux qui ont contribué à la remise sur pied de la mécanique de cette soufflerie et à l'installation de nouveaux équipements. En particulier je tiens à remercier Jean-Pierre Tobeli pour le changement et le contrôle du nouveau moteur de rotation de la veine, véritable âme de cette soufflerie.

Merci aux métrologues. Au Dafe, il y a une équipe expérimentale hors pair et très complémentaire. Merci à Gilles Losfeld, dont la créativité et la curiosité expérimentale n'ont d'égal que sa passion pour la moto et peut-être aussi pour les jeux de mots. Merci à Didier Soulevant, qui a bravé le froid avec moi pour installer l'artillerie lourde, aligner des nappes épaisses, calibrer des caméras, et déchainer un spectacle de fumée et de lumière, en toute sécurité. Merci à Philipe Geffroy, de m'avoir initié au fil chaud, l'instrument qui rend les choses méchantes, mais qui révèle les turbulences. Merci à Yves Le Sant, le chef de cette joyeuse unité, pour le ballon de rugby en mousse qu'il m'a laissé, mais surtout pour ces discussions bien sympa sur la PIV, et CUDA (c'est quoi déjà ?). Merci pour ton travail sur Folki-PIV et pout ta bonne humeur constante. Merci aux éminences grises du DTIM avec qui j'ai bien appris (et bien rigolé aussi). Bonne continuation pour cette collaboration ALPIV.

Au quotidien, il règne une très bonne ambiance entre les doctorants. Merci à Benoit pour ses coups de mains en expé, à Alexandre pour ses roulades. Je repars avec un camarade planchiste parisien de plus qu'en arrivant en la personne de Vincent, croyez-moi c'est important.

Je me suis bien marré avec une équipe pleine d'énergie composée de coureurs, de motards, et d'amateurs de Vespas, notamment lors du Marathon du Médoc. Merci pour cette expérience unique.

Merci à l'équipe qui anime le Dafe. Merci à Claire et Dominique pour leur soutien.

Merci à la Direction des ressources humaines de l'ONERA.

Je tiens aussi à remercier Sabine Ortiz et Denis Sipp qui m'ont permis d'aborder l'enseignement avec les petites classes à l'ENSTA et les enseignements d'approfondissement à l'Ecole polytechnique.

Merci à mes amis, mes parents, mes soeurs et à Julie.

Cette thèse, financée par une bourse DGA, a été réalisée au Département d'Aérodynamique Fondamentale et Expérimentale (Dafe) de l'Onera, à Meudon, du 1er octobre 2008 au 17 juin 2011.

Table des matières

Notations

Le tableau suivant regroupe les principales notations et abréviations employées à travers ce manuscrit :

U_0	:	Vitesse de débit dans le plan de sortie du jet
D_0	:	Diamètre de la conduite de sortie du jet
Re_0	:	Nombre de Reynolds en sortie du jet
S_0	:	Nombre de swirl en sortie du jet
S	:	Nombre de swirl : paramètre de contrôle du jet tournant
θ_0	:	Epaisseur de quantité de mouvement de la couche limite dans le plan de sortie du jet
Ω_0	:	Vitesse angulaire dans le plan de sortie du jet
$\dot{M}_0$	:	Débit du jet dans le plan de sortie
χ	:	Taux de contraction
D_c	:	Diamètre de la conduite en amont de la contraction
Ω_c	:	Vitesse angulaire du nid d'abeille en amont de la contraction
S_c	:	Nombre de swirl en amont de la contraction

(X, Y, Z) et (x, y, z)	:	Coordonnées Cartésiennes physiques et adimensionnées
(R, θ, Z) et (r, θ, z)	:	Coordonnées cylindriques physiques et adimensionnées
(u_r, u_θ, u_z)	:	Composantes cylindriques du vecteur vitesse moyenne adimensionné
(u'_r, u'_θ, u'_z)	:	Composantes cylindriques des fluctuations du vecteur vitesse adimensionné
$(\omega_r, \omega_\theta, \omega_z)$	:	Composantes cylindriques du vecteur vorticité moyenne adimensionné
$(\omega'_r, \omega'_\theta, \omega'_z)$	:	Composantes cylindriques des fluctuations du vecteur vorticité adimensionné
Ω_z	:	Vitesse angulaire adimensionnée sur l'axe du jet tournant
δ_ω	:	Epaisseur du cisaillement de vitesse axiale de la couche de mélange
δ_λ	:	Epaisseur de cisaillement total de la couche de mélange
$\langle u_i u_j \rangle$	:	Composantes du tenseur des tensions de Reynolds
d_{ij}	:	Composantes du tenseur des déformations
k	:	Energie cinétique turbulente (TKE)
k_m	:	Maximum de l'énergie cinétique turbulente dans la couche de mélange
r_m	:	Position radiale du maximum de l'énergie cinétique turbulente dans la couche de mélange
$C_{u_\theta u_\theta}$	:	Corrélation spatiale de la vitesse azimutale
$C_{\omega_z \omega_z}$	:	Corrélation spatio-temporelle de la vorticité axiale
$C_{\omega_z \omega_z}$	:	Corrélation spatio-temporelle de la vorticité axiale avec la vitesse axiale
$C_{\omega_z^2 u_z}$	:	Corrélation spatio-temporelle du carré de la vorticité axiale avec la vitesse axiale

PIV	:	Vélocimétrie par images de particules
SPIV	:	PIV stéréoscopique
HS-SPIV	:	SPIV à haute cadence
L_{PIV}	:	Taille physique des pixels du capteur des caméras PIV
$\mathcal{L}_{\mathrm{FI}}$	:	Taille des fenêtres d'interrogation PIV en pixels
L_{FI}	:	Taille des fenêtres d'interrogation PIV dans l'espace physique
F_{acq}	:	Fréquence d'acquisition PIV
N	:	Nombre de clichés SPIV
N_{ech}	:	Nombre de clichés dans un bloc de données HS-SPIV
N_B	:	Nombre blocs de données HS-SPIV
N_θ	:	Nombre de positions azimutales dans le maillage cylindrique HS-SPIV
N_r	:	Nombre de positions radiales dans le maillage cylindrique HS-SPIV
u_c	:	Vitesse de convection adimensionnée
f	:	fréquence adimensionnée
m	:	nombre d'onde azimutal
$\rho(f)$	:	Coefficient de corrélation entre la dérivée spatiale et la dérivée temporelle d'une onde de fréquence f
$\lambda^{(n)}(m,f)$	:	n-ième valeur propre de la décomposition POD associée au nombre d'onde azimutal m et à la fréquence f
$\phi_i^{(n)}(m,f)$	:	Composante i du mode POD n associé au nombre d'onde azimutal m et à la fréquence f

Introduction

Comment propulser un avion tout en minimisant les nuisances sonores ? Comment mélanger des réactifs pour réaliser une combustion qui limite la génération de suies ? Jets et couches de mélange sont impliqués dans des applications industrielles variées. De par la taille des objets considérés, la vitesse et la nature des fluides utilisés, les écoulements des applications sont très souvent turbulents.

(a) : Les réacteurs d'un Airbus A380 [110]

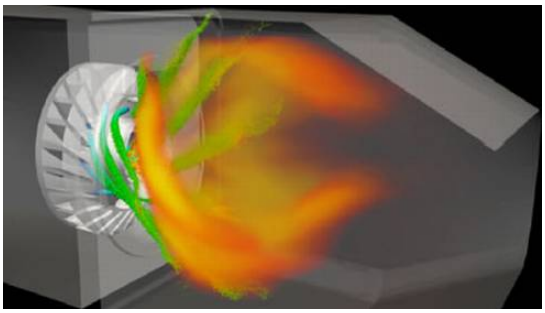

(b) : Chambre de combustion à swirl [28]

FIGURE 1 – Quelques applications industrielles

Les jets et les couches de mélange appartiennent, avec les sillages, à la classe des écoulements turbulents cisaillés libres. La prédiction "au premier ordre" du comportement moyen de ces écoulements, basée sur l'utilisation de modèles de turbulence standards, ne pose pas de problème majeur. Mais une prédiction précise du taux de croissance spatial et du taux de turbulence de ces écoulements ou, de manière encore plus évidente, la prédiction de phénomènes instationnaires comme ceux responsables du bruit émis, se heurte à des difficultés. En effet, les jets et les couches de mélange s'avèrent très sensibles à leurs conditions aux limites, celles qui prévalent dans l'éjecteur, ainsi que dans leur environnement, à savoir l'écoulement dans lequel ils se développent. Ils sont en particulier sensibles aux sources de bruit, aux vibrations mécaniques et aux fluctuations du débit [11, 56, 58, 63]. Par ailleurs, si l'on connait toutes les sources de bruit, ces écoulements peuvent être affectés de façon importante par une petite modification de la géométrie, comme un faible changement de courbure [13]. C'est de ce type de modification dont allons traiter, en imposant une rotation à un écoulement de jet initialement rectiligne. A titre d'exemple, pour les applications industrielles représentées à la figure 1, la rotation est faible en sortie de réacteurs (a), mais très importante dans une chambre de combustion à swirl (b).

La figure 2 est une visualisation par tomoscopie laser du développement de la turbulence dans un jet cylindrique non tournant à bas nombre de Mach produit par le dispositif utilisé dans ce travail. Le jet est caractérisé par le diamètre de la conduite D_0 dont il

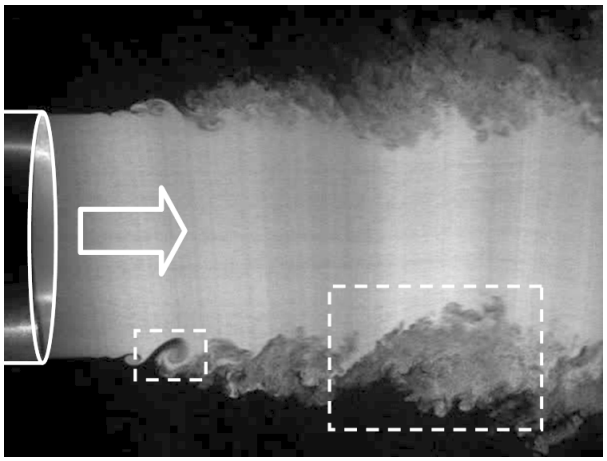

FIGURE 2 – Visualisation par tomoscopie laser du développement initial d'un jet, de nombre Reynolds $Re_0 \approx 10^5$, avec une couche limite initialement laminaire. Le rectangle de petite taille indique une structure résultant de l'instabilité initiale. Le second, de plus grande taille, indique une structure cohérente dans la partie turbulente de l'écoulement.

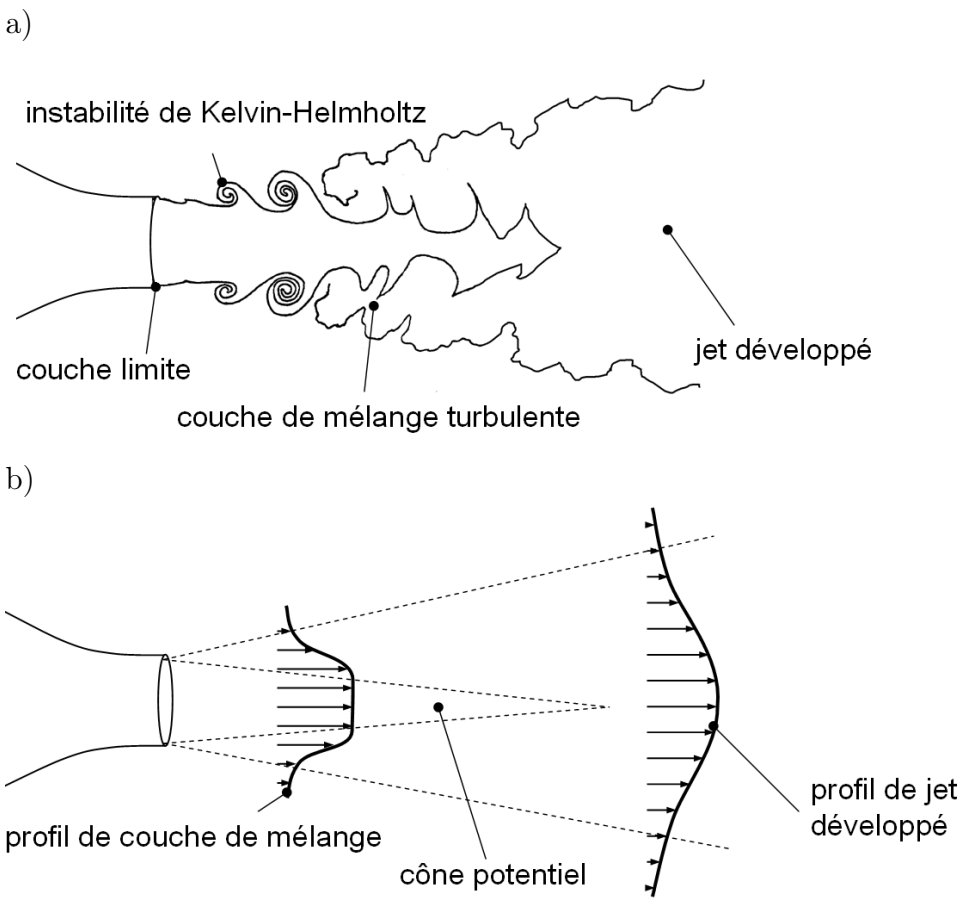

FIGURE 3 – (a) : Dessin représentant la visualisation de la figure 2, d'après Yule [123]. (b) : Schéma de l'écoulement moyen.

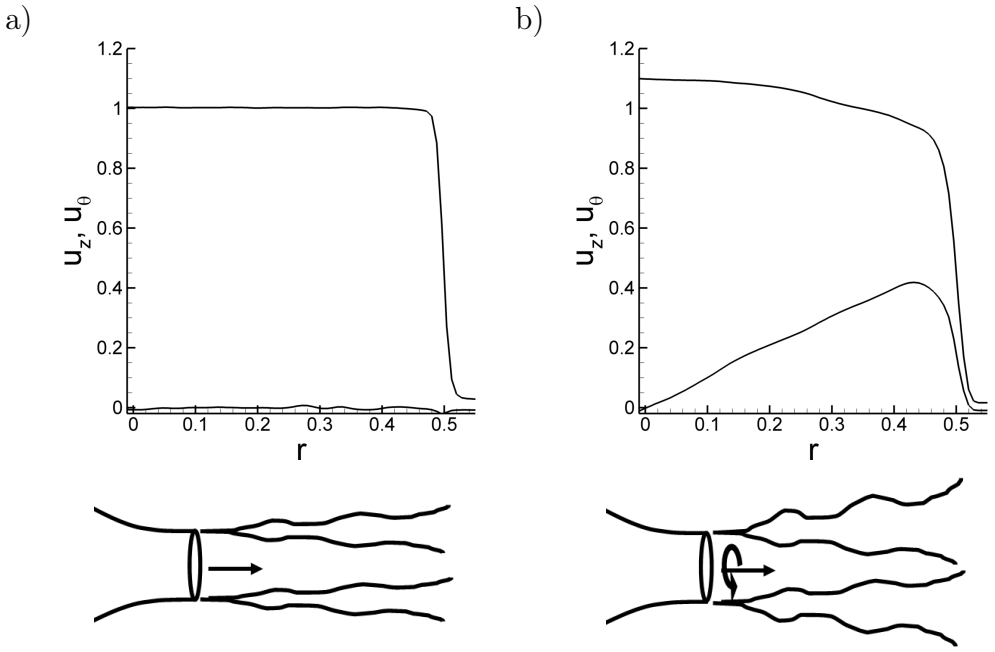

FIGURE 4 – Jet (a) et jet tournant (b) : exemples de profils de vitesses axiales et azimutales et schéma de principe.

débouche avec une vitesse U_0, ce qui permet de définir le nombre de Reynolds Re_0 de l'écoulement. Dans le cas où le profil de vitesse axial est initialement uniforme sur une bonne portion de la conduite, la couche limite qui caractérise la région de contact avec la conduite possède une épaisseur petite devant D_0. Comme schématisé sur la figure 3, cette couche limite, qui est ici de nature laminaire, subit l'instabilité de Kelvin-Helmholtz et forme une couche de mélange axisymétrique dans laquelle la turbulence se développe. La zone intérieure de fluide de vitesse moyenne uniforme U_0 est dénommée le cône potentiel. Plus en aval, la turbulence envahit l'ensemble du jet et le profil de vitesse prend une forme de gaussienne caractéristique des jets développés.

La question que nous nous posons dans cette thèse est schématisée par la figure 4 : comment se comporte le jet si l'on impose une rotation solide de vitesse angulaire Ω_0 à l'écoulement dans la conduite ? C'est alors un paramètre, le nombre de swirl $S_0 = \frac{\Omega_0 D}{2U_0}$, qui quantifie le rapport entre la rotation et la vitesse axiale du jet. La dépendance du jet à ce paramètre a déjà été étudiée, en ce qui concerne les mécanismes d'instabilité qui apparaissent dans les jets tournants [38, 39], ainsi que sur le plan de la modification de la dynamique de l'écoulement à bas nombre de Reynolds [10, 74]. De précédentes études ont aussi été consacrées à cette thématique à plus haut nombre de Reynolds [19, 31, 82]. Avant de présenter la démarche et le plan de notre étude dans la section 0.4, nous présenterons donc les jets et les jets tournants sur le plan bibliographique. La section 0.1 présente ainsi des phénomènes d'instabilités linéaires qui peuvent se développer avec le swirl. La section 0.2 présente les structures cohérentes qui ont étés décrites dans ces écoulements turbulents, ainsi que certains des effets de courbure et de rotation sur ces dernières. Pour finir, nous décrivons dans la section 0.3 les effets de courbures sur les écoulements cisaillés turbulents du point de vue de la description statistique de la turbulence, avec le cas particulier des jets tournants turbulents.

FIGURE 5 – Instabilité de Kelvin-Helmholtz observée dans une couche de nuages [121].

0.1 Instabilités de jets et de jets tournants

0.1.1 Principe

La théorie de l'instabilité locale permet de d'établir l'évolution de perturbations infinitésimales dans un modèle parallèle d'écoulement supposé stationnaire, le champ de base. S'il existe un référentiel dans lequel une perturbation peut croître indéfiniment, l'écoulement est dit linéairement instable. Si toutes les perturbations tendent à décroitre dans tous les référentiels, il est linéairement stable [18]. Dans le cas de jets et de couches de mélange, qui sont des écoulements ouverts, les éventuelles instabilités peuvent être de deux types différents. Lorsque l'écoulement est instable, il est important de savoir si les perturbations qui croissent sont irrémédiablement advectées, ou si elles sont capables de remonter l'écoulement par leur vitesse de groupe. Dans le premier cas, l'écoulement est dit convectivement instable et il se comporte comme un amplificateur de bruit : il amplifie les perturbations amont mais n'a pas de dynamique propre. Dans le second cas, l'écoulement est dit absolument instable, et il est susceptible de développer un mode global qui oscille à sa propre fréquence [53].

En résolvant les équations de Navier-Stokes linéarisées sur le champ de base et en utilisant une décomposition de Fourier dans chaque direction d'invariance, on obtient une relation de dispersion qui permet par exemple de déterminer la pulsation et l'amplification spatiale d'un mode propre de pulsation réelle $2\pi f$, dans le cas d'une analyse spatiale. Dans la suite, nous nous plaçons dans ce cadre pour présenter quelques mécanismes et critères d'instabilités qui sont susceptibles de se produire dans un jet tournant.

0.1.2 Instabilité de Kelvin-Helmholtz

Couche de mélange et jet

L'instabilité de Kelvin-Helmholtz est observée sur la figure 2, près de la sortie de la conduite. Elle se manifeste à l'interface entre deux couches de fluide de vitesse différentes, par exemple dans les couches de cisaillement de l'atmosphère, voir figure 5. Une condition nécessaire d'instabilité est que le profil ait un point d'inflexion. Pour une couche de mélange plane d'épaisseur de vorticité δ_ω entre un fluide au repos et un fluide à la vitesse U_0 le taux d'amplification spatial maximal correspond à une fréquence réduite égale à $f \approx 0.034\delta_\omega/U_0$ [84]. En l'absence d'un contre-courant suffisant, l'instabilité est convective [52].

Dans le cas d'un jet cylindrique, la décomposition en modes normaux s'effectue de manière discrète selon l'azimut qui est 2π périodique, et on note m le nombre d'onde azimutal. Dans les études de stabilité, la résolution par décomposition de Fourier mène à une écriture de la forme $\exp(i(kz + m\theta - 2\pi ft))$. Contrairement à la couche de mélange, un profil de vitesse de jet possède à priori deux échelles caractéristiques, à savoir δ_ω

qui caractérise le cisaillement et D la largeur du jet. La revue de Michalke [85] détaille l'évolution de la fréquence f et du mode m le plus amplifié en fonction de l'évolution du profil du champ de base lors du développement spatial d'un jet, c'est à dire de l'amont vers l'aval (voir figure 3 (b)). Cette étude montre que quand la couche de mélange est fine ($\delta_{omega} \ll D$), le mode $m = 0$ domine et sa fréquence caractéristique dépend de δ_ω comme pour une couche de mélange plane. Au-delà d'une certaine valeur de δ_ω/D nait une dépendance de f à D, puis le mode $m = 1$ devient le plus instable. Dans un profil de jet pleinement développé et sous certaines conditions, le mode $m = 0$ peut même devenir stable.

Instabilité de Kelvin-Helmholtz dans le jet tournant

Dans le jet tournant, le mécanisme de Kelvin-Helmholtz reste à l'oeuvre, et le cisaillement acquiert une composante azimutale. Si on se limite à ce mécanisme d'instabilité, les modes azimutaux $m > 0$ doivent alors devenir plus instables que les modes $m < 0$ car leur vecteur d'onde est mieux aligné avec la direction du cisaillement local [37]. Ces modes $m > 0$ correspondraient à des hélices qui s'enroulent spatialement dans le sens opposé à la rotation du jet mais qui tournent temporellement dans le sens du jet. Cependant, une étude de stabilité complète révèle que ce sont les modes $m < 0$ qui dominent [39], l'instabilité de Kelvin-Helmholtz n'étant pas le seul mécanisme d'instabilité dans un jet tournant.

0.1.3 Instabilité centrifuge

Critères

L'instabilité centrifuge est un second mécanisme qui peut affecter les écoulements tournants. Le critère d'instabilité de Rayleigh [100] s'applique aux écoulements tournants sans vitesse axiale, les tourbillons purs. Il s'agit d'une condition nécessaire d'instabilité, qui devient nécessaire et suffisante pour les perturbations $m = 0$ [37]. Cette condition équivaut à trouver un rayon tel que le moment angulaire décroisse lorsque l'on s'éloigne du centre du tourbillon. Dans le cas général, ceci s'écrit :

$$\frac{d}{dr}(ru_\theta)^2 \leq 0 \tag{1}$$

On peut retrouver ce critère par une analyse de particule déplacée en considérant l'équilibre entre le gradient de pression et la force centrifuge. Les tourbillons usuels qui tendent vers l'irrotationnalité en dehors du coeur sont donc nécessairement centrifugalement stables. Par contre, le profil de vitesse azimutale du jet tournant comme celui de la figure 4 (b) est nécessairement instable pour les perturbations $m = 0$, car la vitesse azimutale décroit de manière brutale. En se limitant maintenant au cas d'un cisaillement subissant une courbure, comme représenté sur la figure 6, il est possible de dériver du critère de Rayleigh une condition nécessaire d'instabilité simple. Localement, on substitue au repère cylindrique le repère curviligne (s, n) de courbure r_c. En introduisant la vitesse $u_\theta = \frac{u_s}{r_c} r + \frac{\partial u_s}{\partial n}(r - r_c)$ du cisaillement courbé dans le critère (1) de Rayleigh, on obtient alors le critère de d'instabilité de Bradshaw [12] :

$$B = e(e + 1) \leq 0, \tag{2}$$

avec $e = (u_s/r_c)/(\partial u_s/\partial n)$, qui représente le rapport du temps caractéristique du cisaillement sur celui de la rotation, ou encore l'épaisseur du cisaillement sur le rayon de courbure.

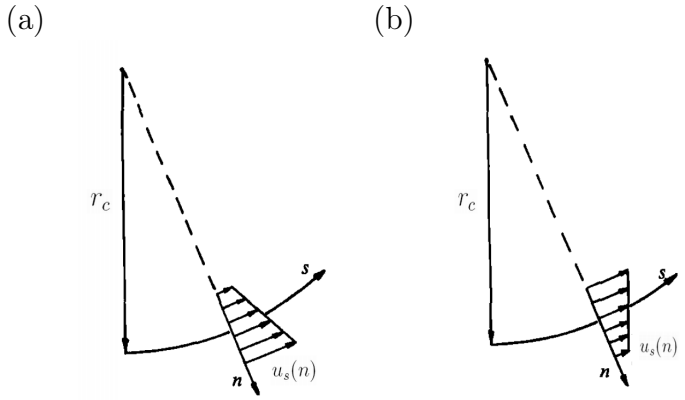

FIGURE 6 – Schéma de la courbure de rayon r_c d'un écoulement cisaillé dans une configuration stabilisante (a) et déstabilisante (b), d'après Holloway and Tavoularis [49].

Instabilité centrifuge généralisée

Un jet tournant possède un profil de vitesse azimutale centrifugalement instable et un profil de vitesse axiale. Une étude de stabilité complète s'avère nécessaire car le critère de Rayleigh n'est plus applicable. L'étude de stabilité de Gallaire and Chomaz [39] montre que jusqu'à un premier seuil critique $S_0 \approx 1$, à partir duquel un mode absolument instable apparait, les instabilités dans les jets tournants sont uniquement convectivement instables. Par un mécanisme d'instabilité centrifuge généralisée, les modes azimutaux $m < 0$ deviennent plus instables lorsque S_0 augmente, au contraire des modes $m > 0$. Ces modes déstabilisés $m < 0$ s'enroulent spatialement dans la direction de l'écoulement mais tournent temporellement dans le sens opposé. Les résultats de Gallaire and Chomaz [39] sont en accord avec la prédiction théorique asymptotique de Leibovich and Stewartson [73], qui prédit le taux de croissance de petites échelles dans la limite où $m \to -\infty$ et qui généralise le critère de Rayleigh.

0.1.4 Ondes d'inertie

Enfin, un dernier mécanisme linéaire est celui des ondes d'inertie ou ondes de Kelvin. Ce sont des ondes neutres qui peuvent se propager dans des écoulements tournants dont une partie du coeur est en rotation solide. Le mécanisme de rappel est lié à la force de Coriolis et ces ondes se propagent de manière anisotrope [46]. Elles peuvent jouer un rôle stabilisant dans le coeur du jet tournant [38]. Dans un écoulement de rotation solide et de vitesse axiale uniforme, les travaux de Benjamin [8] montrent qu'il existe une valeur critique du swirl $S_0 \approx 1.9$ qui correspond à une vitesse de groupe nulle pour laquelle ces ondes peuvent remonter l'écoulement. Un éclatement tourbillonnaire peut alors se produire, en analogie avec l'apparition d'un ressaut hydraulique dans un écoulement de surface libre ou d'un choc dans un écoulement compressible.

Dans les jets, l'éclatement survient pour des nombres de swirls plus bas et s'observe par l'apparition d'un point d'arrêt sur l'axe et d'une bulle de recirculation axisymétrique, ce qui a pour effet d'élargir considérablement l'écoulement [10, 74]. De nouvelles instationnarités apparaissent également à cause de la nature absolument instable de l'écoulement [104]. A titre d'exemple, la figure 7 présente une visualisation de l'éclatement dans un jet à bas nombre de Reynolds [10] ainsi qu'une visualisation à plus haut nombre de Reynolds réalisé à l'ONERA.

a) b)

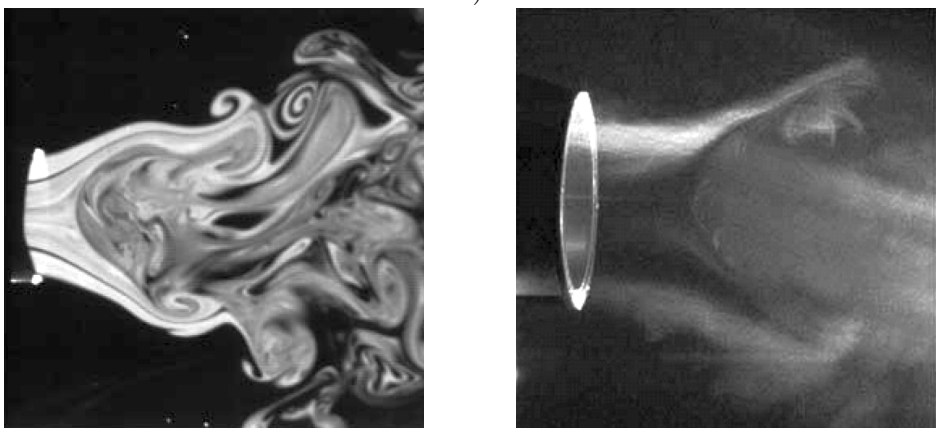

$Re_0 = 1022$ [10] $Re_0 \approx 50000$

FIGURE 7 – Visualisation par tomoscopie laser de l'éclatement tourbillonnaire dans les jets pour deux nombres de Reynolds.

0.2 Structures cohérentes dans les couches de mélange et les jets turbulents

0.2.1 Vers une définition des structures cohérentes

Sur la figure 2, une organisation des instationnarités par instabilité de Kelvin-Helmholtz est clairement apparente dans la zone d'instabilité initiale, mais aussi dans la zone turbulente. Ces structures organisées de la zone turbulente, dénommées structures cohérentes, sont décrites depuis près de cinquante ans [14]. Plusieurs études se sont attachées à préciser le concept de structures cohérentes afin de les détecter à partir des réalisations instantanées de champs de vitesse turbulents. En ce qui concerne les structures de type tourbillons, les candidats "naturels" pour les détecter comme la vorticité, l'enstrophie, ou encore un minimum de pression ne sont pas suffisants pour identifier de manière toujours satisfaisante une structure [61]. Des critères basés sur les invariants du gradient du vecteur vitesse ont alors étés définis [20, 61]. Plus qu'une manière de visualiser la turbulence, l'étude des structures cohérentes permet d'identifier des mécanismes physiques intéressants si les structures considérées sont énergétiquement ou dynamiquement importantes. Des modèles théoriques sont alors parfois proposés pour mieux les décrire. Les "hairpin vortices" des couches limites représentent un exemple de structures qui ont d'abord été visualisées puis détectées dans les écoulements turbulents, avant d'être dynamiquement modélisées [62].

0.2.2 Modes d'instabilité linéaire

La première classe de structures cohérentes que nous considérons trouve son origine dans les mécanismes d'instabilité linéaire du champ moyen, comme c'est le cas pour les structures de la figure 2. Dans les jets et les couches de mélange, des moyens variés ont été mis en oeuvre pour distinguer ces modes des autres fluctuations turbulentes. Outre les critères de détection évoqués ci-dessus, les moyens d'étude incluent le forçage périodique de l'écoulement [23], l'acquisition de statistiques conditionnelles [123, 125] ou des analyses statistiques de type POD (proper orthogonal decomposition) [22, 27].

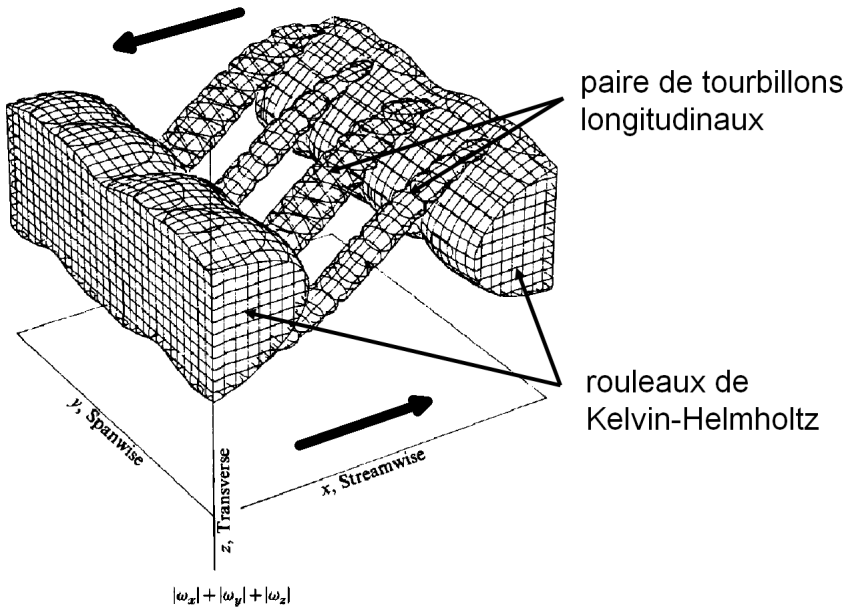

FIGURE 8 – Représentation de la somme des modules des composante de la vorticité par Metcalfe et al. [83] obtenue par un calcul DNS d'une couche de mélange. L'écoulement initial est une couche de mélange schématisée par les flèches.

Déterminer le mode le plus amplifié par une analyse de stabilité linéaire du champ moyen permet souvent de prédire l'aspect et la fréquence caractéristique spatiale ou temporelle de la structure cohérente dominante dans l'écoulement [47]. Toutefois, l'identification de tels modes doit reposer sur une comparaison entre le taux de croissance du mode de stabilité et celui de la structure cohérente forcée par une excitation de même fréquence. Sur ce point, le résultat n'est pas souvent convaincant [40].

En effet, l'amplification des modes d'instabilité linéaire dans les écoulements turbulents est modifiée par des interactions non-linéaires de ces structures entre elles et avec les autres échelles, ce qui finit par détruire la cohérence imposée par le forçage. Pour une revue des études qui traitent des mécanismes non-linéaires qui affectent les instabilités de Kelvin-Helmholtz, on pourra consulter Ho and Huerre [47]. Enfin, il est reconnu que la dynamique de ces structures cohérentes dépend fortement de conditions initiales comme en particulier le nombre de Reynolds, la nature des couches limites initiales, l'intensité et le contenu spectral des fluctuations résiduelles de l'écoulement [63].

0.2.3 Tourbillons longitudinaux

Couche de mélange plane

Comme cela a été extensivement décrit dans les couches de mélange planes, des tourbillons longitudinaux se superposent à l'instabilité primaire de Kelvin-Helmholtz [6, 9, 83]. La figure 8 représente la somme des modules des composantes de la vorticité dans une couche de mélange qui se développe, obtenue par simulation directe des équations de Navier-Stokes (DNS) par Metcalfe et al. [83]. Nous pouvons identifier les rouleaux de Kelvin-Helmholtz qui s'étendent dans la direction notée y sur la figure. On distingue aussi des tourbillons longitudinaux inclinés dans la région entre deux rouleaux de Kelvin-Helmholtz consécutifs. Des études théoriques ont permis d'identifier un mécanisme d'instabilité secondaire opérant sur les rouleaux issus de l'instabilité de Kelvin-Helmholtz [76, 90]. La longueur d'onde selon y des paires de tourbillons est fixée par l'épaisseur de

la couche de mélange et leur origine semble liée à l'étirement intense de perturbations de vorticité axiale dans la zone située entre deux rouleaux de Kelvin-Helmholtz consécutifs.

Couche de mélange axisymétrique

La figure 9 présente de haut en bas une série de coupes de différents écoulements de jet. Dans la colonne de gauche, la coupe s'effectue entre deux anneaux de Kelvin Helmholtz consécutifs. Lorsque l'on transpose ce type de coupe à la couche de mélange plane de la figure 8, cette coupe représente un plan $x = \text{cste}$ entre les deux rouleaux de Kelvin-Helmholtz consécutifs. Dans la colonne de droite de la figure 9, la coupe s'effectue au travers d'un anneau de Kelvin Helmholtz. La coupe équivalente de la couche de mélange plane de la figure 8 est une coupe à travers un rouleau de Kelvin Helmholtz par un plan $x = \text{cste}$ qui correspond au début ou à la fin de la figure 8. Martin and Meiburg [80] détaillent la croissance simultanée de perturbations axiales et azimutales dans un modèle d'une couche de mélange axisymétrique à l'aide d'une méthode de filaments de vorticité. Comme le montrent les figures 9 (a) et (b) issues de cette étude, on constate que la vorticité axiale se concentre dans la région entre deux anneaux de Kelvin-Helmholtz. Cette étude montre donc que la perturbation azimutale s'amplifie et se localise sous forme tourbillons dans la zone entre deux anneaux. Des tourbillons longitudinaux ont aussi étés observées expérimentalement, par Liepmann and Gharib [75] dans un jet à nombre de Reynolds modéré $Re_0 = 5500$, comme on peut le voir sur les figures 9 (c) et (d). Ces auteurs ont aussi mis en évidence l'importance dynamique de ces structures dans le processus d'entrainement, qui augmente de manière continue le débit de fluide mis en mouvement par le jet lorsqu'on s'éloigne de l'orifice de sortie.

Influence de la couche limite initiale

Les couches de mélange et les jets qui sont décrits ci-dessus ont la particularité de provenir de couches limites initialement laminaires. Les paires de tourbillons longitudinaux ont souvent dans ce cas une position fixe, qui est déterminée par des dissymétrie infimes de l'expérience. Ces tourbillons longitudinaux ne sont plus fixes lorsque les couches limites sont initialement turbulentes [5, 94]. De plus, l'étude par DNS effectuée par Rogers and Moser [102] d'une couche de mélange temporelle issue d'une couche limite turbulente montre qu'en l'absence d'un forçage organisant les rouleaux de Kelvin-Helmholtz, il devient difficile d'observer des tourbillons longitudinaux, même de manière instantanée. Dans une couche de mélange axisymétrique issue d'une couche limite turbulente Citriniti and George [22] ont mis en évidence par des observations du champ de vitesse axiale (réduit par POD) des perturbations azimutales évoquant la présence de paires tourbillons longitudinaux dans la région entre deux anneaux de Kelvin Helmholtz consécutifs. Deux de ces pseudo-visualisations sont présentées dans la figure 9 à travers la région entre deux anneaux de Kelvin Helmholtz consécutifs (e) et à travers un anneau de Kelvin-Helmholtz (f). Comme l'illustrent leurs travaux, une caractérisation quantitative et statistique des tourbillons longitudinaux semble effectivement nécessaire pour mieux les décrire dans les couches de mélanges issues de couches limites turbulentes.

Tourbillons longitudinaux dans d'autres écoulements cisaillés

Des tourbillons longitudinaux sont présents dans d'autres écoulements turbulents cisaillés, comme les cisaillements homogènes [101] et les couches limites [62]. Comme le

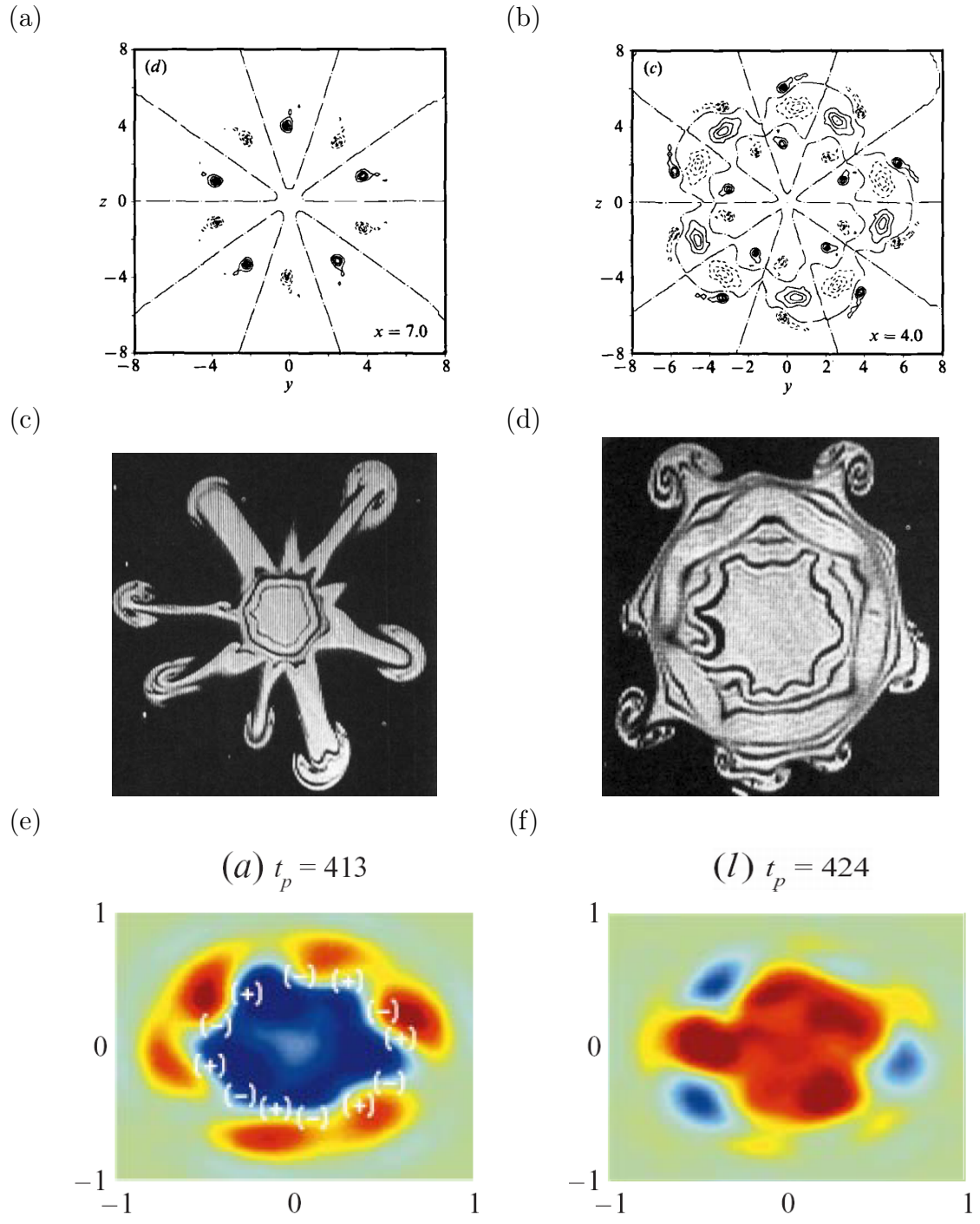

FIGURE 9 – Comparaison de différentes observations des tourbillons longitudinaux dans des couches de mélange axisymétriques mettant en évidence la robustesse du phénomène. La colonne de gauche est une coupe à travers la région entre deux anneaux de Kelvin-Helmholtz, celle de droite une coupe au travers d'un anneau. (a) et (b) : contours de vorticité axiale obtenus par simulation de filaments de vorticité (Martin and Meiburg [80], figure 12). (c) et (d) : visualisation de colorants pour $Re_0 = 5500$ (Liepmann and Gharib [75], figure 12). (e) et (f) : contours de fluctuation de vitesse axiale projetée sur une base POD (bleu=négatif, rouge=positif) pour $Re_0 = 8 \times 10^4$ (Citriniti and George [22], figure 13). Les signes (+) et (-) représentent la position hypothétique des tourbillons longitudinaux positifs et négatifs.

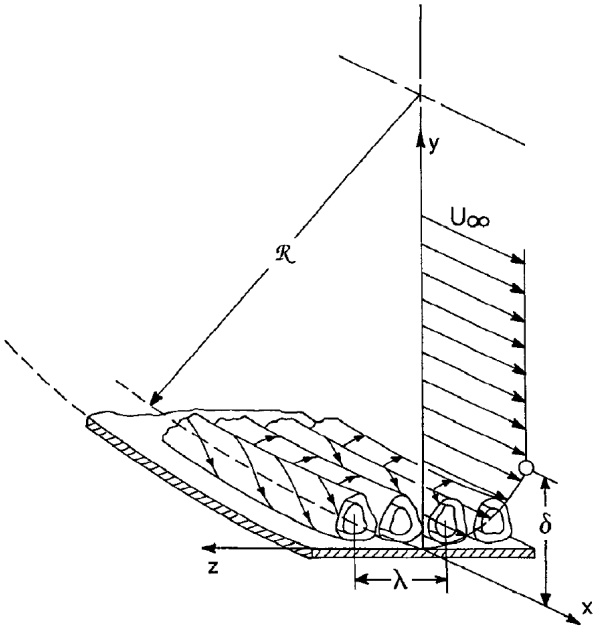

FIGURE 10 – Schéma issu de Saric [106] représentant des tourbillons de couche limite de Görtler sur une paroi concave.

décrit Townsend [116], un cisaillement moyen se décompose en une déformation irrotationelle d'étirement-compression et une rotation. Si on considère un champ turbulent initialement isotrope, l'application du cisaillement amplifie donc les fluctuations de vorticité dans la direction d'étirement, alors que la rotation réoriente cette vorticité en permanence. Ceci a pour effet de produire des tourbillons longitudinaux dont l'inclinaison dépend de la durée d'application du cisaillement, ceci avant qu'un équilibre ne soit atteint [101].

0.2.4 Effets de la courbure sur les structures cohérentes des écoulements cisaillés

Le critère d'instabilité centrifuge de Bradshaw de la section 0.1.3 permet de prédire qu'une couche limite se développant le long d'une paroi concave subit un effet de courbure déstabilisant. Une étude de stabilité montre qu'une instabilité centrifuge s'y manifeste par l'apparition de paires de tourbillons dits de Görtler [106]. Comme schématiquement représenté sur la figure 10, leur longueur d'onde transverse λ est de l'ordre de l'épaisseur de couche limite δ. Dans les couches limites turbulentes, des structures similaires sont parfois observées de manière intermittente, avec une position spatiale qui peut être fixe ou aléatoire, selon les conditions d'essais [2, 48].

Plesniak et al. [94] ont imposé une courbure stabilisante ou déstabilisante à une couche de mélange. Ces auteurs ont constaté que les tourbillons longitudinaux fixes de la couche de mélange étaient amplifiés par la courbure déstabilisante, et atténués par une courbure stabilisante. La courbure déstabilisante cause aussi une augmentation de l'énergie cinétique turbulente et du taux de croissance de la couche de mélange. Ces effets seront décrit dans la section 0.3. Loiseleux and Chomaz [77] ont étudié par une technique de visualisation l'évolution des instationnarités dans un jet tournant, avant le seuil d'éclatement. Ils ont observé que l'instabilité $m = 0$ de Kelvin-Helmholtz était atténuée par la rotation, et que la symétrie des tourbillons longitudinaux était brisée.

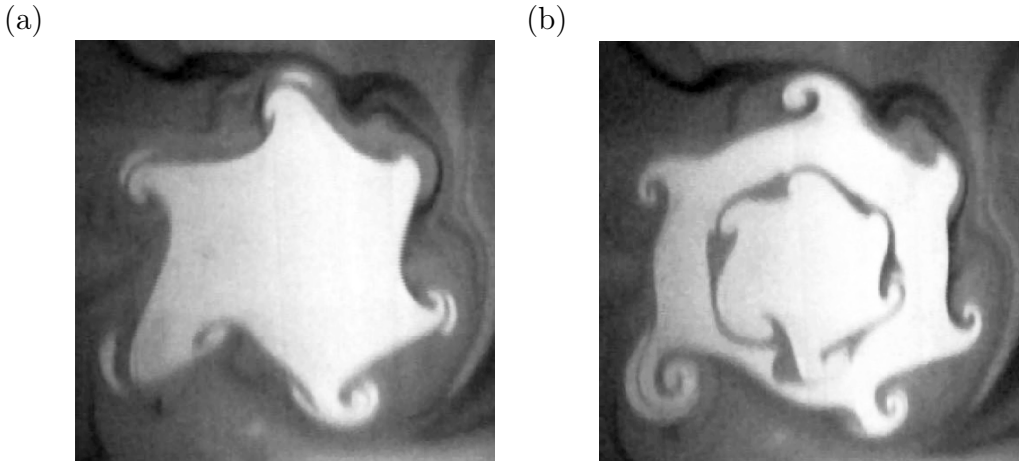

FIGURE 11 – Visualisations des tourbillons longitudinaux dans un jet tournant par Loiseleux and Chomaz [77]. (a) : coupe à travers la région entre deux anneaux de Kelvin Helmholtz consécutifs. (b) coupe à travers un anneau de Kelvin-Helmholtz. Le jet tourne ici dans le sens horaire.

La figure 11 présente une de leurs figures pour un nombre de swirl modéré de l'ordre de 0.4. La rotation de leur jet s'effectue dans le sens horaire. En effectuant une coupe dans un anneau de Kelvin-Helmholtz, on observe la présence de tourbillons tournant dans un sens antihoraire, ce qui est opposé à la rotation d'ensemble et donc dit anticyclonique, à l'extérieur et à l'intérieur de la couche de mélange. Enfin, une étude de la couche de mélange axisymétrique d'un jet tournant à plus haut nombre de Reynolds par McIlwain and Pollard [81] montre que le swirl désorganise les anneaux de Kelvin-Helmholtz mais semble renforcer les tourbillons longitudinaux. Ces résultats sont cohérents avec les conclusions de l'étude de jets tournants acoustiquement forcés de Panda and McLaughlin [92]. L'étude détaillée de l'effet de la rotation sur les tourbillons longitudinaux sera l'un des objets de ce travail.

0.2.5 Structures cohérentes de la turbulence homogène en rotation

Lors de la mise en rotation d'une turbulence initialement homogène, les tourbillons tendent à s'aligner avec l'axe de la rotation. Deux mécanismes qui mettent en jeu les ondes d'inertie sont proposés pour rendre compte de ce phénomène, l'un basé sur un mécanisme linéaire [112], l'autre non-linéaire [15]. Une prédominance des tourbillons cycloniques (dont la vorticité est de même signe que la rotation) est observée dans les expériences [50, 87]. Ceci peut s'expliquer par l'instabilité centrifuge des tourbillons anticycloniques [109]. Une autre explication serait que lors de l'étirement d'un tourbillon selon l'axe de rotation, la rotation ajoute une contribution à la vorticité des tourbillons cycloniques au détriment de la vorticité des tourbillons anticycloniques, comme mis en évidence par Gence and Frick [41].

0.3 Approche statistique de la turbulence dans les écoulements cisaillés et courbés

Dans cette section, nous abordons les effets de la courbure à l'aide d'une description statistique de la turbulence qui se base sur les équations de Navier-Stokes moyennées, donc plus proche d'une démarche de modélisation.

0.3.1 Turbulence cisaillée homogène

Cas de référence rectiligne

La turbulence cisaillée homogène fonde les modèles de turbulence [65], et ses propriétés sont bien décrites dans les ouvrages de référence [95, 116]. Dans le système de coordonnés cartésien (x, y, z), la vitesse moyenne s'écrit $(\frac{\partial u}{\partial y} y, 0, 0)$ et les fluctuations de la vitesse sont notés (u', v', w'). Dans cet écoulement homogène exempt de diffusion turbulente, l'équation de l'énergie cinétique turbulente k s'écrit :

$$\frac{Dk}{Dt} = -\langle u'v' \rangle \frac{\partial u}{\partial y} - \epsilon, \tag{3}$$

où la production $P = -\langle u'v' \rangle \frac{\partial u}{\partial y}$ résulte du travail de la tension de Reynolds $\langle u'v' \rangle$ sur le gradient moyen $\frac{\partial u}{\partial y}$, et où ϵ désigne le terme de dissipation. Comme le montre Pope [95], le long d'une ligne de courant, l'énergie cinétique turbulente croit exponentiellement avec un temps caractéristique $\tau_k = \frac{k}{\epsilon} / \left(\frac{P}{\epsilon} - 1\right)$. Typiquement, on a $\frac{P}{\epsilon} \approx 1.7$, $\langle u'v' \rangle / 2k \approx 0.14$ et $\frac{k}{\epsilon}$ est proportionnel à l'échelle de temps du cisaillement. L'équation qui gouverne $\langle u'v' \rangle$ s'écrit alors

$$\frac{D\langle u'v' \rangle}{Dt} = -\langle v^2 \rangle \frac{\partial u}{\partial y} + \Phi_{uv} - \epsilon_{uv}, \tag{4}$$

où $\Phi_{uv} = \frac{\partial}{\partial y} \left(\langle p'v' \rangle \rho \right)$ est un terme de corrélation pression-gradient de vitesse qui redistribue les fluctuations entre les composantes du tenseur de Reynolds et ϵ_{uv} un terme de dissipation. Nous avons pris soin de décrire dans le cas d'un cisaillement uniforme rectiligne l'énergie cinétique k et la tension de Reynolds $\langle u'v' \rangle$, qui sont à la base des modélisations de la turbulence. Nous utilisons maintenant ce cas de référence pour décrire l'effet de la rotation ou de la courbure sur cet écoulement.

Effet d'une courbure

Holloway and Tavoularis [49] ont étudié une turbulence homogène cisaillée le long d'une ligne de courant de rayon de courbure r_c schématisé sur la figure 6. On se place ici dans le repère curviligne (s, n, b) associé à une ligne de courant de vitesse moyenne u_s. L'équation gouvernant k dans ce repère s'écrit [13] :

$$\frac{Dk}{Dt} = -\langle u'_s u'_n \rangle (1 + e) \frac{\partial u_s}{\partial n} - \epsilon, \tag{5}$$

où le paramètre local de courbure $e = (u_s / r_c) / (\partial u_s / \partial n)$ a été défini dans la section 0.1.3. A première vue, cette équation suggère qu'une petite courbure e affectera les grandeurs turbulentes d'une variation relative de l'ordre de e, mais les effets observés sont souvent beaucoup plus intenses dans les expériences [13]. Celles-ci montrent notamment qu'une courbure déstabilisante a pour effet d'augmenter le facteur d'anisotropie $\langle u'_s u'_n \rangle / 2k$ de

manière importante, ce qui va contribuer à une augmentation supplémentaire de k. L'évolution de la tension de Reynolds est quant à elle régie par

$$\frac{D\langle u'_s u'_n\rangle}{Dt} = \left(-(1+e)\langle u'^2_n\rangle + 2e\langle u'^2_s\rangle\right)\frac{\partial u_s}{\partial n} + \Phi_{sn} - \epsilon_{sn}. \tag{6}$$

Dans le terme de production par le gradient de vitesse, l'approximation $\langle u'^2_n\rangle \approx \langle u'^2_s\rangle$ montre que l'apport direct de la courbure sera aussi d'ordre e, et donc ne permet toujours pas d'expliquer une augmentation plus importante. Il est donc nécessaire de considérer les corrélations pression-gradient de vitesse $\Phi_{sn} = \frac{\partial}{\partial n}\left(\langle p' u'_n\rangle/\rho\right)$ et la dissipation ϵ_{sn}. Les expériences [49] confirment qu'une courbure déstabilisante affecte les corrélations pression-gradient de vitesse en faveur de $\langle u'_s u'_n\rangle$, alors que la dissipation décroît légèrement. Une prédiction correcte des effets de courbure doit donc s'appuyer sur une modélisation des effets de courbure sur les termes de corrélation pression-gradient de vitesse tels Φ_{sn}, qui affectent l'anisotropie du tenseur de Reynolds. C'est ce que peuvent réaliser les modèles de turbulence de type Reynolds stress model (RSM) [45, 65, 111]. Une approche linéaire de type distorsion rapide (RDT) corrigée de manière ad hoc pour tenir compte des non-linéarités permet également d'assez bien rendre compte de la sensibilité de ce terme à la rotation cf. Salhi and Cambon [105]. Ceci signifie que des mécanismes linéaires tels les instabilités centrifuges et les ondes de Kelvin se cachent derrière la forte sensibilité de la turbulence cisaillée en présence de courbure, ou de la rotation.

0.3.2 Couche de mélange turbulente

Cas de référence rectiligne

La couche de mélange est aussi un écoulement très largement documenté dans les ouvrages de référence [95, 114, 116]. Nous résumons brièvement quelques généralités. En aval d'une zone de transition issue directement de la couche limite initiale, l'intensité turbulente se stabilise et atteint une valeur d'équilibre. Au vu du faible épaississement de l'écoulement, une hypothèse de couche mince peut être introduite et conduit à simplifier les équations qui régissent cet écoulement libre. Il est alors facile de montrer que la couche de mélange est un écoulement auto-semblable : toutes les grandeurs ont un profil semblable qui ne dépend que de y/δ et donc de largeur δ, qui croit linéairement. Une démonstration rigoureuse, détaillée par George [42], fait appel à l'équation de k pour démontrer la croissance linéaire de δ. Cette équation s'écrit dans l'hypothèse de couche de mélange :

$$\frac{Dk}{Dt} = -\langle u'v'\rangle\frac{\partial u}{\partial y} - \frac{\partial}{\partial y}\left(< (k' + \frac{p'}{\rho})v' >\right) - \epsilon. \tag{7}$$

Par rapport à l'équation (3) de k pour le cisaillement homogène, on remarque l'apparition du terme de transport de la fluctuation d'énergie par les fluctuations de vitesse radiale et de pression. L'analyse de similitude permet alors d'obtenir :

$$\frac{d\delta}{dx} \propto \frac{R_s}{K_s} \propto \frac{R_s}{u_0^2} \propto \frac{T_s}{u_0^3} \propto \frac{D_s\delta}{u_0^3}, \tag{8}$$

où R_s, K_s, T_s, D_s sont respectivement les échelles asymptotiques de la tension de Reynolds $\langle u'v'\rangle$, de l'énergie cinétique k, des corrélations $< (k' + \frac{p'}{\rho})v' >$, et de la dissipation. Lorsque l'écoulement est auto-semblable, on peut montrer que $\frac{d\delta}{dx}$ ainsi que chacun de ces termes doivent être constants. Ceci implique que la dissipation est indépendante

de la viscosité, ce qui n'est vérifié que si l'écoulement est pleinement turbulent, auquel cas $D_s \propto \frac{u_0^3}{\delta}$. Enfin, contrairement à certaines idées couramment admises, il faut noter que les écoulements auto-semblables ne sont pas indépendants des conditions initiales. C'est même plutôt l'inverse comme en témoigne la grande dispersion des taux de croissance et des valeurs stabilisées des quantités obtenues lors des expériences et des calculs [55, 56, 63]. Mais ceci ne contredit pas pour autant l'hypothèse d'auto-similitude [42].

Effet d'une courbure

Des études expérimentales ont décrit l'effet d'une courbure sur les couches de mélange [16, 79, 94]. Les équations qui gouvernent k, et les composantes du tenseur de Reynolds, sont modifiées de manière similaire à l'équation (5) [13]. Comme pour le cas du cisaillement, une faible courbure déstabilisante peut entraîner une augmentation conséquente de l'activité turbulente et de l'anisotropie $\langle u_s' u_n' \rangle / 2k$. Le taux de croissance de la couche de mélange est alors supérieur, comme le suggère la relation (8).

0.3.3 Jets tournants turbulents

Cas de référence non-tournant

Pour terminer cette revue bibliographique, nous présentons certains des effets de la rotation sur les jet turbulents. Comme nous l'avons montré au début de ce chapitre, un jet issu d'un profil de vitesse bouchon se décompose schématiquement en trois zones. Tout d'abord, une couche de mélange axisymétrique se développe entre le coeur potentiel de vitesse U_0 et l'écoulement au repos. Localement, cette zone peut être décrite comme une couche de mélange plane. La seconde zone est la transition de la couche de mélange axisymétrique. Les deux premières zones représentent le champ proche du jet. La troisième et dernière zone est l'écoulement de jet développé, qui s'appelle aussi le champ lointain. Dans cette dernière zone, de même que pour la couche de mélange, une analyse auto-semblable [1, 95] mène à une croissance linéaire de la largeur du jet. On peut se référer aux études de Hussein et al., Wygnanski and Fiedler [57, 122] pour une vérification expérimentale détaillée de cette hypothèse. L'échelle de vitesse décroît comme l'inverse de la distance à l'origine $(z - z_0)$, conformément à la conservation de l'intégrale du flux de quantité de mouvement par unité de masse G_z, qui s'écrit, dans l'hypothèse de couche mince et en négligeant les moments d'ordre deux :

$$G_z = 2\pi \int_0^{+\infty} u_z^2 r \mathrm{d}r. \tag{9}$$

Le débit local par unité de masse noté $\dot{M}$ et défini par

$$\dot{M} = 2\pi \int_0^{+\infty} u_z r \mathrm{d}r, \tag{10}$$

augmente alors linéairement avec $(z - z_0)$, ce qui permet une caractérisation de la capacité d'entraînement des jets.

Effets de la rotation

Pour un jet tournant, la projection radiale des équations de Navier-Stokes montre que la composante de vitesse azimutale u_θ réduit la pression dans le jet et l'intégrale du

flux de de quantité de mouvement devient :

$$G_z = 2\pi\rho \int_0^{+\infty} u_z^2 - \frac{u_\theta^2}{2} r \mathrm{dr}. \tag{11}$$

L'intégrale du flux de moment angulaire G_θ s'écrit quant à elle

$$G_\theta = 2\pi\rho \int_0^{+\infty} u_z u_\theta r^2 \mathrm{dr}. \tag{12}$$

Ces deux quantités sont conservées axialement lors de la mise en rotation du jet, et peuvent être utilisées pour bâtir un nombre de swirl intégral, sous la forme :

$$S_I = \frac{2G_\theta}{G_z D_0}. \tag{13}$$

Comme le soulignent Farokhi et al. [32], plusieurs profils de u_z et u_θ peuvent correspondre à une même valeur de S_I. La génération de l'écoulement tournant par des moyens variés comme des ailettes [89, 92], des injections tangentielles de fluide [19, 32, 44], un écoulement de Poiseuille tournant [31, 98, 103] ou encore un nid d'abeille tournant [10, 74] conduit en particulier à des écoulement initialement assez différents. Cependant, G_z et G_θ sont constants alors que l'échelle locale D augmente linéairement à cause de la croissance du jet. Le nombre de swirl local tend alors vers zéro comme $1/z$. L'échelle caractéristique de vitesse azimutale décroît quant à elle comme $1/z^2$ [30], comme le confirme l'expérience de Shiri et al. [108].

Problématiques des jets tournants turbulents

Si les effets du swirl tendent à disparaitre vers l'aval du jet, ils ont une action importante sur le champ proche, et celle-ci est d'autant plus difficile à prévoir que les mécanismes d'instabilités peuvent varier selon les types de profils de vitesse initiaux. Différentes études ont constaté une augmentation de la turbulence, du taux de croissance et de l'entrainement du jet dans le champ proche des jet tournant [44, 89, 92]. De manière quelque peu surprenante, peu de travaux sont disponibles sur l'effet de la rotation sur les couches de mélange axisymétriques. Mehta et al. [82] ont généré une couche de mélange axisymétrique de jet tournant, et ont étudié deux valeurs d'un nombre de swirl basé sur la vitesse azimutale maximale $S = 0.2$ $S = 0.4$, en plus du cas de référence $S = 0$. Le taux de croissance augmente seulement pour $S = 0.4$. Ces auteurs détaillent l'évolution des tensions de Reynolds qui augmentent toutes avec le swirl. Outre l'observation d'oscillations dans la direction axiale d'origine indéterminée de certaines tensions de Reynolds, la configuration expérimentale de Mehta et al. ne fournit pas à la turbulence une distance de développement suffisante pour atteindre un état d'équilibre proche de l'auto-similitude, ce qui ne permet pas de décrire la production turbulente de manière complète. Malgré l'étude de McIlwain and Pollard [81], un lien entre l'évolution des structures cohérentes de l'écoulement et celle des statistiques de la turbulence comme le tenseur de Reynolds n'a pas été clairement établi.

Au-delà d'une valeur critique du nombre de swirl, un éclatement tourbillonnaire, similaire à celui qui est observé à bas nombre de Reynolds, altère profondément la nature de l'écoulement [19, 92]. Un déficit de vitesse apparait sur l'axe du jet, et l'intensité de la turbulence peut devenir très élevée. A la différence des études de jet tournant à bas nombre de Reynolds [10, 74], voir section 0.1.4, il n'existe à notre connaissance

pas de caractérisation paramétrique fine du phénomène d'éclatement à haut nombre de Reynolds.

La soufflerie R4Ch du centre ONERA de Meudon, qui sera présentée dans le chapitre 1, permet de générer un écoulement à haut nombre de Reynolds en rotation solide avec une vitesse angulaire qui peut être précisément fixée. Elle semble donc idéalement adaptée à l'étude de jets tournants. Une précédente thèse utilisant cette installation a permis de comprendre pourquoi seulement certaines configurations expérimentales de génération du jet tournant permettaient d'obtenir des conditions initiales contrôlées [68]. C'est dans ce contexte que cette thèse a débuté.

0.4 Organisation du manuscrit

0.4.1 Démarche de l'étude

Cette thèse a commencé avec l'ambition de couvrir, si le temps imparti le permettait, l'ensemble des régimes d'un jet turbulent, depuis le jet classique vers les jets modérément tournants, jusqu'à l'éclatement. Les deux premières études se sont alors révélées suffisamment riches pour que nous y consacrions toute cette thèse et l'éclatement tourbillonnaire n'a pas été traité.

Une configuration expérimentale a d'abord été déterminée dans le but d'étudier les effets d'une rotation modérée sur une couche de mélange axisymétrique. Par rapport à l'écoulement étudié par Mehta et al. [82], nous avons décidé de mettre au point une configuration expérimentale permettant d'obtenir une turbulence proche d'un état d'équilibre en générant une couche de mélange initialement plus fine. De plus, nous explorons une gamme de nombres de swirl plus large de manière paramétrique en variant la vitesse de rotation du jet.

Une fois que la configuration d'essai fut fixée, l'étude des résultats des campagnes de mesures, en particulier celle réalisée par PIV à haute-cadence, s'est révélée très riche. Nous avons alors cherché à comprendre les phénomènes que nous observions et nous les avons comparés avec ceux décrits dans la littérature, notamment ceux sur le jet non-tournant. Nous avons alors identifié certaines problématiques pour lesquelles un éclairage nouveau pourrait être utile. Tout d'abord, la dynamique du mode $m = 1$ a souvent été moins décrite que celle du mode $m = 0$ [115]. Ensuite, comme nous l'avons montré dans la sous-section 0.2.3, l'étude des tourbillons longitudinaux dans les couches de mélanges turbulentes axisymétrique nécessite d'être approfondie sur un plan quantitatif. Ces deux points ont étés naturellement intégrés dans notre travail.

0.4.2 Plan

Notre démarche d'étude reste résolument expérimentale. Dans une première partie, nous tâcherons d'apporter un soin particulier à la description des moyens expérimentaux. Le chapitre 1 décrit la soufflerie de jet tournant R4Ch, et détaille les choix qui ont mené à la configuration d'essais. Le chapitre 2 présente la mesure de l'écoulement par PIV. Nous décrivons le principe de cette technique, ainsi que sa mise en oeuvre pratique. L'algorithme de dépouillement, auquel nous avons contribué, est présenté dans l'annexe A. Une étude des incertitudes de mesure est proposée dans l'annexe B.

Dans une deuxième partie, nous présentons les résultats obtenus sous la forme d'articles. Dans le chapitre 3, nous proposons une méthode expérimentale qui détermine les

vitesses de convection de structures turbulentes à travers le plan de mesure de PIV à haute cadence, qui est transverse à l'écoulement. La validité de l'hypothèse de Taylor est évaluée pour le jet sans rotation et le jet tournant. Cette étude permet de valider la reconstruction de l'organisation spatiale des structures cohérentes, que nous utilisons pour décrire la dynamique de la couche de mélange axisymétrique dans le chapitre 4. Une interaction entre les modes $m = 0$ et $m = 1$, les tourbillons longitudinaux et le cisaillement moyen est considérée. Enfin, le chapitre 5 aborde les effets du swirl sur la couche de mélange axisymétrique sous plusieurs aspects. Nous décrivons ses effets sur le développement du jet dans son ensemble, sur la production de la turbulence dans la couche de mélange ainsi que sur la dynamique des tourbillons longitudinaux. Le manuscrit s'achève par une conclusion synthétisant les travaux présentés et proposant des perspectives pour de futures études.

Première partie

Moyens expérimentaux

1 La soufflerie R4Ch

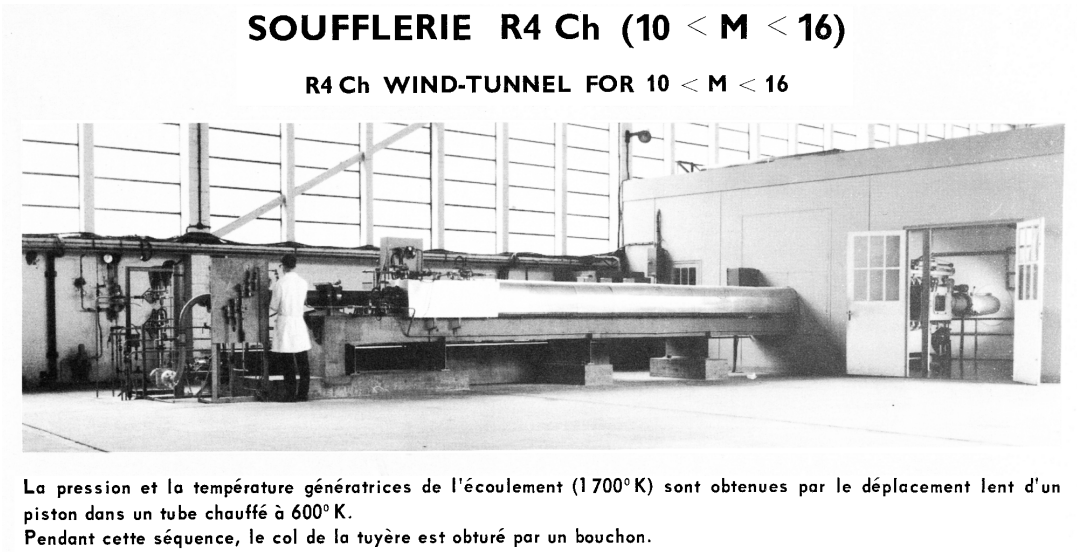

FIGURE 1.1 – Photographie antérieure à 1969 de la soufflerie hypersonique R4Ch de Meudon [91].

1.1 Historique

La soufflerie R4Ch est l'ancienne soufflerie hypersonique à rafale numéro 4 du centre ONERA de Chalais-Meudon. Elle fut modifiée au début des années 80 pour devenir une soufflerie basse vitesse dédiée à l'étude de distorsions sur une turbulence homogène. A cet effet, la particularité de cette soufflerie est de posséder une section tournante comprenant un nid d'abeille, ce qui permet d'imposer une rotation solide à l'écoulement. L'effet de la rotation sur une turbulence homogène a été étudié lors de la thèse de Laurent Jacquin [59, 60]. D'autres études ont ensuite été menées pour étudier les effets d'autres distorsions [29]. Enfin, un dernier chapitre de l'histoire de cette installation s'est ouvert avec l'étude des jets tournants. Les premières études se sont heurtées à l'apparition inexpliquée de turbulence dans le plan de sortie du jet, au-delà d'une certaine valeur du nombre de swirl [59, 96]. La thèse de Benjamin Leclaire [68] a permis de comprendre l'apparition d'une dynamique sous-critique dans l'écoulement tournant de conduite. Cette dynamique est responsable des turbulences observées dans le plan de sortie lorsqu'une contraction est utilisée en aval du nid d'abeille [69]. Nous reviendrons dans la sous-section 1.3 sur ce phénomène, que nous avons cherché à éviter afin de générer une couche de mélange axisymétrique de jet tournant mince et avec un coeur potentiel non turbulent.

(a)

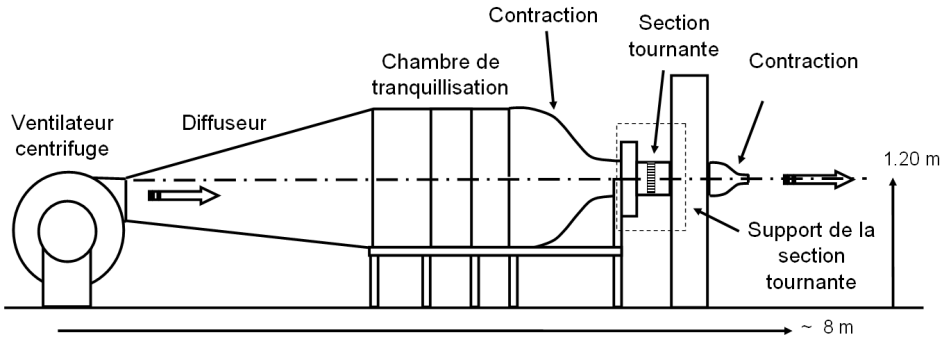

(b)

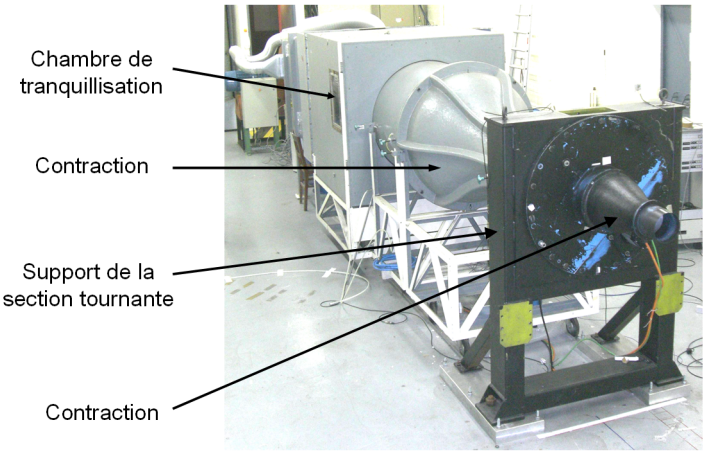

(c)

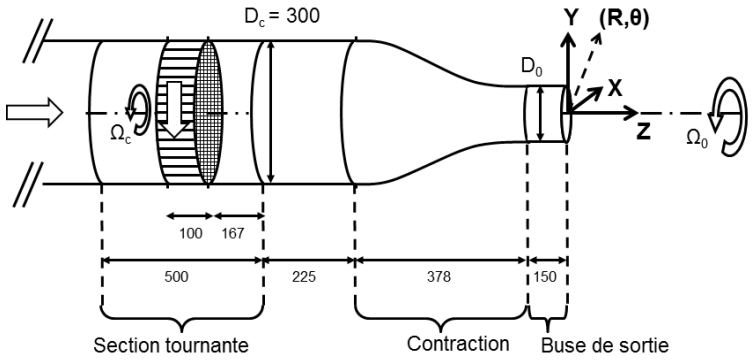

(d)

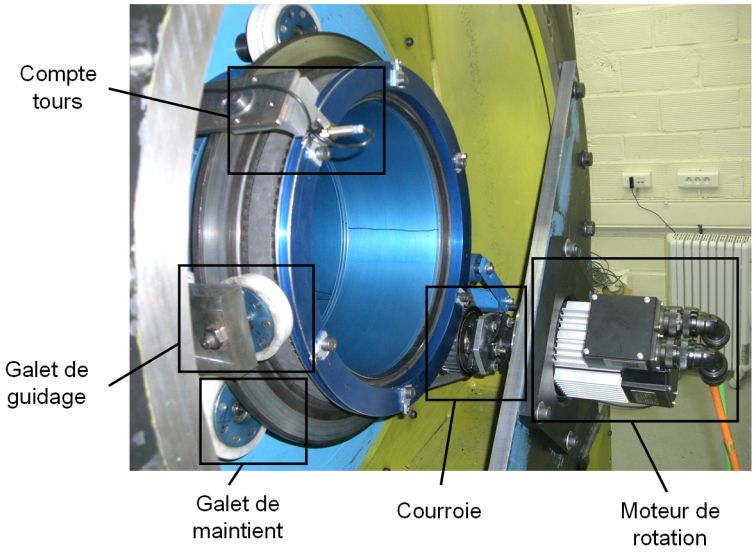

FIGURE 1.2 – La soufflerie R4Ch actuelle : (a) schéma d'ensemble, (b) vue en perspective depuis l'aval, (c) schéma détaillé de la section aval (dimensions sont en mm) et (d) éléments de la section tournante lors d'un démontage d'une partie de son support (en noir sur la figure (b)).

1.2 Fonctionnement de l'installation

1.2.1 Description

La figure 1.2 montre un schéma d'ensemble et une vue de la soufflerie. Un ventilateur centrifuge engendre un écoulement qui est ralenti dans un diffuseur vers une chambre de tranquillisation dont la section est un carré de côté $1m$ et qui comporte des éléments filtrants. Ensuite, une première contraction accélère l'écoulement vers une conduite cylindrique de diamètre $D_c = 0.3m$. Dans cette conduite se trouve la section tournante de longueur $L_t = 0.5m$ qui comprend le nid d'abeille de longueur $10cm$ et de maille $1.5mm$. La géométrie de cette section est schématisée sur la figure 1.2 (c) . La section tournante est maintenue par six points de contact à l'extérieur de la conduite, constitués de deux triplets de galets en téflon montés sur des roulements à billes. Une paire supplémentaire de galets en contact avec un rail azimutal guide la section afin de limiter les déplacements horizontaux. L'ensemble est entrainé par une courroie (facteur de démultiplication de 3.3) mue par un moteur tournant à la vitesse angulaire Ω_m. Certains de ces éléments sont illustrés dans la figure 1.2 (d). La commande numérique du moteur permet de fixer la vitesse angulaire $\Omega_c = \Omega_m/3.3$ de la section tournante, qui peut atteindre 1000 rpm . La mesure de la vitesse de rotation moyenne obtenue par un compte-tours à induction est en parfait accord avec la consigne, des fluctuations de vitesse angulaire n'excédant pas 1% de cette valeur.

En aval de la section tournante se trouve une autre portion de section fixe et de même diamètre $D_c = 0.3m$, qui peut être prolongée par des éléments amovibles. Le jet débouche alors dans le milieu au repos de la pièce, mais il est possible d'adjoindre une contraction vers un diamètre de sortie D_0 inférieur à D_c (rapport de surface $\chi = \frac{D_c^2}{D_0^2}$) pour accélérer à nouveau l'écoulement.

1.2.2 Echelle de vitesse axiale U_0

Lorsque que l'écoulement est mis en rotation, on ne peut plus se référer aux sondes de Pitot internes à l'installation pour mesurer la vitesse axiale. De plus, le profil de vitesse axial se déforme [3, 68], ce que nous détaillerons ultérieurement. Suite à la thèse de B. Leclaire, il est donc apparu que le débit serait un paramètre de contrôle expérimental pertinent. Un débitmètre venturi a donc été donc installé à l'amont du ventilateur, comme on peut le voir sur la figure 1.3 (a). Lors d'une étude préliminaire, il a été constaté que l'utilisation de ce système nuisait à la qualité de l'écoulement car il engendrait des fluctuations du débit inexpliquées à de basse fréquences. Grâce à des visualisations par injection de fumée, nous avons identifié qu'un battement se produisait à l'intérieur du débitmètre. Nous avons supposé que ceci pouvait être lié à une captation chaotique par la prise d'air, ou à un décollement survenant dans le diffuseur à l'aval de la section étroite du débitmètre. Nous avons résolu ce problème en réalisant un nouveau débitmètre aux formes plus arrondies et comportant un nid d'abeille à l'amont, voir la figure 1.3 (b). Le débit a alors été déterminé à l'aide de deux mesures de pressions statiques affleurant la paroi du débitmètre en deux endroits où la section est différente, comme schématisé dans la figure 1.3 (c). Dans l'hypothèse d'un écoulement uniforme de vitesse U_A dans la section initiale de diamètre $D_A = 0.3m$ et de vitesse U_B dans la section qui suit, de diamètre $D_B = 0.15m$, la conservation du débit théorique $\dot{M}^{\text{théo}}$ s'écrit :

$$\dot{M}^{\text{théo}} = \frac{\pi}{4} U_A D_A^2 = \frac{\pi}{4} U_B D_B^2. \tag{1.1}$$

(a) (b)

(c)

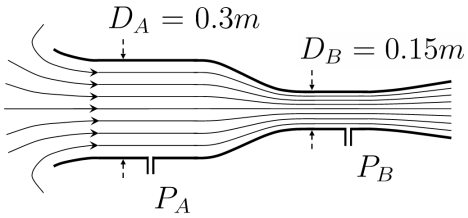

FIGURE 1.3 – Débitmètre Venturi de départ (a) et version améliorée installée (b), ainsi qu'un schéma de principe (c).

En supposant alors le fluide parfait, l'application de la relation de Bernoulli sur la ligne de courant tangente à la paroi entre les points A et B permet d'écrire :

$$P_A + \frac{1}{2}\rho U_A^2 = P_B + \frac{1}{2}\rho U_B^2, \tag{1.2}$$

d'où :

$$\dot{M}^{\text{théo}} = \frac{\pi}{4}\sqrt{\frac{2\Delta P}{\rho}}\frac{D_A^2 D_B^2}{\sqrt{D_A^4 - D_B^4}}. \tag{1.3}$$

La différence $\Delta P = P_A - P_B$ est mesurée par un capteur de pression différentiel à membrane. Le choix d'un capteur adapté aux vitesses considérées est important pour limiter aux maximum l'incertitude de mesure. Ici la différence de pression est de l'ordre de $300Pa$, nous avons donc choisi un capteur Statham de gamme 0.05 PSI. La masse volumique ρ est déterminée en utilisant la loi des gaz parfait. Ceci nécessite alors une mesure de la pression atmosphérique P_a, et de la température de l'écoulement T_0, obtenue avec un thermocouple et une sonde de type PT-100. Dans la pratique, la relation (1.3) n'est pas exacte, notamment à cause de la croissance d'une couche limite dans le dispositif. Le débit réel de l'écoulement dans le débitmètre s'écrit :

$$\dot{M} = K\dot{M}^{\text{théo}}, \tag{1.4}$$

où K est un coefficient de décharge tabulé [36] de l'ordre de 0.9 pour ce type de débitmètre. Entre le débit $\dot{M}$ obtenu à l'amont du ventilateur et le débit en sortie de l'installation noté $\dot{M}_0$, il y a aussi la possibilité de faibles fuites à travers certains éléments de la soufflerie. Nous avons donc choisi de déterminer expérimentalement K' tel que

$$\dot{M}_0 = K'\dot{M}^{\text{théo}}. \tag{1.5}$$

Nous avons alors obtenu $K' = 0.93$ dans les conditions d'essai. La vitesse de débit en sortie est alors définie par :

$$U_0 = \frac{\dot{M}_0}{\pi D_0^2/4}. \tag{1.6}$$

Nous verrons que les mesures par PIV du débit $\dot{M}_0^{\mathrm{PIV}}$ dans le plan de sortie confirment que $\dot{M}_0 \approx \dot{M}_0^{\mathrm{PIV}}$.

1.2.3 Paramètre de rotation S

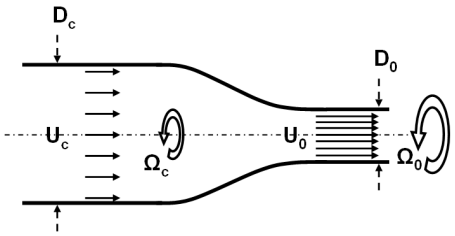

FIGURE 1.4 – Schéma de la contraction d'un écoulement tournant.

La figure 1.4 offre une vue schématique de l'effet de la contraction de taux $\chi = \frac{D_c^2}{D_0^2}$ sur l'écoulement tournant à la vitesse Ω_c dans la section de diamètre D_c à l'aval du nid d'abeille. L'écoulement amont à la contraction, de vitesse de débit $U_c = U_0/\chi$ est caractérisé par le nombre de swirl amont,

$$S_c = \frac{\Omega_c D_c/2}{U_c}, \tag{1.7}$$

l'écoulement aval étant caractérisé par le nombre de swirl de sortie

$$S_0 = \frac{\Omega_0 D_0/2}{U_0}. \tag{1.8}$$

En supposant pour simplifier, qu'à l'amont et à l'aval de la contraction l'écoulement est axial, uniforme et en rotation de corps solide, la conservation du flux de moment angulaire impose que $\Omega_0 = \chi\Omega_c$. La contraction a donc pour effet de multiplier la vitesse axiale et la vitesse angulaire par χ mais de diviser le diamètre par $\sqrt{\chi}$. Le nombre de swirl de sortie est donc inférieur au nombre de swirl de conduite ($S_0 = S_c/\sqrt{\chi}$). Nous bâtissons alors un nombre de swirl S qui sera notre paramètre de contrôle expérimental :

$$S = \frac{\chi\Omega_c D_0/2}{U_0}. \tag{1.9}$$

Cette expression fait intervenir une estimation $\Omega_0 \approx \chi\Omega_c$ de la vitesse angulaire de sortie ainsi que la vitesse de débit en sortie du jet U_0. Il d'agit donc d'un nombre de swirl représentatif de l'écoulement en sortie. Les mesures PIV réalisées dans le plan de sortie nous permettrons de montrer que $S_0 \approx S$.

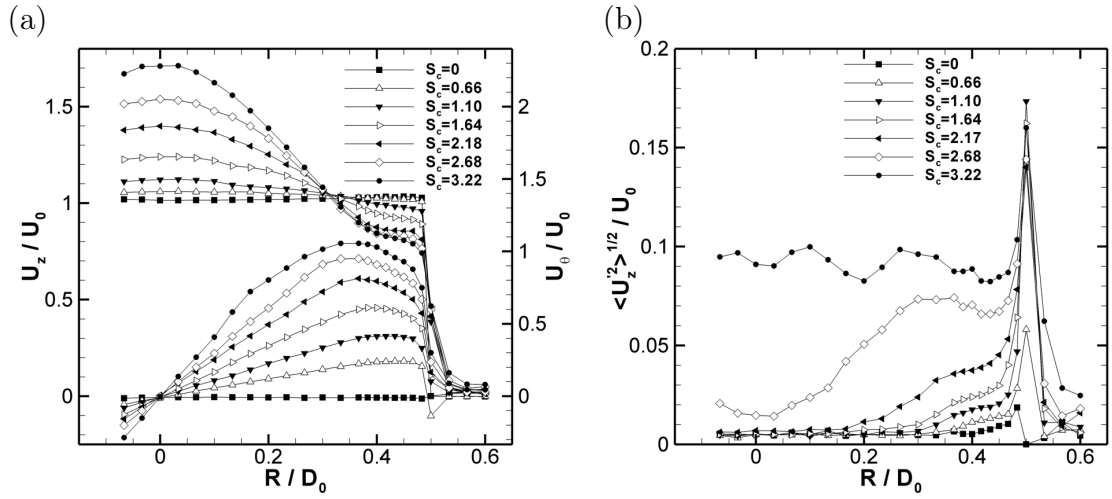

FIGURE 1.5 – (a) : Vitesse axiale et azimutale moyenne U_z et U_θ dans le plan de sortie du jet (normalisé par U_0), pour différentes valeurs du nombre de swirl de conduite S_c et pour $\chi = 4$. (b) : profil radial du taux de turbulence axial. Mesures au fil chaud d'après B. Leclaire [68, 69] pour $U_0 \approx 11.5 m.s^{-1}$.

1.3 Définition de la configuration d'essai

1.3.1 Choix d'une contraction

Avantages...

Comme décrit dans l'introduction, section 0.4.1, notre objectif est de réaliser une expérience sur l'effet de la rotation sur une couche de mélange axisymétrique. Au début de ce travail, nous disposions de conduits de contractions tels que $\chi = 1, 4, 9$ et 18.4. L'utilisation de contractions est courante dans les souffleries, en particulier pour générer des jet. Au premier abord, elles offrent plusieurs avantages qui sont par ordre d'importance :

1. Une réduction du rapport entre l'épaisseur de couche limite sur le diamètre de sortie θ/D_0, grâce à un fort gradient de pression favorable. Ceci est utile pour atteindre une turbulence cisaillée en équilibre dans la couche de mélange. En effet, la distance nécessaire pour atteindre l'équilibre des tensions turbulentes est proportionnelle à θ_0 [11].
2. Une réduction du taux de turbulence résiduel en sortie, comme on peut le montrer au moyen d'une approche de type distorsion rapide [4].
3. Une réduction du rapport entre le diamètre du jet et les distances qui fixent les conditions aux limites. La distance de $1.20m$ entre l'axe du jet et le sol représente $4D_0$ pour $\chi = 1$, $8D_0$ pour $\chi = 4$... Ainsi, pour un débit caractéristique de la plage d'utilisation, la prise d'air du ventilateur cause un courant de retour dissymétrique de l'ordre de $0.1 m.s^{-1}$. Gardant le débit fixé, utiliser une contraction augmente la vitesse de sortie et donc diminue l'impact de ce courant de retour.
4. Une réduction de la taille des champs de mesurés par PIV. La mesure PIV dans l'air se révèle problématique lorsqu'il faut illuminer des champs de taille supérieure à $300mm$ avec l'énergie des pulses laser.

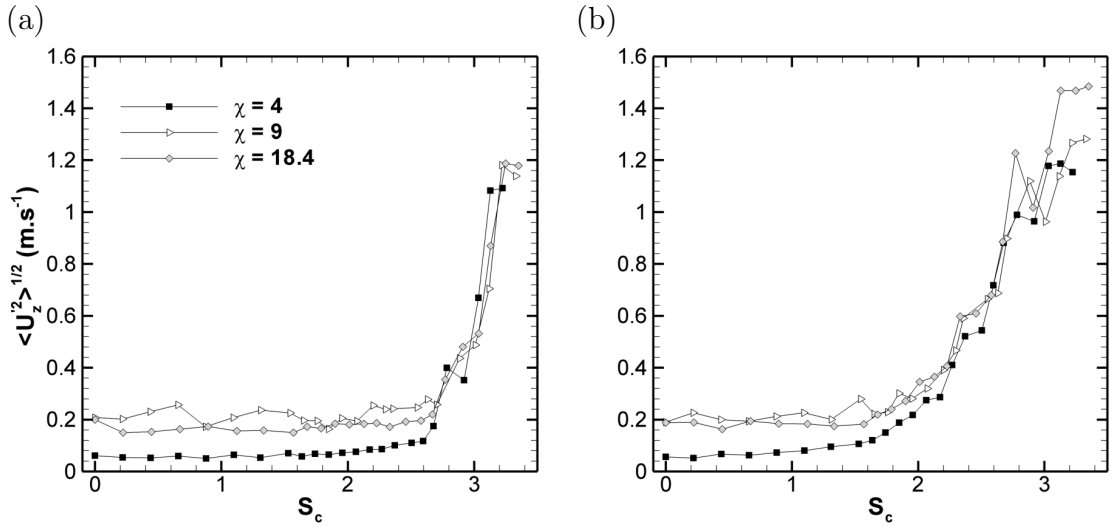

FIGURE 1.6 – Evolution de la rms de la vitesse axiale en fonction du swirl de conduite S_c, en $R/D_0 = 0$ (a) et $R/D_0 = 0.3$ (b) et pour différents taux de contraction χ. Mesures au fil chaud d'après B. Leclaire [68, 69] pour $U_0 \approx 11.5 m.s^{-1}$.

...Inconvénients

La figure 1.5 présente les profils de vitesse axiale et azimutale moyenne (a), ainsi que le taux de turbulence axial (b) en sortie du jet obtenus par B. Leclaire [68, 69] pour $\chi = 4$ par des mesures au fil-chaud, et pour différentes valeurs de S_c. Le profil de vitesse axiale moyenne est initialement en forme de "bouchon" et se déforme sous l'action de la rotation. Comme expliqué par Batchelor [3], cette déformation du profil de vitesse axiale provient d'un effet de gauchissement de la vorticité axiale durant la contraction de écoulement tournant. La figure 1.5 (b) montre que le taux de turbulence associé à la composante axiale de la vitesse augmente avec le swirl de conduite S_c, d'abord dans une zone adjacente à la paroi pour $S_c \leq 1.64$, puis dans l'ensemble du jet, pour $S_c \geq 2.17$. Le taux de turbulence est alors élevé, proche de 10% dans l'ensemble du jet. Alors qu'il semble possible d'attribuer l'augmentation du taux de turbulence près la paroi à un mécanisme d'instabilité centrifuge en lien avec la décroissance du moment angulaire dans cette région, l'apparition de turbulence dans le coeur du jet est surprenante. Une brève revue bibliographique révèle que ce phénomène est aussi observé dans d'autres expériences lorsqu'une contraction est employée [64, 92, 107]. Il est parfois attribué au mécanisme de mise en rotation de l'écoulement [92]. Une telle condition initiale est gênante en regard de notre projet qui est décrire la dynamique propre de la couche de mélange axisymétrique.

La figure 1.6, due à B. Leclaire, représente l'évolution de la rms de la vitesse axiale en sortie du jet sur l'axe de la conduite ($R/D_0 = 0$) (a) et pour $R/D_0 = 0.3$ (b), en fonction de S_c et pour différents taux de contractions χ. Cette figure révèle que l'apparition de turbulence dans le plan de sortie est pilotée par le swirl S_c de la conduite amont à la contraction et non par le nombre de swirl de sortie S, et ce indépendamment du taux de contraction χ utilisé. Comme démontré dans les références [68–70], l'origine physique de ce phénomène est liée à l'apparition de nouveaux mécanismes d'instabilités centrifuges généralisées et de nouvelles structures cohérentes de grande échelle dans le coeur de l'écoulement, suite à l'apparition d'ondes de Kelvin axisymétriques stationnaires de grande amplitude dans la conduite pour $S_c \geq 2$. Si l'on souhaite obtenir une configura-

tion expérimentale de jet tournant pour laquelle ces phénomènes n'apparaissent pas, en considérant le cas le plus défavorable, donc à $R/D_0 = 0.3$ (figure 1.6 (b)), il faut alors se placer dans la limite $S_c \leq 1.6$. Ceci limite donc le nombre de swirl qu'il est possible d'atteindre en sortie à la valeur $S_0 \leq \frac{1.6}{\sqrt{\chi}}$. Le choix $\chi = 4$ permet alors de couvrir la gamme la $0 \leq S_0 \leq 0.8$ tout en bénéficiant de l'avantage d'utiliser une contraction.

1.3.2 Choix portant sur la vitesse et sur la nature des couches limites en sortie

Nous devons maintenant fixer l'échelle de vitesse U_0 définie en section 1.2.2. Des contraintes expérimentales limitent sa valeur. Par exemple, chercher à résoudre la dynamique instationnaire du jet avec une fréquence d'acquisition maximale du système PIV $F_{acq} \approx 3kHz$ ou vouloir atteindre $S = 0.8$ alors que $\Omega_c \leq 1000$ rpm impose que $U_0 \leq 30m.s^{-1}$. De plus, la vitesse minimale pour obtenir une bonne stabilité de l'écoulement est $U_c \approx 2.5m.s^{-1}$ dans la section droite $D_c = 0.3m$ avant la contraction, d'où $U_0 \geq 10m.s^{-1}$ en sortie dans la configuration $\chi = 4$. Enfin, nous avons estimé qu'il était préférable que la couche limite dans le plan de sortie soit turbulente. En effet, l'ajout de swirl a pour effet de forcer la transition vers une couche limite turbulente à cause des effets de courbure qui entrainent apparition de tourbillons instationnaires de Goertler [69]. La transition de la couche limite s'effectue $48mm$ avant le plan de sortie par une bande de particules de carbure de silicium qui ont un diamètre nominal de $0.25mm$.

1.4 Conditions de sortie

1.4.1 Paramètres et grandeurs sans dimension

Le nombre de Reynolds qui caractérise l'écoulement de jet est défini par :

$$Re_0 = \frac{U_0 D_0}{\nu}. \tag{1.10}$$

Au cours des expériences effectuées au cours de cette thèse, nous avons fixé $U_0 \approx 21.6m.s^{-1}$ et donc $Re_0 = 2.14 \times 10^5$ à $\pm 1\%$. Dans la suite, nous serons souvent amenés à considérer des grandeurs adimensionnés en utilisant comme échelles la masse volumique ρ, le diamètre du jet D_0 et la vitesse U_0. Dans la mesure du possible, les quantités correspondant à des grandeurs physiques seront dénotées par des lettres capitales, alors que les quantités adimensionnées seront dénotées par des lettres minuscules soit par exemple pour les coordonnées cylindriques (R, θ, Z) et (r, θ, z). Dans ce repère, les composantes du vecteur de vitesse moyenne adimensionnée sont (u_r, u_θ, u_z), et les fluctuations sont notées (u'_r, u'_θ, u'_z). En faisant usage de cet adimensionnement, le débit $\dot{m}_0$ en sortie du jet est :

$$\dot{m}_0 = 2\pi \int_0^{1/2} u_z(z = 0, r) r dr, \tag{1.11}$$

et la vitesse de débit est donc :

$$u_0 = \frac{2\pi \int_0^{1/2} u_z(z = 0, r) r dr}{2\pi \int_0^{1/2} r dr} = 8 \int_0^{1/2} u_z(z = 0, r) r dr. \tag{1.12}$$

La détermination de cette quantité par une mesure PIV à $z = 0.1$ donne une constante proche de 0.99, quel que soit le nombre de swirl. Ceci confirme que $\dot{M}_0 \approx \dot{M}_0^{\mathrm{PIV}}$, comme

S	0.10	0.20	0.30	0.40	0.51	0.61	0.71	0.81
S_0	0.10	0.20	0.31	0.41	0.51	0.62	0.72	0.82

TABLE 1.1 – Valeurs du nombre de swirl de sortie S_0, eq. (1.8) en fonction du swirl de consigne S, eq. (1.8).

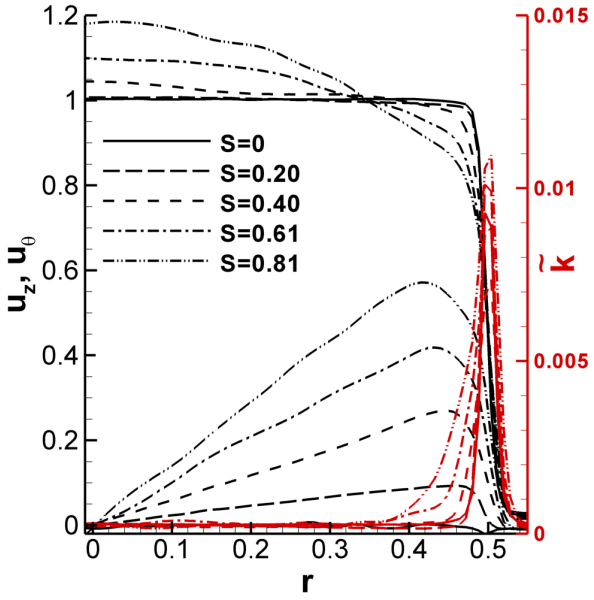

FIGURE 1.7 – Vitesses axiale et azimutale moyennes extraites à $z = 0.1$ d'un plan PIV pour différentes valeurs de S. En rouge, une estimation notée $\tilde{k}$ de l'énergie cinétique turbulente. Cette valeur est baisée par la résolution spatiale de ce plan PIV qui se trouve inadaptée à l'étude de cette échelle de cisaillement.

énoncé en section 1.2.2. La mesure PIV permet aussi de relier le nombre de swirl de l'écoulement en sortie S_0 (1.8) au paramètre de swirl S (1.9). La gamme de valeurs couvertes dans cette étude est donnée dans le tableau 1.1. Comme suggéré dans la sous-section 1.2.3, on constate que $S_0 \approx S$.

1.4.2 Profils de vitesse

La figure 1.7 représente les profils de vitesse axiale et azimutale moyenne à $z = 0.1$ dans la configuration expérimentale de référence, pour des valeurs de S couvrant la gamme de nombres de swirl étudiés (tableau 1.1). Ces profils ont été obtenus au plus près du plan de sortie du jet par mesure PIV, et cette technique de mesure sera détaillée dans le chapitre 2. On note un bon accord avec les mesures fil-chaud réalisée par B. Leclaire (figure 1.5), même si les conditions d'essais ($U_0 \approx 11.5 m.s^{-1}$ pour B. Leclaire contre $U_0 \approx 21.5 m.s^{-1}$ dans le cas présent), ainsi que la longueur de section fixe qui sépare la section tournante ($0.675m$ contre $0.225m$) diffèrent. En rouge est représentée l'estimation $\tilde{k}$ de l'énergie cinétique turbulente, qui est baisée par la faible résolution spatiale de ce champ PIV par rapport à la faible largeur de la couche de cisaillement (voir annexe B.1.5 pour plus de détails). Néanmoins, cette grandeur permet de constater que la turbulence est localisée dans la zone cisaillée : nous avons bien généré une couche de mélange axisymétrique tournante mince avec un coeur potentiel contenant peu de perturbations turbulentes. Plus précisément, et en accord avec les résultats de B. Leclaire, nous avons mesuré par fil chaud que le taux de fluctuation de la vitesse axiale était de l'ordre de 0.5% dans le coeur du jet, et ce jusqu'à $S = 0.81$.

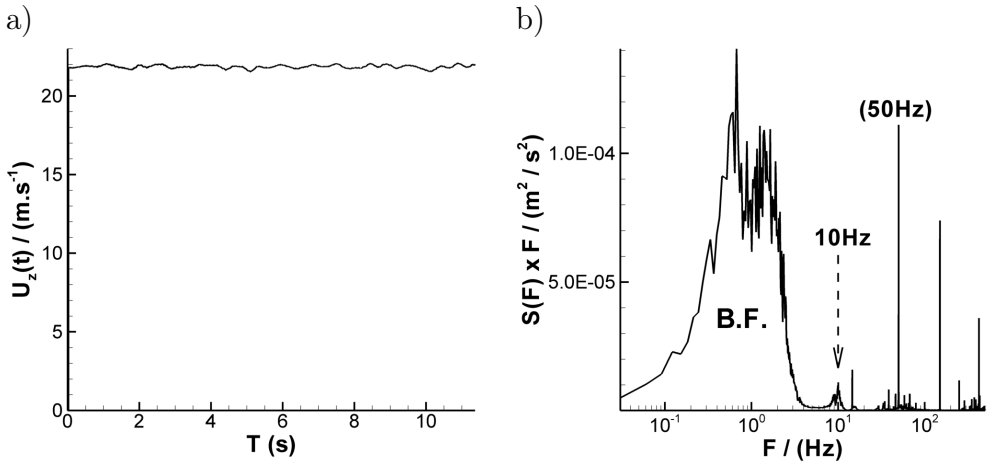

FIGURE 1.8 – (a) : trace temporelle de la vitesse axiale mesurée au moyen d'un fil-chaud en sortie du jet et sur l'axe ($r = 0, z = 0$) pour $S = 0$. (b) : spectre de ce signal représenté de telle sorte que l'aire sous la courbe soit une énergie, alors que l'abscisse est logarithmique. On note la prédominance de très basses fréquences notés B.F.

1.4.3 Nature des fluctuations dans le coeur du jet

Nous avons cherché à caractériser la nature des perturbations résiduelles dans le coeur du jet. La figure 1.8 (a) est une trace temporelle du signal de vitesse axiale mesuré au moyen d'un fil-chaud dans le plan de sortie du jet et sur l'axe pour $S = 0$. On constate que les fluctuations, de faible amplitude, ont un temps caractéristique de l'ordre de 1 à $2s$. Ceci est confirmé par une analyse spectrale, dont le résultat est représenté dans la figure 1.8 (b) de telle sorte que l'aire sous la courbe soit une énergie alors que l'abscisse est logarithmique. Cette représentation confirme que la majorité de l'énergie des fluctuations est contenue dans de basses fréquences, $0.1 \leq F \leq 3Hz$. Sur ce spectre, on observe aussi une faible quantité d'énergie autour de $10Hz$, fréquence qui peut correspondre à un des harmoniques du ventilateur de l'installation. Le pic à $50Hz$ est un artefact de mesure qui provient d'effets électromagnétiques lors de la mesure fil-chaud et n'est pas énergétiquement significatif. Enfin, dans le cas du jet tournant, il faut s'attendre à ce que l'écoulement soit perturbé à la fréquence qui correspond à la vitesse angulaire du nid d'abeille et à ses harmoniques, comme l'ont montré les précédentes études utilisant cette installation [59, 68].

1.4.4 Profil de couche limite pour $S = 0$

Pour terminer la description de la configuration de référence, nous présentons un profil de la couche limite pour $S = 0$. Cette mesure est réalisée au moyen d'un fil-chaud au plus près du plan de sortie du jet. L'écoulement mesuré ici n'est pas à proprement parler une couche limite, car il se trouve déjà séparé de la paroi de la buse de sortie. Cependant, les résultats de l'étude de Morris and Foss [88] sur la transition d'une couche limite turbulente vers une couche de mélange, montrent qu'une partie de la structure de la couche limite se conserve alors que la séparation a déjà eu lieu, jusqu'à une distance qui représente quelques épaisseurs de quantité de mouvement depuis la séparation, et ici

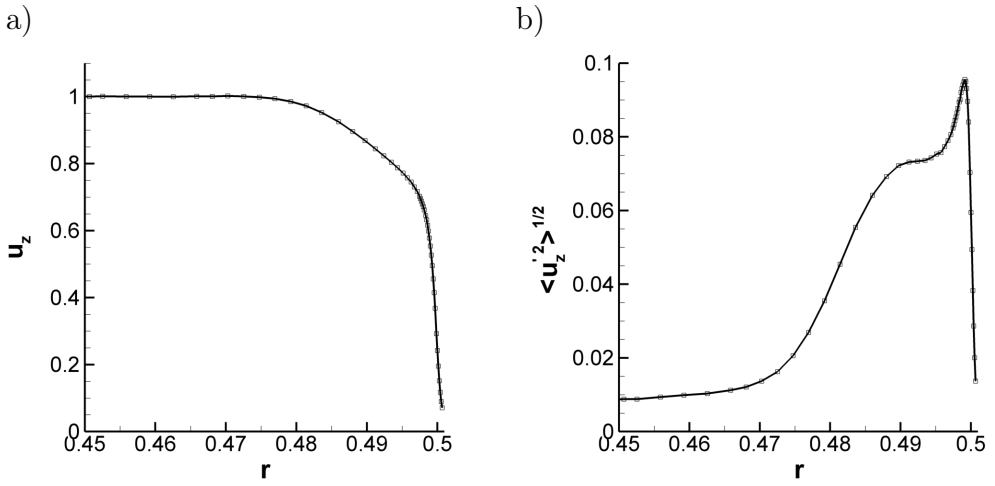

FIGURE 1.9 – Profil de couche limite (a) et de fluctuation de vitesse axiale (b) réalisé à $z \approx 0.003$ avec une sonde fil chaud pour $S = 0$.

nous avons $\theta_0 \approx 0.36mm$. La formule utilisée est

$$\theta_{(z\approx 0.003)} = \int_0^{0.5} u_z(r,z)\,(1 - u_z(r,z))\,dr, \tag{1.13}$$

où nous avons tronqué volontairement l'intégration à la position de la paroi avant la séparation ($r = 0.5$). Comme la mesure est réalisée à $z \approx 0.003$ ($Z \approx 0.5mm$) du plan de sortie, l'écoulement conserve donc des caractéristiques similaires au profil de la couche limite avant séparation. Le rapport d'aspect vaut $\frac{\delta}{\theta} \approx 1.4$, ce qui, combiné avec le pic de fluctuation observé près de la paroi sur la figure 1.9 (b), caractérise la couche limite comme étant turbulente. Son nombre de Reynolds basé sur l'épaisseur de quantité de mouvement vaut $Re_\theta \approx 515$. Compte-tenu de la faible épaisseur, une mesure de la couche limite dans le cas du jet tournant avec une sonde à deux fils n'a pas été possible. Cependant, l'observation qualitative de l'évolution des profils de la figure 1.9 montre que la structure fine reste similaire, avec un pic d'énergie cinétique près de la paroi plus élevé. Quant à la structure de la région extérieure, nous avons observé une extension de la zone turbulente vers le centre du jet jusqu'à $r = 0.4$, comme le suggérait la figure 1.7. Ce point sera détaillé lors de l'analyse de la structure de la turbulence de la couche de mélange axisymétrique, dans la partie II chapitre 5. Le prochain chapitre décrit en détail la technique PIV et les mesures que nous avons réalisées.

2 Vélocimétrie par Image de Particules (PIV)

2.1 Introduction

2.1.1 Pourquoi utiliser la PIV ?

Le jet tournant est un écoulement tridimensionnel. Plusieurs techniques peuvent être envisagées pour réaliser des mesures des trois composantes de la vitesse instantanée (mesures 3C). Nous avons identifié quelques-uns de leurs avantages et inconvénients, résumés dans le tableau ci-dessous :

	Avantages	Inconvénients
Sonde de pression multi trous (3C)	mesure de la pression	mesure stationnaire directivité réduite
Fil-chaud (2C ou 3C)	résolution spatiale	directivité réduite étalonnage
LDV (2C ou 3C)	résolution spatiale	mise en place ensemencement
PIV stéréoscopique (3C)	facilité d'utilisation directivité libre champs instantanés 3C	résolution spatiale sensibilité

Si la PIV se démarque par sa mise en oeuvre plus aisée, son principal avantage est aussi de mesurer un champ de vitesse instantané, ce qui permet d'obtenir une vision spatiale des structures cohérentes de la turbulence.

2.1.2 Principe général

D'une certaine manière, la Vélocimétrie par Image de Particules (PIV) résulte du perfectionnement d'une technique de visualisation vers une technique de mesure quantitative. La figure 2.1 issue de Raffel et al. [99] représente une disposition des éléments de base utilisés lors d'une mesure PIV. Nous invitons le lecteur intéressé par un exposé général de la PIV à consulter cet ouvrage, auquel nous ferons plusieurs fois référence dans ce chapitre. Nous considérons un écoulement transportant des particules passives visibles et de diamètre d_p. Une nappe laser est générée grâce à une source laser et à un montage optique. Cette nappe définit dans l'écoulement un plan de mesure qui est observé avec une unique caméra si on cherche à déterminer les deux composantes de la vitesse dans ce plan, et avec deux caméras si l'on souhaite obtenir la composante hors plan de la vitesse. Si l'on considère une seule caméra, le plan de mesure est un plan

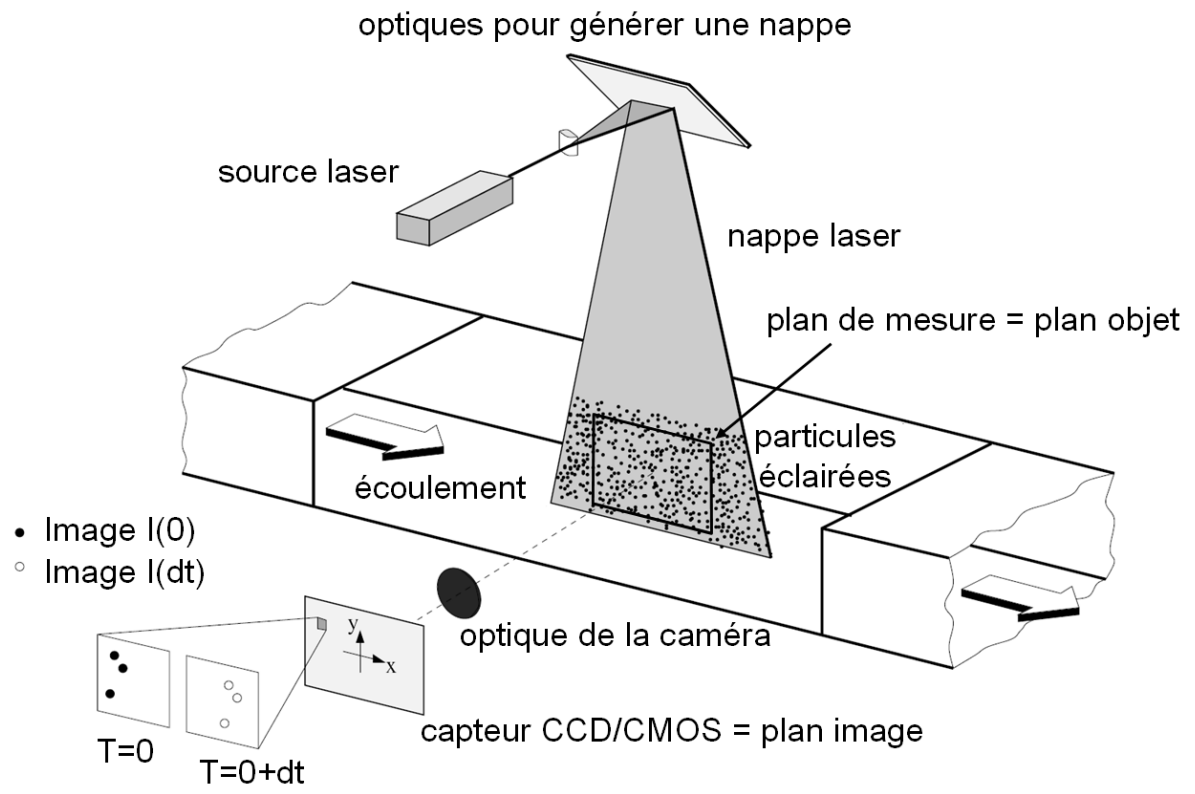

FIGURE 2.1 – Schéma adapté de Raffel et al. [99] décrivant les éléments à la base d'une mesure PIV.

objet dont l'image coïncide avec le plan du capteur. Une paire d'images consécutives séparées par un temps inter-image dt met donc en évidence un déplacement des particules dans le plan de mesure. Sous certaines conditions, cette paire d'images permet alors de remonter à un champ de vitesse 2C en utilisant un algorithme de traitement d'images. L'expérimentateur doit respecter quelques contraintes sur l'ensemencement de l'écoulement, l'épaisseur de la nappe utilisée ainsi que sur la durée du temps inter-image dt. La configuration utilisant deux caméras permet d'obtenir le champ de vitesse 3C dans le plan de mesure par une reconstruction stéréoscopique à partir des deux paires d'images consécutives. Nous présenterons tout d'abord les montages PIV réalisés et leurs particularités, avant d'aborder la détermination des déplacements.

2.2 Mise en oeuvre expérimentale

2.2.1 Systèmes PIV utilisés

Nous avons utilisé deux systèmes PIV. L'un est de type PIV stéréoscopique classique (SPIV), et l'autre de PIV stéréoscopique à haute cadence (HS-SPIV). Les principales caractéristiques des deux systèmes et des acquisitions réalisées sont résumées dans le tableau 2.1. Comme on le constate à la lecture de ce tableau, la fréquence d'acquisition du système HS-SPIV est très supérieure à celle du système classique, ce qui va permettre d'étudier la dynamique instationnaire de certains phénomènes. Cependant, comme nous le détaillerons par la suite, deux caractéristiques importantes peuvent rendre la mise en oeuvre de la HS-SPIV plus délicate. Tout d'abord, à cause de la plus faible énergie des pulses laser, le contraste et l'intensité des images PIV seront dégradées. Ensuite, la taille plus importante des pixels du capteur rendra difficile le fait d'obtenir des particules de

diamètre de l'ordre de deux pixels comme préconisé traditionnellement pour éviter les effets de peak-locking [99].

		SPIV	HS-SPIV
source laser	type	Nd-YAG	Nd-YLF
	longueur d'onde	$\lambda = 532nm$	$\lambda = 527nm$
	énergie d'un pulse	$\approx 200mJ$	$\approx 20mJ$
	durée d'un pulse	$\approx 6ns$	$\approx 100ns$
caméras	modèle	Imager Intense (LaVision)	Phantom V 12.1 (Vision Research)
	capteur	CCD [a] 1280×1024	CMOS [b] 1280×800
	taille des pixels	$L_{\text{SPIV}} = 6.45\mu m$	$L_{\text{HS-SPIV}} = 20\mu m$
	dynamique	12 bits	12 bits
acquisition	fréquence d'acquisition nominale	$F_{\text{acq}} = 4Hz$	$F_{\text{acq}} = 2.5kHz$
	nombre d'échantillons	$N = 5000$	$N_{ech} \times N_B = 2100 \times 30$

a. CCD : couple charged device
b. CMOS : complementary metal oxide semiconductor

TABLE 2.1 – Caractéristiques principales des systèmes PIV utilisés au cours de cette thèse.

2.2.2 Réglages

Montage des caméras

La figure 2.2 est un schéma qui représente le principe du montage de PIV stéréoscopique. La configuration qui permet d'obtenir des incertitudes de reconstruction équivalentes pour les trois composantes de la vitesse est celles où l'axe d'observation des caméras est incliné de $\theta = 45°$ de part et d'autre de la normale au plan de mesure [99]. Nous avons donc cherché à réaliser nos mesures sous cette condition. On peut noter sur cette figure la présence d'un adaptateur Scheimpflug sur chaque caméra. Ce dernier permet de pivoter d'un angle α le plan de l'objectif pour maintenir la netteté de l'image alors que la caméra n'est pas face au plan de mesure (condition de Scheimpflug [97]).

Les montages de PIV stéréoscopique que nous avons réalisés diffèrent par la position des caméras vis-à-vis de la direction d'émission de la nappe laser. Or, la diffusion de la lumière par les particules n'est pas isotrope (diffusion de Mie), et il est plus favorable d'observer les particules en diffusion avant, face à la source lumineuse [99]. Les configurations d'observation retenues sont représentés dans la figure 2.3. La SPIV est utilisée pour réaliser des coupes dans les plans (Y,Z) longitudinaux. Compte tenu de la puissance laser disponible pour ce système, nous avons pu privilégier une configuration optique d'accès simple et symétrique vis-à-vis de la nappe. La HS-SPIV est utilisée pour étudier la dynamique instationnaire de l'écoulement dans un plan $z = 2$ transverse. Les caméras sont disposées face au sens d'émission de la nappe laser (diffusion avant), et l'angle moitié entre les deux caméras a été réduit de $\theta \approx 45°$ vers $\theta \approx 37°$, de manière à maximiser l'intensité des particules sur les images. Dans cette configuration, ceci augmente la précision

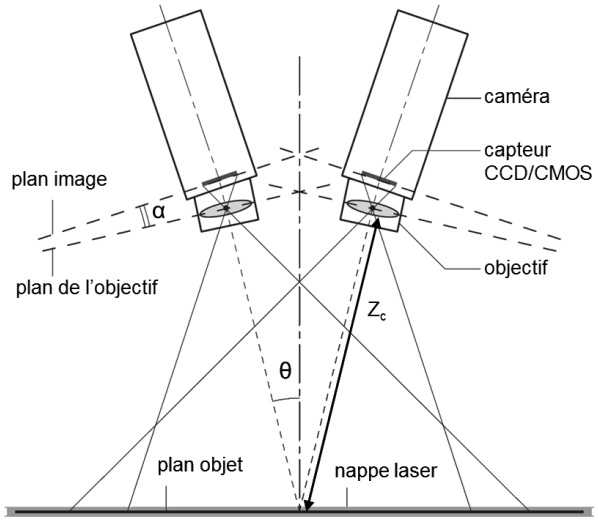

FIGURE 2.2 – Schéma du montage de deux caméra en configuration stéréoscopique avec condition de Scheimpflug, d'après [117].

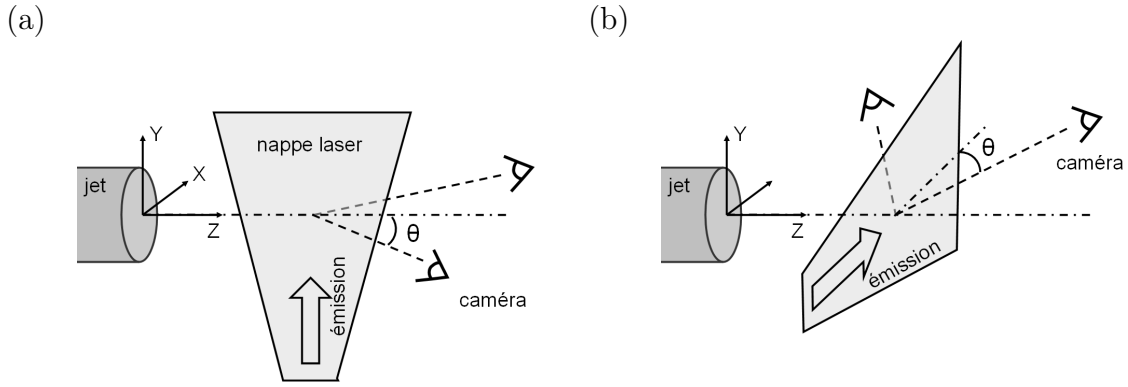

FIGURE 2.3 – Disposition des caméras par rapport à l'émission de la nappe laser pour la SPIV (a) et la HS-SPIV (b).

de la détermination de la composante axiale de la vitesse au détriment des composantes situées dans le plan (X,Y). Par ailleurs, les caméras HS-SPIV ont été pivotées de 90° de telle sorte que l'intégralité des capteurs CMOS soit utilisée malgré la perspective.

Ensemencement

Au cours de ces expériences, nous avons utilisé un générateur de particules de type Topas ATM 210, qui disperse un aérosol du Di-Méthyl-Hexyl-Sebacate (DEHS) de masse volumique $\rho_p \approx 0.9 \times 10^3 kg.m^{-3}$. Une taille de goutte calibrée inférieure à $d_p = 1\mu m$ est obtenue grâce à l'atomiseur de Laskin du générateur. Le temps caractéristique de la réponse de ces particules à une perturbation de l'écoulement s'écrit [99]

$$\tau_p = \frac{d_p^2}{18\nu}\frac{\rho_p}{\rho} \approx 10^{-11} s. \tag{2.1}$$

Ceci nous assure que les particules suivent toutes les échelles du mouvement, car le temps caractéristique de l'échelle de Kolmogorov est donné par

$$\tau_K = \sqrt{\nu \frac{D_0}{U_0^3}} \approx 1.5 \times 10^{-5} s. \tag{2.2}$$

Pour calculer le champ des vitesses à partir d'images PIV, il est préférable d'utiliser un ensemencement homogène dans tout le plan de mesure [119]. Nous avons donc ensemencé aussi bien l'écoulement au repos que le coeur du jet. Nous avons utilisé la soufflerie pour mélanger l'aérosol dans toute la pièce avant l'acquisition. Il est alors impossible de distinguer jet de l'écoulement au repos sur les clichés PIV. Cependant, lors de l'utilisation de la HS-SPIV, l'énergie de la nappe laser est diffusée entre l'optique de génération et le plan de mesure lors de la traversée de la pièce ensemencée, ce qui réduit de manière significative l'énergie déjà limitée de ces pulses laser. Nous avons donc réduit la densité d'ensemencement dans la pièce par rapport au coeur du jet, au détriment de l'homogénéité globale. On peut alors distinguer le coeur du jet qui est plus ensemencé que l'écoulement au repos. Ceci a pour effet de réduire la qualité de la corrélation des images PIV au niveaux des interfaces où l'inhomogénéité est visible.

Taille apparente des particules

Avec les fines particules utilisées, le diamètre de l'image d'une particule sur le capteur de la caméra, noté d_p^I, est lié à la longueur d'onde de la source laser plus qu'au diamètre physique d_p de la particule elle-même, grâce à des effets de diffraction importants. Le diamètre d_p^I s'écrit [99]

$$d_p^I = \sqrt{(M d_p)^2 + (2.44 f_\# (M+1)\lambda)^2}, \tag{2.3}$$

où M est le rapport de grandissement entre le plan image et le plan objet, $f_\#$ est l'ouverture de l'objectif, c'est à dire le rapport de sa longueur focale sur le diamètre d'ouverture du diaphragme. Enfin, λ est la longueur d'onde de la lumière utilisée. Dans les configurations optiques étudiées, $M \approx 10^{-1}$, de telle sorte que le premier terme de l'équation (2.3) sera négligeable. En revanche une ouverture conséquente du diaphragme ($f_\# = 2.2$) diminue fortement les effets de diffraction. Afin d'éviter cela nous avons imposé $f_\# \geq 8$. Rappelons que $d_p \approx 1\mu m$ et $\lambda \approx 0.5\mu m$. On obtient donc grossièrement

$$d_p^I \approx \sqrt{(10^{-7})^2 + (10^{-5})^2} \approx 10\mu m. \tag{2.4}$$

Comme le montre le tableau 2.1, il existe une différence entre la taille d'un pixel du capteur SPIV ($L_{\text{SPIV}} = 6.45\mu m$) et celle d'un pixel du capteur HS-SPIV ($L_{\text{HS-SPIV}} = 20\mu m$). Ceci entraine qu'en termes de pixels couverts, la taille des particules sur l'image n'est pas la même (environ 2 pixels pour SPIV contre 1 pour HS-SPIV). Pour le système HS-SPIV ce diamètre de 1 pixel est propice à l'apparition de peak-locking. Ce phénomène qui sera expliqué dans la sous-section 2.3.1 biaise la détermination des déplacements vers les valeurs entière de pixels [99]. Il n'est pas ici possible d'augmenter $f_\#$ pour y remédier car les images ne sont alors plus assez lumineuses. Nous avons donc été contraints de réaliser les acquisitions HS-SPIV avec $f_\# = 8$. Ayant effectivement détecté un peak-locking lors d'acquisitions préliminaires, nous avons donc utilisé un léger floutage des images afin d'étendre artificiellement la taille des particules [117]. Ceci a eu pour effet de faire disparaître ces effets.

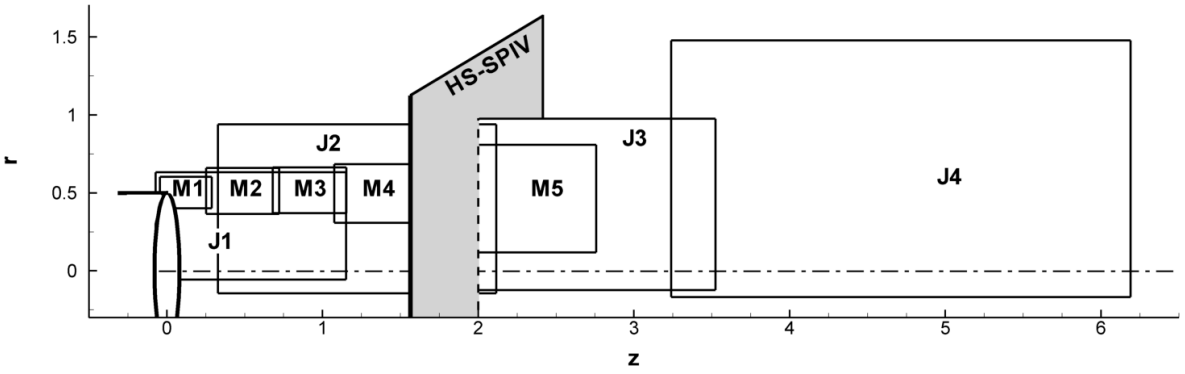

FIGURE 2.4 – Schéma résumant les différents plans PIV réalisés au cours de cette thèse.

Temps inter-images

La valeur que l'on fixe pour le temps inter-image dt dépend principalement de la vitesse de l'écoulement et du rapport de grandissement M. Le réglage de dt fait alors intervenir deux contraintes antagonistes. D'une part, on souhaite observer des déplacements de particules conséquents, de l'ordre de 10 pixels, afin d'avoir une meilleure précision relative lors de la détermination des déplacements. D'autre part, pour les temps inter-image trop longs, les particules peuvent sortir de la nappe laser lors d'un déplacement transverse, et la détermination des déplacements devient alors impossible par perte de corrélation.

2.2.3 Plans réalisés

La figure 2.4 offre un récapitulatif des plans PIV réalisés par rapport au jet. Tout d'abord la SPIV a été utilisée pour réaliser des plan longitudinaux à l'écoulement de jet. Les plans J1 à J4 couvrent l'écoulement dans son ensemble, à basse résolution spatiale. Les plans M1 à M5 sont centrés sur la couche de mélange. Leur taille est variée de manière à maintenir une résolution spatiale adaptée à l'épaisseur croissante de la couche de mélange. Pour chacun de ces plans, $N = 5000$ doubles paires d'images ont été acquises à $4Hz$, pour toutes les valeurs de S de 0 à 0.81 figurant dans le tableau 1.1. Compte tenu de la basse fréquence de l'acquisition, chacun des champs de vitesse peut être considéré comme statistiquement indépendant du précédent. Enfin, un plan transverse à l'écoulement a été réalisé à $z = 2$ avec le système HS-SPIV à la fréquence d'acquisition $F_{\text{acq}} = 2.5kHz$. 30 blocs de 2100 paires d'images ont été enregistrés pour $S = 0$, $S = 0.20$, $S = 0.40$, $S = 0.61$ et $S = 0.81$. Le tableau 2.2 regroupe quelques-uns des autres paramètres de ces plans, et la section suivante détaille à présent la méthode employée pour obtenir les champs de déplacement à partir des doubles paires d'images.

2.3 Détermination des champs de vitesse

2.3.1 Estimation d'un champ de déplacement 2C

Principe des fenêtres d'interrogations

L'estimation du champ de déplacement entre deux images est une problématique étudiée depuis plusieurs dizaines d'années [51]. Cette problématique dépasse le cadre

	J1	J2	J3	J4	M1	M2	M3	M4	M5	HS-SPIV
focale (mm)	105	85	85	50	200	200	200	200	105	85
$f_\#$	8	8	8	8	16	11	11	8	8	8
Z_c (m)	1.7	2.3	2.4	2.3	1.4	1.7	1.8	2.2	1.8	1.2
dt (μs)	31	50	50	75	6/8	10	10	13	31	60
L_N (mm)	2	3	3	3	0.5	1	1	1	2	2.5

TABLE 2.2 – Principaux réglages des plans PIV de la figure 2.4. Z_C est la distance approximative de la caméra jusqu'au plan de mesure, et L_N est une estimation de l'épaisseur de la nappe obtenue à l'aide d'un papier thermique.

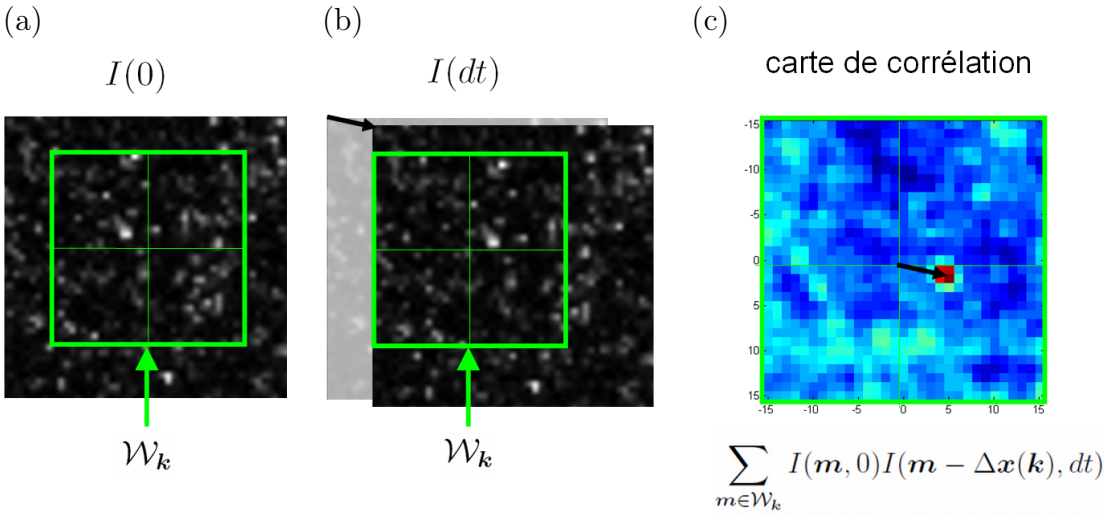

FIGURE 2.5 – Schéma représentant un gros plan sur une paire d'image PIV. la fenêtre d'interrogation $\mathcal{W}_k$ centrée sur le pixel k appliquée aux images $I(0)$ (a) et $I(dt)$ (b) pour calculer la carte de corrélation (c) définie par eq. (2.5).

de la PIV et concerne aussi d'autres types de mesures comme par exemple celle des déformations d'un matériau solide ainsi que d'autres domaines comme celui de la vision par ordinateur. Parmi toutes les techniques développées, nous ne présenterons qu'un seul type de méthode dit à fenêtres d'interrogation, qui domine dans le domaine de la PIV grâce à sa facilité d'implémentation et à sa robustesse. Pour commencer, nous considérons un champ de déplacement 2C d'un motif de particules entre deux images $I(0)$ et $I(dt)$ prises aux instants 0 et dt, comme représenté figures 2.5 (a) et (b). Les images sont divisées en sous-domaines dits "fenêtres d'interrogation" (FI) notés $\mathcal{W}_k$ qui sont centrés sur un pixel $\mathbf{k}$. Le sous-domaine $\mathcal{W}_k$ est souvent un carré de côté $\mathcal{L}_{\text{FI}}$ pixels. La fonction de corrélation en deux points, centrée sur $\mathbf{k}$ et réduite au sous-domaine $\mathcal{W}_k$ entre l'image $I(0)$ et l'image $I(dt)$ et est définie par

$$CC(\mathbf{k}, \Delta\mathbf{x}(\mathbf{k})) = \sum_{\boldsymbol{m}\in\mathcal{W}_k} I(\boldsymbol{m},0)I(\boldsymbol{m}-\Delta\boldsymbol{x}(\boldsymbol{k}),dt). \tag{2.5}$$

Cette fonction est représentée figure 2.5 (c) pour les deux images (a) et (b). Rechercher le déplacement $\Delta\mathbf{x}(\mathbf{k})$ qui maximise cette fonction revient à déterminer le déplacement

qui, dans le domaine $\mathcal{W}_{\boldsymbol{k}}$ autour du point $\mathbf{k}$, déplace le motif de particules entre l'image $I(0)$ à l'image $I(dt)$.

Résolution pratique du problème

Pour déterminer $\Delta\mathbf{x}(\mathbf{k})$ d'après (2.5), une méthode courante adoptée dans la communauté PIV consiste à évaluer cette fonction de corrélation en utilisant des transformations de Fourier rapide (FFT). La position $\Delta\mathbf{x}(\mathbf{k})$ du maximum, visible en rouge sur la figure 2.5 (c), est alors recherchée de manière exhaustive. Les valeurs de $\Delta\mathbf{x}(\mathbf{k})$ sont à priori discrètes car l'image est échantillonnée sur les pixels du CCD. Un procédé de "peak-fitting" permet alors de déterminer des déplacements sub-pixélliques de l'ordre de $0.1px$ si le pic de corrélation s'étend sur plusieurs pixels. Dans cette approche, le déplacement doit être suffisamment petit par rapport à la taille de la fenêtre d'interrogation ($\Delta\mathbf{x}(\mathbf{k}) \leq \frac{\mathcal{L}_{\text{FI}}}{4}$) sinon il y a une dégradation de la corrélation par perte de particules. Cette limite est résolue par l'utilisation de méthodes itératives multi-grilles où l'on utilise une succession de fenêtres d'interrogation de taille décroissante ainsi qu'une déformation itérative des fenêtres d'interrogations. Enfin notons qu'il est trop coûteux de réaliser cette détermination du déplacement $\Delta\mathbf{x}(\mathbf{k})$ pour chaque pixel $\mathbf{k}$ de l'image. On détermine donc souvent le déplacement sur un maillage réduit de telle sorte que les fenêtre ne se recouvrent que partiellement (notion d'overlap).

Récemment, Champagnat et al. [17] ont proposé d'utiliser une autre approche pour déterminer $\Delta\mathbf{x}(\mathbf{k})$. Ces travaux auxquels nous avons contribué sont présentés en annexe A et sont issus d'une collaboration scientifique enrichissante entre l'équipe métrologie du DAFE, et une équipe du DTIM (Département Traitement de l'Information et Modélisation) de l'ONERA. Cette approche est implémentée dans le logiciel FOLKI-SPIV que nous avons utilisé lors des dépouillements PIV de cette thèse. L'approche consiste à minimiser la somme des différences mises au carré

$$SSD(\mathbf{k}, \Delta\mathbf{X}(\mathbf{k})) = \sum_{\boldsymbol{m}\in\mathcal{W}_{\boldsymbol{k}}} \left(I(\boldsymbol{m}, 0) - I(\boldsymbol{m} - \Delta\boldsymbol{x}(\boldsymbol{k}), dt)\right)^2 . \tag{2.6}$$

La minimisation s'effectue par une descente de gradient de type Gauss-Newton, ce qui permet de s'affranchir du procédé de peak-fitting. L'approche est résolument multi-résolution grâce à l'utilisation d'une pyramide d'images. Ce point particulier, ainsi que d'autres améliorations et détails sont décrits dans l'annexe A. Un avantage de cette méthode est d'être massivement parallèlisable. Ceci permet une implémentation sur les processeurs des cartes graphiques (GPU) ce qui permet un dépouillement des données très rapide pour un prix modeste. Sur une même configuration, le temps de calcul diminue d'un facteur 50 en utilisant les GPU par rapport à un logiciel de PIV classique qui ne les utilise pas.

Peak-locking

Quelle que soit l'approche de dépouillement, lorsque le diamètre de l'image des particules devient inférieur à 2 px l'estimation des déplacements s'accompagne d'un biais, couramment dénommé peak-locking, qui favorise les déplacements $\Delta\mathbf{x}(\mathbf{k})$ entiers. Ceci s'explique car le pic de corrélation, voir figure 2.5 (c), devient alors trop fin pour permettre une interpolation subpixellique. Ce biais s'apparente à un phénomène de repliement spectral qui apparaît lors de l'échantillonnage par le capteur CCD/CMOS d'images contenant des fréquences spatiales trop élevées. Pour éviter cette limitation, il faut s'assurer que le diamètre de l'image des particules soit supérieur à 1 px.

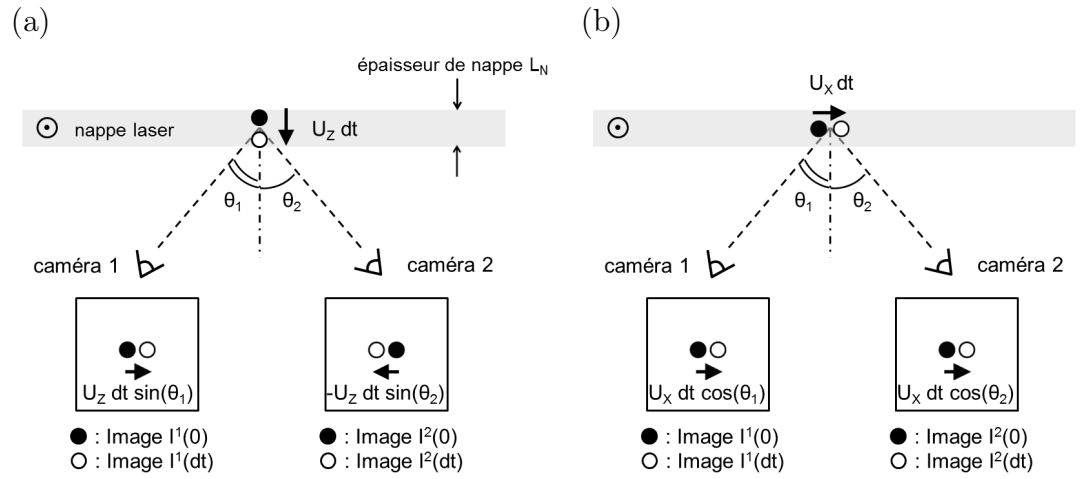

FIGURE 2.6 – Principe de la reconstruction stéréoscopique pour la PIV. Le déplacement d'une particule se déplaçant hors de la nappe (a) se distingue de celui d'une particule se déplaçant dans la nappe (b).

2.3.2 Estimation d'un champ de déplacement 3C

Principe

La PIV stéréoscopique (SPIV) imite la vision binoculaire en faisant appel à deux points de vue pour reconstruire la composante hors-plan du mouvement. La figure 2.6 est un schéma illustrant la possibilité de distinguer un déplacement hors-plan d'un déplacement horizontal dans la nappe à l'aide de ce principe. L'approche algorithmique classique consiste à déterminer d'abord le champ de déplacement 2C noté $\Delta\mathbf{x}^i(\mathbf{k})$ pour chaque caméra i avant de reconstruire un champ de déplacement 3C noté $\Delta\mathbf{X}(\mathbf{k})$ dans le plan de mesure. Pour chaque vecteur vitesse, ceci implique de résoudre un système surdéterminé de 4 équations à 3 inconnues. Sa résolution par la méthode des moindres carrés permet de définir une erreur de reconstruction.

Méthode FOLKI-SPIV

La méthode que nous utilisons pour la reconstruction stéréoscopique généralise la minimisation de la fonction définie par (2.6) et se déroule en une seule étape. Tout d'abord, il est nécessaire d'établir une relation entre le plan image de chaque caméra et le plan de mesure. Il existe une transformation non-linéaire projective qui permet de relier la position d'un point objet noté $\mathbf{X} = (X, Y, Z)^T$ et situé dans le repère attaché au plan de mesure et la position noté $\mathbf{x}^i = (x^i, y^i)^T$ de son image dans le repère attaché au plan image de la caméra i. Pour chaque caméra i, cette relation s'écrit :

$$\mathbf{x}^i = \mathbf{F}^i(\mathbf{X}), \tag{2.7}$$

comme nous l'avons schématisé sur la figure 2.7. La détermination de cette fonction $\mathbf{F}^i$ correspond à une opération d'étalonnage réalisée à l'aide d'une mire étalon placée dans le plan de mesure (plan de la nappe laser). $\mathbf{F}^i$ est recherchée sous la forme d'une loi de calibration de type pin-hole qui modélise la vision du plan de mesure par chaque caméra [33]. Une méthode de détermination de la loi de calibration à partir des images de la mire est implémentée dans le logiciel AFIX [67].

Pour de faibles déplacements, la linéarisation de la relation (2.7) permet de relier un déplacement $\Delta\boldsymbol{x}^i$ dans le plan du capteur CCD/CMOS au déplacement $\Delta\boldsymbol{X}$ du plan de

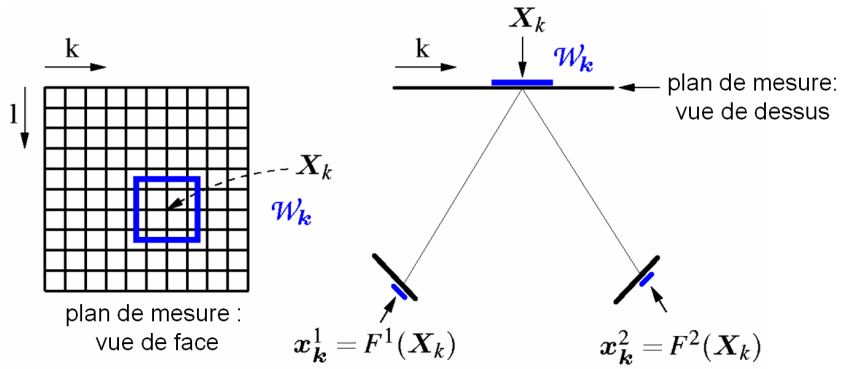

FIGURE 2.7 – Schéma de principe simplifié représentant la correspondance entre le plan de mesure (plan objet) et le plan du capteur CCD/CMOS (plan image) pour deux caméras (exposants $i = 1$ et 2) en configuration stéréoscopique. Un maillage régulier de points $\mathbf{X_k}$, indexé par $\mathbf{k} = [k, l] \in \mathcal{G} = \{0, ..., K-1\} \times \{0, ..., L-1\}$, est défini directement dans le plan de mesure. La calibration de la caméra permet d'obtenir la fonction $\mathbf{F}^i$, (voir le texte pour plus de détails). Le sous-domaine $\mathcal{W}_k$ représente une fenêtre d'interrogation dans le plan de mesure.

mesure :

$$\nabla \boldsymbol{F}^i \Delta \boldsymbol{X} = \Delta \boldsymbol{x}^i. \tag{2.8}$$

Le déplacement 3C $\Delta\mathbf{X}(\mathbf{k})$ autour du point $\mathbf{k}$ est alors celui qui minimise

$$SSD_{3C}(\mathbf{k}, \Delta\mathbf{X}(\mathbf{k})) = \sum_{i=1}^{2} \sum_{\boldsymbol{k'} \in \mathcal{W}_k} \left(I^i(\boldsymbol{x}^i_{\boldsymbol{k'}}, 0) - I^i(\boldsymbol{x}^i_{\boldsymbol{k'}} - \nabla \boldsymbol{F}^i \Delta \boldsymbol{X}(\boldsymbol{k}), dt) \right)^2. \tag{2.9}$$

La première des deux sommes de l'eq. (2.9) porte sur les images des deux caméras, cette méthode permet donc de combiner les deux déterminations 2C ainsi que la reconstruction stéréoscopique de l'approche classique en une seule étape. La recherche rapide du minimum de (2.9) qui permet de déterminer $\Delta\mathbf{X}(\mathbf{k})$ est la même que celle utilisée pour la relation (2.6), et permet aussi de gagner un temps important lors du dépouillement. Pour plus de détails, on pourra consulter Leclaire et al. [71].

Self-calibration

La calibration des caméras implique qu'il faille positionner la mire dans le plan de la nappe pour définir le plan de mesure. Si cette opération n'est pas réalisée parfaitement, des erreurs de reconstruction stéréoscopique importantes peuvent apparaitre [118]. Nous avons utilisé la procédure de self-calibration qui permet de rectifier ces erreurs [120]. Une scène de particules éclairées par la nappe laser photographiée par caméra 1, à un instant 0, est rectifiée dans le plan de mesure pour donner $(\boldsymbol{F}^1)^{-1}[I^1(0)]$. La même scène photographiée au même instant par la caméra 2 donne l'image rectifiée $(\boldsymbol{F}^2)^{-1}[I^2(0)]$. Si la mire de calibration a été parfaitement alignée avec la nappe, ces deux images doivent être identiques. La procédure de self-calibration permet d'obtenir des fonctions d'étalonnage $\boldsymbol{F}^1$ et $\boldsymbol{F}^2$ qui vérifient cette condition.

Paramètres de dépouillement

Comme décrit dans l'annexe A, FOLKI-SPIV possède un nombre réduit de paramètres de dépouillement, ce qui est un avantage par rapport au côté arbitraire de certaines "recettes" existant dans les algorithmes classiques. Les principaux paramètres sont

le nombre de niveaux $J_{\mathrm{FI}} = 3$ de la pyramide d'images et le nombre d'itérations $N_{\mathrm{FI}} = 5$ donnés à la méthode de Gauss-Newton à chaque niveau de la pyramide d'images. Une analyse spécifique a montré que les résultats ne variaient pas si on modifiait ces paramètres. Un autre paramètre important est la largeur de la fenêtre d'interrogation fixé à $\mathcal{L}_{\mathrm{FI}} = 31$ pixels. Comme détaillé dans l'annexe A, la résolution spatiale de la méthode dépend seulement de ce paramètre. Nous avons généré des images synthétiques de PIV pour évaluer quantitativement la résolution spatiale de la méthode. Nous avons montré que cette dernière est identique à celle d'une moyenne glissante sur la taille de la fenêtre $\mathcal{W}_{\boldsymbol{k}}$ de taille $\mathcal{L}_{\mathrm{FI}}$. Or, il est légitime pour un expérimentateur de chercher à obtenir la meilleure résolution spatiale possible. Nous avons constaté qu'augmenter la résolution spatiale en diminuant $\mathcal{L}_{\mathrm{FI}}$ conduisait à une incertitude plus importante sur l'estimation de $\Delta\mathbf{X}(\mathbf{k})$. Le choix de $\mathcal{L}_{\mathrm{FI}} = 31$ pixels résulte donc d'un compromis résolution/bruit. Un dernier paramètre secondaire est celui de l'échantillonnage des résultats, cette étape est rendue nécessaire par le fait que FOLKI-SPIV retourne un résultat dense, sur échantillonné (1 vecteur/1 pixel). Puisqu'il n'est pas utile d'échantillonner les résultats au-delà de la résolution spatiale de la méthode, nous avons décimé les résultats tous les 13 px pour SPIV, mais tous les 30 px pour HS-SPIV pour faciliter le stockage et le post-traitement du large volume de données de ces acquisitions.

2.4 Conclusion

Dans cette première partie, nous avons détaillé les choix expérimentaux ainsi que les considérations pratiques sous-jacentes qui concernent l'utilisation de la soufflerie R4 (chapitre 1) ainsi que le moyen de mesure PIV (présent chapitre). L'annexe B prolonge cette présentation en détaillant les erreurs affectant les mesures réalisées lors de cette thèse, ainsi que les incertitudes liées à l'estimation de grandeurs statistiques. Nous abordons à présent l'analyse des phénomènes physiques mis à jour par ces campagnes de mesure, le chapitre 4 étant consacré à la dynamique de la couche de mélange axisymétrique du jet non-tournant et le chapitre 5 à l'étude du jet tournant. Avant de commencer, nous étudions la validité expérimentale de l'hypothèse de Taylor pour le jet sans rotation, et le jet tournant.

Deuxième partie

Résultats

3 Etude expérimentale de l'hypothèse de Taylor

Ce chapitre est consacré à une étude expérimentale de l'hypothèse de Taylor. L'hypothèse introduite par Taylor en 1938 [113] relie le spectre spatial de perturbations convectées dans un écoulement au spectre temporel d'une mesure réalisée en un point. L'expérimentateur applique alors ce principe sous la forme d'une approximation plus que d'une hypothèse [86]. Dans la partie qui suit, nous introduisons une méthode, qui a fait l'objet d'une lettre publiée dans Physics of Fluids [25], dans le but d'évaluer l'hypothèse de Taylor dans le jet grâce aux expériences de PIV à haute cadence dans le plan $z = 2$ transverse à l'écoulement. Nous faisons appel à une définition de la vitesse de convection similaire à celle récemment définie par Del Alamo and Jiménez [26], et nous utilisons l'équation de la conservation de la masse pour estimer la dérivée selon z de la fluctuation de vitesse axiale u'_z. Notons que l'on trouve une utilisation similaire de la continuité dans la référence [27] et que les résultats obtenus en ce qui concerne les vitesses de convection sont conformes à ceux de précédentes études utilisant d'autres moyens expérimentaux [24, 54, 124]. A nos yeux, la nouveauté de la présente étude est surtout d'apporter une estimation expérimentale de la validité de cette hypothèse, qui peut se trouver limitée par la physique des phénomènes comme par le domaine de validité des mesures.

Ensuite, dans la section 3.1 nous appliquons cette méthode pour estimer l'hypothèse de Taylor dans le jet tournant. Puis, dans la section 3.2, nous proposons une extension du principe pour déterminer la vitesse de phase de structures cohérentes représentées par des modes POD.

PHYSICS OF FLUIDS **23**, 051701 (2011)

Taylor's hypothesis convection velocities from mass conservation equation

S. Davoust[a] and L. Jacquin[b]
ONERA/DAFE, 8, rue des Vertugadins, 92190 Meudon, France

(Received 23 December 2010; accepted 7 April 2011; published online 16 May 2011)

We propose to use the continuity equation to calculate convection velocities provided by the Taylor hypothesis for flow structures crossing a measurement plane. This is carried out in Fourier space to identify a velocity associated to each frequency. High-speed PIV experimental data of an axisymmetric mixing layer is used to implement the method. We show that as expected the Taylor hypothesis fails for the lowest frequencies and predicts the convection velocity to be close to the mean velocity for the higher ones. The method is compared to one of the definitions proposed by Del Álamo and Jiménez [J. Fluid Mech. **640**, 5 (2009)]. © *2011 American Institute of Physics*. [doi:10.1063/1.3584004]

In turbulent flow experiments, Taylor's frozen flow hypothesis is commonly used and various definitions for convection velocity have been investigated in previous studies.[1,2] In particular, the limitation of the approximation for large scale turbulent structures is a matter of questions. As discussed by Zaman and Hussain,[2] a good choice for a convection velocity is crucial but not sufficient to infer a structure's spatial shape from temporal data. Recently, Del Álamo and Jiménez[3] proposed new definitions of the convection velocity of Fourier spectral components. Compared to previous methods, these require only Fourier analysis along time (or space) and a local derivative along space (or time). The convection velocity of a spectral component is then defined by these authors as the change of frame that minimizes the difference between the turbulent fluctuation and a frozen wave.[3] A method is proposed and tested here, along similar principles, and which is especially suited to experiments using plane measurements normal to the mean flow.

Taylor's hypothesis was initially introduced to infer spatial information from single probe measurements and has also been applied to simultaneous acquisitions using hot-wire rakes to study large scale structures.[4] More recently, it has been applied to high-speed stereo particle image velocimetry (SPIV) to reconstruct the velocity gradient tensor using time sequences of all three components of velocity in a streamwise-normal plane for a variety of flows.[5–7] In the following, we use relevant flow scales to obtain non-dimensional variables. We suppose the (x, y) measurement plane to be orthogonal to the main direction of convection (z) of the flow. In that measurement plane, the fluctuation velocity $\vec{u} = (u_x, u_y, u_z)^T$ is a function of (x, y, t). Combining the continuity equation (in the case of incompressible flow) and Taylor's hypothesis with a convection velocity u_c leads to compare the divergence of velocity components in the (x, y) plane to the time-derivative of out of plane velocity component

$$\vec{\nabla}_{xy} \cdot \vec{u} = \frac{\partial u_x}{\partial x} + \frac{\partial u_y}{\partial y} = -\frac{\partial u_z}{\partial z} = \frac{1}{u_c}\frac{\partial u_z}{\partial t}. \tag{1}$$

Using this principle, we now seek a convection velocity, at a fixed spatial location (x, y), and for each Fourier spectral component of frequency f. This is accomplished by obtaining a statistical relationship between spectral components of the Fourier transforms of $-\frac{\partial}{\partial z}u_z$ (given by $\vec{\nabla}_{xy} \cdot \vec{u}$) and $\frac{\partial}{\partial t}u_z$. We consider N independent blocks of data noted $\vec{u}^{(k)}(x, y, t)$, with $1 \le k \le N$. For each block, the Fourier transform of $\vec{\nabla}_{xy} \cdot \vec{u}^{(k)}$ and that of $\frac{\partial}{\partial t}u_z^{(k)}$ provide, for each frequency f, the two spectral components $(\vec{\nabla}_{xy} \cdot \hat{\vec{u}}^{(k)}, i2\pi f \hat{u}_z^{(k)})$. Here, $\hat{\vec{u}}^{(k)}$ is the spectrum of $\vec{u}^{(k)}(x, y, t)$ and for clarity, the (x, y, f) dependency has been omitted. Given the frequency f, the complex series of points $(\vec{\nabla}_{xy} \cdot \hat{\vec{u}}^{(k)}, i2\pi f \hat{u}_z^{(k)})$ is sketched in Fig. 1 for $1 \le k \le N$.

If we consider an ideal traveling wave of frequency f and phase velocity $u_c(f)$, Taylor's approximation is exact and all the scattered points in Fig. 1 should be aligned along the line of slope $u_c(f)$. When applied to a convected turbulent flow, the approximation is not exact and a scatter, to which experimental measurement uncertainty can also contribute, appears. The dispersion of this scatter is measured by the complex correlation coefficient, defined for each frequency f as

$$\rho(f) = \frac{\langle (i2\pi f \hat{u}_z)(\vec{\nabla}_{xy} \cdot \hat{\vec{u}})^* \rangle}{\sqrt{\langle \left| \vec{\nabla}_{xy} \cdot \hat{\vec{u}} \right|^2 \rangle \langle |i2\pi f \hat{u}_z|^2 \rangle}}. \tag{2}$$

Here, $\langle . \rangle = \frac{1}{N}\sum_{k=1}^{N} .^{(k)}$ denotes the sample average. This correlation coefficient is similar to the one defined by Del Álamo and Jiménez[3] in Eq. (2.6). It measures the validity of Taylor's approximation, including effects from experimental measurement uncertainty: one has $\rho = 1$ for a frozen turbulence and no measurement noise. For each frequency f, the present method provides the convection velocity by estimating an optimal slope $u_c(f)$ for the correlation plot in Fig. 1. This can be done in several manners. Considering the experimental noise in both directions of the plot, a robust and intrinsic manner to compute $u_c(f)$ is to use a principal component analysis. Given the Hermitian correlation matrix (3), $u_c(f)$ corresponds to the direction of the largest eigenvalue's eigenvector (λ_1 and $\overrightarrow{e_1}$ on Fig. 1),

[a]Electronic mail: samuel.davoust@onera.fr.
[b]Electronic mail: jacquin@onera.fr.

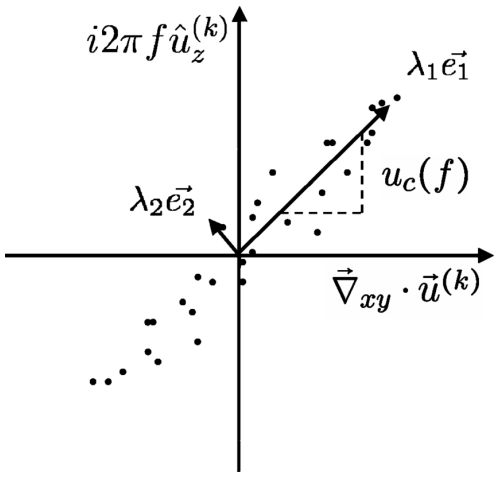

FIG. 1. Qualitative sketch of the determination of convection velocity $u_c(f)$ associated to f: scatter plot of the experimental blocks of $(\vec{\nabla}_{xy}\cdot\vec{u}^{(k)}, i2\pi f\hat{u}_z^{(k)})$. $u_c(f)$ is obtained as the slope of the first eigenvector $(\vec{e_1})$ of matrix (3).

$$\begin{pmatrix} \langle\left|\vec{\nabla}_{xy}\cdot\vec{\hat{u}}\right|^2\rangle & \langle(i2\pi f\hat{u}_z)(\vec{\nabla}_{xy}\cdot\vec{\hat{u}})^*\rangle \\ \langle(\vec{\nabla}_{xy}\cdot\vec{\hat{u}})(i2\pi f\hat{u}_z)^*\rangle & \langle|i2\pi f\hat{u}_z|^2\rangle \end{pmatrix}. \quad (3)$$

The actual result for $u_c(f)$ is complex (with a negligible imaginary part in the limit where ρ tends to 1): only the real part represents the physical convection velocity. In the limit where ρ tends to 1, the present method and the definition proposed for experimental use by Del Álamo and Jiménez[3] (Eq. 2.17) give the same analytical expression. We will show that the experimental implementation of the two methods can lead to different results.

The present method has been tested using PIV data obtained in the near field of a high Reynolds number (2.14×10^5) incompressible jet of air. The exit velocity is $U_0 = 21.6$ m s^{-1}, and the exit diameter is $D = 0.15$ m. The exit condition is a top-hat velocity profile with thin turbulent boundary layers. At the exit, the axial velocity rms in the core of the flow is 0.5% of U_0. Figure 2 is a sketch of the experimental high-speed (2.5 kHz) SPIV setup. The measurement plane is normal to the jet axis and located at $Z = 2D$ downstream of the jet exit. It extends radially up to $R/D = 0.8$ in all directions from the center of the jet. We now describe the main features of the flow at $Z = 2D$. When necessary, U_0 and D are used to scale physical quantities: for example, (Z, R, U, F) become (z, r, u, f) in non-dimensional form. As can be seen in Fig. 3, the jet is composed of a potential core and of a turbulent axisymmetric mixing layer. The vorticity thickness is $\delta = 0.36D$ and grows linearly in the z direction like $\delta/D = 0.013 + 0.172z$ for $0.5 \le z \le 2.5$. As described by previous workers,[4,8] the main unsteady features for such a flow are

- Large scale oscillations of the entire jet dominated by $m = 0$ and $m = 1$ modes at reduced frequencies (Strouhal numbers) $0.3 \le f \le 0.8$;
- Production of streamwise vortical structures in the mixing layer;

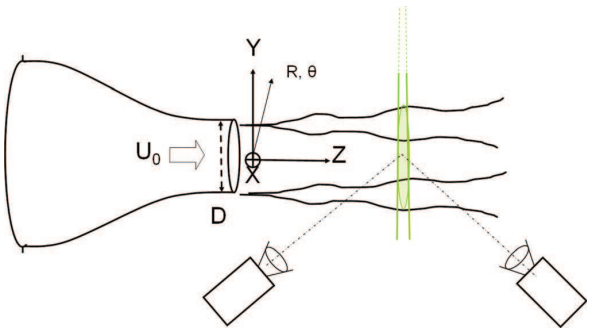

FIG. 2. (Color online) Experimental setup: a jet cross-section located at $Z = 2D$ is imaged using a high-speed stereo PIV system.

- Smaller scale turbulence with a –5/3 spectrum in the mixing layer.

SPIV acquisitions, along with hot-wire measurements, confirm that the present flow can indeed be described as above. Only a brief analysis of our data-set is performed here, a complete description will be published elsewhere. The sampling frequency is $F_a = 2.5$ kHz ($f = 17.4$) and an amount of 30 blocks of 2048 consecutive vector fields is acquired. One can show that spatial filtering by PIV interrogation windows amounts to a –3 dB cut-off expected to occur near 1 kHz ($f = 7$). Fig. 4 shows two power density spectra of the axial velocity at two radial positions. At the center of the mixing layer ($r = 0.52$), a fully developed turbulence (–5/3 slope) is observed. The beginning of the inertial range is captured by the hot-wire and not very well by the SPIV which experiences the low-pass filtering described above. The end of the inertial range cannot be observed, with the Kolmogorov frequency $F_K \approx 100$ kHz. In the core of the jet, the spectra displays a broad peak around 80 Hz ($f = 0.55$), corresponding to the passage the $m = 0$ and $m = 1$ structures. In previous studies, the dynamics of these structures has been intensively studied and their convection velocity u_c assumed to be close to 0.6 (Ref. 4).

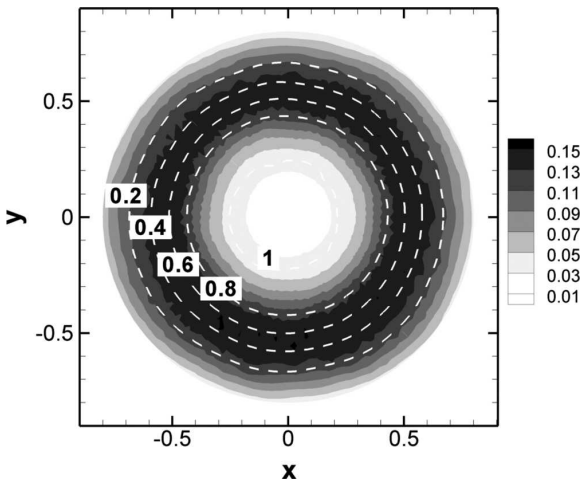

FIG. 3. Non-dimensional plot for mean axial velocity (dashed lines) and axial fluctuation rms (grey levels) at $z = 2$.

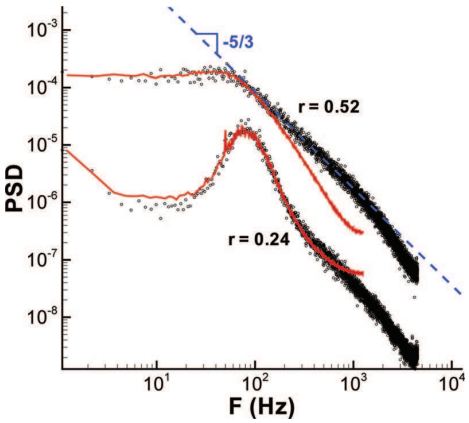

FIG. 4. (Color online) Power spectral density of axial velocity using high-speed SPIV in solid line (red online) and hot-wire in black circles at $z=2$ for $r=0.24$ and $r=0.52$. Dashed line (blue online) denotes a $-5/3$ slope.

The method described above is now applied. The (x, y) plane instantaneous divergence of velocity fluctuations is computed using a Cartesian grid and a second order central difference scheme in both directions. Relative uncertainty on the instantaneous velocity is estimated to 1.5%. In each direction, the PIV vectors are spaced by 5.4 mm. According to Raffel *et al.*[9] (p. 192), one can expect an uncertainty of 40 s^{-1} on velocity gradients with the chosen derivation scheme. The scale of the velocity gradient's fluctuations is that of the mixing layer's mean shear. One can deduce that the relative uncertainty on the velocity gradient fluctuations should be 10%. The computed divergence and the axial velocity fluctuations needed by the method are then interpolated onto a cylindrical mesh. For each block, the time recording of the velocity vector is Fourier transformed using a FFT (2048 samples). Given a frequency f, the matrix (3) (at a given (r, θ)) is computed with a statistical average over the 30 data blocks. Because of the flow's axisymmetry, converged statistical results such as matrix (3) spatially depend only on r; we also perform an azimuthal average.

The correlation coefficient ρ defined in Eq. (2) is a measure of the validity of Taylor's hypothesis. Figure 5 shows its real part ρ_r as a function of frequency f and radius r. In the center of the mixing layer (near $r=0.5$), correlation remains high for $0.4 \leq f \leq 4$: this range of scales of the developed turbulence is compatible with a Taylor hypothesis. In the external region ($r \geq 0.75$), the correlation is poor. This reflects the failure of the hypothesis in a zone where the local turbulence intensity is rather high. Finally, in the core of the jet ($r \leq 0.5$), the approximation is, say, correct for $0.4 \leq f \leq 0.9$, which is the frequency range of most of the large scale oscillations of the core. Higher frequencies exhibit a degraded correlation coefficient. An explanation is that the core contains only low amplitude high frequency fluctuations that are out of the SPIV dynamic range resolution (1.5% of the core axial velocity). Note that low frequency $f \leq 0.3$ fluctuations do occur in the core, but we could have anticipated that the Taylor hypothesis is not correct for such long spatial wavelengths (greater than 1.5 D) in this spatially evolving shear flow.

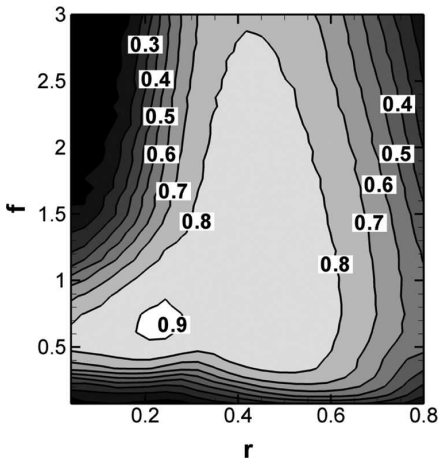

FIG. 5. Contours-plot of the real part ρ_r of correlation coefficient (2), indicating regions of validity of the Taylor hypothesis in the (r, f) plane.

Only zones where ρ_r is sufficiently high are meaningful for computation of the convection velocity, and here we have set $\rho_r \geq 0.7$. In the following, results obtained using the present method are compared with those from definition proposed by Del Álamo and Jiménez[3] in Eq. (2.17). Though this definition was reported by the authors not to be the most adapted for the analysis of their direct numerical simulation (DNS) data, it is the only one we can compute using this experimental setup. In the sequel, we will refer to it as DAJs method. In Figure 6, $u_c(f)$ corresponding to $f=0.64$ is plotted versus r. The result obtained with the present method is in qualitative agreement with that obtained by implementing DAJs method. Interestingly, using the present method, the convection velocity is almost constant and close to 0.6 in the core of the jet, a value which is usually used to study large scale structures in the near field of jets.[4] Moving on to higher frequencies, previous authors have reported that convection velocity tended to be closer to the mean flow velocity.[10] A

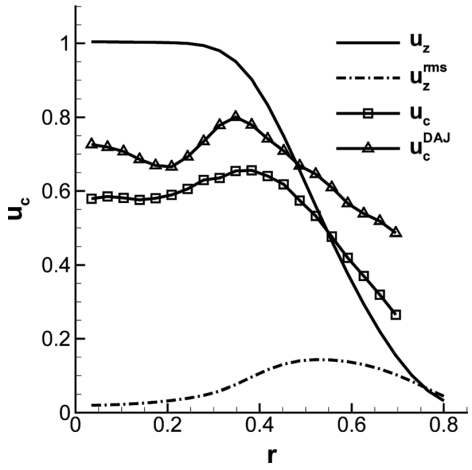

FIG. 6. Convection velocities profiles corresponding to $f=0.64$. u_c is computed with the present method and u_c^{DAJ} with the definition given in Del Álamo and Jiménez (Ref. 3) by Eq. (2.17). Also shown are the mean axial velocity u_z and the axial velocity rms u_z^{rms}.

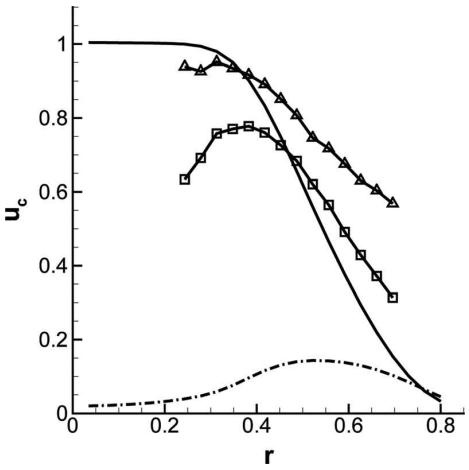

FIG. 7. Convection velocities profiles corresponding to $f = 1.4$: same legend as Fig. 6.

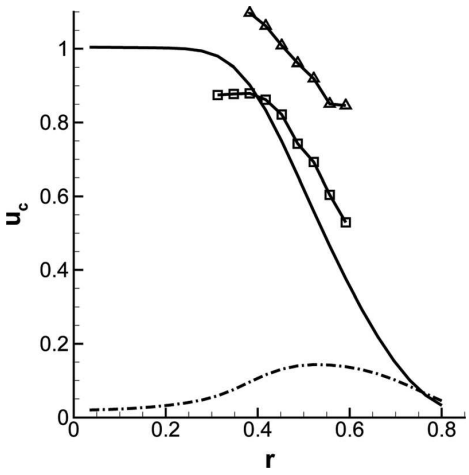

FIG. 8. Convection velocities profiles corresponding to $f = 2.5$: same legend as Fig. 6.

case where $f = 1.4$ is shown in Fig. 7. First, one can note that the extent of the region where $\rho_r \geq 0.7$ is reduced, as explained above. Second, we observe that the results from DAJs method differ significantly from ours. The present method is close to the mean flow for $r \geq 0.4$, while that of DAJ is closer for $r \leq 0.4$ Testing the two methods for $f = 2.5$ ($F = 360\ Hz$) leads to Figure 8. This is a difficult test because the PIV filtering is suspected to degrade the correlation coefficient, the zone where $\rho_r \geq 0.7$ being further reduced. One observes that the present method gives a convection velocity profile close to the mean flow profile. In contrast, when computed with DAJs method, the convection velocity is greater than U_0, which is not what one would expect for a free shear flow. As suggested to us by one of the referees, the finite difference scheme may be a source of errors at high frequencies, which interfere with the PIV cells wavelength. Further experimental investigations using a higher spatial resolution are needed to investigate this behavior.

An experimental method to deduce flow convection velocities from measurement planes orthogonal to the streamwise direction has been presented. The convection velocity of a spectral component of the streamwise velocity is defined as the principal direction of the spectral covariance matrix of time and streamwise derivative. The continuity equation is used to evaluate the streamwise derivative. In the case of cross-flow measurements, the present work can be used to assess the validity of the Taylor hypothesis and determine convection velocities directly, without having to use two planes to compute streamwise derivatives. The method was implemented in the near field of an experimental jet flow using high-speed SPIV. Regarding Taylor's hypothesis, there are zones where it is invalid because of the limited resolution of SPIV and others because of physical phenomena. In the zones where it is valid, the convection velocity of the most energetic large scale structures is almost uniform and close to 0.6. In the mixing layer, scales pertaining to the beginning of the –5/3 inertial range seem to be convected with the mean velocity. This is also the case for dissipative scales in the far field of a jet.[11]

[1]J. A. B. Wills, "On convection velocities in turbulent shear flows," J. Fluid Mech. **20**, 417 (1964).
[2]K. B. M. Q Zaman and A. K. M. F. Hussain, "Taylor hypothesis and large-scale coherent structures," J. Fluid Mech. **112**, 379 (1981).
[3]J. C. Del Álamo and J. Jiménez, "Estimation of turbulent convection velocities and corrections to Taylor's approximation," J.Fluid Mech. **640**, 5 (2009).
[4]J. H. Citriniti and W. K. George, "Reconstruction of the global velocity field in the axisymmetric mixing layer utilizing the proper orthogonal decomposition," J. Fluid Mech. **418**, 137 (2000).
[5]C. W. H van Doorne and J. Westerweel, "Measurement of laminar, transitional and turbulent pipe flow using stereoscopic PIV," Exp. Fluids **42**, 259 (2007).
[6]J. Vétel, A. Garon, and D. Pelletier, "Vortex identification methods based on temporal signal-processing of time-resolved PIV data," Exp. Fluids **48**, 441 (2010).
[7]B. Ganapathisubramani, K. Lakshminarasimhan, and N. T. Clemens, "Investigation of three-dimensional structure of fine scales in a turbulent jet by using cinematographic stereoscopic particle image velocimetry," J. Fluid Mech. **598**, 141 (2008).
[8]K. B. M. Q Zaman and A. K. M. F. Hussain, "Natural large-scale structures in the axisymmetric mixing layer," J. Fluid Mech. **138**, 325 (1984).
[9]M. Raffel, C. E. Willert, S. T. Wereley, and J. Kompenhans, *Particle Image Velocimetry. A Practical Guide*, 2nd ed. (Springer Verlag, Berlin, Germany, 2007).
[10]A. K. M. F. Hussain and A. R. Clark, "Measurements of wavenumber-celerity spectrum in plane and axisymmetric jets," AIAA J. **19**, 51 (1981).
[11]B. Ganapathisubramani, K. Lakshminarasimhan, and N. T. Clemens, "Determination of complete velocity gradient tensor by using cinematographic stereoscopic PIV in a turbulent jet," Exp. Fluids **42**, 923 (2007).

3.1 Cas du jet tournant

3.1.1 Validité

Cette méthode est maintenant appliquée à l'écoulement de jet tournant. La figure 3.1 présente l'évolution du coefficient de corrélation avec le nombre de swirl. De $S = 0$ à $S = 0.40$, l'aspect de la zone où la corrélation est correcte reste identique mais le niveau de la corrélation se dégrade légèrement. Pour $S = 0.61$ et $S = 0.81$ cette dégradation s'accentue , mais la zone de corrélation élevée s'étend vers le coeur du jet. Nous proposons d'interpréter ces observations de la manière suivante. Tout d'abord, on s'attend à ce que l'accroissement de la vitesse moyenne azimutale avec le nombre de swirl dégrade de manière progressive la corrélation entre la dérivé axiale de la fluctuation axiale et sa dérivée temporelle. En effet, la vitesse de convection des structure va progressivement acquérir une composante azimutale. Prendre en compte ceci nécessiterai de modifier la méthode pour y inclure une recherche de la direction de la vitesse de convection. Ensuite, nous verrons dans le chapitre 5 que les niveaux de turbulence augmentent de manière conséquente pour $S = 0.61$ et $S = 0.81$. Nous nous attendons alors à une dégradation supplémentaire de la corrélation car l'hypothèse de Taylor est valide dans la limite des faibles taux de turbulence [78]. Enfin, le fait que la zone de corrélation s'étende vers le coeur du jet résulte indirectement du raccourcissement du cône potentiel plus court du jet tournant pour $S = 0.61$ et $S = 0.81$. A faible swirl, le faible taux de turbulence dans le coeur du jet (inférieur à 1.5%) avait pour effet de dégrader la corrélation à cause de la sensibilité limitée de la PIV. La présence d'un signal turbulent de plus forte amplitude dans le coeur du jet tournant permet donc indirectement d'obtenir une meilleure corrélation.

3.1.2 Vitesse de convection axiale dans la couche de mélange

La figure 3.2 représente l'évolution avec S de u_c avec la fréquence réduite f au milieu de la couche de mélange ($r = 0.52$). Sur cette figure, on constate que lorsque l'hypothèse de Taylor est valide dans la couche de mélange, l'approximation $u_c = 0.6$ reste correcte dans la gamme de fréquences $0.5 \leq f \leq 2.5$. Malgré ce résultats, nous avons vu que la validité de l'hypothèse de Taylor se dégrade de manière complexe pour le jet tournant. Il faudra donc considérer cette approximation avec prudence.

3.2 Vitesse de phase d'un mode POD

3.2.1 Principe

Cette dernière section propose d'utiliser le principe de la méthode pour déterminer la vitesse de phase d'un mode POD. Si on suppose que l'écoulement est invariant par translation selon la direction z, les oscillations globales de fréquence spatiale k et temporelles f de l'écoulement s'écrivent sous la forme

$$\vec{u}(x, y, z, t) = Re(\vec{\hat{q}}(x, y)e^{2\pi i(kz - ft)}), \tag{3.1}$$

où $\vec{\hat{q}}(x, y)$ est le mode de l'oscillation. Si k et f sont réels, cette oscillation est une onde qui se propage avec une amplitude constante. La vitesse de phase u_ϕ de cette onde est alors simplement

$$u_c = \frac{f}{k} \tag{3.2}$$

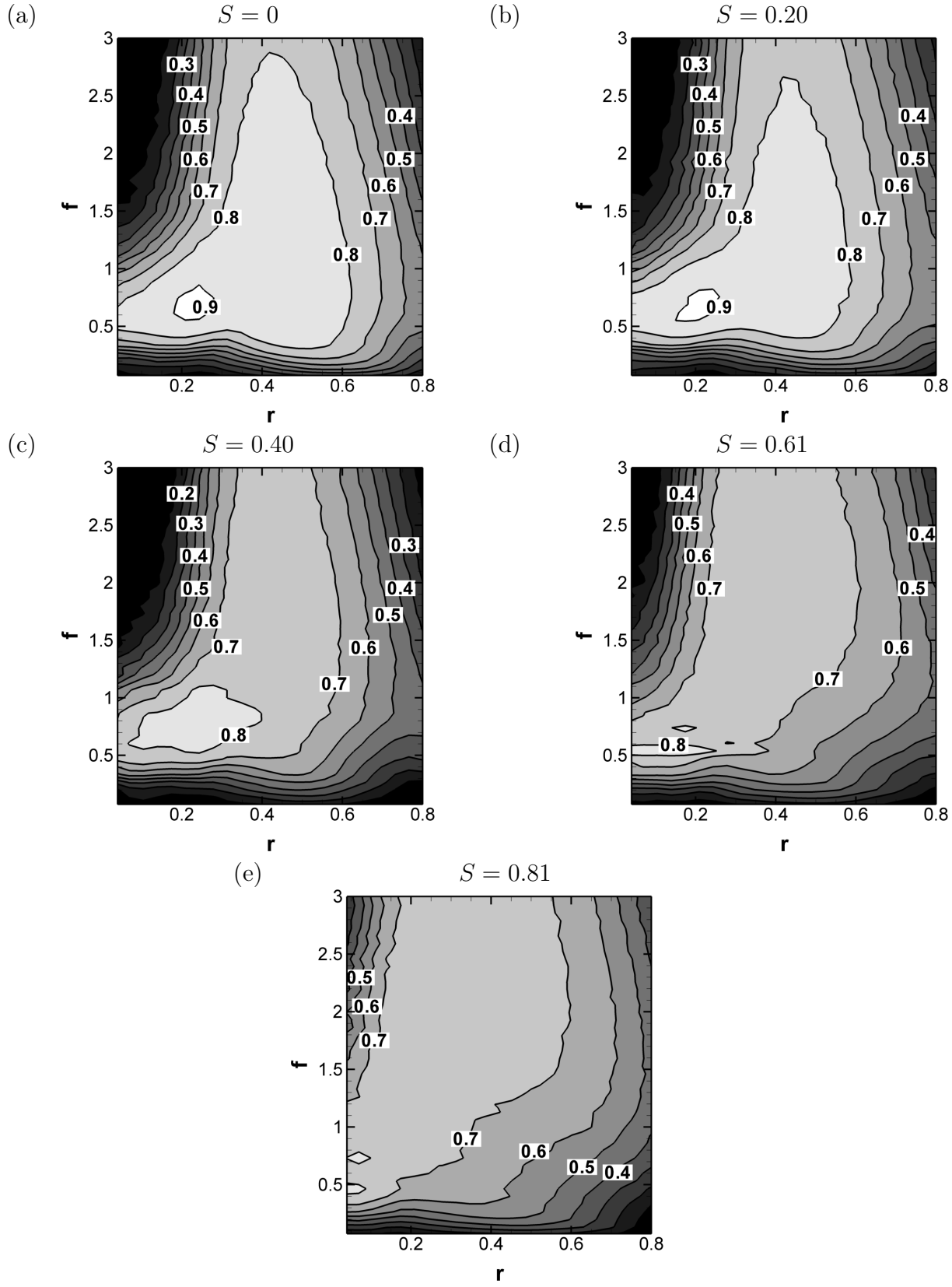

FIGURE 3.1 – Evolution dans le plan (r, f) de la partie réelle du coefficient de corrélation ρ_r avec le nombre de swirl S. La valeur de ρ_r fixe le degré de validité de l'hypothèse de Taylor.

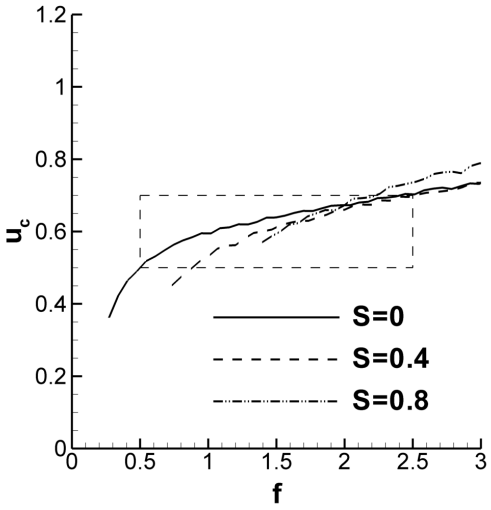

FIGURE 3.2 – Vitesse de convection en $r = 0.52$ pour les valeurs de S indiquées. Le seuil $\rho_r \geq 0.7$ a été appliqué.

Si on réalise une mesure restreinte au plan $z = z_0$ du champ de vitesse $\vec{u}(x, y, z_0, t)$ de cette onde, il est néanmoins possible de remonter à sa fréquence spatiale k si l'écoulement est incompressible car

$$\frac{\partial u_z}{\partial z}(z_0) = Re\left(ik\hat{q}_z\, e^{2\pi i(kz_0 - ft)}\right) \tag{3.3}$$

$$= -(\vec{\nabla}_{xy} \cdot \vec{u})(z_0) = Re\left(\vec{\nabla}_{xy} \cdot \vec{\hat{q}}\, e^{2\pi i(kz_0 - ft)}\right) \tag{3.4}$$

d'où

$$k = \frac{\vec{\nabla}_{xy} \cdot \vec{\hat{q}}}{i\hat{q}_z}. \tag{3.5}$$

En recombinant cela avec (3.2), il vient :

$$u_c = \frac{if\hat{q}_z}{\vec{\nabla}_{xy} \cdot \vec{\hat{q}}}, \tag{3.6}$$

Cette relation est de la même forme que l'équation (2.17) de Del Alamo and Jiménez [26]. Notons que dans le cas d'une onde incompressible idéale u_c est bien réel.

La décomposition POD que nous allons détailler dans le chapitre suivant permet de projeter les spectres temporels du vecteur vitesse notés $\vec{\hat{u}}(x, y, f)$ obtenus dans le plan $z = 2$ sur une base optimale de modes spatiaux $\vec{\phi}^{(n)}$:

$$\vec{\hat{u}}(x, y, f) = \sum_{i=1}^{N} \hat{a}^{(n)}(f)\vec{\phi}^{(n)}(x, y, f). \tag{3.7}$$

Le spectre est alors une superposition de modes orthogonaux $\vec{\phi}^{(n)}$, qui sont individuellement similaires aux modes d'oscillations $\vec{\hat{q}}$. On peut donc définir une vitesse de phase associée au mode POD par :

$$u_{\phi^{(n)}} = \frac{if\hat{\phi}_z^{(n)}}{\vec{\nabla}_{xy} \cdot \vec{\hat{\phi}}^{(n)}}. \tag{3.8}$$

$u_{\phi^{(n)}}$ est alors une fonction de l'espace (x, y) à priori complexe, car rien ne garantit que la propagation du mode se fasse à la manière d'une onde isolée d'amplitude constante. L'argument complexe de $u_{\phi^{(n)}}$ permet de quantifier ceci.

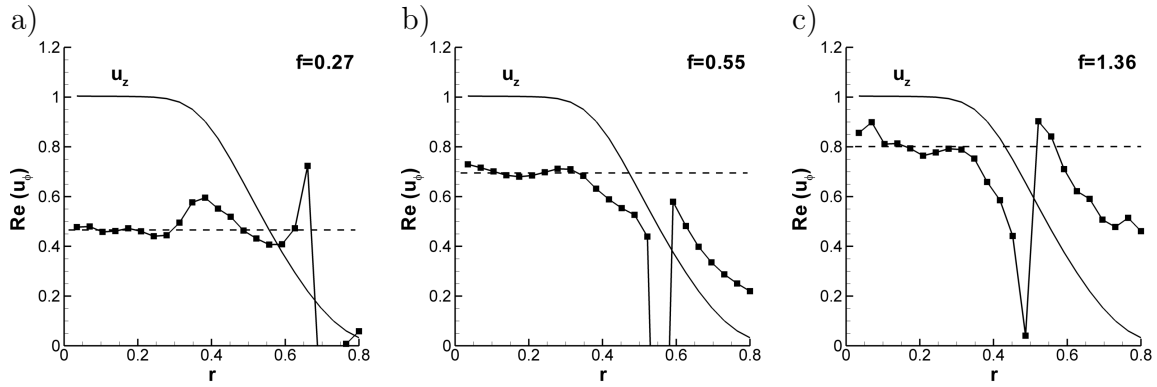

FIGURE 3.3 – Vitesse de convection (-■-) des modes POD $n = 1, m = 0$ pour $f = 0.27$ (a), $f = 0.55$ (b) et $f = 1.36$ (c) et vitesse moyenne (-). La ligne horizontale en pointillés permet de déterminer la position radiale où la vitesse moyenne est égale à la vitesse du mode dans le coeur du jet.

3.2.2 Mise en oeuvre

Sans entrer dès maintenant dans les détails de la décomposition POD, notons que pour le jet les coordonnées sont cylindriques ($(x, y) = (r, \theta)$), et la décomposition de Fourier s'effectue aussi selon l'azimut ($(r, \theta) \rightarrow (r, m)$). Nous nous limitons ici au cas $m = 0$ et au mode POD $n = 1$. $\vec{\nabla}_{xy} \cdot \vec{\phi}$ se réduit donc à $\frac{1}{r}\frac{\partial}{\partial r}(r\phi_r^{(1)})$. La figure 3.3 présente la partie réelle de la vitesse convection de ces modes POD pour 3 fréquences réduites f. On constate que les profils de vitesse de convection sont presque uniformes dans le coeur du jet. Dans les trois cas, un accident survient autour du rayon où la vitesse axiale est proche de la vitesse de convection du mode dans le coeur du jet. Ceci est dû à un effet numérique lors de la division par $\frac{1}{r}\frac{\partial}{\partial r}(r\phi_r^{(1)})$, car $\phi_r^{(1)}$ possède un maximum dans la couche de mélange. On peut cependant remarquer que la théorie des instabilités linéaires produit aussi des singularités lorsque la vitesse de phase d'un mode de stabilité (qui est uniforme dans la direction non-homogène) est égale à la vitesse du champ de base [53]. Par contre, la valeur de vitesse de phase du mode POD dans le coeur du jet augmente avec la fréquence, alors que la vitesse de phase des modes de stabilité d'un champ de base proche de ce champ moyen décroît avec la fréquence f [85]. Ce chapitre a permis d'évaluer la validité de l'hypothèse de Taylor dans le jet sans rotation et dans le jet tournant. Dans les chapitres qui suivent, l'hypothèse de Taylor sera implémentée, avec $u_c = 0.6$, pour reconstruire la structure spatiale de la dynamique de la couche de mélange axisymétrique, avec ou sans rotation.

4 Dynamique d'une couche de mélange axisymétrique turbulente

Malgré l'abondance des caractérisations expérimentales, numériques et théoriques du champ proche des jets non-tournants, la base de données expérimentales que nous avons obtenue avec la HS-SPIV peut permettre d'apporter un nouvel éclairage sur les phénomènes qui pilotent la dynamique turbulente de cet écoulement. Comme nous le décrirons, nous avons mesuré les trois composantes des grandes échelles du champ des vitesses de manière simultanée et à haute cadence dans le plan transverse $z = 2$. Concernant les modes $m = 0$ et $m = 1$, nos mesures 3C confortent les précédentes observations, et détaillent la dynamique du mode $m = 1$. Notre étude se concentre alors sur les tourbillons longitudinaux, pour lesquels les études quantitatives sont rares à grand nombre de Reynolds. Une organisation particulière des fluctuations de vorticité axiale est mise en lumière. Nous présentons un scénario qualitatif détaillant l'interaction entre ces tourbillons longitudinaux, les modes $m = 0$ et $m = 1$ et le champ moyen.

Under consideration for publication in J. Fluid Mech.

Dynamics of $m = 0$ and $m = 1$ modes and of streamwise vortices in a turbulent axisymmetric mixing layer

By S. DAVOUST, L. JACQUIN AND B. LECLAIRE

ONERA, Department of Fundamental and Experimental Aerodynamics
8 rue des Vertugadins, 92190 Meudon, France

(Received 29 April 2011 and in revised form 27 November 2011)

The near field of a $Re_0 = 2.14 \times 10^5$ and low Mach number cylindrical jet has been investigated by means of a high-speed stereo PIV set-up providing the spatio-temporal velocity field in a transverse plane, two diameters downstream of the jet exit. Proper Orthogonal Decomposition (POD) and spatio-temporal correlations are used to identify some of the main dynamical features of this flow. We show that the flow is dominated by streamwise vortices whose production and spatial organization can be related to $m = 0$ and $m = 1$ perturbations, and to the mean shear of the mixing layer. A dynamical scenario is proposed which describes this interaction, in accordance with our observations.

1. Introduction

Organization of turbulence in a jet flow has remained an active field of research since early studies such as that of Crow & Champagne (1971), due to the needs of accurate predictions in the fields of mixing, combustion and acoustics. In that respect, the description, modeling and control of the large scale structures have been recognized as major objectives. The main features characterizing the near field of a jet are $m = 0$ and $m = 1$ oscillations of the jet column, along with streamwise vortical structures in the mixing layer and smaller scale turbulence.

Linear stability theory has been successful in describing the shear instability mechanisms that allow growth of $m = 0$ and $m = 1$ modes in a parallel base flow. Michalke (1984) provides a review of spatial stability studies where various jet profiles are gathered. In the case where the axisymmetric mixing layer thickness θ is small compared to the jet diameter D, $m = 0$ is the instability mode that is most amplified at frequencies that scale with θ. As that thickness grows, the maximum amplification frequencies decrease and finally scale with D, the most amplified mode switching from $m = 0$ to $m = 1$. Further downstream, in a fully developed turbulent jet region, the Gaussian shaped base flow is only unstable to the $m = 1$ mode.

At high Reynolds number, links between the experiments and theory are more difficult to establish. In previous studies, authors have educed large scale structures in cylindrical jet flows through phased-locked measurements with a controlled excitation or through conditional sampling techniques (Crow & Champagne 1971; Yule 1978; Zaman & Hussain 1984). They have described the $m = 0$ large scale vortical structures and their interaction (pairing), but the complete azimuthal organization of the flow could not be determined. Also, initial conditions (boundary layer in the exit plane, core flow quality) are known to strongly affect the flow (Bradshaw 1966; Hussain & Zedan 1978; Kim & Choi 2009), even in the so-called self-similar region (George 1989). The use of the Proper Orthogonal Decomposition (POD) technique by Glauser & George (1987) on the jet flow has opened

the way to study 'natural' large scale structures, without having to impose an organized periodic forcing nor an a priori conditional data acquisition. This technique has been used in a variety of flows, such as a plane turbulent mixing layer in a study by Delville *et al.* (1999). In the jet, a POD of the axial velocity component was implemented by Citriniti & George (2000) and by Jung *et al.* (2004) using a rake of 138 hot-wires covering the jet in transverse planes. At two and three diameters from the jet exit nozzle, these authors described the cycle of axial velocity fluctuations keeping only $m = 0$ and $m = 3-6$ azimuthal modes. They showed that large scale $m = 0$ fluctuations take the form of 'volcano bursting' events, and inferred the existence of streamwise vortices from the organization of the axial velocity perturbation. Iqbal & Thomas (2007) reconstructed the three-component cross-correlation spectral tensor using two radial rakes of two-component hot-wires. Compared with an analysis restricted to the axial velocity component, adding the radial and azimuthal components highlights the importance of $m = 1$ modes: these modes have important energy content very early in the jet development, starting roughly at three diameters from the exit. Further downstream, the three-components POD analysis of Iqbal & Thomas (2007) shows that the most energetic mode switches from $m = 0$ to $m = 1$. Note that a scalar implementation of the POD using only the axial velocity component reveals an eventual dominance of $m = 2$ modes (Jung *et al.* 2004; Gamard *et al.* 2004; Iqbal & Thomas 2007). Tinney *et al.* (2008*a*) analyzed the downstream evolution of a transonic jet ($M = 0.85$) using cross plane (r, θ) stereo PIV planes and POD. These authors then applied a linear stochastic estimation technique using the unsteady pressure field to reconstruct the low order dynamics (Tinney *et al.* 2008*b*), and 'volcano bursting' events similar to that observed by Citriniti & George (2000) were also evidenced.

Regarding the streamwise vortex structures, in the two dimensional mixing layer, theoretical and numerical investigations (Neu 1984; Lin & Corcos 1984) show that these structures can be produced by the streamwise strain field between two subsequent spanwise rollers caused by the primary instability. Because of numerous observations of streamwise vortices there, this region is often referred to as the braid region. The most amplified spanwise wavelength of these streamwise vortices was found to scale with that of the primary instability. In the case of an axisymmetric mixing layer, the numerical study by Martin & Meiburg (1991) showed that initial azimuthal perturbations also lead to the development of streamwise vortices, organized into pairs in the braid region. An experimental study by Liepmann & Gharib (1992) details the dynamics of these streamwise structures in a low Reynolds number circular jet. This study confirmed this organization, i.e. pairs in the braid region, and showed that they actively contributed to the entrainment process of the jet in the form of intense side-jets. Note that these structures were also revealed by flow visualization in a plane mixing layer (Bernal & Roshko 1986) and a circular jet (Paschereit *et al.* 1992; Suprayan & Fiedler 1994) for higher, transitional Reynolds numbers, i.e. such that the incoming boundary layer is laminar. This was also confirmed by LES computations performed in a jet by McIlwain & Pollard (2002). In a fully turbulent self-similar flow, i.e. sufficiently far from the initial onset of the turbulent regime, direct visual observation becomes difficult. In such a flow, Citriniti & George (2000) proposed a scenario that details the life-cycle of these structures. They used POD to reduce the flow complexity, and proposed an interpretation of the streamwise velocity variations in terms of streamwise vorticity organization. Their analysis demonstrated that the vortices contribute to the entrainment process, and that they are strengthened in the braid region. Sample flow field reconstructions performed by Iqbal & Thomas (2007) suggested that streamwise vortices may connect the $m = 0$ modes. In addition, the azimuthal distribution of streamwise vortices and their downstream evolution has been characterized by azimuthal spectra of velocity components (Jung *et al.* 2004; Gamard

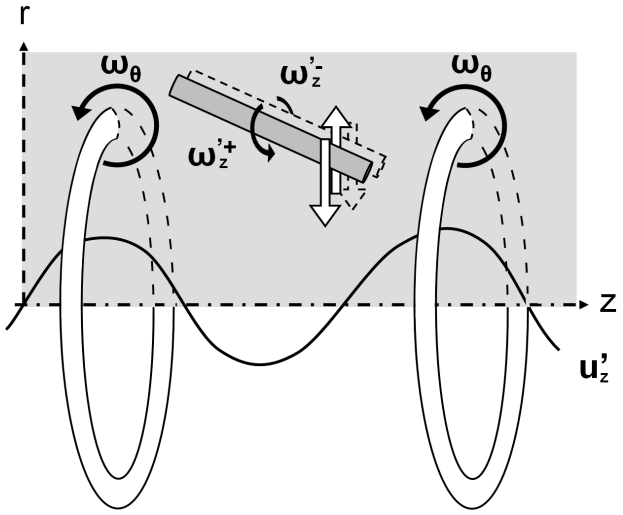

FIGURE 1. Schematic description of the organization of the axisymmetric mixing layer from various studies in the literature (see the text for details), involving $m = 0$ fluctuations and streamwise vortices of alternate signs. The solid line which crosses the z-axis is the spatial fluctuation of the axial velocity on the jet axis.

et al. 2004; Iqbal & Thomas 2007; Tinney *et al.* 2008*a*). These studies have shown a predominance of an $m = 5$ organization of these vortices in the near field, giving way to lower a azimuthal organization downstream.

The currently accepted dynamical picture of the axisymmetric mixing layer, arising from the synthesis of the above cited studies, is qualitatively sketched in figure 1 and can be described as follows. First, due to the mean axial shear, the Kelvin-Helmholtz instability produces trains of $m = 0$ vortex rings. In turn, these rings induce velocity fluctuations in the jet core, and an intense strain in the braid region, the latter promoting the growth of streamwise vorticity. As sketched in the figure, this occurs in the form of an azimuthal array of vortices of alternate signs in the braid region, whose axes are inclined with respect to the streamwise direction. As detailed above, this has been observed in computations of the growth of perturbations upon initially laminar round jets (see e.g. Martin & Meiburg 1991), flow visualizations in transitional Reynolds number jets (see e.g. Liepmann & Gharib 1992), and deduced from pseudo-visualizations based on reduced POD projection of velocity in fully turbulent jets, by Citriniti & George (2000) and Iqbal & Thomas (2007). In this flow, as noted by Citriniti & George (2000), the mechanism that creates the streamwise vortices is not fully determined, and could originate from an instability stemming from the interaction between two consecutive $m = 0$ vortex rings, or from the strain field in the braid region itself. This stresses the importance of further experimental investigations in the near field of a turbulent jet flow.

Recently, the use of high-speed stereo PIV in cross plane (r, θ) has allowed a new description of both the small scale (Ganapathisubramani *et al.* 2008) and the large scale (Matsuda & Sakakibara 2005) structures of turbulence in the far field of circular jets. In the present article, the same technique will be used in the near field in order to refine and complete the mechanisms described by figure 1. We use a high-speed stereo PIV system to access the flow dynamics of a 2.14×10^5 Reynolds number and low Mach number round jet, in a cross-plane located two diameters downstream of the exit. Thanks to this technique, the dynamics of streamwise vorticity can be quantitatively discriminated. This reveals important new findings regarding its spatial organization, such as the existence of radial arrays of opposite signed vorticity. Our also study provides further details on the $m = 0$ and $m = 1$ fluctuations. The interaction between these modes and the streamwise

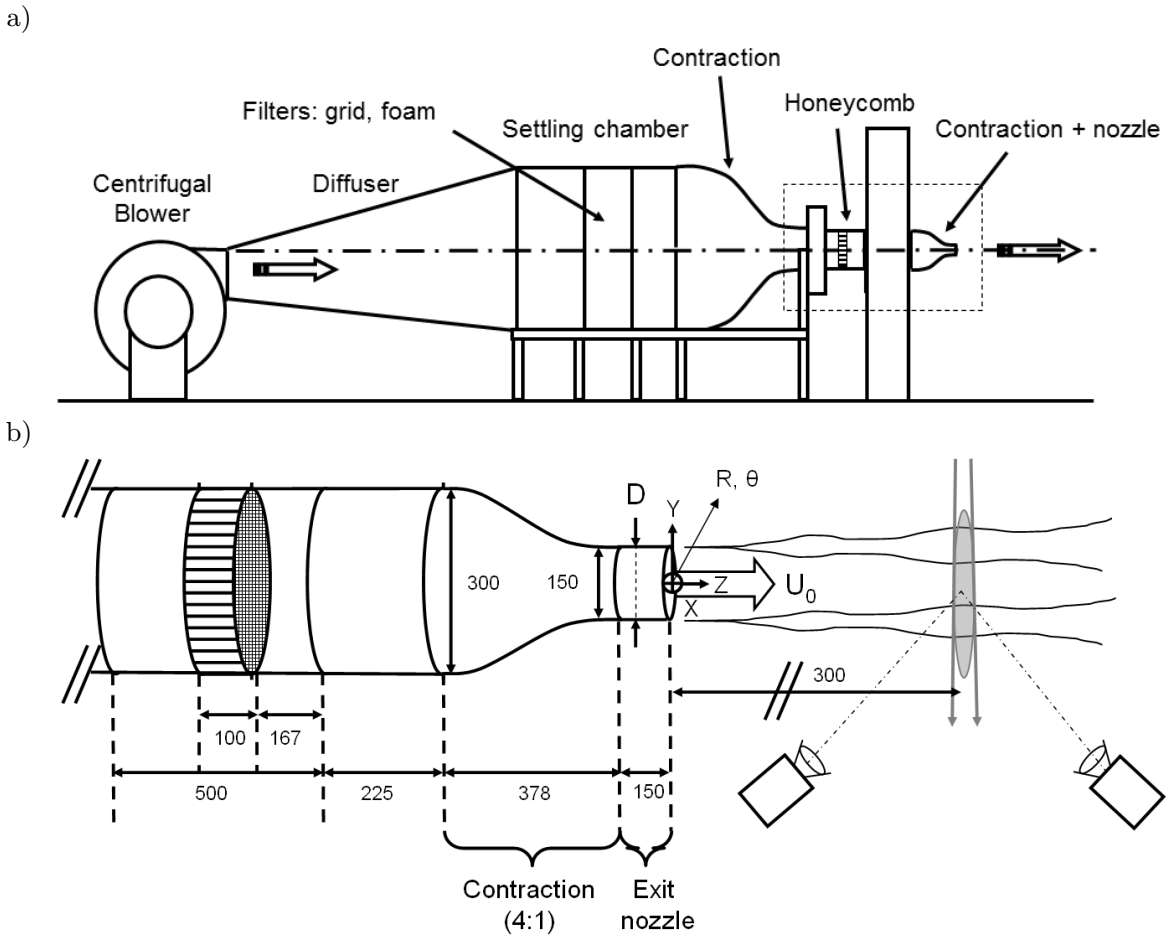

FIGURE 2. (a): Diagram of the jet facility (ONERA R4Ch wind tunnel). (b): Close-up on the contraction and nozzle (dimensions in millimeters), along with the high-speed stereo PIV setup, including the cross-plane light sheet and two high-speed cameras in a stereoscopic arrangement.

vortices, and their relative spatial and temporal organization is inferred by the cross-statistics between streamwise vorticity and streamwise velocity.

The remainder of this article is organized as follows. First, section 2 details the experiment and the data post-processing tools. In section 3, POD is used to describe the dynamical features of $m = 0$ and $m = 1$ modes. The preferential motion of the $m = 1$ mode is detailed. Section 4 presents the structure of the streamwise vortices by considering their spatio-temporal shape. Their interaction with $m = 0$ and $m = 1$ fluctuations leads to a global dynamical portrait discussed in section 5.

2. Experiment and data processing

2.1. *Experimental setup*

2.1.1. *Jet facility*

A cylindrical jet is produced by means of a blow-down wind tunnel, see figure 2 (a). This wind tunnel has been previously used by Jacquin *et al.* (1990) to study the effects of rotation on homogeneous turbulence and by Leclaire & Jacquin (2012) in a study on the generating conditions of a swirling jet. The flow is generated by a centrifugal blower, followed by a diffuser that ends in a settling chamber. The flow then undergoes a first contraction from a $1m$ square section to a $L_d = 0.725m$ long cylindrical duct of diameter $D_d = 0.3m$, the latter enclosing a $0.1m$ long honeycomb. The jet, of exit diameter

$D = 0.15m$, is terminated by a contraction and a thin nozzle, whose dimensions are provided in figure 2 (b). The exit velocity on the axis is $U_0 = 21.6m.s^{-1}$, the corresponding Reynolds number based on D being $Re_0 = 2.14 \times 10^5$. The boundary layer at the nozzle wall is tripped $48mm$ upstream of the jet exit section with a $1cm$ long circular strip of silicon carbide "carborundum" grains with nominal diameter $0.25mm$. The strip was glued onto the nozzle on surface defined using constant distances from the exit plane. We measured that this yields a thin turbulent axisymmetric boundary layer in the exit plane, with momentum thickness θ such that $D/\theta = 415$, which in turn guarantees the axisymmetry of the mean flow in the $z = 2$ measurement plane (see section 2.2 for further details on that point). The exit profile is top-hat and the turbulence intensity $\sqrt{< U_z'^2 >}/U_0$ measured with a hot-wire is lower than 0.5%. The energy of most of these fluctuations is located in the very low frequency domain (between 0.1 and $2Hz$), much lower than the typical frequencies due to turbulence in the jet near field.

2.1.2. *Non-dimensionalized quantities*

In the following, non-dimensionalized quantities will be mainly considered, and calculated using the jet diameter D and exit velocity U_0. Corresponding dimensional and dimensionless quantities will be respectively identified by upper-case and lower-case names, e.g. (R, θ, Z) and (r, θ, z) for the cylindrical coordinate system. In this frame of reference, the components of the mean velocity vector are (u_r, u_θ, u_z), and a prime will be used to denote the fluctuations. Dimensionless time and frequency are noted t and f; the latter will also be referred to as Strouhal number.

2.1.3. *High-speed stereo PIV setup*

The main results presented in this paper have been obtained by means of high-speed stereo PIV (HS-SPIV) performed in a cross-plane located at $z = 2$. The jet and the room are seeded with Di-Ethyl-Hexyl-Sebacate (DEHS) particles, whose nominal diameter is less than $1\mu m$. We use two Phantom $V12.1$ high-speed cameras equipped with $105mm$ lenses at an $f_\# = 8$ aperture, set on one side of the jet in forward scattering configuration (see figure 2b) so as to maximize signal intensity (Tropea *et al.* 2007). A high repetition rate double pulse Nd-YLF - $527nm$ laser, synchronized with the cameras, is used to generate a $2.5mm$ thick light sheet. The time delay between two pulses is set to $T_i = 60\mu s$, corresponding to a maximum displacement of 7 pixels on the cameras CCDs. The cameras are focused onto a double-sided calibration plate under the Scheimpflug principle. Calibration is performed using a pin-hole model, followed by a self-calibration procedure using particle images to correct any misalignment between the plate and the laser sheet. 30 blocks of 2048 double frame image pairs were recorded at $F_a = 2.5kHz$. With an estimation method similar to that used in Citriniti & George (2000), this provides roughly 4000 statistically independent samples (for further details, see Davoust 2011).

Vector maps are computed from the particle images using FOLKI-SPIV, a novel and very fast one step Stereo PIV algorithm implemented on GPU. Using an NVIDIA GTX480 board, this method typically computes a Stereo vector field from 1200×800 pixels images in less than $0.25s$ (see, respectively Leclaire *et al.* 2009; Champagnat *et al.* 2011, for the new stereo paradigm and for the principle of the GPU implementation in the two-component PIV case, respectively). The interrogation window (IW) size is set to 31 pixels and, accordingly to the spatial resolution yielded by the algorithm (see Champagnat *et al.* 2011), the vector fields are sampled every 30 pixels, i.e. every $5.4mm$ in the object plane. This provides 46×52 vectors and covers the jet up to $r = 0.8$ radially. The spatial and temporal resolution of this measurement, as well as its overall accuracy, will be discussed in more detail in sections 2.3 and 2.4.

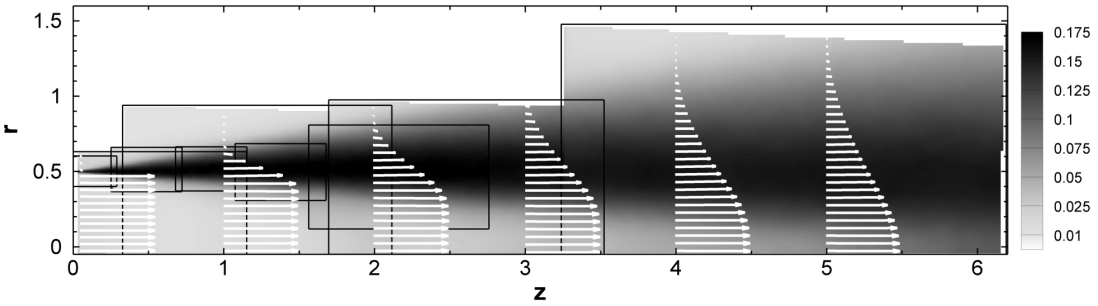

FIGURE 3. Development of the jet monitored by conventional SPIV in several longitudinal planes (black rectangles). Grey levels indicate the value of axial fluctuation rms. White vectors are selected mean velocity profiles: the exit velocity represents 0.5 horizontal unit.

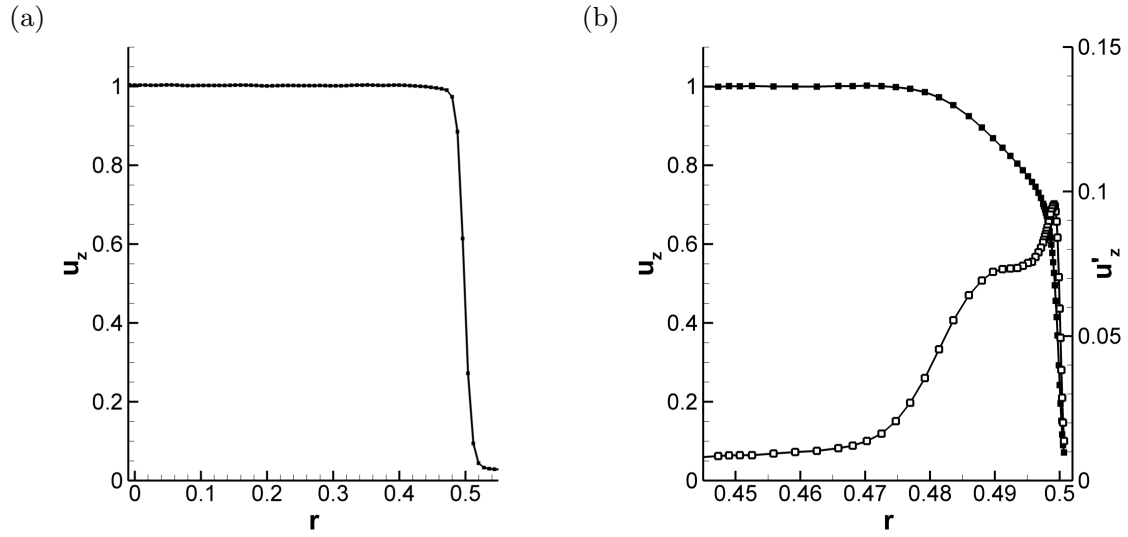

FIGURE 4. (a): Exit mean axial velocity measured at $z = 0.1$ using conventional SPIV. (b): Exit mean axial velocity (■) and axial turbulent intensity (□) measured at $z = 0.003$ using a single hot-wire probe, close-up on the near-wall region.

2.2. *Jet flow-field overview*

Prior to the study of the unsteady flow dynamics in a cross-sectional plane, we have also characterized the axial development of the jet by means of conventional Stereo PIV (SPIV) in several longitudinal planes. Results are summarized in figure 3. Here, the development of the flow is consistent with previous studies on jets, with a top-hat initial velocity profile (see also figure 4 (a)) and a thin turbulent boundary layer (see figure 4 (b)). As described by Bradshaw (1966), we observe in figure 5 (a) that, in the transition region following the nozzle exit, the maximum axial velocity fluctuation rms in the shear layer increases monotonously in the axial direction and reaches a plateau value of $u'_z = 0.17$, which is characteristic of a self-similar evolution of the shear-layer. This value is close to the results of Hussain & Zedan (1978), with similar exit boundary conditions, and is here attained around $z = 0.5$. In the mixing layer, the vorticity thickness, defined as

$$\delta_\omega = 1 \Big/ \left[-\frac{\partial u_z}{\partial r} \right]_{\max}, \tag{2.1}$$

grows linearly as $\delta_\omega = 0.013 + 0.172 \times z$ for $0.5 \leqslant z \leqslant 2.5$, as 5(b) shows. For $z \geqslant 2.5$, the mixing layer azimuthal curvature starts to have a significant effect, and the maximum axial velocity rms slightly decreases until the potential core disappears, around $z = 5$.

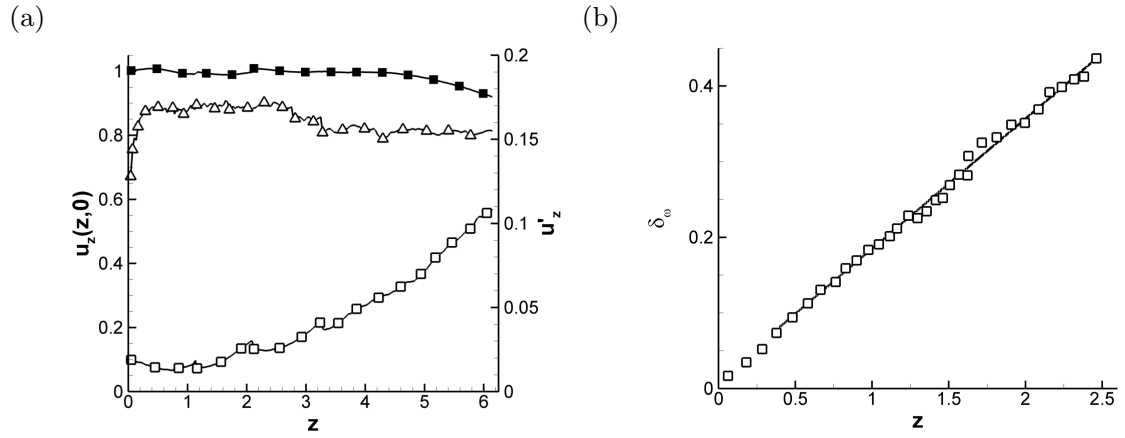

FIGURE 5. (a): Downstream evolution of centerline mean axial velocity (■), centerline turbulent axial intensity (□) and shear layer turbulent axial intensity (△). (b): Evolution of the vorticity thickness δ_ω in the shear layer. The line represents the $\delta_\omega = 0.013 + 0.172 \times z$ fit over $0.5 \leqslant z \leqslant 2.5$.

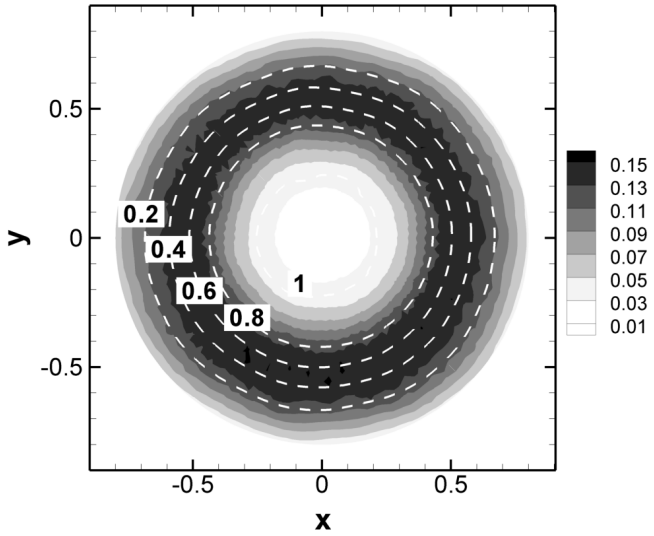

FIGURE 6. Mean axial velocity (dashed lines) and axial fluctuation rms (grey levels) at $z = 2$, HS-SPIV measurement.

Note that the center-line axial velocity does not vary significantly until $z = 5.5$ where it has decreased to 0.95, whereas the axial fluctuation rms grows monotonously. This behavior, represented in figure 5 (a), is consistent with previous measurements such as, for instance, that presented by Iqbal & Thomas (2007, figures 4 and 6). It has also motivated the choice of $z = 2$ transversal plane for the unsteady flow characterization. Indeed, at this location, the axisymmetric mixing layer is fully developed, and thin enough so that radial curvature are not dominant. Besides, the limited laser power of the high-speed PIV system also precluded the investigation further downstream locations, due to the spreading of the jet. The axisymmetry of the mean flow field obtained at $z = 2$ by HS-SPIV is represented in figure 6. The difference between the axial velocity rms levels obtained by HS-SPIV and conventional SPIV in a longitudinal plane (see figure 3) will be now investigated.

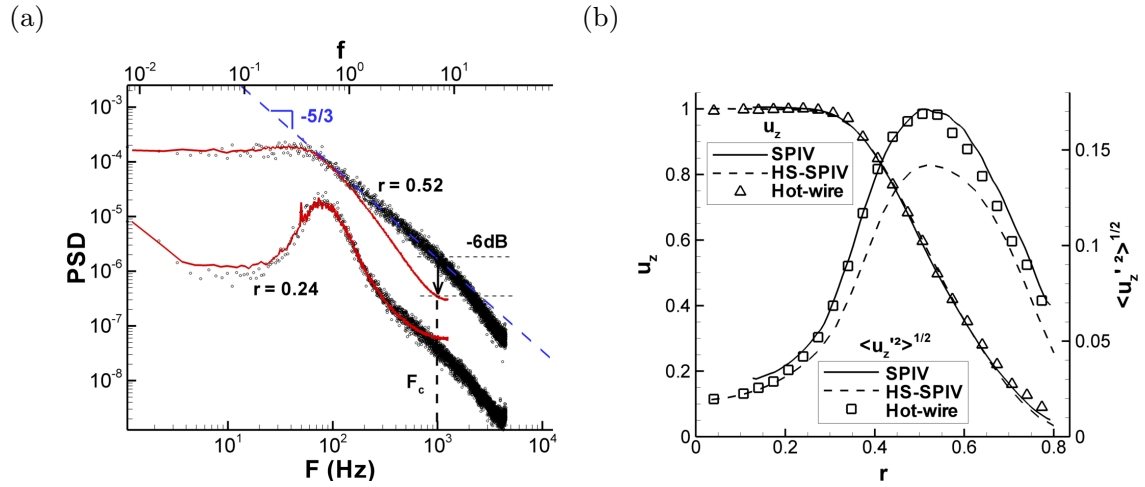

FIGURE 7. (a): Comparison of power spectral density of axial velocity using HS-SPIV (smooth line) and hot-wire (small symbols) signals at $z = 2$ for $r = 0.24$ and $r = 0.52$, as a function of both dimensional (F), and dimensionless frequency (f). A long-dashed line identifies the $-5/3$ slope. (b): Mean and rms axial velocity profiles obtained at $z = 2$ with HS-SPIV in the cross-plane, conventional SPIV in the longitudinal plane, and hot-wire anemometry.

2.3. *Comparison of PIV and hot-wire results at* $z = 2$

2.3.1. *Spatial and temporal sampling effects*

Spatial aliasing of the data is a frequently encountered issue when measuring a turbulent flow, which may dictate specific choices for the probing material. Citriniti & George (2000), for instance, overcame that problem by using probes with long wires to equip their hot-wire rake. In our case however, it turns out that no specific precaution is needed since the PIV algorithm already acts as a spatial low-pass filter, being equivalent (at best) to a spatial convolution of the velocity field by the PIV interrogation window (IW), which is a square top-hat window (Champagnat *et al.* 2011). The 31 pixels IW thus yields a $-3dB$ spatial PIV cutoff at 66 pixels, corresponding to a physical length $L_c = 12mm$. At $r = 0.5$, this spatial PIV cut-off corresponds to an $m = 40$ azimuthal wave number.

The temporal low-pass filtering behavior of HS-SPIV has also been quantified, by means of comparisons with hot-wire measurements. In figure 7 (a), power spectral density (PSD) of HS-SPIV data is compared to PSD of hot-wire signals, both in the potential core ($r = 0.24$) and in the fully turbulent mixing layer region ($r = 0.52$), at $z = 2$. The hot-wire PSD was obtained with 30 blocks of 8192 samples, low-pass filtered at $3kHz$ ($-3dB$ cut-off) before acquisition at $9kHz$, using a Dantec P11 single wire probe ($1.25mm$ long, $5\mu m$ diameter sensor). At $r = 0.24$, the broad peak around $80Hz$ corresponds to a Strouhal number $f = \frac{FD}{U_e} = 0.55$. This peak characterizes the jet column instability, and the $f = 0.55$ value is in agreement with the findings of previous studies with similar experimental setups (Hussain & Zaman 1981; Jung *et al.* 2004). As noted by Thomas (1991) and Iqbal & Thomas (2007), there is a rather large dispersion of reduced frequencies for the peak in the literature, which may be ascribed to the sensitivity of $m = 0$ modes to forcing by the jet facility. At $r = 0.52$, the hot-wire spectrum displays at least one decade of the $F^{-5/3}$ inertial cascade, before the effect of the low-pass filtering used in this acquisition is felt. The HS-SPIV power density spectra were obtained by a double averaging process, both over the 30 data blocks acquired, and over the azimuth for each radius considered. For this type of measurement, no temporal filtering can be used prior to acquisition. However, it is expected that the HS-SPIV spatial filtering affecting structures smaller than L_c should also produce a temporal filtering of high frequencies. Given L_c, a rough estimate of this

cut-off frequency F_c can be given, using a Taylor hypothesis with a uniform convection velocity chosen as $0.6U_0$. As we can observe in figure 7 (a), at this cut-off frequency $F_c = \frac{0.6U_0}{L_c} \approx 1kHz$, attenuation of the PIV velocity signal energy is more than $-6dB$ below that of the hot-wire signal. Recalling that the HS-SPIV acquisition frequency is set at $F_a = 2.5kHz$, one can thus see that the limited spatial resolution of the PIV indeed also prevents temporal aliasing. However, note that some white noise may remain at high frequencies due to the uncertainty affecting the determination of the velocity field by PIV.

To sum up, due to this intrinsic spatial and temporal low-pass filtering behavior of the PIV processing, no significant trace of spatial or temporal aliasing was found to affect the data. As seen in figure 7 (a), this results in a good agreement between hot-wire and HS-SPIV up to $200Hz$, so that the dynamics of the large scale structures is truthfully characterized.

2.3.2. *Mean flow quantities*

Mean and rms axial velocity profiles obtained at $z = 2$ from hot-wire measurements and conventional SPIV in the longitudinal plane (figure 3) are compared to HS-SPIV measurements in figure 7 (b). All three measurements lead to an identical mean axial velocity profile, except in the outer region of the jet, where the hot-wire is biased by the high local turbulence intensity (Bruun 1995). Hot-wire and longitudinal SPIV give close results for the rms profile, while cross-plane HS-SPIV captures roughly 85% of the maximum rms, as a consequence of the filtering of turbulence explained in section 2.3.1.

2.4. *Uncertainty estimation and data post-processing*

In this experiment, the uncertainty affecting the velocity field is estimated to correspond to a 0.1 pixel displacement, consistently with the traditionally agreed-upon value for PIV uncertainty (Raffel *et al.* 2007). This represents $0.3m.s^{-1}$, that is, 1.5% of U_0. The axial vorticity is computed using a circulation-based method, also described in Raffel *et al.* (2007), yielding an expected uncertainty of $30s^{-1}$. This corresponds to a maximum relative uncertainty of 10%, since the axial vorticity is of same magnitude as the maximum shear in the mean axial velocity profile, here $400s^{-1}$.

For post-processing purposes, the acquired data were transformed from Cartesian (x, y) into cylindrical (r, θ) coordinates using a bilinear interpolation. The number of radial steps was set to $N_r = 23$, and the number of azimuthal steps to $N_\theta = 128$, in order to maintain a grid dimension similar to the Cartesian grid in the outer part of the jet. However, this clearly oversamples the PIV data close to the jet axis.

2.5. *Justification of Taylor's hypothesis*

Most of the present study is carried out using HS-SPIV measurements in a single $z = 2$ cross-plane measurement. The local spatial structure of the flow upstream and downstream from this plane can be related, to a certain extent, to temporal evolutions measured in that plane, by means of the Taylor hypothesis. For example, considering the axial velocity, this hypothesis states that:

$$\frac{\partial u'_z}{\partial z} = -\frac{1}{u_c}\frac{\partial u'_z}{\partial t}, \tag{2.2}$$

where u_c denotes a convection velocity to be determined. Knowing the conditions of validity of this hypothesis is thus crucial to derive scenarios on the spatial organization of the structures, such as that proposed in figure 1. Except for the simple case of a uniform convection, it has been shown by Zaman & Hussain (1981) that Taylor's hypothesis does not faithfully unroll in space complex phenomena such as vortex pairing,

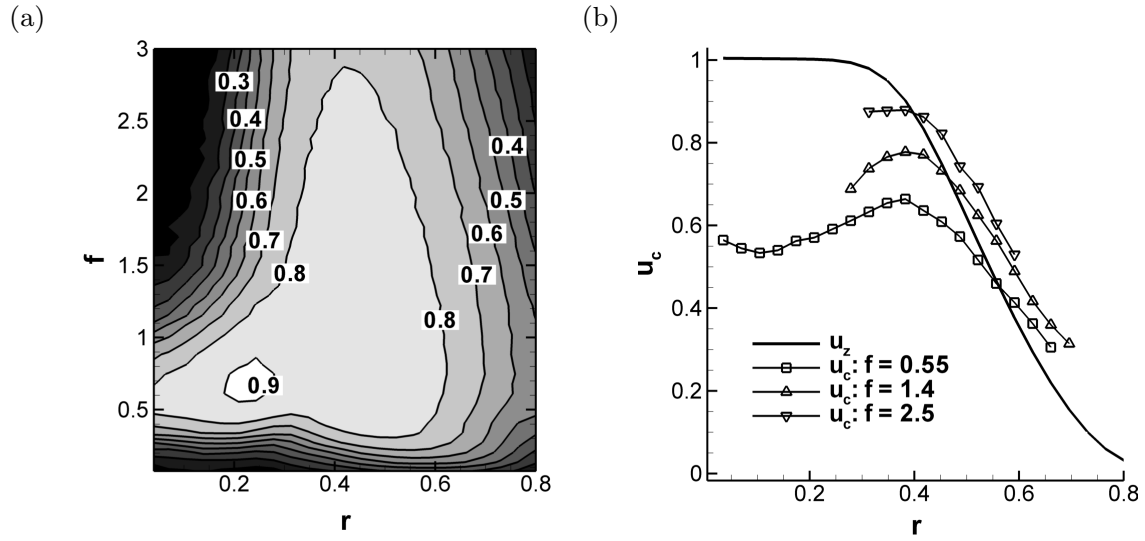

FIGURE 8. (a): contour-plot of correlation coefficient ρ, defined in eq. (2.3), in the (r, f) plane, indicating regions of validity of the Taylor hypothesis. (b): convection velocity profiles computed for $f = 0.55, 1.4$ and 2.5, and for which $\rho \geqslant 0.7$. Also shown is the mean axial velocity profile. All data correspond to $z = 2$.

for instance. Following Del Álamo & Jiménez (2009), Davoust & Jacquin (2011) have recently proposed a new method to compute the convection velocity of the structures associated with a specific frequency, together with an indicator of the validity of the frozen flow approximation. Here, the method is used to compute the convection speed of the streamwise velocity component using the HS-SPIV measurement in the $z = 2$ cross-plane, which is orthogonal to the streamwise direction. Considering the axial velocity fluctuation $u'_z(r, \theta, t)$ and given a frequency f, the correlation ρ between the Fourier transform of its time derivative and that of its spatial streamwise derivative is defined as:

$$\rho(r, f) = \frac{< (i2\pi f \check{u}_z)(-\frac{\partial \bar{\check{u}}_z}{\partial z}) >_\theta}{\sqrt{< \left|\frac{\partial \check{u}_z}{\partial z}\right|^2 >_\theta < |i2\pi f \check{u}_z|^2 >_\theta}}. \tag{2.3}$$

For a given data block, $\check{u}_z(r, \theta, f)$ is the time Fourier coefficient related to frequency f, while $\bar{\check{u}}_z$ denotes its conjugate. Also, $<>_\theta$ represents the average over both the data blocks (see section 2.1.3) and the azimuthal positions corresponding to r. In this method pertaining to incompressible flow, the divergence of the velocity vector in the measurement plane, $\vec{\nabla}_{xy} \cdot \vec{u} = \frac{\partial u_x}{\partial x} + \frac{\partial u_y}{\partial y}$, where (x, y) are the cartesian lateral directions, is used to evaluate the streamwise derivative of $\check{u}_z$, according to:

$$\frac{\partial \check{u}_z}{\partial z} = -\vec{\nabla}_{xy} \cdot \check{\vec{u}}. \tag{2.4}$$

Note that Delville *et al.* (1999) made a similar use of the continuity equation to determine the convection velocity of spanwise-homogeneous perturbations in a turbulent plane mixing layer. Here, the convection velocity $u_c(r, f)$ is then computed as the principal direction of the correlation matrix built from $i2\pi f \check{u}_z$ and $\vec{\nabla}_{xy} \cdot \check{\vec{u}}$. Figure 8 (a) and (b) respectively plot the correlation coefficient ρ in the (r, f) plane, and the convection velocity $u_c(r, f)$ for $f = 0.55, 1.4$ and 2.5. As expected, the correlation coefficient corresponding to the lowest frequencies $f \leqslant 0.3$, is degraded: the approximation is not valid for very large structures. For $f = 0.55$ (the most energetic frequency in the core of the jet), Taylor's hypothesis is more relevant, with ρ being larger than 0.7 throughout most of the profile. As seen in figure 8 (b), the computed convection velocity is found almost

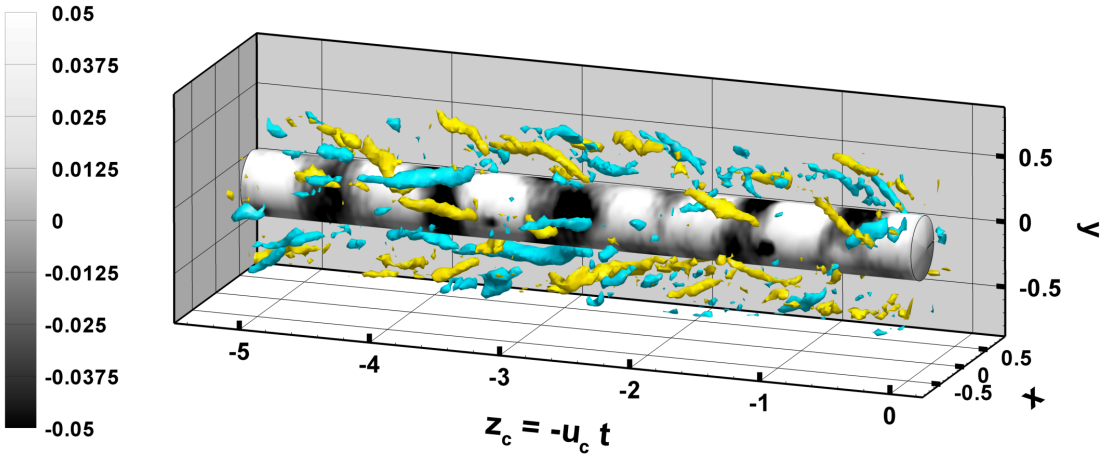

FIGURE 9. Example of pseudo-spatial flow reconstruction along $z_c = -u_c\, t$ (arbitrary origin) from HS-SPIV data in the $z = 2$ plane, using Taylor's hypothesis with $u_c = 0.6$. The streamwise velocity fluctuation u'_z at $r = 0.24$ is represented by grey contours. Yellow and blue isosurfaces respectively identify $\omega'_z = +4$ and $\omega'_z = -4$ iso-values of the streamwise vorticity fluctuation.

constant and close to 0.6 in the jet core. It decreases on the low velocity side of the mixing layer, where ρ decreases as well. Considering higher frequencies, corresponding to the beginning of the inertial range in the turbulent spectrum, one notes that the convection velocity profile is closer to the mean velocity profile, in accordance with the idea that small scale turbulence can be, on average, considered as convected by the mean flow.

Also, Taylor's approximation should fail at the exterior of the jet, due to the high local turbulent intensity. This leads to define a rough validity criteria using ρ: we see in figure 7 (b) that for $r \geqslant 0.7$, the local turbulence intensity is greater than 100% which implies that the Taylor approximation is clearly not applicable and in this region where $r \geqslant 0.7$, figure 8 (a) shows that $\rho \leqslant 0.7$. We can therefore expect that Taylor's hypothesis will be invalid in regions when $\rho \leqslant 0.7$. It is interesting to note that in the core region of the jet, Taylor's approximation should be applicable since the local turbulence intensity is low, yet we observe in figure 8 (a) that $\rho \leqslant 0.7$ for $f \geqslant 1.5$. As shows the power spectral density given in figure 7 (a), these high frequency turbulent structures are only weakly energetic and therefore have a low signal to noise ratio when measured by PIV. The low values of ρ at high frequency on the jet core thus reflect the dominance of experimental noise rather than the failure of the Taylor hypothesis.

To conclude, as far as the most energetic large scale structures are concerned ($0.5 \leqslant f \leqslant 1$), the Taylor hypothesis provides a correct local approximation of the streamwise derivative using temporal data. As shown by Zaman & Hussain (1981) in the near field of a jet, it is preferable to use a constant convection velocity. The present analysis confirms that a uniform convection velocity of $0.6U_0$ (as used by Citriniti & George 2000) is indeed a correct choice. As an example, a time sequence acquired by HS-SPIV is transformed into the pseudo-spatial sequence shown in figure 9. As will be extensively used in the remainder of this article, this is obtained by introducing a reconstructed pseudo-axial coordinate, $z_c = -u_c\, t$. It should be stressed that this pseudo-spatial coordinate describes the local spatial aspect of turbulence near $z = 2$. From this pseudo-reconstruction, we observe that the jet core velocity fluctuations correspond to $m = 0$ modes perturbed by $m = 1$ modes, while streamwise-oriented vortical structures dominate the mixing layer.

2.6. *Proper Orthogonal Decomposition*

2.6.1. *General principle*

As we follow a similar approach to that presented in several previous studies (e.g. see Citriniti & George 2000), only some of the key points of the POD technique are recalled here. POD modes are the normalized functions that maximize their mean projection with the data series in the sense of the turbulent kinetic energy. POD is here applied in the radial, inhomogeneous direction. Due to the axisymmetry and the statistical stationarity, the Fourier decomposition is naturally used along the (θ, t) directions, along which POD modes actually degenerate into Fourier modes. For each data block taken individually (see Appendix A.1 for the sampling parameters of each block), and each velocity fluctuation component u_i $(i = r, \theta, z)$, the signal is first Fourier transformed along θ and t:

$$\hat{u}_i(r, m, f) = \int_0^{t_0} \int_0^{2\pi} \exp^{-j(2\pi f t + m\theta)} u_i'(r, \theta, t) d\theta dt, \tag{2.5}$$

where t_0 is the acquisition duration of a data block. Then, following Citriniti & George (2000) POD modes $\phi_i^{(n)}(r, m, f)$ for the introduced velocity spectra are sought such that:

$$\int_0^{r_0} B_{ij}(r, r', m, f) \phi_j^{(n)}(r', m, f) dr' = \lambda^{(n)}(m, f) \phi_i^{(n)}(r, m, f). \tag{2.6}$$

Here, r_0 is the radial extent of the POD. The Hermitian kernel B_{ij} is the weighted two point cross-spectrum computed by:

$$B_{ij}(r, r', m, f) = r^{1/2} < \hat{u}_i(r, m, f) \bar{\hat{u}}_j(r', m, f) > r'^{1/2}, \tag{2.7}$$

the over bar denotes the conjugate complex, and <> denotes the average over all data blocks. Solutions to equation (2.6) are ordered following the magnitude of the (real) eigenvalue $\lambda^{(n)}(m, f)$, which represents the amount of fluctuating energy at frequency f for the azimuthal mode m. The complex eigenfunction $\phi_i^{(n)}(r, m, f)$ indicates the corresponding radial distribution of the mode vibration. By construction, these eigenfunctions are orthogonal.

Being a simple basis change, POD contains all information of the original signal, which may be reconstructed as follows:

$$\hat{u}_i(r, m, f) = \frac{1}{r^{1/2}} \sum_n \hat{a}^{(n)}(m, f) \phi_i^{(n)}(r, m, f), \tag{2.8}$$

where $\hat{a}^{(n)}(m, f)$ is defined as the projection of the velocity spectrum $\hat{u}_i$ onto the (n, m, f) POD mode:

$$\hat{a}^{(n)}(m, f) = \int_0^{r_0} r^{1/2} \hat{u}_i(r, m, f) \bar{\phi}_i^{(n)}(r, m, f) dr. \tag{2.9}$$

Practical implementation of this POD, and useful properties pertaining in particular to the symmetries in the POD modes, are detailed in Appendices A.1 and A.2.

2.6.2. *Energy convergence*

The POD method aims at reducing the complexity of the initial data. This is supposed to be the case if a large portion of the signal energy can be associated to a few modes. To assess this, it is customary to investigate the percentage $E_r^{(n)}$ of turbulent kinetic energy contained in each POD mode n, given by:

$$E_r^{(n)} = \frac{\sum_{m,f} \lambda^{(n)}(m, f)}{\sum_n \sum_{m,f} \lambda^{(n)}(m, f)}. \tag{2.10}$$

		$n=1$	$n=2$	$n=3$
POD on velocity vector	Present study	56.1	14.4	7.2
POD on axial velocity	Present study	65.6	20.7	8.6
	Jung *et al.* (2004) ($z=2$, $Re_0=1.56\times10^5$)	66.2	19.0	10.1

TABLE 1. Percentage of the total energy summed over all azimuthal modes m and frequencies f, $E_r^{(n)}$, contained in the $n=1$, 2 and 3 POD modes.

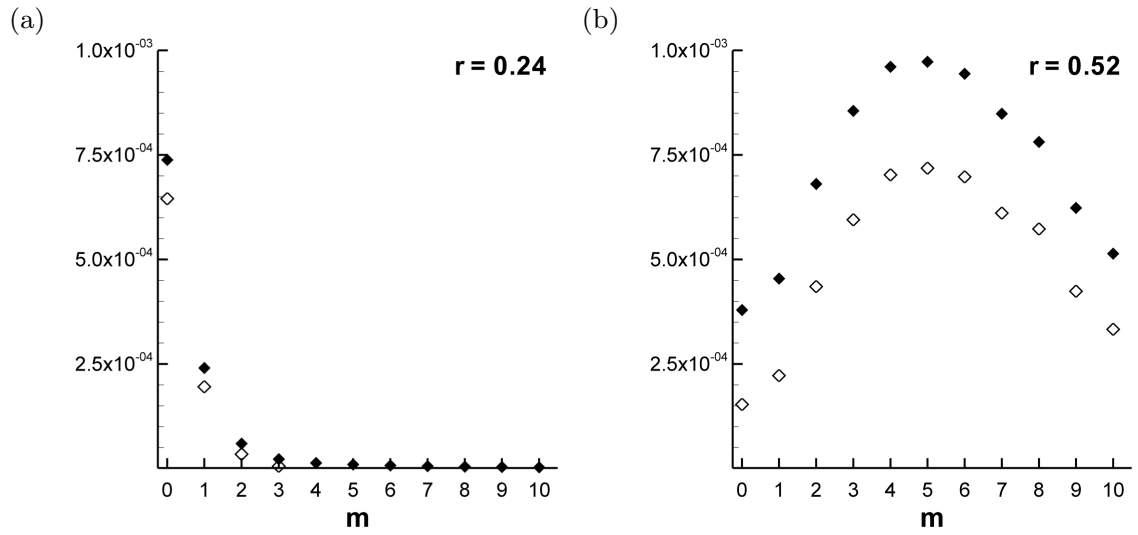

FIGURE 10. Azimuthal spectrum ($m \geqslant 0$) of axial velocity, at $r=0.24$ (a) and $r=0.52$ (b). Filled symbols: full spectrum $Sm_z(r,m)$, open symbols: $n=1$ POD approximation $Sm_z^{(1)}(r,m)$.

This expression indeed defines a fraction of the total turbulent kinetic energy integrated along r, which appears in the denominator. Values of $E_r^{(n)}$ for $n=1,2$ and 3 are given in table 1. It is observed that nearly 80% of the total energy is captured by the first three modes. If one restricts POD to the axial velocity component, a comparison can be made between the present results and that obtained by Jung *et al.* (2004). This is also reported in the table, where an excellent agreement is found. Note that in order to perform this comparison, we have used a spatial sampling grid that matches as closely as possible that used by Jung *et al.* ($N_r=6, N_\theta=32$).

3. Description of $m=0$ and $m=1$ perturbation dynamics

3.1. *Energy and frequency contents*

In this section, the relative contribution of $m=0$ and $m=1$ perturbations to the global turbulent kinetic energy is investigated, as well as the ability of a truncated POD to account for this contribution, which will be further investigated in section 3.2. Truncation is performed here by retaining only the most energetic mode of the basis, $n=1$. Introducing first the (unweighted) two-point cross-spectrum S_{ij}, defined by

$$S_{ij}(r,r',m,f) = <\hat{u}_i(r,m,f)\bar{\hat{u}}_j(r',m,f)> = \frac{B_{ij}(r,r',m,f)}{r^{1/2}r'^{1/2}}, \tag{3.1}$$

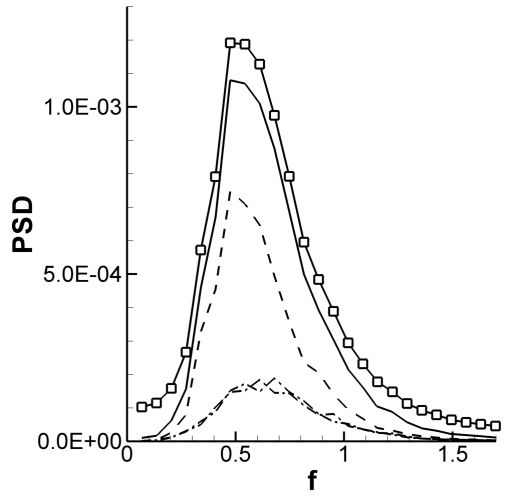

FIGURE 11. Frequency spectrum of the axial velocity at $r = 0.24$, for $f \geqslant 0$. Line with squares $(-\,\square\,-)$ stands for the full spectrum, and is a close-up of the lower red curve in figure 7(a), here with a linearly scaled x axis. The full line $(-)$ corresponds to the $(n = 1, m = [-1, 0, 1])$ POD truncation $Sf^{(1)}_{z,-1\leqslant m\leqslant 1}(r, f)$. The dashed line $(--)$ is the contribution from the projection on the $(n = 1, m = 0)$ POD mode, and the dashed-dotted line $(-\cdot-)$ that from the $(n = 1, m = \pm 1)$ modes.

the fraction of kinetic energy contained in component i of the fluctuating velocity, corresponding to mode m and at radius r, is then obtained as the azimuthal spectrum

$$Sm_i(r, m) = \int S_{ii}(r, r, m, f)df = \frac{1}{r}\int B_{ii}(r, r, m, f)df. \tag{3.2}$$

The corresponding spectrum for the $n = 1$ truncated POD can be directly expressed from the eigenfunctions ϕ_i, and is given by

$$Sm_i^{(1)}(r, m) = \frac{1}{r}\int \lambda^{(1)}(m, f)|\phi_i^{(1)}(r, m, f)|^2 df. \tag{3.3}$$

Figure 10 compares the evolution with m of $Sm_z^{(1)}$ and Sm_z, for both $r = 0.24$ (potential core) and $r = 0.52$ (mixing layer). Note that a very similar figure would have been obtained by considering the total turbulent kinetic energy instead of the axial component only. Also, symmetry considerations easily show that $Sm_z(r, -m) = Sm_z(r, m)$ (see Appendix A.2), which is why only the $m \geqslant 0$ values are plotted here. In this figure, one first observes that the jet core is weakly turbulent and quasi-exclusively characterized by $m = 0$ and $m = 1$ fluctuations. In subfigure (a), the peak for $m = 0$ corresponds to an rms amplitude roughly equal to 0.03 (i.e., 3% of U_0). On the other hand, in the middle of the mixing layer (subfigure b), the regime is fully turbulent and characterized by highly energetic $0 \leqslant m \leqslant 10$ modes. The energy is more regularly distributed with m, with a maximum around $m = 4-6$. This consistent with the findings of previous studies mentionned in the introduction. Figure 10 also shows that $Sm_z^{(1)}$ provides a very good approximation of Sm_z in the jet core, and that larger discrepancies in terms of captured energy are observed in the shear layer, though the global trend with m is retrieved. Consequently, restricting to the following on the $n = 1$, $m = 0 - 1$ POD modes will allow faithful characterization of the dynamics of the jet core, and also an optimal accounting for the $m = 0$ and $m = 1$ part of the shear layer dynamics which is correlated to the jet core.

The large predominance of $m = 0$ and $m = 1$ in the jet core is also evidenced by the

frequency spectrum. Similar to the azimuthal spectrum, this quantity is defined as

$$Sf_i(r,f) = \sum_m S_{ii}(r,r,m,f), \tag{3.4}$$

and its counterpart pertaining to the $n = 1$ truncated POD is obtained as

$$Sf_i^{(1)}(r,f) = \frac{1}{r}\sum_m \lambda^{(1)}(m,f)|\phi_i^{(1)}(r,m,f)|^2. \tag{3.5}$$

In figure 11, we represent Sf_z at $r = 0.24$ together with $Sf^{(1)}_{z,-1\leqslant m\leqslant 1}$, which is defined as in (3.5), the sum being performed for $-1 \leqslant m \leqslant 1$ only. Note that the former curve is in fact a close-up of the lower spectrum appearing in figure 7(a), in the vicinity of the $f = 0.55$ peak, considering dimensionless quantities and linear scales for the axes. The agreement between both quantities is found very good, confirming both the large predominance of modes $-1 \leqslant m \leqslant 1$ in the jet core, as well as the ability of the $n = 1$ truncated POD to model the flow there. Also, considering separately the contributions of $m = 0$ and of $m = \pm 1$ modes shows more precisely the origin of the $f = 0.55$ peak on the global spectrum, which arises from the superimposition of an $m = 0$ peak close to $f = 0.5$, and of a broader $m = \pm 1$ peak centered roughly around $f = 0.65$. For the $m = 0$ mode, it is instructive to compute the reduced frequency St_θ based on the computed mixing layer momentum thickness θ. Here $\theta = 7.30 \times 10^{-2}$ at $z = 2$, one thus obtains $St_\theta = 0.0365$, which is very close to the 0.036 value predicted by stability theory (Ho & Huerre 1984).

3.2. *Reduced-order dynamics*

3.2.1. $m = 0$ *eigenmodes*

Since the present POD is performed on velocity spectra, the POD eigenmodes are complex functions of radius r and so an inverse Fourier transform can be used to represent these modes in physical space. Recalling decomposition (2.9), this transform can be applied to a weighted eigenfunction, by considering

$$Re\left(\frac{1}{r^{1/2}}\phi_i^{(n)}(r,m,f)e^{j2\pi ft}\right). \tag{3.6}$$

This quantity characterizes the n^{th} POD eigenmode for azimuthal mode m at frequency f, with an arbitrary phase.

Taylor's hypothesis and the reconstructed pseudo-axial coordinate $z_c = -u_c t$ provides a representation of the POD mode in a longitudinal plane. Figure 12 shows two examples for frequencies $f = 0.55$ and $f = 1$. Each mode corresponds to an array of alternate positive and negative $m = 0$ azimuthal vorticity rings. This sign alternance owes simply to the fact that these modes only represent the fluctuating velocity. Superimposing the mean flow to reconstruct snapshot-like fields would cancel out the patch of negative azimuthal vorticity, leading to arrays of positive azimuthal vorticity rings, consistent with dyed flow visualizations or results from numerical simulations, such as that of Martin & Meiburg (1991). From figure 12, the corresponding spacing $\sigma_{m=0}$ between two such rings can be estimated to be slightly larger than 1. This value is in good agreement with the strongest frequency of the $m = 0$ spectrum, $f_{m=0} = 0.55$ (see figure 11), which leads to the estimate $\sigma_{m=0} = \frac{u_c}{f_{m=0}} \approx 1$, using the convection velocity $u_c = 0.6$. Importantly, note also that the global structure of the mode is similar between $f = 0.55$ and $f = 1$. Apart from the streamwise wavelength which changes as u_c/f, the radial the extent of the perturbations in the jet core is comparable; such a remark holds for all frequencies of the spectrum. Therefore, the mode organization at $f = 0.55$ may be singled out to estimate the strength of the $m = 0$ azimuthal vortex rings in the mixing layer. The bottom subfigures 12(a)

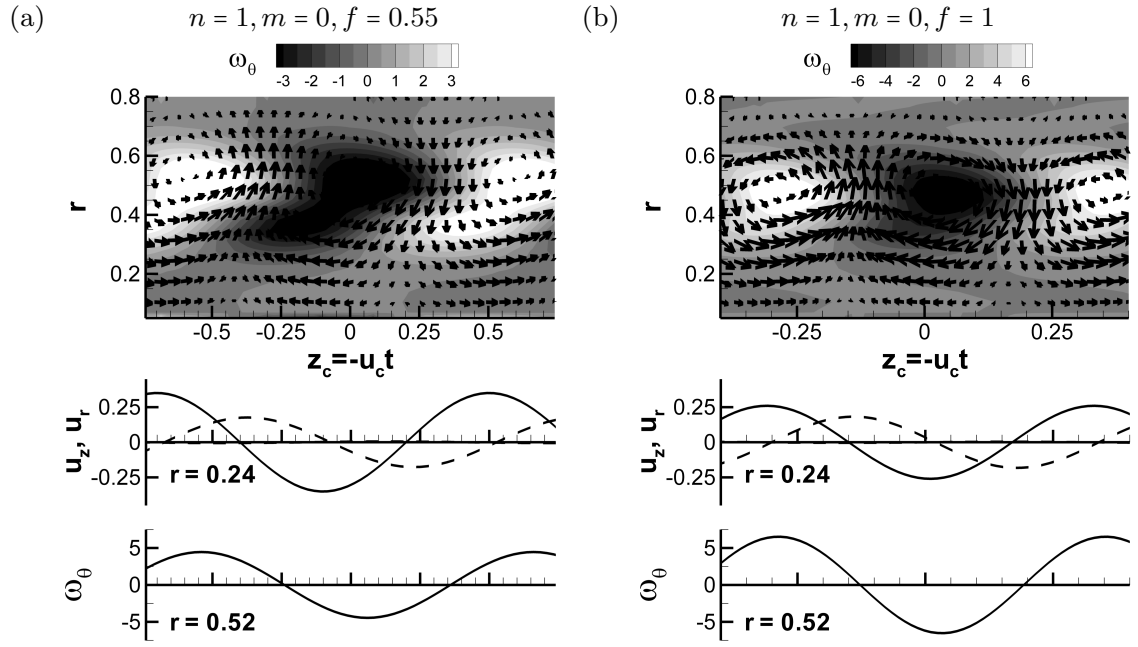

FIGURE 12. Pseudo-spatial distribution of the POD eigenmode according to eq. (3.6) for $n = 1$, $m = 0$, $f = 0.55$ (a) and $f = 1$ (b). Negative (black) and positive (white) azimuthal vorticity contours are shown at the top. The simultaneous evolutions of axial (full line) and radial (dashed line) velocity measured at $r = 0.24$, along with that of the azimuthal vorticity ω_θ at $r = 0.52$ are shown at the bottom. Note the change in the abcissa scale. The phase and amplitude are arbitrary, the latter depending on the eigenfunction normalization.

(where the ordinate scale is given by the normalization of the POD eigenfunctions), first show that the ratio of azimuthal vorticity fluctuation (at $r = 0.52$) to jet core axial velocity (at $r = 0.24$) is roughly $5/0.25 = 20$. Recalling then that the rms amplitude of the $m = 0$ axial velocity fluctuation is equal to 0.03 at $r = 0.24$ (see section 3.1), the characteristic scale of the azimuthal vorticity conveyed by the $m = 0$ mode is thus found equal to $20 \times 0.03 = 0.6$ ($0.6\frac{U_0}{D}$ in physical units). This important scale will be considered later to discuss the dynamical scenario in section 5.3.

3.2.2. $m = \pm 1$ *eigenmodes*

Similar to figure 12, figure 13 shows two examples of POD eigenmodes according to eq. (3.6) and corresponding to $n = 1$, $m = 1$ and -1 at frequency $f = 0.55$. Here as well, similar spatial organizations are obtained throughout the frequency spectrum for these modes. Note that, in contrast to figure 12, iso-contours at the top of each subfigure denote the mode azimuthal velocity (not vorticity), which is non-zero for $m = \pm 1$. Besides, as appears in the figure and can be shown theoretically (see Appendix A.2), modes with same f and opposite values of m have opposite values of this azimuthal velocity component. This remark may help understand that, while a $m = 1$ or $m = -1$ mode taken individually appears as a rotating disturbance of the jet, the superposition of two such modes may lead to a global motion which can still consist in a rotation or helix, or simply to a flapping. Selection of one of these particular motions depends on the relative phases of the two modes, flapping being obtained when these phases are equal, since it has no azimuthal velocity. In the following two paragraphs, further diagnosis tools will be introduced to determine the respective probability of occurrence of each of these motions in the jet.

(a) $n = 1$ *POD projection of* $m = \pm 1$ *dynamics.* To further characterize the dynamics

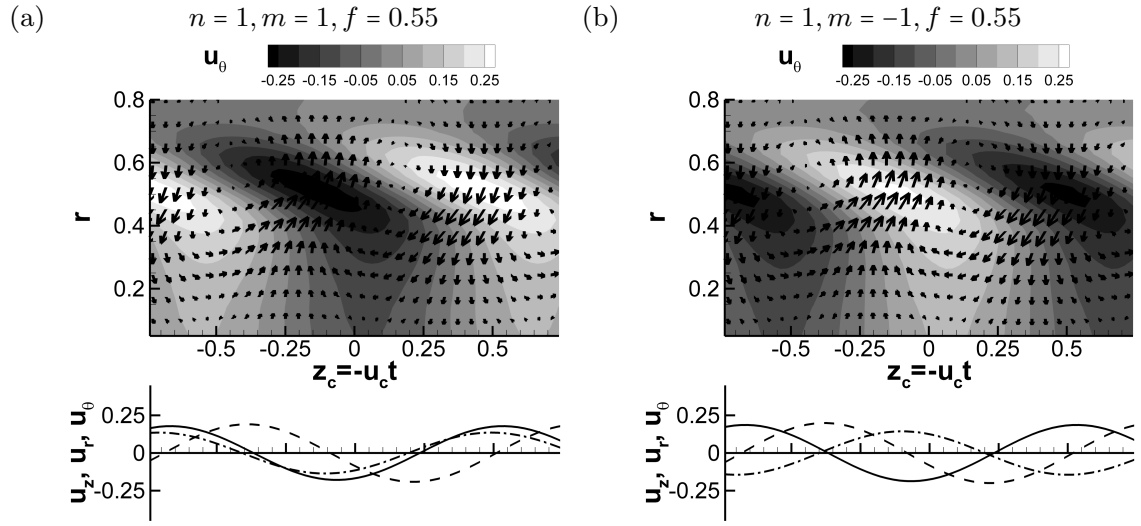

FIGURE 13. Pseudo-spatial distribution of the POD eigenmodes according to eq. (3.6) for $n = 1, m = -1$ (a) and $n = 1, m = 1$ (b) at $f = 0.55$. Negative (black) and positive (white) azimuthal velocity contours are shown at the top. The simultaneous evolutions of axial (full line), radial (dashed line) and azimuthal (dash-dotted line) velocity measured at $r = 0.24$ are shown at the bottom.

of the $m = \pm 1$ modes, we consider the physical space velocity fluctuation $u_i'(r,\theta,t)_{m=\pm1}$, defined as:

$$u_i'(r,\theta,t)_{m=\pm1} = \tilde{u}_i(r,t)_{m=1}e^{j\theta} + \tilde{u}_i(r,t)_{m=-1}e^{-j\theta}. \tag{3.7}$$

Here, $\tilde{u}_i(r,t)_m$ is the m^{th} coefficient of the theta Fourier transform of u_i':

$$\tilde{u}_i(r,t)_m = \int_0^{2\pi} u_i'(r,\theta,t)e^{-jm\theta}d\theta. \tag{3.8}$$

Due to symmetry considerations, $\tilde{u}_i(r,t)_{m=-1} = \bar{\tilde{u}}_i(r,t)_{m=1}$, so that

$$u_i'(r,\theta,t)_{m=\pm1} = 2Re\left(\tilde{u}_i(r,t)_{m=1}e^{j2\pi\theta}\right). \tag{3.9}$$

This equation shows that, considering a fixed point (r,θ), the time history of $m = \pm 1$ fluctuations in the global flow is fully contained in $\tilde{u}_i(r,t)_{m=1}$: its trajectory in the complex plane repesents the $m = \pm 1$ deformation of the jet column.
Projecting the velocity fluctuation onto the $n = 1$ truncated POD, this coefficient becomes

$$\tilde{u}_i^1(r,t)_{m=1} = \int \hat{a}^1(1,f)\phi_i^{(1)}(r,1,f)e^{-j2\pi ft}df. \tag{3.10}$$

Sample trajectories of $\tilde{u}_i^1(r,t)_{m=1}$ at $r = 0.24$ corresponding to a helical and a flapping pattern are shown in figure 14 (a) and (b). It appears that the POD provides a smoothed approximation to the original $m = 1$ coefficient given by eq. (3.8). The amplitude of both helical and flapping motion is close to 0.02, which is in accordance with the $m = 1$ value in the azimuthal spectrum of figure 10 (a). As could be expected from the broadband character of the frequency spectrum (see figure 11), the $m = \pm 1$ motions are neither a pure rotation, nor a flapping, but a more complex evolution in which these patterns are transiently encountered.
We now focus on the axial velocity component ($i = z$) at $r = 0.24$. Note that choosing a different observation radius within the jet core would provide similar results, because the POD modes are regular there. In the following, this quantity will be characterized

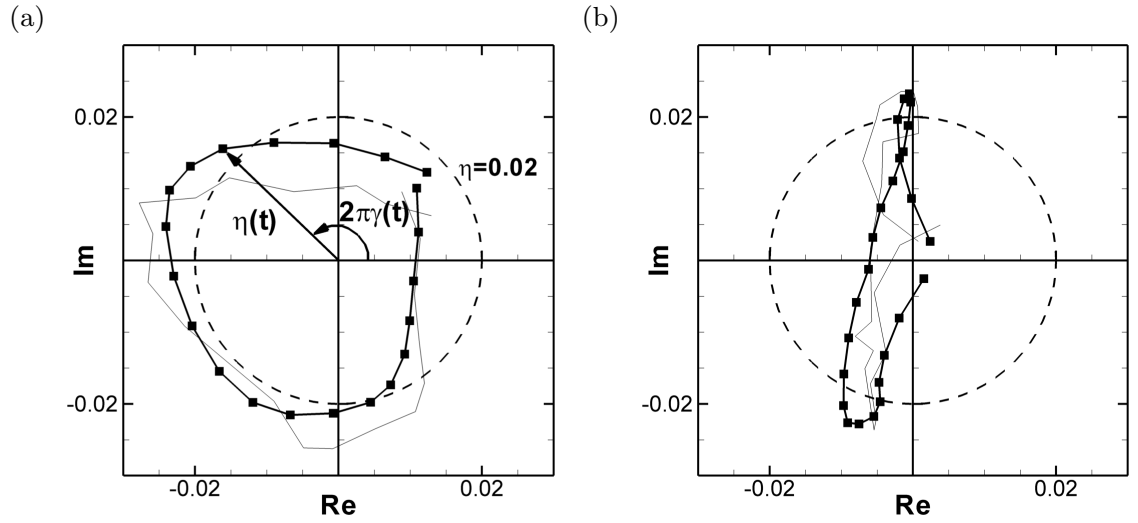

FIGURE 14. Sample trajectories in the complex plane of $\tilde{u}_z^1(r = 0.24, t)_{m=1}$ ($n = 1$ POD, full line with symbols) and $\tilde{u}_z(r = 0.24, t)_{m=1}$ (entire flow, thin line) indicating a helical motion (a), and a flapping (b). The definition of amplitude η and argument $2\pi\gamma$ (see eq. (3.11)) is illustrated in (a). Symbols indicate acquisition sampling steps. The $\eta = 0.02$ circle, which will be used for identification purposes, is drawn as a dashed line (see the text for further details).

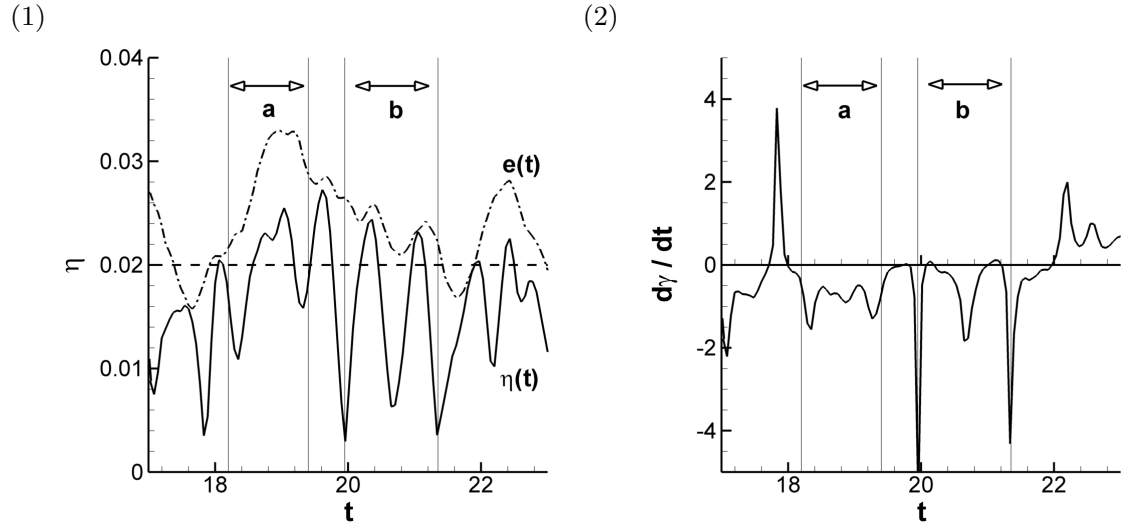

FIGURE 15. Evolution with time of (1) modulus η and (2) phase derivative $d\gamma/dt$ in a sample flow realization. In subfigure (1), the dash-dotted line corresponds to the modulus envelope $e(t)$. The horizontal dashed line represents a 0.02 threshold. Time intervals a and b correspond to the trajectories shown in figures 14 (a) and (b).

through its amplitude $\eta(t)$ and complex argument $2\pi\gamma(t)$, such that:

$$\tilde{u}_z^1(r = 0.24, t)_{(m=1)} = \eta(t)e^{j2\pi\gamma(t)}. \tag{3.11}$$

Figure 15 characterizes the $m = \pm 1$ dynamics through the time history of η and $d\gamma/dt$ as a function of time, the latter being chosen here instead of γ in order to avoid the use of a phase unwrapping method. The helical motion shown in figure 14 (a) corresponds to time interval labeled (a) in figure 15. During this event, $d\gamma/dt$ is negative and varies around 0.8 (this yields the precession frequency), while η oscillates around 0.02. For a perfect helix, both quantities would be constant. In the case of the flapping motion shown in

figure 14 (b), which corresponds to time interval labeled (b) in figure 15, $d\gamma/dt$ exhibits strong negative peaks, while η oscillates sharply between 0 and 0.025. This is indeed consistent with flapping, which in an ideal realization would lead to a Dirac comb for $d\gamma/dt$, and to the absolute value of a sine function for η. Also, note that (b) covers a time interval roughly equal to 1.4, corresponding to a frequency $f = 0.7$. Both this value and the precession frequency of (a) are close to the maximum of the $m = 1$ part of the frequency spectrum shown in figure 11, indicating that these transient patterns are an important ingredient of the $m = \pm 1$ dynamics.

(b) Statistical analysis of $m = \pm 1$ dynamics. We now seek a quantitative description of the relative importance between flapping and rotation. This is done by introducing the envelope e of the oscillations of η with time, which is represented by a dash-dotted line in figure 15 (1). This quantity is computed with Hilbert transforms as described in Sangwine & Le Bihan (2007), and may be used to characterize the instantaneous strength of the oscillating mode. We use it here to extract the most powerful $m = \pm 1$ dynamical events. In order to statistically discriminate helical motions from flapping motions in strong $m = \pm 1$ modes, we introduce $p(\eta \geqslant \alpha | e \geqslant \alpha)$, the conditional probability that the $m = \pm 1$ amplitude η is greater than a given threshold α, knowing that the envelope e is also greater than than this threshold. Restricting the computation of this probability to a sample trajectory, for a true helical motion whose amplitude is greater than a given α, one should obtain $p(\eta \geqslant \alpha | e \geqslant \alpha) = 1$, since the amplitude remains constant in that case, while for a flapping, the value should be lower than unity due to the oscillatory behaviour of the amplitude. In practice, returning for example to figure 14, both sample trajectories satisfy $e \geqslant 0.02$, as shown by figure 15(1). To graphically illustrate the value of $p(\eta \geqslant 0.02 | e \geqslant 0.02)$, the $\eta = 0.02$ iso-contour has been plotted as a dashed circle. For the flapping motion (subfigure b), one obtains $p(\eta \geqslant 0.02 | e \geqslant 0.02) = 0.23$, i.e. 23% of the snapshots in the trajectory satisfy the $\eta \geqslant 0.02$ condition. One can note that points satisfying the same condition in figure 14 (a) represent 52% of the trajectory (i.e. $p(\eta \geqslant 0.02 | e \geqslant 0.02) = 0.52$), which indicates that the helical character of the motion is more pronounced. Figure 16 (a) shows the portion of trajectories verifying $e \geqslant \alpha = 0.02$, extracted from one block of 512 successive snapshots. This figure shows that only one trajectory in this sample (shown as a red line) has a significant continuous portion such that $\eta \geqslant \alpha$, indicating that ± 1 modes tend to be statistically dominated by flappings.
The computation of $p(\eta \geqslant \alpha | e \geqslant \alpha)$ as a function of α using the entire data-set is plotted in figure 16 (b). It can be seen that $p(\eta \geqslant \alpha | e \geqslant \alpha)$ decreases with α, which shows that strong $m = \pm 1$ modes preferentially tend to be flapping motions. In this figure, $p(e \geqslant \alpha)$ is also plotted to show the rare character of events such that $\alpha \geqslant 0.03$. Returning to the global flow, this relatively low amplitude of the $m = \pm 1$ modes compared to the $m = 0$ modes in the core, see figure 11, implies that $m = \pm 1$ modes amount to a perturbations compared to the dominant $m = 0$ vorticity rings. This may for example be evidenced by the perturbed $m = 0$ streamwise velocity fluctuations of the jet core in figure 9.

4. Dynamics of streamwise vortices

This section describes the structure of streamwise vortices, the dynamical element of the scenario sketched in figure 1 in the region localized between two vortex rings. Coherent streamwise vortices are abundant in all flow realizations such as the one shown in figure 9. To characterize them, we use the axial vorticity, which here leads to similar educed structures as the λ_2 criterion (Jeong & Hussain 1995).

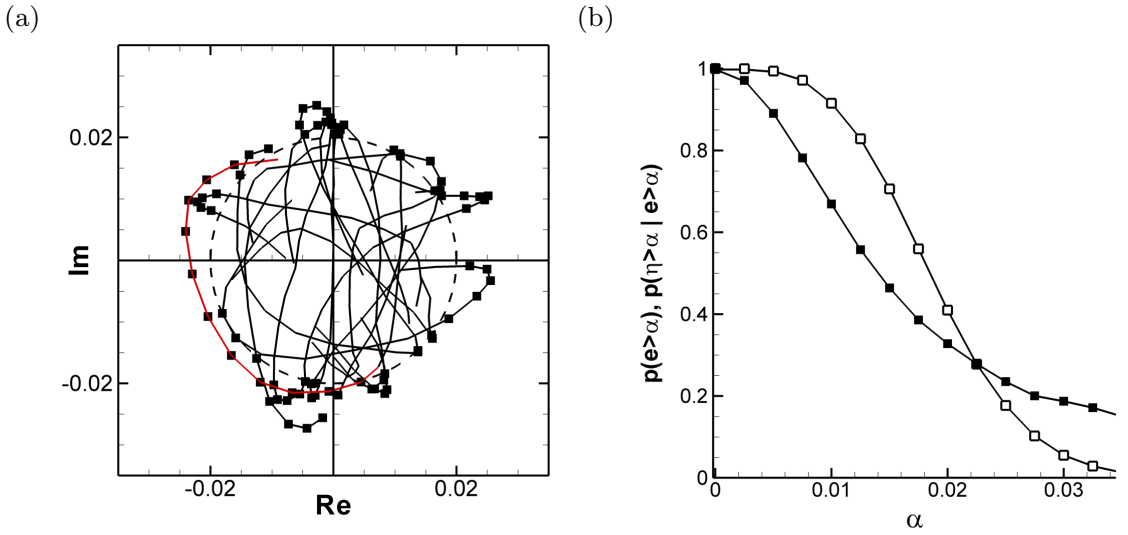

FIGURE 16. (a): Ensemble of sub-trajectories of $\tilde{u}_i^1(r = 0.24, t)_{m=1}$ such that $e \geqslant \alpha = 0.02$, extracted from a sample trajectory of 512 snapshots. Points such that also $\eta \geqslant \alpha = 0.02$ are marked by symbols. The only trajectory found to correspond to a helical motion in this sample has been singled out in red. (b): Entire data-set: evolution of probabilities $p(\eta \geqslant \alpha | e \geqslant \alpha)$ (■) and $p(e \geqslant \alpha)$ (□) as a function of α.

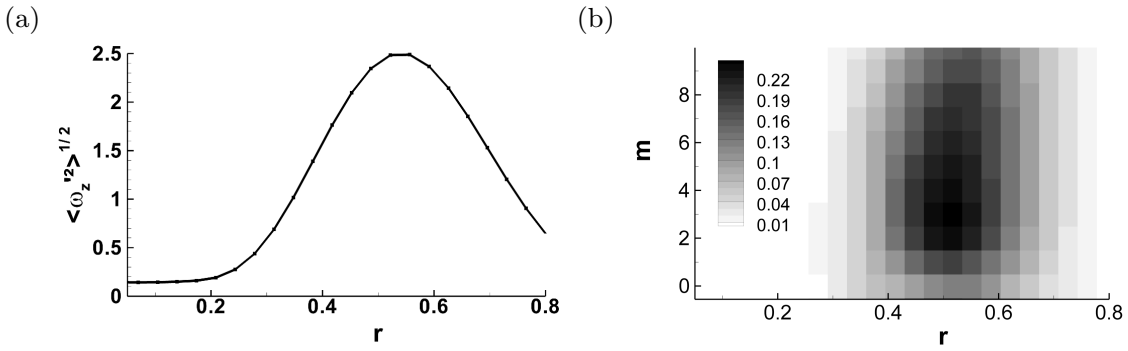

FIGURE 17. Streamwise vorticity fluctuation rms at $z = 2$ as a function of r (a), together with its azimuthal power spectrum (in grey levels, linear scale) as a function of azimuthal mode m and radius r (b).

4.1. *Organization in the longitudinal and cross-sectional plane*

Figure 17 (a) represents the dimensionless axial vorticity fluctuation rms profile. The energy of the fluctuations is concentrated in the mixing layer, being maximum at its center, in the vicinity of $r = 0.52$. This maximum is roughly equal to 2.5, which is close to the azimuthal vorticity of the mean flow: indeed, as the vorticity thickness near $z = 2$ is $\delta_\omega = 0.36$ (see section 2.2), the mean azimuthal vorticity is found roughly equal to $1/0.36 = 2.8$. On this curve, note that the plateau reached for $r \leqslant 0.2$ is the consequence of the uncertainty on the determination of the instantaneous axial vorticity; this level is indeed consistent with the 10% relative uncertainty estimated in section 2.4. As shown by the Fourier azimuthal spectrum in figure 17 (b), these fluctuations do not have a coherent periodic azimuthal organization, but rather a broad distribution over the azimuth centered around $m = 3$. Even if this may appear contradictory with the azimuthal spectrum of axial velocity fluctuations in the mixing layer(see figure 10(b)), which peaks near $m = 5$, the contradiction is only apparent since the radial and azimuthal velocity,

from which streamwise vorticity is built, concentrate their fluctuating energy in lower azimuthal modes (see Appendix B for more details).

In order to gain further insight about the spatial structure of vorticity fluctuations, we introduce the axial vorticity auto-correlation function:

$$C_{\omega_z\omega_z}(r,r',\theta',t') = \frac{<\omega'_z(r,\theta,t)\omega'_z(r',\theta+\theta',t+t')>_\theta}{<\omega'^2_z(r,\theta,t)>_\theta}. \tag{4.1}$$

The flow being azimuthally invariant, statistically, the average operator $<>_\theta$ includes both an average over the data blocks, and over θ. As ω'_z is relevant for vortex eduction, contours of $C_{\omega_z\omega_z}$ represent the statistical shape of a probable vortex around probing radius r. In figure 18, column (a) represents $t' = 0$ cross-sectional cuts of this quantity. Note that we use the $r'\theta'$ instead of θ' azimuthal curvilinear coordinate, as depicted in the explanatory sketches in this figure. From subfigure (1.a) to (3.a), the probing point progresses radially outwards, from $r = 0.38$ to $r = 0.66$. One can see that $C_{\omega_z\omega_z}$ is a symmetric function of θ', consistent with the statistical invariance in azimuth. The patch of positive correlation centered around the probing point $(r'\theta' = 0, r' = r)$ exhibits a circular shape with a radius close to 0.1. These subfigures also reveal the existence of zones of negative $C_{\omega_z\omega_z}$ neighboring this principal patch, indicating the occurrence of opposite sign vorticity in the statistical sense. This leads to a global portrait featuring arrays of alternate sign vortices, which are not preferentially distributed along the azimuth as depicted in figure 1, but rather along the radius. Note that the fact that vorticity is not strongly distributed along the azimuth is consistent with the absence of azimuthal wavenumber selection in the spectrum of figure 17.

The organization of this streamwise vorticity in the longitudinal (r', z'_c) plane appears in the left column of figure 18 (subfigures b), where one has made use of Taylor's hypothesis by introducing $z'_c = -u_c t'$, with convection velocity $u_c = 0.6$ (see section 2.5). Interpretation of this pseudo-reconstructed spatial correlation should be given with care, especially outside of the mixing layer region (say for $r \geqslant 0.7$), where the validity of the Taylor hypothesis was shown to be degraded (see section 2.5). This group of subfigures completes the above conclusion by showing the streamwise extension of these axially elongated, radially organized vortices. From the plot at $r = 0.52$ (subfigure 2.b), a characteristic length σ_{ω_z} of these vortices at the center of the mixing layer can be obtained, using the streamwise extent of the 0.1 auto-correlation contour. This leads to $\sigma_{\omega_z} = 0.5$, which is lower than the $\sigma_{m=0} = 1$ spacing between successive $m = 0$ rings found in section 3.2.1, both in the $m = 0$ POD mode shape and through frequency considerations. Subfigures (b) also show a preferential inclination angle in the longitudinal plane of the auto-correlations of axial vorticity, and thus of the streamwise vortices. Still at the center of the mixing layer ($r = 0.52$), contours are inclined from the z'_c axis by an angle close to 20°. One notes that this is similar to the equilibrium value of 22° obtained by Rogers & Moin (1987) from the spatial auto-correlation of vorticity in a homogeneous turbulent shear flow. As r increases (resp. decreases) from this location, so that the inhomogeneous character of the flow becomes influential, this angle is observed to increase (resp. decrease). This evolution is plotted in figure 19. Again, note that outside of the mixing layer, this can only indicate a trend, as it is not legitimate to infer the vorticity inclination from the HS-SPIV data in zones where the Taylor hypothesis is not valid with a large enough degree of confidence.

Figures 20 and 21 show examples of snapshots (either actual, or Taylor pseudo reconstructed snapshots) in which this flow organization is particularly obvious, in cross-sectional and longitudinal cuts, respectively. In figure 20, four vortices have been singled out, which exhibit opposite vorticity in their direct radial neighborhood. In particular,

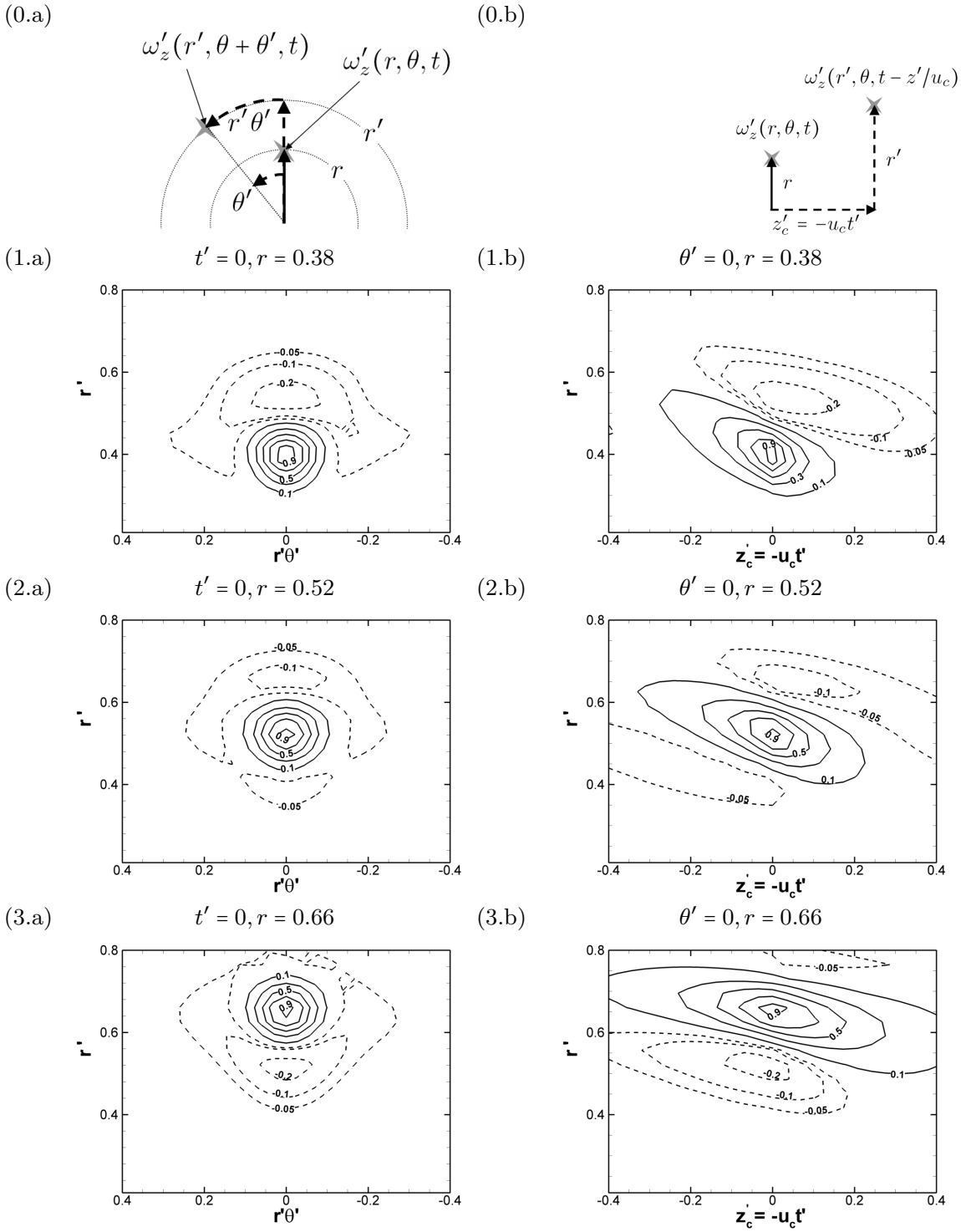

FIGURE 18. Iso-contours of streamwise vorticity auto-correlation $C_{\omega_z\omega_z}(r, r', \theta', t')$. (0.a) and (0.b): Explanatory diagrams for probing locations. Left column (a): $(r', r'\theta')$ cross sections for $t' = 0$. Right column (b): spatial pseudo-reconstruction using Taylor's hypothesis: (r', z_c') cross sections for $\theta' = 0$.

vortex labeled 1, which is close to the jet core, has an opposite vortex located radially outward, leading to an overall vorticity structure very close to the correlation contours obtained in figure 18 (1.a) for $r = 0.38$. Vortex labeled 2 in figure 20, located in the center of the mixing layer, is surrounded radially by opposite sign vorticity, reminiscent of the contours of subfigure 18 (2.a), in which the negative correlation tends to become symmet-

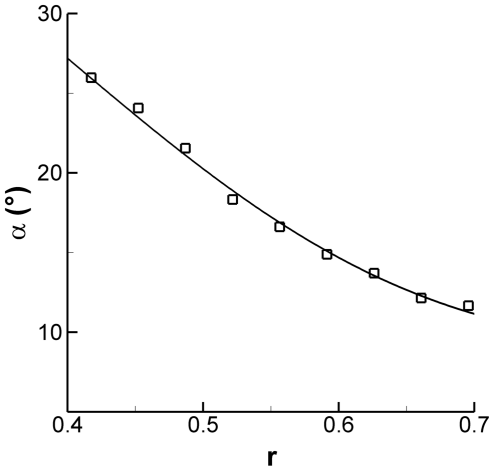

FIGURE 19. Streamwise vorticity inclination angle from the z_c' axis as a function of r. The line is a polynomial fit of the data.

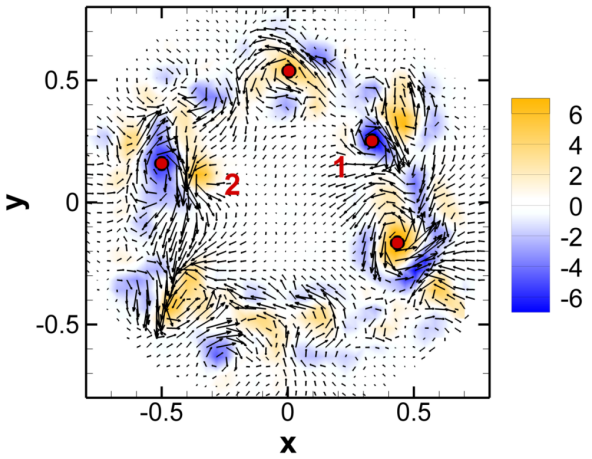

FIGURE 20. Snapshot of the flow streamwise vorticity fluctuation ω_z', corresponding to $z_c = -0.378$ in figure 9. Four vortices have been identified by red circles, see the text for details.

ric about $r' = r$. In figure 21, the instantaneous azimuthal velocity fluctuation, obtained both by conventional SPIV (subfigures a to c), and by Taylor pseudo-reconstruction from cross-plane HS-SPIV data (subfigure d) is represented in the longitudinal plane. First of all, the validity of the present use of Taylor's hypothesis is confirmed, as shown by the good agreement between the two series of measurements (compare in particular b and d). This allows to educe the vortex axes in subfigures (a) to (c), by noting that large gradients of azimuthal velocity with a change of sign in these subfigures coincide with axial vorticity patches in subfigure (d). These axes are represented by solid or dashed lines, depending on the sign of the inferred axial velocity. The selected snapshots are indeed representative of the whole data-set, as they nicely match the spatial organization observed in the correlation plots of figure 18. They show arrays of inclined, opposite signed vortices, whose inclination does not depend on the vorticity sign, and varies with the radius in agreement with the evolution shown in figure 19. Importantly, figure 21 also shows that this organization appears to be a very robust feature of the present mixing layer, since it is observed from $z = 1$ to $z = 3$.

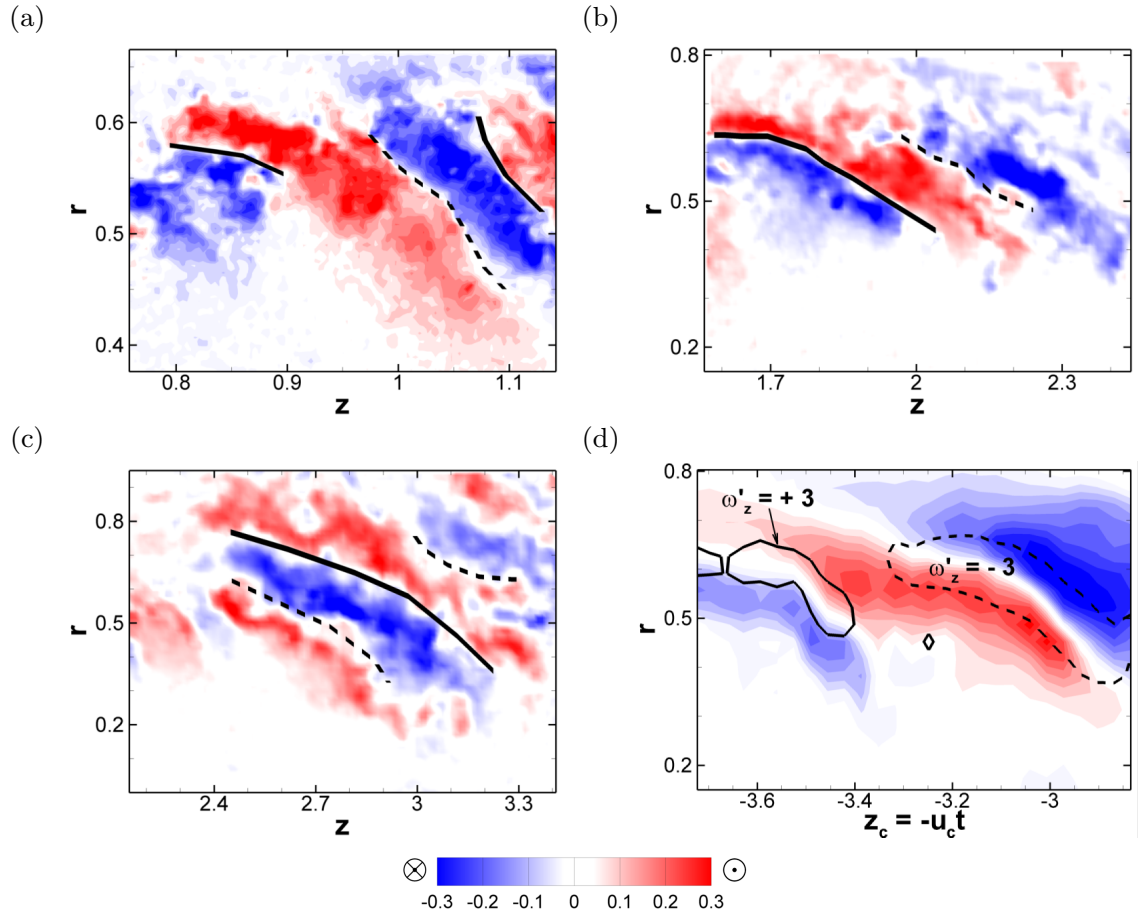

FIGURE 21. Snapshots of azimuthal velocity contours. (a) to (c): samples from conventional SPIV in the longitudinal plane, close-ups centered around $z = 1$ (a), $z = 2$ (b) and $z = 3$ (c); solid (resp. dashed) lines in these figures are hypothesized locations of the centers of positive (resp. negative) streamwise vortices cut by the longitudinal planes. (d): Taylor pseudo- reconstruction from HS-SPIV data in the $z = 2$ cross-plane, with $\omega_z = \pm 3$ streamwise vorticity contours, shown as solid and dashed lines. The time origin for this subfigure is the same as in figure 9. Compared to the conventional SPIV planes, the HS-SPIV reconstruction spans a larger portion of the jet, therefore the spatial resolution is lower, which explains the smoother contours.

4.2. *Inclination of the vortices in the axial-azimuthal plane*

Whereas figures 18 and 21 have shown that successive radial vortices of opposite sign have the same inclination angle in the longitudinal plane, figure 9 suggests that this is not the case in an axial-azimuthal plane. Since this may not be characterized by the auto-correlation function (4.1), which displays an azimuthal symmetry, we introduce its restriction to streamwise vorticity of the same sign. In figure 22(a), contours of the restriction to positive streamwise vorticity in the $(z'_c, r'\theta')$ plane are compared to that of the full auto-correlation. The former are indeed tilted with respect to the latter, allowing to estimate the relative angle β between the vortex and the streamwise axis in the azimuthal direction. Note that if negative streamwise vorticity had been considered, tilting in the opposite direction would have been observed, leading to an opposite value of β. Similarly to the inclination angle α of the vortex axis in the longitudinal plane, β also depends on the radial position, as shown by figure 22(b). Larger tilt values are obtained close to the jet core, with an approximate maximum value of 20°, while the outer part of the mixing layer is characterized by very moderate values, on the order of 5°.

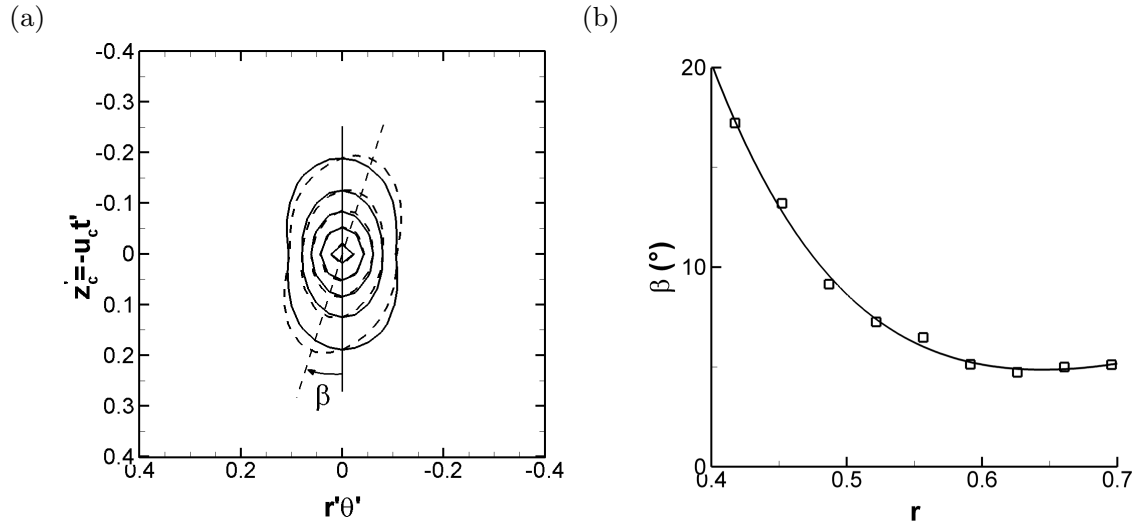

FIGURE 22. (a): Iso-contours of streamwise vorticity auto-correlation in a $(z'_c, r'\theta')$ cross section for $r = 0.52$; full auto-correlation function (solid lines) and restriction to positive streamwise vorticity (dashed lines). Contour lines start from 0.1 and are equi-spaced by 0.3. (b): tilting angle β of the positive streamwise vorticity as a function of r. The line is a polynomial fit of the data.

Note that the tilt of a given vortex axis in an axial-azimuthal plane is consistent with the organization shown in figures 18 and 21. For a given vortex, such as that depicted by a solid line in figure 21(c), this angle can be understood by considering the induction effects due to the two opposite signed neighboring vortices. Such an argument was also introduced by Jeong *et al.* (1997) to explain the tilting angle of near-wall coherent structures, which display a similar alternating sign organization. More details on this similarity, along with a mechanism that explains the origin of these successive opposite signed vortices in this axisymmetric mixing layer will be proposed in section 5.3.

5. Interaction between $m = 0$ and $m = 1$ modes and streamwise vortices

5.1. *Correlation of streamwise vorticity and velocity*

Sections 3 and 4 have described the structure and dynamics of the $m = 0$ and $m = \pm 1$ modes, and of streamwise vorticity in the mixing layer, respectively. The aim of this section is now to characterize the degree of correlation of these two dynamical features. As we have characterized the $-1 \leqslant m \leqslant 1$ modes by the axial velocity fluctuation, and the streamwise vortices by the axial vorticity fluctuation, it is thus natural to introduce the correlation of streamwise enstrophy $(\omega_z'^2)$ with axial velocity to investigate their possible interaction:

$$C_{\omega_z^2 u_z}(r, r', \theta', t') = \frac{< \omega_z'^2(r, \theta, t) u_z'(r', \theta + \theta', t + t') >_\theta}{< \omega_z'^2(r, \theta, t) >_\theta \sqrt{< u_z'^2(r, \theta, t) >_\theta}}. \tag{5.1}$$

This triple correlation coefficient is used as follows: given a streamwise vortex located at fixed r, $C_{\omega_z^2 u_z}$ shows the correlation of this vortex with the local axial velocity fluctuation u_z', at $(r', \theta + \theta', t + t')$, i.e. the value of the conditional axial velocity fluctuation at r' associated with the presence of streamwise vorticity at r. As in the previous sections, we then use Taylor's hypothesis to derive a three-dimensional space correlation, by introducing $z'_c = -u_c t'$. Consistent with our goal to characterize the interaction of streamwise vortices with $m = 0$ and $m = \pm 1$ modes, we study iso-contours of $C_{\omega_z^2 u_z}$ for three probing points in the mixing layer (where streamwise vortices occur), $r = 0.38$, 0.52

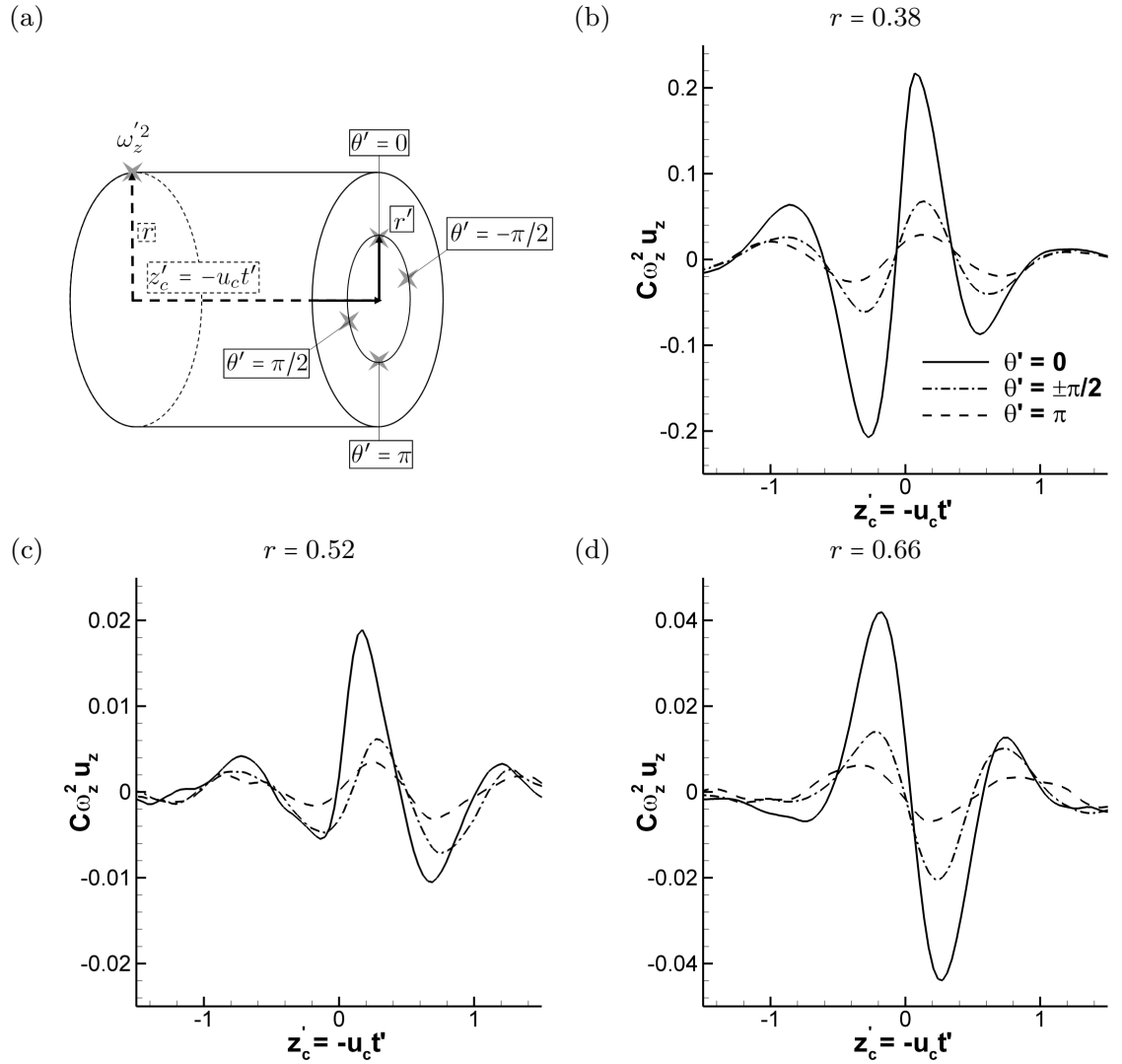

FIGURE 23. Correlation of streamwise enstrophy and velocity fluctuations $C_{\omega_z^2 u_z}(r, r', \theta', t')$ as a function of z_c'. As sketched in (a), r corresponds to the location of streamwise enstrophy and is set to r = 0.38 (b), 0.52 (c) and 0.66 (d). The streamwise velocity is measured close to the jet axis, at r' = 0.24, and at selected values of θ'. Note the different ordinate scales for each subfigure.

and 0.66, the axial velocity fluctuation u_z' being systematically considered in the jet core region, at r' = 0.24. Recalling the correlation results of figure 18 and the snapshots shown in figure 21, these radial positions for the probing of streamwise enstrophy respectively correspond to the downstream end, the middle (in the axial sense), and the upstream end of a streamwise vortex. Results are shown in figure 23. To facilitate their analysis, we also introduce a synthetic sketch, figure 24, depicting the location of the streamwise vortices relative to m = 0 and m = ±1 perturbations implied by this figure. This diagram is in fact a new version of the mixing layer dynamics sketch presented in the introduction (figure 1), modified so as to include the present findings.

As we can see in figures 23 (b) to (d), streamwise vortices and m = 0 modes are indeed correlated, the conditional streamwise velocity perturbation clearly having an m = 0 component. Indeed, at each probing radius r, correlation shows a spatial oscillation with the same phase for all separation angles θ'. One can also note that the spatial period of the oscillations is close to $\sigma_{m=0}$ = 1, the wavelength of the m = 0 rings (see section 3.2.1).

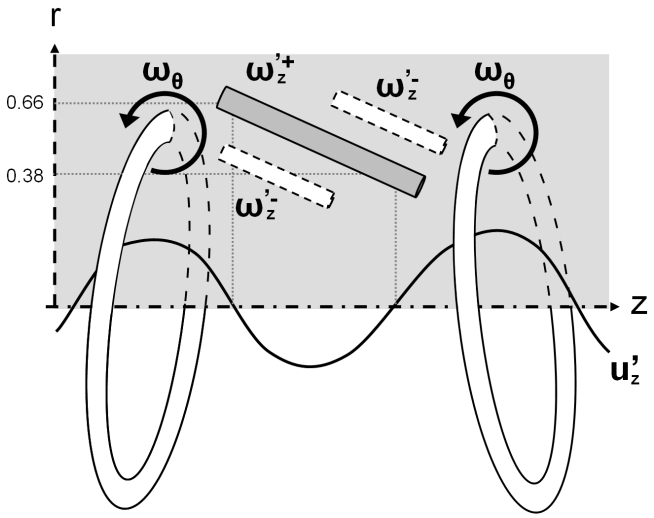

FIGURE 24. Schematic view of the turbulent axisymmetric mixing layer organization arising from the present experiments. Note the preferential presence of opposite sign vorticity above and below a streamwise vortex and the tilting of the $m = 0$ modes, which is a manifestation of the $m = \pm 1$ in the core. As in figure 1, the solid line shows the value of u'_z at the centre of the jet, which is qualitatively similar to that found at $r = 0.24$.

Recalling the $m = 0$ POD mode structure in figure 12, which shows the relative position of the vorticity rings and of $u'_z(r' = 0.24)$, one can then locate axially the streamwise vortices with respect to these rings, in a statistical manner. Focusing first on subfigure 23(b), for $r = 0.38$, note that the probing point for ω'^2_z is located at an axial station where $u'_z(r' = 0.24)$ sharply increases, crossing the zero value for slightly negative z'_c. This means that the downstream end of a streamwise vortex statistically coincides with the upstream part of an $m = 0$ ring. In the same way, the upstream end of the vortex, identified here by radial position $r = 0.66$ (figure 23 d), is statistically located at a streamwise location where the induced axial velocity decreases and changes sign, thus in the downstream part of an $m = 0$ ring. Regarding the middle of the vortex, for $r = 0.52$ (figure 23 c), correlation levels are much weaker but the streamwise location seems to correspond to the minimum of induced axial velocity. Consequently, these curves show that the streamwise vortices are statistically located in the so-called braid region, i.e. between two subsequent $m = 0$ rings, as depicted in figure 24.

The correlation curves in figure 23 also bear the trace of $m = \pm 1$ perturbations, and allow inference of the particular synchronization that statistically exists between these perturbations, the $m = 0$ rings and the streamwise vortices. In fact, these curves show that, when a streamwise vortex exists, the form of the coexisting $m = \pm 1$ modes is consistent with the particular tilting of the $m = 0$ rings depicted in figure 24. Indeed, such a tilting, for which the $m = 0$ rings are locally brought close to one another precisely at the location of the streamwise vortex, could underlie the dependence of the correlation amplitude with the azimuth. Supposing such an organization indeed leads to a velocity fluctuation whose amplitude at $r' = 0.24$ decreases with θ', being maximum for $\theta' = 0$ and minimum for $\theta' = \pi$. Besides, this organization is dynamically consistent, as this tilting of the $m = 0$ rings due to the $m = \pm 1$ mode locally enhances the streamwise stretching, thus preferentially promoting streamwise vortices there.

5.2. *Relative magnitude of two production mechanisms for streamwise vortices*

In figures 23 (b) to (d), the amplitude of the triple correlation is found to be globally small, especially at the center of the mixing layer ($r = 0.52$). This suggests that the

unsteady axial stretching due to the $m = 0$ modes, even with the increased amplitude linked to the $m = \pm 1$ tilt, can only be a partial source for the production of these vortices. The strength of this mechanism can be linked to the characteristic scale of azimuthal vorticity due to $m = 0$ rings. Restricting to the most energetic $m = 0$ POD mode, this scale has been estimated to 0.6 (see section 3.2.1). The second production mechanism is the stretching due to the mean shear of axial velocity (Rogers & Moin 1987). Its importance is directly dependent on the magnitude of the mean shear itself, which is $1/\delta_\omega = 2.8$, where the vorticity thickness is $\delta_\omega = 0.36$, see section 2.2. The comparison of the magnitude of the two mechanisms therefore suggests that it is not the $m = 0$ vortex rings which produce the streamwise vorticity, rather, the latter is predominantly produced by the mean shear. This explains an observation by Citriniti & George (2000) that streamwise vortices, even if they are strengthened in the braid region, can also be observed in the other locations of the cycle. Supplementary stretching by the unsteady $m = 0$ strain in fact acts as a partial spatial synchronization of the streamwise vortices in the braid region, as shown in the previous section.

While this conclusion is of importance, care should be taken when extrapolating it to other experiments. As a matter of fact, different initial conditions may produce different $m = 0$ unsteady azimuthal vorticity to mean shear vorticity ratios. In Martin & Meiburg's numerical investigation (1991), the authors observe that nearly all the mean flow vorticity rolls up in $m = 0$ vortex rings, subsequently leading to a spectacular organization of streamwise vorticity. We can also expect that for low Reynolds number transitional jets, the initial stages of Kelvin-Helmholtz instability saturation create a stronger $m = 0$ unsteady azimuthal vorticity than that obtained in fully turbulent jet flows such as the present one. This could explain the stronger and highly organized streamwise vortex structures observed in the flow visualizations of Liepmann & Gharib (1992). Even self-similar turbulent flows remain dependent on initial conditions (George 1989). These vary from one experiment to another and can have a direct effect on the $m = 0$ structures: for example, the amplitude of the $m = 0$ mode in the near field of the jet experiment of Jung *et al.* (2004) is significantly higher than that measured in the experiment of Iqbal & Thomas (2007). It has also been previously established that a small $m = 0$ forcing could organize the $m = 0$ large scale structures and alter mean flow characteristics such as the growth rate and turbulence intensity levels (Crow & Champagne 1971). Since these different initial conditions produce different $m = 0$ unsteady azimuthal vorticity to mean shear vorticity ratios, one can expect different levels or types of organization of streamwise vortices. Keeping this in mind is crucial since streamwise vortices play an essential role in the entrainment process (Liepmann & Gharib 1992), and provide a major contribution to the Reynolds stresses (Nickels & Marusic 2001), in the far field of a jet. In fully turbulent flow, their intermediate spatial scale indicates that they are an active bridge between instability like modes (strongly dependent on initial conditions) and smaller scale turbulence.

5.3. *A mechanism to account for the organization of opposite sign vorticity*

In section 4.1, we have observed that, in a longitudinal plane, a streamwise vortex is radially surrounded by vortices with opposite signed vorticity (see the sketch in figure 24). In boundary layer turbulence, wall-normal organization of opposite vorticity has been reported near the wall by Kim (1983) and Jeong *et al.* (1997). Our observations have some common points with the results from these studies, such as the similar orientation of the structures (see in particular section 4.2). It is however not clear whether the physical mechanisms proposed to explain this near-wall organization are relevant in a free shear flow. In the near field of a jet, the numerical studies of Martin & Meiburg (1991)

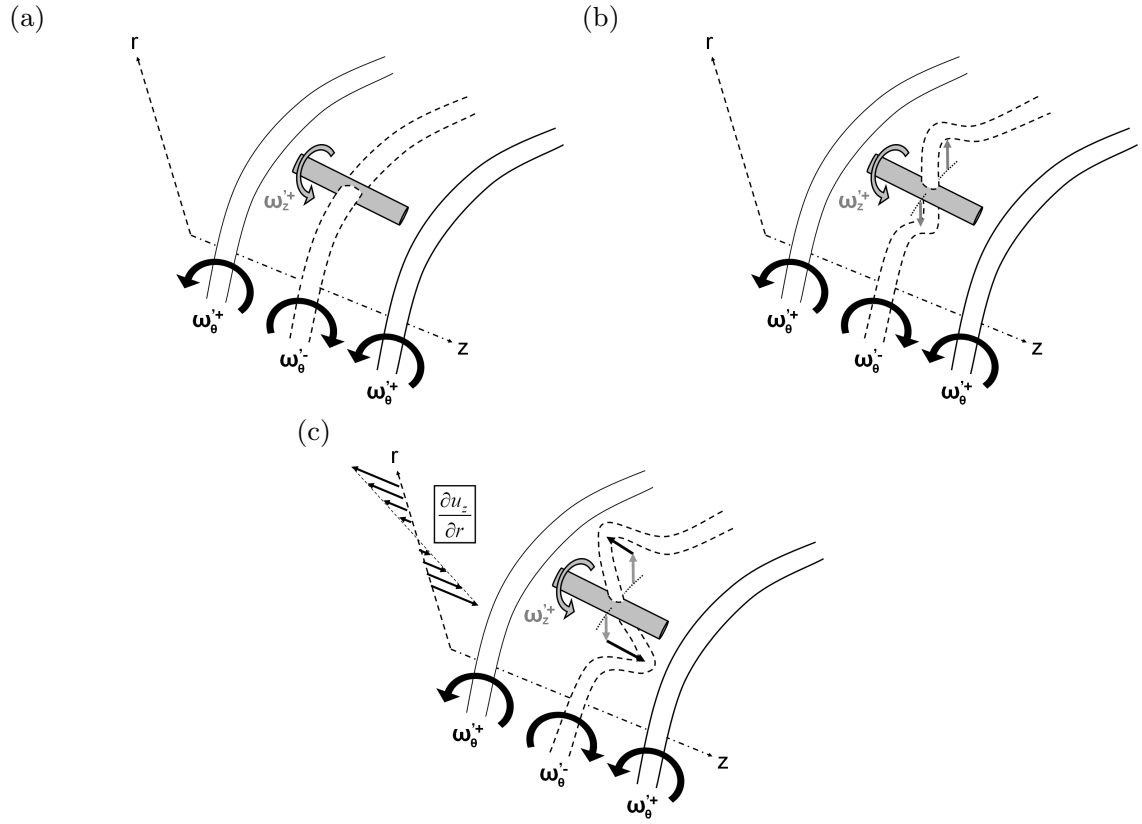

FIGURE 25. Mechanism accounting for the generation of opposite sign streamwise vorticity, derived from the present results. (a): initial most probable position of a streamwise vortex with respect to an $m = 0$ mode. (b): tilting of the negative azimuthal vorticity of the $m = 0$ mode by the streamwise vortex. (c) tilting and stretching of the deformed ring by the mean shear.

and Brancher *et al.* (1994) have shown that the vorticity dynamics arising from initially perturbed axisymmetric mixing layers can locally produce such opposite signed vorticity radial arrays in the $m = 0$ rings, when streamwise vorticity is wrapped around the rings. This, however, does not account for what is observed in the present experiment, where the radial organization is observed above and below streamwise vortices that are located preferentially in the region surrounding the rings (braid region), not in the rings themselves. In addition, in these computations, the azimuthal and the streamwise vorticity perturbation are of the same order, while in the present fully turbulent flow, azimuthal vorticity is weak compared to streamwise vorticity. Indeed, the characteristic scale of the azimuthal $m = 0$ modes was estimated to be 0.6 in section 3.2.1, while that of streamwise vorticity is 2.5 (see section 4.1). Therefore, the wrapping of streamwise vorticity around the $m = 0$ ring is unlikely in the present turbulent flow; it is even the contrary that should occur.

In figures 25 (a) to (c), a mechanism which combines a strong streamwise vortex, a weaker $m = 0$ azimuthal vorticity perturbation and the mean shear is proposed. Note that while the streamwise vortex considered here has a positive streamwise vorticity, using a negative one leads to the same conclusions. As shown in section 5.1 and sketched in subfigure 25 (a), in a frame convected with the $m = 0$ structure, the streamwise vortex is preferentially located in the braid region. In that region, it can be deduced from the shape of the $m = 0$ POD modes that the azimuthal vorticity fluctuation is negative (see section 3.2.1). In the paragraph above, we have established that the $m = 0$ azimuthal vorticity fluctuations are of small amplitude compared to the streamwise vorticity. In

this case, the streamwise vorticity will therefore tilt the negative $m = 0$ azimuthal vorticity fluctuation, as sketched in subfigure 25 (b), thus creating radial vorticity. Finally, the mean shear produces streamwise vorticity that has an opposite sign to the streamwise vortex considered, by tilting and stretching, see subfigure 25 (c). The ingredients of this mechanism are thus the mean shear associated with the streamwise velocity profile, the streamwise vortex, and the streamwise-periodic azimuthal vorticity, arising here from a pseudo-periodic instability mode, and may thus be at work in other situations where these features are present. Interestingly, evidence of similar arrangement of opposite vorticity around streamwise vortices is indeed observed, though not discussed by the authors, in the plane mixing layer simulation of Metcalfe *et al.* (1987), see their figure 19. We suspect that in past experiments, this organization could not be discriminated, as smoke flow visualizations were used, for which only the vorticity at the interface between marked and unmarked fluid is seen. Also, it may not have been detected in homogeneous turbulent shear flow, in which there is no periodically organized azimuthal (transverse) vorticity. To sum up, as shown by figure 24, streamwise vortices are preferentially produced by the mean shear and spatially organized by the $m = 0$ induced strain, these three elements interacting to produce organized opposite signed vorticity above and below the streamwise vortices.

6. Conclusion

Turbulent structures have been described in a turbulent round jet using high-speed stereo PIV two jet diameters downstream of the exit plane. POD has firstly been used to describe the $m = 0$ and $m = 1$ large scale structures. The form of the $m = 1$ modes was shown to be statistically closer to a flapping than to a helix. The spatial organization and the life cycle of streamwise vortices was then investigated. Vorticity auto-correlation shows that alternate sign vortices are preferentially organized into streamwise-radial rather than azimuthal arrays. Correlation between streamwise enstrophy and velocity shows that the streamwise vorticity is mainly produced by the mean shear, the $m = 0$ vortex rings acting as a quasi-periodic, weak forcing which preferentially locates streamwise vortices in the braid region. Strong streamwise vortices are also aligned with $m = 1$ modes. Finally, a triadic interaction between $m = 0$ vorticity, streamwise vorticity and the mean shear has been proposed, which accounts for the radial organization of opposite sign vorticity.

Our study quasi-exclusively focuses on the $z = 2$ cross-plane, therefore it would be important to verify the validity of the proposed scenario in farther downstream stations, and also in other situations such as with different initial conditions, or even in a plane mixing layer. New experimental techniques such as volumetric PIV, or numerical simulations reproducing the large scales of turbulence should also bring useful information by providing a true spatial representation which was presently approximated by a local pseudo-reconstruction based on Taylor's hypothesis. Firm evidence for the proposed scenario could be obtained using such experimental or numerical means.

Appendix A. POD details

A.1. *Implementation of the POD*

The output of the HS-SPIV acquisitions is reorganized into $1 \leqslant j_b \leqslant N_b$ blocks of velocity fluctuations. Each block of velocity fluctuation vector $(u'_r, u'_\theta, u'_z)_{j_b}$ is sampled in space ($1 \leqslant j_r \leqslant N_r = 23$ and $1 \leqslant j_\theta \leqslant N_\theta = 128$), and in time ($1 \leqslant j_t \leqslant N_t$). The radial extent

of the decomposition is set to $r_0 = 0.8$. In order to reach a good convergence on the POD results, we found it best to lower the frequency resolution in order to increase the number of blocks: we used $N_b = 210$ blocks and $N_t = 256$ samples for each block, providing an estimated 6% convergence of the cross-spectrum, and a $9.76Hz$ ($f \approx 0.07$) frequency resolution. This is acceptable since the spectral peak for large scale events is rather broad.

The following steps are taken to compute the POD modes:

(a) Each block is doubly Fourier transformed using two Fast Fourier Transforms with top hap windowing.

(b) The radius weighted, discrete cross-spectrum is estimated with the block average.

(c) The discretized Hermitian eigensystem system is solved as to obtain the eigenvalues and eigenfunctions.

It was shown by Tinney (2009) that inadequate large spatial separation between probes could cause significant numerical integration errors. A convergence study showed that the present results were not sensitive to the choice of a coarser grid by reduction of N_r and N_θ, nor to a reduction of the number of samples N_b by a factor 2. Increasing the frequency resolution does not change the nature of the present results as well. Reduction of the radial extent r_0 of the integral in eq. (2.6) tends to give more relative importance to modes in the jet core region.

A.2. *Symmetry properties*

A.2.1. *Statistical invariance in physical space*

Time and azimuthal angle being statistically invariant directions for the flow, the statistical average includes the block average along with the azimuthal average and is noted $< \ >_\theta$. The spatio-temporal correlation of two velocity components i and j is noted f_{ij} and is computed as:

$$f_{ij}(r, r', \theta', t') = < u_i(r, t, \theta) u_j(r', t + t', \theta + \theta' >_\theta . \tag{A 1}$$

Within statistical error, for $(ij) = (rr), (\theta\theta), (zz), (rz), (zr)$ we observe a θ' symmetry, i.e.:

$$f_{ij}(r, r', \theta', t') = f_{ij}(r, r', -\theta', t'), \tag{A 2}$$

while for $(ij) = (r\theta), (\theta r), (z\theta), (\theta z)$ a θ' antisymmetry holds:

$$f_{ij}(r, r', \theta', t') = -f_{ij}(r, r', -\theta', t') \tag{A 3}$$

In the case where $t' = 0$ these symmetries are identical with that obtained by Tinney *et al.* (2008a) with spatial correlations.

A.2.2. *Invariance in Fourier space*

Owing to the real nature of the velocity components, one has:

$$\hat{u}_i(r, -m, -f) = \bar{\hat{u}}_i(r, m, f), \tag{A 4}$$

$$\hat{u}_i(r, m, -f) = \bar{\hat{u}}_i(r, -m, f). \tag{A 5}$$

As a result, for the weighted spectral cross-correlation B_{ij} defined in eq. (2.7):

$$B_{ij}(r, r', -m, -f) = \bar{B}_{ij}(r, r', m, f), \tag{A 6}$$

$$B_{ij}(r, r', m, -f) = \bar{B}_{ij}(r, r', m, -f). \tag{A 7}$$

In addition, B_{ij} inherits specific properties from the symmetries of the spatio-temporal

cross correlations f_{ij} detailed in A.2.1, from which it can also be computed:

$$B_{ij}(r,r',m,f) = r^{1/2}\int_0^{t_0}\int_0^{2\pi} f_{ij}(r,r',\theta',t')\exp^{j(2\pi ft'+m\theta')}\,d\theta' dt' r'^{1/2}. \tag{A 8}$$

It is easy to show that for $(ij) = (rr),(\theta\theta),(zz),(rz),(zr)$ one then has

$$B_{ij}(r,r',m,-f) = \bar{B}_{ij}(r,r',m,f), \tag{A 9}$$

and that for $(ij) = (r\theta),(\theta r),(z\theta),(\theta z)$:

$$B_{ij}(r,r',m,-f) = -\bar{B}_{ij}(r,r',m,f). \tag{A 10}$$

In summary, given B_{ij} at (m,f), values of B_{ij} at $(-m,f)$, $(m,-f)$ and $(-m,-f)$ are known upon applying the symmetry corresponding to each ij case.

A.2.3. *Consequences: symmetries in the POD*

Since the POD eigenvalues $\lambda^{(n)}(m,f)$ are real, using the symmetries of $B_{ij}(r,r',m,f)$, it is straightforward to show that:

$$\phi_i(r,-m,-f) = \bar{\phi}_i(r,-m,-f), \tag{A 11}$$

$$\phi_i(r,m,-f) = \bar{\phi}_i(r,-m,f), \tag{A 12}$$

and that

$$\phi_r(r,m,-f) = \bar{\phi}_r(r,m,f), \tag{A 13}$$

$$\phi_\theta(r,m,-f) = -\bar{\phi}_\theta(r,m,f), \tag{A 14}$$

$$\phi_z(r,m,-f) = \bar{\phi}_z(r,m,f). \tag{A 15}$$

Regarding the projection coefficient of a data block onto a POD mode $\hat{a}^{(n)}(m,f)$, symmetry considerations restrict to:

$$\hat{a}^{(n)}(-m,-f) = \bar{\hat{a}}^{(n)}(m,f), \tag{A 16}$$

$$\hat{a}^{(n)}(m,-f) = \bar{\hat{a}}^{(n)}(-m,f). \tag{A 17}$$

Appendix B. Azimuthal power spectra of velocity components

The full azimuthal power spectra of radial, azimuthal and axial velocity fluctuations are given in figures 26 (a), (b) and (c). In the jet core, radial and azimuthal velocity spectra are dominated by $m = 1$ modes, while the axial spectrum is dominated by the $m = 0$ mode. In the mixing layer, the axial velocity spectrum possesses a broad peak centered around $m = 5$. Note that the spectrum of axial velocity is also given in figures 10 (a) and (b) at two radii corresponding to the jet core and the mixing layer. In the mixing layer, the spectra for radial and azimuthal fluctuations are dominated by lower azimuthal modes than the axial spectrum. Namely, a large portion of the energy in the radial spectrum is distributed along $m = 0$ and $m = 1$, while the azimuthal spectrum has a broad peak centered near $m = 2$. Similar results were obtained at a higher Mach number and at $z = 3$ by Tinney *et al.* (2008*a*), see their figure 17 i, (a) to (c).

REFERENCES

Bernal, L.P. & Roshko, A. 1986 Streamwise vortex structure in plane mixing layers. *Journal of Fluid Mechanics* **170**, 499–525.

Bradshaw, P. 1966 The effect of initial conditions on the development of a free shear layer. *Journal of Fluid Mechanics* **26** (02), 225–236.

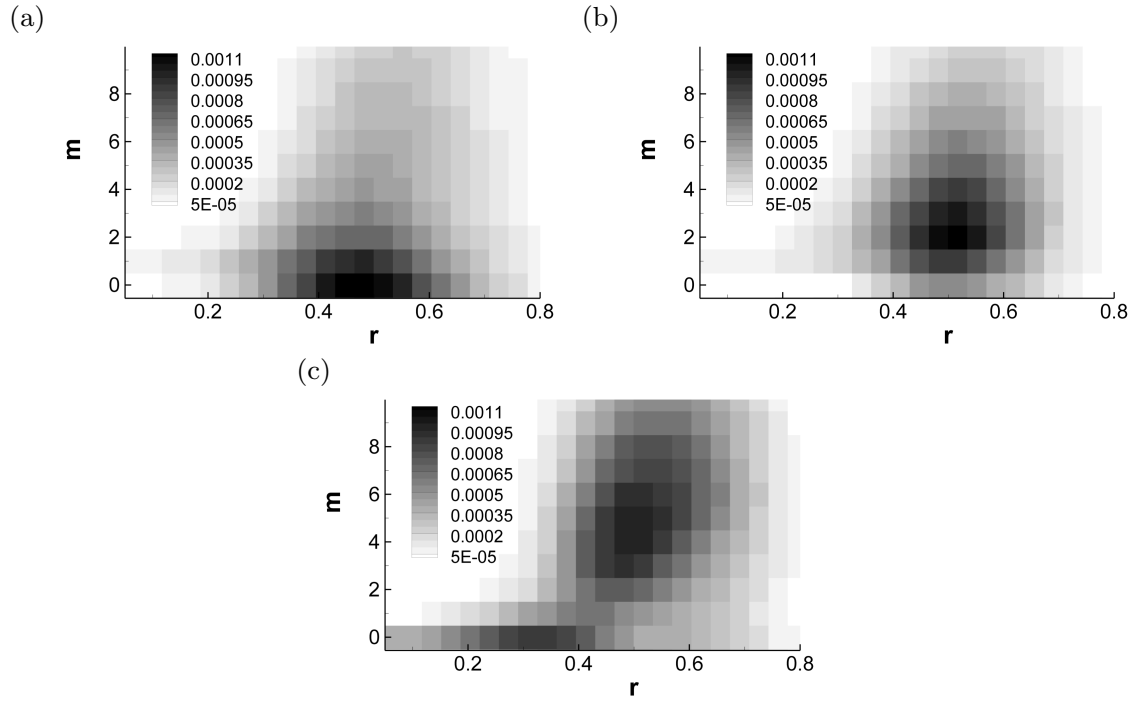

FIGURE 26. Azimuthal power spectrum (in grey levels, linear scale) as a function of azimuthal mode m and radius r for radial (a), azimuthal (b) and axial (c) velocity fluctuations, $z = 2$ plane.

BRANCHER, P., CHOMAZ, J.M. & HUERRE, P. 1994 Direct numerical simulations of round jets: Vortex induction and side jets. *Physics of fluids* **6** (5), 1768–1774.

BRUUN, H. H. 1995 *Hot-wire anemometry: principles and signal analysis*. Oxford University Press, USA.

CHAMPAGNAT, F., PLYER, A., LE BESNERAIS, G., LECLAIRE, B., DAVOUST, S. & LE SANT, Y. 2011 Fast and accurate PIV computation using highly parallel iterative correlation maximization. *Experiments in Fluids* **50**, 11691182.

CITRINITI, J.H. & GEORGE, W.K. 2000 Reconstruction of the global velocity field in the axisymmetric mixing layer utilizing the proper orthogonal decomposition. *Journal of Fluid Mechanics* **418**, 137–166.

CROW, S.C. & CHAMPAGNE, F.H. 1971 Orderly structure in jet turbulence. *Journal of Fluid Mechanics* **48** (03), 547–591.

DAVOUST, S. 2011 Dynamics of large scale structures in turbulent jets with or without the effect of swirl. PhD thesis, ONERA, Ecole Polytechnique.

DAVOUST, S. & JACQUIN, L. 2011 Taylor's hypothesis convection velocities from mass conservation equation. *Physics of Fluids* **23** (5).

DEL ÁLAMO, J.C. & JIMÉNEZ, J. 2009 Estimation of turbulent convection velocities and corrections to Taylor's approximation. *Journal of Fluid Mechanics* **640**, 5–26.

DELVILLE, J., UKEILEY, L., CORDIER, L., BONNET, J.P. & GLAUSER, M. 1999 Examination of large-scale structures in a turbulent plane mixing layer. Part 1. Proper orthogonal decomposition. *Journal of Fluid Mechanics* **391**, 91–122.

GAMARD, S., JUNG, D. & GEORGE, W.K. 2004 Downstream evolution of the most energetic modes in a turbulent axisymmetric jet at high reynolds number. Part 2. The far-field region. *Journal of Fluid Mechanics* **514** (-1), 205–230.

GANAPATHISUBRAMANI, B., LAKSHMINARASIMHAN, K. & CLEMENS, N. T. 2008 Investigation of three-dimensional structure of fine scales in a turbulent jet by using cinematographic stereoscopic particle image velocimetry. *Journal of Fluid Mechanics* **598**, 141–175.

GEORGE, W.K. 1989 The self-preservation of turbulent flows and its relation to initial conditions and coherent structures. *Advances in Turbulence* pp. 39–74.

GLAUSER, M.N. & GEORGE, W.K. 1987 Orthogonal decomposition of the axisymmetric jet mixing layer including azimuthal dependence. *Advances in turbulence* pp. 357–366.

Ho, C.M. & Huerre, P. 1984 Perturbed free shear layers. *Annual Review of Fluid Mechanics* **16** (1), 365–422.

Hussain, A.K.M.F. & Zaman, K.B.M.Q. 1981 The preferred mode of the axisymmetric jet. *Journal of Fluid Mechanics* **110**, 39–71.

Hussain, A. & Zedan, M.F. 1978 Effects of the initial condition on the axisymmetric free shear layer: effects of the initial momentum thickness. *Physics of Fluids* **21**, 1100.

Iqbal, M.O. & Thomas, F.O. 2007 Coherent structure in a turbulent jet via a vector implementation of the proper orthogonal decomposition. *Journal of Fluid Mechanics* **571**, 281–326.

Jacquin, L., Leuchter, O., Cambon, C. & Mathieu, J. 1990 Homogeneous turbulence in the presence of rotation. *Journal of Fluid Mechanics* **220**, 1–52.

Jeong, J. & Hussain, F. 1995 On the identification of a vortex. *Journal of Fluid Mechanics* **285**, 69–94.

Jeong, J., Hussain, F., Schoppa, W. & Kim, J. 1997 Coherent structures near the wall in a turbulent channel flow. *Journal of Fluid Mechanics* **332**, 185–214.

Jung, D., Gamard, S. & George, W.K. 2004 Downstream evolution of the most energetic modes in a turbulent axisymmetric jet at high reynolds number. Part 1. The near-field region. *Journal of Fluid Mechanics* **514**, 173–204.

Kim, J. 1983 On the structure of wall-bounded turbulent flows. *Physics of Fluids* **26**, 2088.

Kim, J. & Choi, H. 2009 Large eddy simulation of a circular jet: effect of inflow conditions on the near field. *Journal of Fluid Mechanics* **620**.

Leclaire, B. & Jacquin, L. 2012 On the generation of swirling jets: High Reynolds number rotating flow in a pipe with final contraction. *Journal of Fluid Mechanics, in press* .

Leclaire, B., Jaubert, B., Champagnat, F., Le Besnerais, G. & Le Sant, Y. 2009 FOLKI-3C: a simple, fast and direct algorithm for stereo PIV. In *Proceedings of 8th International Symposium on Particle Image Velocimetry - PIV09*. Melbourne.

Liepmann, D. & Gharib, M. 1992 The role of streamwise vorticity in the near-field entrainment of round jets. *Journal of Fluid Mechanics* **245**, 643–668.

Lin, S.J. & Corcos, G.M. 1984 The mixing layer: deterministic models of a turbulent flow. Part 3. The effect of plane strain on the dynamics of streamwise vortices. *Journal of Fluid Mechanics* **141**, 139–178.

Martin, J.E. & Meiburg, E. 1991 Numerical investigation of three-dimensionally evolving jets subject to axisymmetric and azimuthal perturbations. *Journal of Fluid Mechanics* **230**, 271–318.

Matsuda, T. & Sakakibara, J. 2005 On the vortical structure in a round jet. *Physics of fluids* **17**, 025106.

McIlwain, S. & Pollard, A. 2002 Large eddy simulation of the effects of mild swirl on the near field of a round free jet. *Physics of Fluids* **14**, 653.

Metcalfe, R.W., Orszag, S.A., Brachet, M.E., Menon, S. & Riley, J.J. 1987 Secondary instability of a temporally growing mixing layer. *Journal of Fluid Mechanics* **184**, 207–243.

Michalke, A. 1984 Survey on jet instability theory. *Progress in Aerospace Sciences* **21** (3), 159–199.

Neu, J.C. 1984 The dynamics of stretched vortices. *Journal of Fluid Mechanics* **143**, 253–276.

Nickels, T.B. & Marusic, I. 2001 On the different contributions of coherent structures to the spectra of a turbulent round jet and a turbulent boundary layer. *Journal of Fluid Mechanics* **448**, 367–385.

Paschereit, C.O., Oster, D., Long, T., Fiedler, H.E. & Wygnanski, I. 1992 Flow visualization of interactions among large coherent structures in an axisymmetric jet. *Experiments in Fluids* **12** (3), 189–199.

Raffel, M., Willert, C., Wereley, C. & Kompenhans, J. 2007 *Particle Image Velocimetry. A Practical Guide*, 2nd edn. Springer Verlag, Berlin.

Rogers, M.M. & Moin, P. 1987 The structure of the vorticity field in homogeneous turbulent flows. *Journal of Fluid Mechanics* **176**, 33–66.

Sangwine, S.J. & Le Bihan, N. 2007 Hypercomplex analytic signals: Extension of the analytic signal concept to complex signals. In *Proc. EUSIPCO*, pp. 621–624.

Suprayan, R. & Fiedler, H.E. 1994 On streamwise vortical structures in the near-field of axisymmetric shear layers. *Meccanica* **29** (4), 403–410.

Thomas, F.O. 1991 Structure of mixing layers and jets. *Applied Mechanics Reviews* **44**, 119.

Tinney, C.E. 2009 Proper grid resolutions for the proper basis. American Institute of Aeronautics and Astronautics 47th Aerospace Sciences Meeting and Exhibit, Orlando, Florida, USA.

Tinney, C.E., Glauser, M.N. & Ukeiley, L.S. 2008*a* Low-dimensional characteristics of a transonic jet. Part 1. Proper orthogonal decomposition. *Journal of Fluid Mechanics* **612**, 107–141.

Tinney, C.E., Glauser, M.N. & Ukeiley, L.S. 2008*b* Low-dimensional characteristics of a transonic jet. Part 2. Estimate and far-field prediction. *Journal of Fluid Mechanics* **615**, 53.

Tropea, C., Yarin, A.L. & Foss, J.F. 2007 *Springer Handbook of Experimental Fluid Mechanics*. Springer Verlag.

Yule, A.J. 1978 Large-scale structure in the mixing layer of a round jet. *Journal of Fluid Mechanics* **89** (03), 413–432.

Zaman, K.B.M.Q. & Hussain, A.K.M.F. 1981 Taylor hypothesis and large-scale coherent structures. *Journal of Fluid Mechanics* **112**, 379–396.

Zaman, K.B.M.Q. & Hussain, A.K.M.F. 1984 Natural large-scale structures in the axisymmetric mixing layer. *Journal of Fluid Mechanics* **138**, 325–351.

5 La couche de mélange axisymétrique dans un jet tournant turbulent

Nous étudions à présent les effets de la rotation sur la couche de mélange axisymétrique décrite dans le précèdent chapitre. L'écoulement moyen et la structure de la turbulence sont ici d'une complexité supérieure à celle du jet simple et il est donc nécessaire de les décrire précisément. Dans un premier temps, nous décrivons les effets du nombre de swirl au moyen d'une analyse classique des moyennes et des tensions de Reynolds. La structure du tenseur des déformations et du tenseur de Reynolds est détaillée au centre de la couche de mélange, de manière à isoler les différents changements qui affectent la production de l'énergie cinétique turbulente. Les effets des conditions initiales sont distingués des effets d'anisotropie qui conduisent à une augmentation de la production de la turbulence.

Dans un second temps, la dynamique des structures cohérentes est abordée sous l'angle des tourbillons longitudinaux, qui sont, d'après le précédent chapitre, des structures qui dominent énergétiquement dans le jet non-tournant. On montre alors qu'une partie de l'accroissement de la capacité de mélange de la couche de mélange tournante avec le nombre de swirl résulte d'une évolution de l'organisation des paires de tourbillons de signe opposée mise en évidence dans le chapitre précédent. La brisure de symétrie qui sélectionne le signe des tourbillons longitudinaux dans le jet tournant, qui révèle certaines surprises, est examinée.

Manuscript in preparation

On the effects of swirl in a turbulent axisymmetric mixing layer

By S. DAVOUST, L. JACQUIN AND B. LECLAIRE

ONERA, Department of Fundamental and Experimental Aerodynamics
8 rue des Vertugadins, 92190 Meudon, France

(Received ??)

The near field of a $Re_0 = 2.14 \times 10^5$ and low Mach number cylindrical swirling jet is investigated by means of several stereo PIV planes. A swirling axisymmetric mixing layer is obtained from a plug flow with a solid body rotation obtained at the jet exit. The swirl parameter S is varied from $S = 0$ to 0.81. The mean flow and the structure of turbulence are described. As swirl is added, we observe a non-monotonous variation of the growth rate and of turbulence in the mixing layer. This is attributed to a competition between increased turbulent production and a longer recovery toward equilibrium from the initial boundary layer, which is perturbed by the swirl generation mechanism. Sufficiently far from the exit, the structure of turbulence stabilizes. An analysis of the structure of the Reynolds stress tensor in the mixing layer reveals how does the increase of the anisotropy and of the alignment with the strain tensor with swirl lead to an enhanced turbulent production.

The organization of vortical structures in the mixing layer is described through two-point correlations of streamwise vorticity using results from high-speed PIV in a cross-sectional plane. The most significant change in the statistics of the vorticity field is the formation of a tilted vortex pair. Finally, a counter-intuitive effect is observed in the sign selection of the streamwise vorticity fluctuation. While cyclonic streamwise vorticity is moderately favored at the center of the mixing layer, strong anti-cyclonic fluctuations dominate in a region between the jet core and the mixing layer. This is attributed to the conservation of angular momentum during the radial turbulent transport of streamwise vorticity fluctuations.

1. Introduction

In the production of shear flow turbulence, the effects of streamline curvature are 'surprisingly' large compared with what is expected by a rapid inspection of the explicit additional production terms (Bradshaw 1973). Given the shear thickness δ and the radius of curvature of the streamline r_c, the magnitude of the changes affecting turbulence is much larger than those expected from the δ/r_c factor, which affects the supplementary production terms of the Reynolds stress balance equations. Basic turbulence models such as the $k-\epsilon$ one do not capture this effect (Speziale *et al.* 1990). More elaborated modeling approaches have been developed, and the experiments or simulations that are needed for validation can still reveal other unexpected effects.

The effects of curvature or system rotation have been studied in various fundamental turbulent shear flows such as homogeneous shear (Holloway & Tavoularis 1992; Salhi & Cambon 1997), boundary layers (Gillis & Johnston 1983; Hoffmann *et al.* 1985; Barlow & Johnston 1988), and free shear layers (Castro & Bradshaw 1976; Plesniak *et al.* 1994). Curvature may lead to centrifugal type instabilities. Destabilizing/stabilizing curvature tends to enhance/reduce turbulence, thereby increasing/decreasing skin-friction, heat

transfers and mixing. As pointed out by Salhi & Cambon (1997) rapid distortion theory may provide a guide to understand how supplementary distortions such as rotation affect locally homogeneous turbulence. Curvature may also promote or destroy crucial non-linear mechanisms like streamwise vortices in a mixing layer (Plesniak *et al.* 1994). This stresses the importance of understanding curvature or rotation induced non-linear mechanisms.

An important number of studies on the swirling jet studies are devoted to the vortex breakdown phenomenon (see Billant *et al.* 1998; Liang & Maxworthy 2005). Vortex breakdown, which occurs at high values of the swirl number, to be defined later, is not the object of the present work. The near field of the turbulent swirling jet has been investigated in a series of papers (see e.g. Rose 1962; Chigier & Chervinsky 1967; Mehta *et al.* 1991; Naughton *et al.* 1997; Facciolo *et al.* 2007). In all these study increased growth rates, entrainment and turbulence levels, and modifications in the Reynolds stresses are reported. Very few high Reynolds number swirling jets experiments produce a flow close to a rotating plug flow with a turbulence free potential core at the exit. Such an exit condition is interesting because it produces a thin swirling axisymmetric mixing layer that tends towards that obtained with a non-swirling jet obtained from a plug flow in the limit of $S \to 0$. Besides the fact that a well-controlled initial condition is of great importance in the study of free shear flows, in this configuration the mixing layer thickness δ and the jet diameter D can be decoupled to produce a 'thin shear layer' ($\delta \ll D$), upon which helical curvature due to swirl can be added. In contrast, in the experiments in which the jet which is already turbulent at the exit, the flow quickly evolves into a fully developed jet in which δ and D are linked, and the effects of swirl become more complex to analyze (Bradshaw 1973).

To the best of our knowledge only one experiment, by Mehta *et al.* (1991), describes turbulence in such a thin swirling axisymmetric mixing layer. The mean flow, the growth rate and the Reynolds stress in the mixing layer are documented and analyzed for $S = 0$, 0.25 and 0.5 (see eq. (2.5) for the definition of S). Mehta *et al.* attribute the extra production of turbulent stresses to an angular momentum instability. According to these authors, the fact that the $S = 0.25$ configuration seems unaffected by swirl is due to a favorable streamwise pressure gradient in the jet core. The large eddy simulation performed by McIlwain & Pollard (2002) compares the coherent structures in the near field of a turbulent jet generated by a plug flow $S = 0$ to that of a solid body rotating one for $S \approx 0.35$. These authors observe that swirl tends to perturb the Kelvin-Helmholtz $m = 0$ vortex rings, and it promotes streamwise vortices, so that the increase in turbulence and mixing should be attributed to them. Similarly, Panda & McLaughlin (1994) have shown through forcing a turbulent swirling jet that the growth of $m = 0$ and $m = 1$ instabilities was reduced with swirl, whereas the overall spread and entrainment of the jet was increased. This is an important point, since it is known that high Reynolds number homogeneous shear flows (Rogers & Moin 1987), mixing layers (Bernal & Roshko 1986) and jets (Liepmann & Gharib 1992; Citriniti & George 2000; Davoust *et al.* 2011) are dominated by streamwise vortices. Therefore describing the effect of swirl on these structures might reveal to be more important than studying its effects on linear instability modes such as $m = 0$ modes, which tend to be disorganized at low swirls (see also Loiseleux & Chomaz 2003) whereas the $m = 0$ instability should be increased by centrifugal effects (Gallaire & Chomaz 2003).

The aim of the present work is to refine the current description of a swirling axisymmetric mixing layer. We present an experimental parametric study of a thin turbulent swirling axisymmetric mixing layer. Our experiment is similar to that of Mehta *et al.* (1991), but significant changes allow a finer characterization of turbulence. First, we use

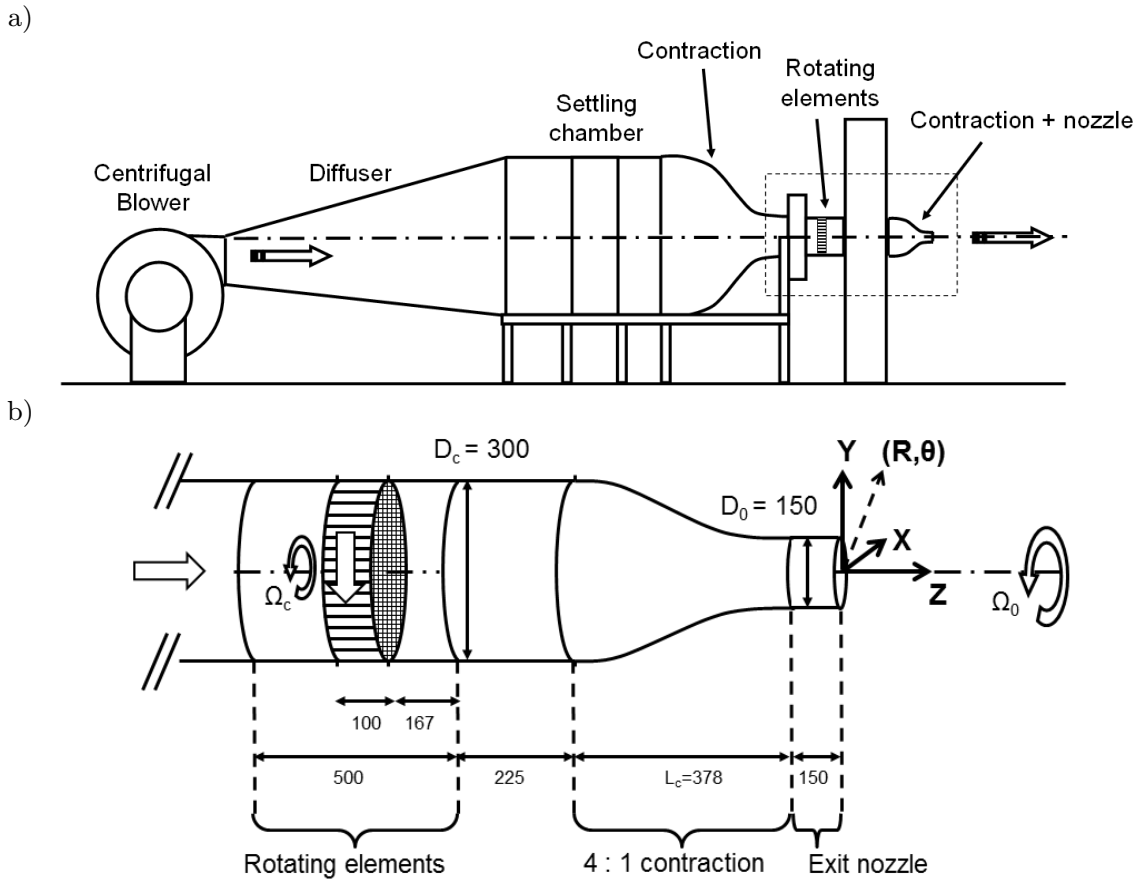

FIGURE 1. R4Ch swirling jet facility (a), and details on the geometry of the swirl generation mechanism (b). Dimensions are expressed in mm.

a thin initial boundary layer and this allows the structure of turbulence to reach equilibrium. Second, a broader range of swirl parameter is covered $0 \leqslant S \leqslant 0.81$ as well as a large range of shear thickness to curvature radius ratio ($0 \leqslant \delta/r_c \leqslant 0.25$). When swirl is imposed, there is an experimental difficulty to isolate curvature effects in the mixing layer itself since the initial condition may also evolve in an uncontrolled manner due to the swirl generation mechanism. We must carefully address this issue before describing production of turbulence, along with the structure of the Reynolds stress tensor. Third, the use of stereoscopic particle image velocimetry (SPIV) allows to measure instantaneous streamwise vorticity and to describe the instantaneous spatial organization of turbulence. The article is organized as follows. Section 2 details the swirling jet facility, the PIV measurements and the initial conditions at the jet exit. In section 3, we analyze the effect of swirl on the development of the jet in the near field. Section 4 details the evolutions in the production of turbulence at the center of the mixing layer. Effects due to the initial conditions are distinguished from those of the swirling flow curvature in the mixing layer, which are analyzed. Finally, section 5 describes the corresponding dynamics of streamwise vorticity through spatio-temporal correlations. Its sign selection, which has not been previously quantified in a turbulent swirling jet, is investigated through an analysis of one-point third order moments.

2. Experiment

2.1. *Swirling jet facility*

Different types of apparatuses may be used to generate swirling jets: inclined vanes (Panda & McLaughlin 1994), tangential injection of fluid (Chigier & Chervinsky 1967; Farokhi *et al.* 1988; Gilchrist & Naughton 2005; Shiri *et al.* 2008), fully developed rotating pipe flow (Facciolo *et al.* 2007), and solid body rotation of a honeycomb (Billant *et al.* 1998; Liang & Maxworthy 2005), which is the technique presently used. The present experiment was designed to produce a swirling jet with low residual turbulence in the jet core and thin boundary layers at the exit. In the case of non-swirling jets, such an exit condition is obtained by means of a final contacting nozzle (ratio χ). When swirl is imposed to the flow upstream of the final contraction, an approximate relationship links the swirl number of the flow upstream of the contraction, noted S_c, and that of the flow at the contracting duct exit, noted S_0. Independently of the precise definition of swirl, a scaling argument provides:

$$S_c \approx S_0 \sqrt{\chi}. \tag{2.1}$$

Accordingly, when targeting moderate values of S_0, the contraction can impose high values of S_c inside the apparatus. As was shown by Leclaire & Jacquin (2011), for too large values of S_c, critical conditions may hold in the duct which may produce strong perturbations in the core of the flow. The mechanism responsible for these changes in the flow dynamics have been fully described in their study, and shown to occur for $S_c \geqslant 2$. In this study, we use a $\chi = 4$ contraction, and we consider $S_0 \leqslant 0.82$ so as to maintain the flow free from this type of perturbations ($S_c \leqslant 1.64$).

2.1.1. *The wind-tunnel*

The present study uses the same facility as Jacquin *et al.* (1990) and Leclaire & Jacquin (2011). The jet is produced by means of a blowdown wind tunnel represented in Figure 1 (a). A centrifugal blower drives the flow, followed by a diffuser that ends in a settling chamber. The flow then undergoes a first contraction from a 1m square cross-section to a circular $D_c = 0.3$m cross-section. As shown in Figure 1 (b), a 0.5m long part of this cylindrical duct can be put into rotation with a controlled angular velocity Ω_c that can reach 1000 r.p.m. The rotating part contains a 10cm long honeycomb with 1.5mm cell diameter.

The jet, of exit diameter $D_0 = 0.15$m, is then generated by a contracting nozzle (contraction ratio $\chi = 4$, $L_c/D_c = 1.26$), ended by a 0.15m long thin edged nozzle. As the contraction tends to relaminarize the upstream turbulent boundary layer, the boundary layer in the nozzle is tripped 48mm upstream of the exit section with a carborandum strip composed of particles of 0.25mm nominal diameter. At the exit, hot-wire measurements indicate that the axial turbulence intensity in the core is 0.5%. This holds up to $S_0 = 0.82$ (see the definition of S_0 below), which is the highest value for which such canonical conditions can be maintained (see Leclaire & Jacquin 2011). As will be seen below, the exit flow is in solid body rotation except for the boundary layers.

2.1.2. *Experimental protocol*

To generate the flow, the power of the centrifugal fan is adjusted in order to attain a given value of the exit bulk velocity

$$U_0 = \frac{\dot{M}_0}{\rho \pi D_0^2/4}, \tag{2.2}$$

S	0	0.10	0.20	0.30	0.40	0.51	0.61	0.71	0.81
S_0	0	0.10	0.20	0.31	0.41	0.51	0.62	0.72	0.82

TABLE 1. Values of swirl parameter S (eq. 2.5) used, and swirl obtained at the exit S_0 (eq. 2.4).

where $\dot{M}_0$ denotes the exit flow rate. This flow rate is controlled with a calibrated Venturi flow meter which is placed upstream of the air intake of the fan. The flow-rate is adjusted so as to reach a fixed Reynolds number

$$Re_0 = \frac{U_0 D_0}{\nu} = 2.14 \times 10^5, \tag{2.3}$$

to within $\pm 1\%$. The bulk exit velocity U_0 and the exit diameter D_0 are also used to build dimensionless quantities, which will now be mainly considered. Corresponding dimensional and non-dimensional quantities will be respectively identified by upper-case and lower-case names, e.g. (R, θ, Z) and (r, θ, z) for the cylindrical coordinate system. In this frame of reference, the components of the mean velocity vector are (u_r, u_θ, u_z), while the components of the mean vorticity vector are $(\omega_r, \omega_\theta, \omega_z)$. A prime will be used to denote the fluctuations.

The exit swirl parameter S_0 is here defined as

$$S_0 = \frac{\Omega_0 D_0/2}{U_0}, \tag{2.4}$$

where Ω_0 is the angular velocity of the exit flow. This quantity cannot be directly imposed in the experiment, while the angular velocity Ω_c of the rotating honeycomb is the actual control parameter. Using U_0 and Ω_c, we then build the swirl parameter S as:

$$S = \frac{\chi \Omega_c D_0/2}{U_0}. \tag{2.5}$$

The same definition of swirl was used by Liang & Maxworthy (2005). Once we have presented the PIV tools in the next section, we will show that the angular velocity Ω_0 of the exit flow is such that one roughly has $\Omega_0 \approx \chi \Omega_c$, so that $S \approx S_0$. In the experiment, the honeycomb angular velocity Ω_c was fixed to attain swirl numbers S ranging from 0 to 0.81, as given in table 1. The digital control of the motor driving the honeycomb insures a 0.1% precision on the mean value of Ω_c with 1% fluctuations. A configuration characterized by S can be reproduced to within ± 0.003.

2.2. *PIV measurements*

2.2.1. *Setup*

Figure 2 provides an overview of the PIV measurement planes. Two distinct stereo PIV systems are employed. The first system is used in the longitudinal planes labeled M1-M5 and J1-J4. It includes two Imager Intense cameras (1280×1024 pixels) equipped with lenses ranging from 50mm to 200mm and synchronized with a double pulse Nd-YAG-532nm laser used to generate a light sheet of variable thickness. The acquisition rate is 4Hz, and the time delay dt between two pulses is adjusted depending on the size of the PIV plane as so to reach a dynamics of 7 pixels on the CCDs of each cameras. $N = 5000$ measurements are recorded for each value of S in table 1. The second system is used to acquire high-speed SPIV data in the $z = 2$ cross-sectional plane labeled HS-SPIV. It

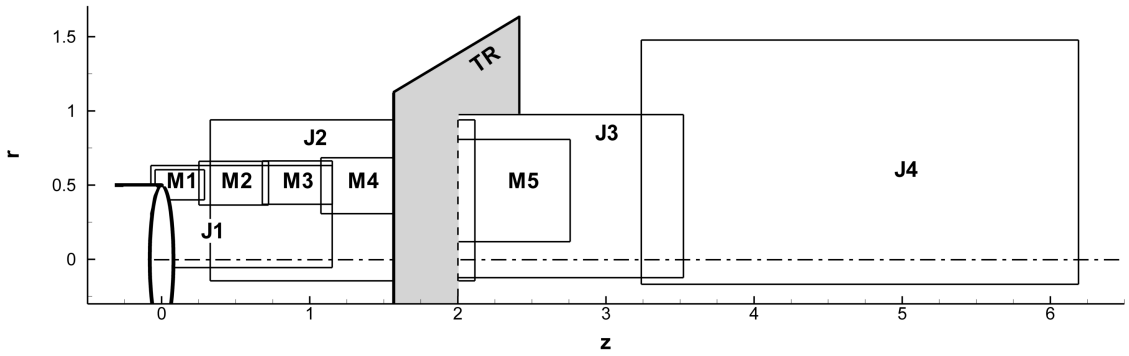

FIGURE 2. Overview of PIV measurements. Axial planes labeled M1-M5 follow the mixing layer growth, while those labeled J1-J4 cover the whole jet. Cross-flow plane HS-SPIV identifies the high-speed SPIV measurement zone.

	J1	J2	J3	J4	M1	M2	M3	M4	M5	HS-SPIV
dt (μs)	31	50	50	75	6/8	10	10	13	31	60
L_N (mm)	2	3	3	3	0.5	1	1	1	2	2.5
L_{IW} (mm)	2.89	4.60	4.59	7.05	0.87	1.29	1.30	1.66	2.88	6.14

TABLE 2. Basic characteristics of the PIV planes of figure 2 such as the time delay between laser pulses dt, laser sheet thickness L_N and physical length of the PIV interrogation window L_{IW}.

is comprised of two Phantom $V12.1$ high-speed cameras (800×1280 pixels) equipped with 105mm lenses and synchronized with a high repetition rate double pulse Nd-YLF-527nm laser which is used to generate a $2.5mm$ thick light sheet. Data is acquired at $F_a = 2.5$kHz, time delay is $dt = 60\mu$s. $N_b = 30$ blocks of $N_{\mathrm{ech}} = 2100$ measurements are recorded for every two value of S in table 1 starting from $S = 0$.

In both cases, the jet and the room are seeded with Di-Ethyl-Hexyl-Sebacate (DEHS) particles, whose diameter is nominally inferior to $1\mu m$. A laser beam which is auto-collimated against the exit plane is used to define the jet axis, which provides a 0.5mm precision when positioning an object in the jet coordinate frame. The cameras are focused on the measurement plane under the Scheimpflug principle. Calibration is performed with a double-sided calibration plate using a pin-hole model, followed by a self-calibration procedure using particle images as in Wieneke (2005) to correct any misalignment between the plate and the laser sheet. Table 2 summarizes additional useful information pertaining to each PIV plane such as the time delay dt, the estimated laser sheet thickness L_N, and the physical vertical size of the PIV interrogation windows (IW) in the measurement plane L_{IW}. In all cases, the size of the IW is set to 31 pixels and the algorithm used to compute the vector maps is briefly described below.

2.2.2. *Vector computation*

Vector maps are computed using a novel and very fast one step 3C approach, typically allowing to compute a stereo vector field in less than $0.25s$, thanks to a GPU-based implementation (see, respectively Leclaire *et al.* 2009; Champagnat *et al.* 2011, for the new stereo paradigm and the principle of the GPU implementation in the two-component

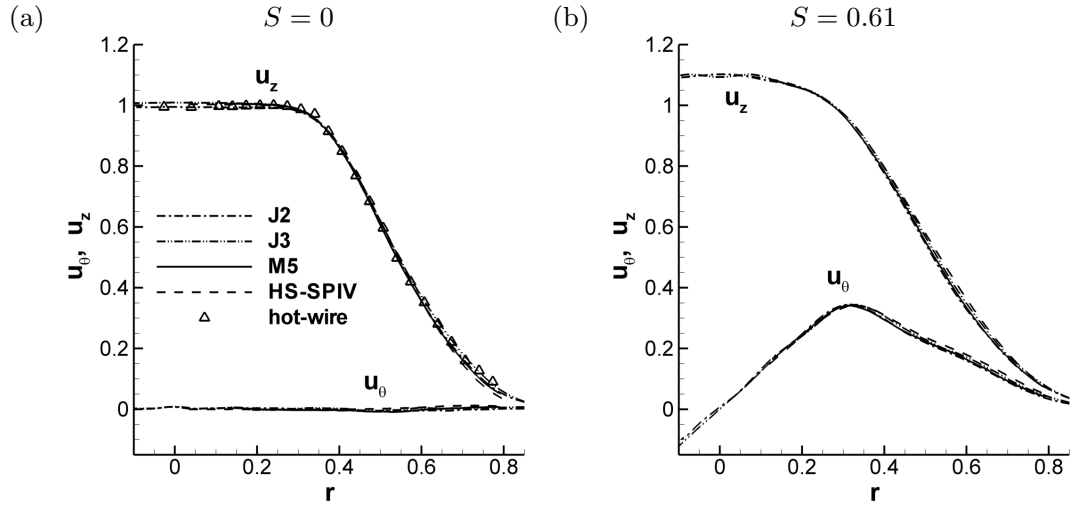

FIGURE 3. Comparison between different PIV measurements at $z = 2$ along with a single hot-wire. Mean axial and azimuthal velocity for $S = 0$ (a) and $S = 0.61$ (b).

PIV case). The algorithm naturally yields a dense result, i.e. a vector for each pixel. As will be detailed below, the spatial resolution is still linked to the IW size as is traditionally the case for IW correlation based PIV (Raffel *et al.* 2007), so that the dense character of the result is rather the maximal spatial sampling possible. Sampling was set to one vector every 13 pixels ($\approx 60\%$ overlap) except for high-speed PIV for which it was reduced to give a vector every 30 pixel because of the large amount of data involved. The overall accuracy of the measurements is discussed below.

2.2.3. *Measurement accuracy*

In this experiment, the uncertainty affecting the determination of velocity vectors from the PIV images is estimated to correspond to a 0.1 pixel displacement, consistently with the traditionally agreed-upon value for PIV uncertainty (Raffel *et al.* 2007). This represents $0.3m.s^{-1}$, that is, 1.5% of U_0. Several bias errors may then affect the velocity vectors including peak-locking, errors in the calibration of the cameras, errors in the spatial positioning of the measurement plane and spatial filtering by the IW. No significant peak-locking was detected in any configuration and spatial filtering is described in the next sub-section 2.2.4. Calibration and spatial positioning errors have been estimated together by comparing the mean velocity obtained by independent overlapping PIV planes. Such a comparison between planes J2, J3, M5 and HS-SPIV is presented in figure 3 for $S = 0$ and $S = 0.61$, also including hot-wire measurements for $S = 0$. The good agreement of all the measurements has lead us to suppose that the uncertainty due to these last two bias errors is below 1%, and this should also affect the instantaneous velocity fields.

For the HS-SPIV measurement plane, axial vorticity is computed using a circulation-based method, described in Raffel *et al.* (2007), yielding an expected uncertainty of $30s^{-1}$. This corresponds to a maximum relative uncertainty of 10%, since the axial vorticity is of same magnitude as the maximum shear in the mean axial velocity profile (here, $400s^{-1}$). The data was transformed from Cartesian (x, y) into cylindrical (r, θ) coordinates using a bilinear interpolation. The number of radial steps was set to $N_r = 23$, and the number of azimuthal steps to $N_\theta = 128$, in order to preserve a constant sampling in the outer part of the jet.

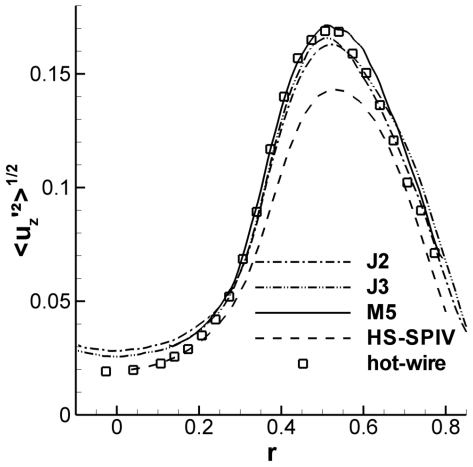

FIGURE 4. Mean and rms axial velocity profiles obtained at $z = 2$ with HS-SPIV in the cross-sectional plane, conventional SPIV in the longitudinal plane, and hot-wire anemometry.

2.2.4. *Spatial filtering*

The spatial resolution of PIV measurements is limited by the IW size Scarano (2003). This has been quantified by the comparison between the rms of axial velocity fluctuations obtained with the different PIV planes to that obtained with a hot-wire measurement, as shown in figure 4. We see that the maximum of the rms profile is well captured by PIV plane M5, while the spatial resolution of the HS-SPIV is clearly not sufficient to do so. At this $z = 2$ location, the spatial resolution of planes J2 and J3 seem to be a lower bound to capture the energetic scales of turbulence. This bound has allowed us to determine the spatial resolution necessary to capture energetic scales at other locations along z, given the local mixing layer thickness. We can therefore estimate that the capture of energetic scales will be compromised when $z \leqslant 0.1$ for plane M1, when $z \leqslant 2$ for J1 to J3 and when $z \leqslant 3.5$ for J4. A comparison was made between two power spectral density obtained at $z = 2$ in the mixing layer and in the jet with hot-wire and HS-SPIV for $S = 0$. As in the work of Foucaut *et al.* (2004) this comparison shows that indeed, the low spatial resolution filters the small scales (high frequencies), but that energetic scales at lower frequencies are well captured. A more detailed discussion is given in Davoust *et al.* (2011).

2.2.5. *Statistical convergence*

Using a scaling based on the vorticity thickness, the temporal integral length scale at $z = 2$ is estimated to $\mathcal{T}_{\text{int}} \approx 0.003$s, and the azimuthal integral length scale $\theta_{\text{int}} \approx 20°$. Given the high number of statistically independent samples in both types of data acquisitions, in every case the uncertainty of first order moments of velocity is below $\pm 0.6\%$, with a 95% confidence interval. Statistical convergence of second order moments obtained in the longitudinal planes with the $N = 5000$ snapshot ensemble average has also been estimated, under the assumption of a normal distribution as described in Benedict & Gould (1996). This provides a 95% confidence interval of ± 0.002, which amounts to a $\pm 5\%$ interval given the fluctuation level of $u' \approx 0.2$. Similarly, two-point correlations are converged to within ± 0.03 in the longitudinal planes, and to within ± 0.04 in the cross-sectional HS-SPIV plane. When possible, throughout the article, uncertainties surrounding statistical quantities will be evaluated by other means such as considering symmetry properties, overlapping measurement and by performing specific convergence studies.

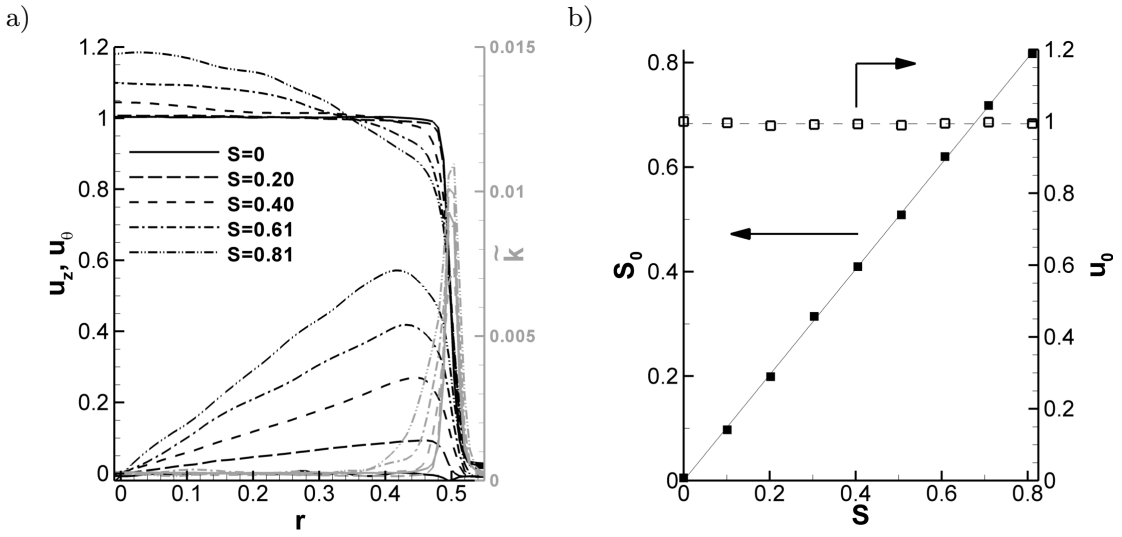

FIGURE 5. (a), Mean axial and azimuthal velocity profiles at $z = 0.1$ in plane $J1$ for $S = 0$ to 0.81, along with an estimation $\tilde{k}$ of turbulent kinetic energy in grey (see the text for more details). (b), corresponding exit swirl number S_0 eq. (2.4) and exit flow bulk velocity u_0 eq. (2.6) as a function of the swirl number S eq. (2.5).

2.3. *Exit conditions*

2.3.1. *Core of the jet*

The swirling jet normalized mean exit velocity profiles measured at $z = 0.1$ are shown in figure 5 (a). The core flow is indeed in solid body rotation. The exit values of swirl S_0, based on the determination of the exit angular velocity Ω_0 from these PIV results and computed using eq. (2.4), are provided in Table 1 and plotted in figure 5 (b) as a function of S. This confirms that the $S_0 \approx S$ relation holds. Going back to figure 5 (a), for $S = 0$, the axial velocity profile is a top hat. When swirl is added, this top hat profile is deformed, as a result of the plug flow with solid body rotation generated by the honeycomb passing through the contraction. As detailed in Batchelor (1967), the tilting of axial vorticity lines during the contraction of the flow results in an increase of axial velocity on the axis, making the profile parabolic. Consequently, a deficit in the axial velocity is observed for $r \geqslant 0.35$. In figure 5 (b), we observe that the normalized exit bulk velocity defined as

$$u_0 = \frac{\int_0^{0.5} u_z(z = 0.1, r) r dr}{\int_0^{0.5} r dr} = 8 \int_0^{0.5} u_z(z = 0.1, r) r dr, \tag{2.6}$$

and computed from the PIV results is constant and close to $u_0 = 1$. Note that since it is the bulk velocity U_0 which is defined in eq. (2.2) and obtained from the Venturi flow meter measurement which is used to normalize U_Z into u_z, the $u_0 = 1$ result simply shows the agreement between two independent exit flow rate measurements (PIV and Venturi flow meter).

2.3.2. *Boundary layer*

For $S = 0$, additional hot-wire measurements closer to the nozzle at $z \approx 0.003$ reveal that the boundary layer is turbulent and that its momentum thickness is quite thin, roughly $0.0024 D_0$. In the case of the swirling jet, measurements were carried out with PIV plane M1. A close-up on the mean axial velocity profile near to the exit ($z = 0.1$) is presented in figure 6 (a). As can be seen, the maximum shear in the mixing layer

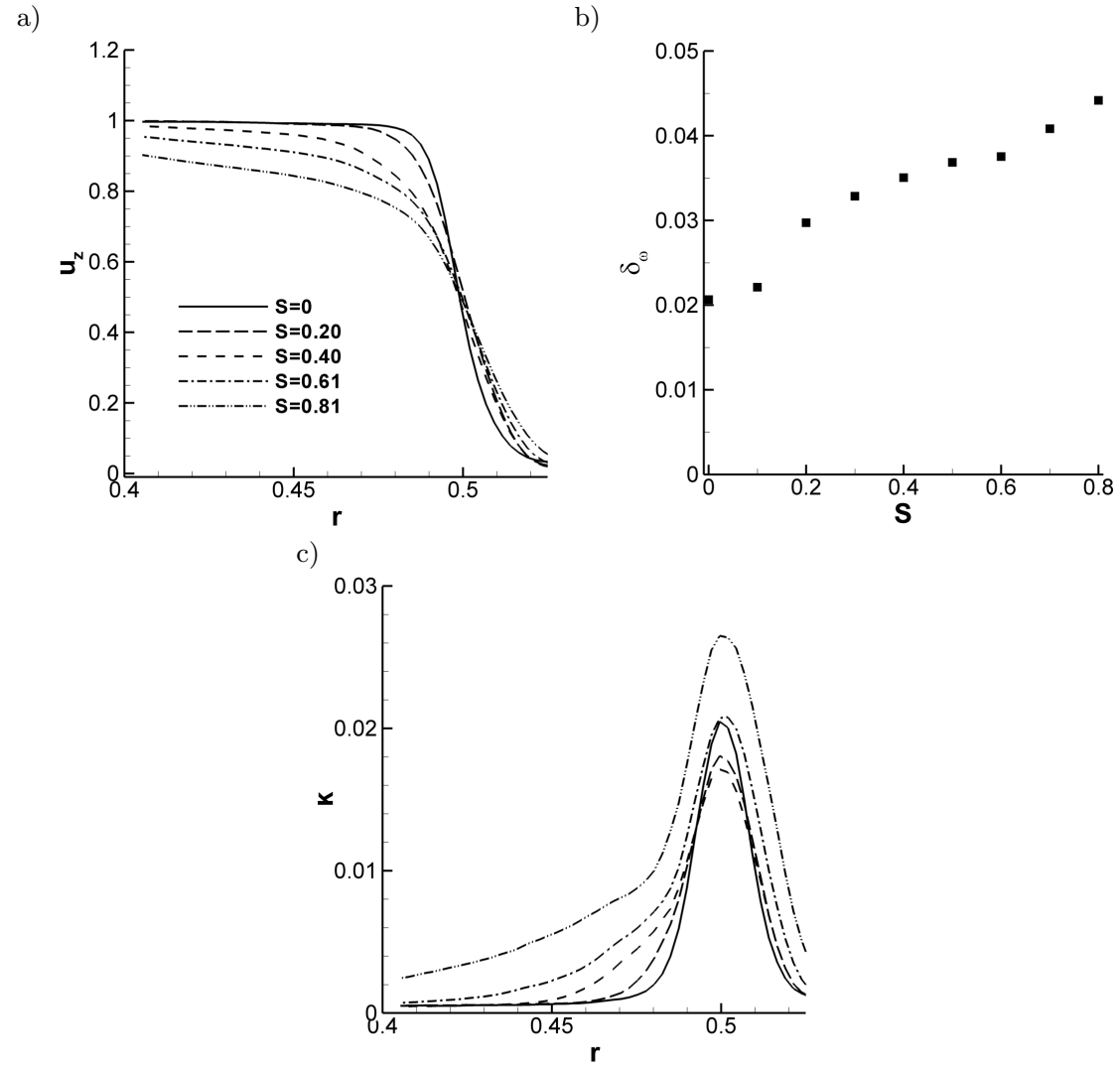

FIGURE 6. Close-up on the exit profiles at $z = 0.1$ using plane $M1$, for increasing values of the swirl S. (a): Mean axial velocity. (b): Azimuthal vorticity thickness δ_ω (2.7) at $z = 0.1$. (c): Turbulent kinetic energy.

decreases with swirl. In figure 6 (b), the shear thickness, defined as

$$\delta_\omega = 1/\left[-\frac{\partial u_z}{\partial r}\right]_{\max}, \tag{2.7}$$

is plotted, and we observe a continuous increase of this thickness with swirl. This may be attributed to the supplementary growth of the boundary layer in the duct due to swirl.

Indeed, given the geometry of the wind-tunnel, represented in figure 1 (b), swirl is expected to affect the boundary layer in a complex manner. Firstly, in the pipe portion upstream of the contraction, referred to as the duct, swirl imposes to the turbulent boundary layer a concave curvature along the helical streamlines. Previous studies, such as the experiment of Barlow & Johnston (1988), show that boundary layer curvature can lead to large perturbative effects, increasing skin-friction, growth and turbulent intensity in the boundary layer together with changes in the global structure of turbulence. These effects typically appear when $\delta/r_c \geqslant 0.01$ where δ is the boundary layer thickness, and r_c the radius of curvature (Hoffmann *et al.* 1985). Barlow & Johnston (1988) also noted the appearance of low-frequency, large scale fluctuations in the outer-part of the layer.

In the present experiment, an analysis of two-point correlation near the wall of the duct by Leclaire & Jacquin (2011) showed that these large scale fluctuations take the form of intermittent Gortler-type vortices, which become significant for values of the upstream swirl $S_c \geqslant 1.3$. Secondly, the contraction imposes a strong favorable pressure gradient. The study of Fernholz & Warnack (1998); Warnack & Fernholz (1998) showed that a strong favorable pressure gradient reduces the boundary layer thickness, and may cause relaminarization, although 'inactive' turbulence may remain from upstream. Thirdly, the contraction imposes a supplementary concave curvature in its first half, followed by a convex curvature in its second half. It is known that the structure of turbulence does not recover instantaneously to such changes (Gillis & Johnston 1983; Bandyopadhyay & Ahmed 1993). At last, since the contraction also reduces the local swirl number, see section 2.1. This may further disalign the mean flow with the structure of turbulence. It is therefore expected that it will take some distance in the nozzle, for the structure of turbulence, to attain an equilibrium, if any. A detailed description of the effect of the contraction on the swirling boundary layer inside the nozzle is out of the scope of the present paper, but it is worth investigating the initial turbulence in the mixing layer.

The estimated turbulent kinetic energy noted $\tilde{k}$ which is provided in figure 5 (a) is highly filtered in the mixing layer because of the limited spatial resolution of the plane J1, see section 2.2.4. Nevertheless, it confirms that the core of the jet is free of turbulence, which is localized in the mixing layer. According to section 2.2.4, the close-up on TKE obtained near $r = 0.5$ at $z = 0.1$ using plane M1 which is shown in figure 6 (c) represents the actual TKE k which does not suffer from filtering. The peak value located at $r = 0.5$ does not increases until $S = 0.81$, but however, we notice that the left leg of the TKE profile gradually extends toward the core of the jet for $S \geqslant 0.40$. Compared to the peak of the TKE, the level of turbulence in this outer portion remains low. Considering the radial extent of this region which is roughly 0.05, this turbulence must be inherited from the boundary layer turbulence. Indeed, it cannot be accounted by a typical 10% spread of mixing layer turbulence from $z = 0$ to $z = 0.1$. In this region, it is then instructive to study the structure of the two-point correlation of azimuthal velocity, defined as:

$$C_{u_\theta u_\theta}(r', z')_{(r,z)} = \frac{\langle u'_\theta(r', z', t) u'_\theta(r, z, t)\rangle}{\langle u'^2_\theta(r, z, t)\rangle}. \tag{2.8}$$

The $\langle\rangle$ average represents the statistical average over the 5000 PIV snapshots. In order to study the spatial correlation associated to the outer part of the boundary layer, the probing location is set at $r = 0.425, z = 0.1$. The evolution of $C_{u_\theta u_\theta}(r', z')_{(0.425,0.1)}$ with swirl is presented in figures 7 a) to e). As can be seen, extended zones of significant spatial correlation appear for $S \geqslant 0.40$. This leads us to suspect that these zone where the TKE increases with S could be traces of Gortler-type structures, inherited from the duct boundary layer. In spite of their weak energy, these coherent turbulent structures may have an effect on the downstream development of the mixing-layer. The non-monotonous behavior of the mixing-layer growth, along with the overall jet development are described int the following section.

3. Effect of swirl on the mean flow

3.1. *Overview*

A global view of the gradual effects of swirl on the jet development is provided in figures 8 (a) to (e). From $S = 0$ to $S = 0.81$, apart from the appearance and the increase of the azimuthal velocity, one can observe several changes, which are pronounced only for $S = 0.61$ and $S = 0.81$. First, the length of the potential core decreases. This is

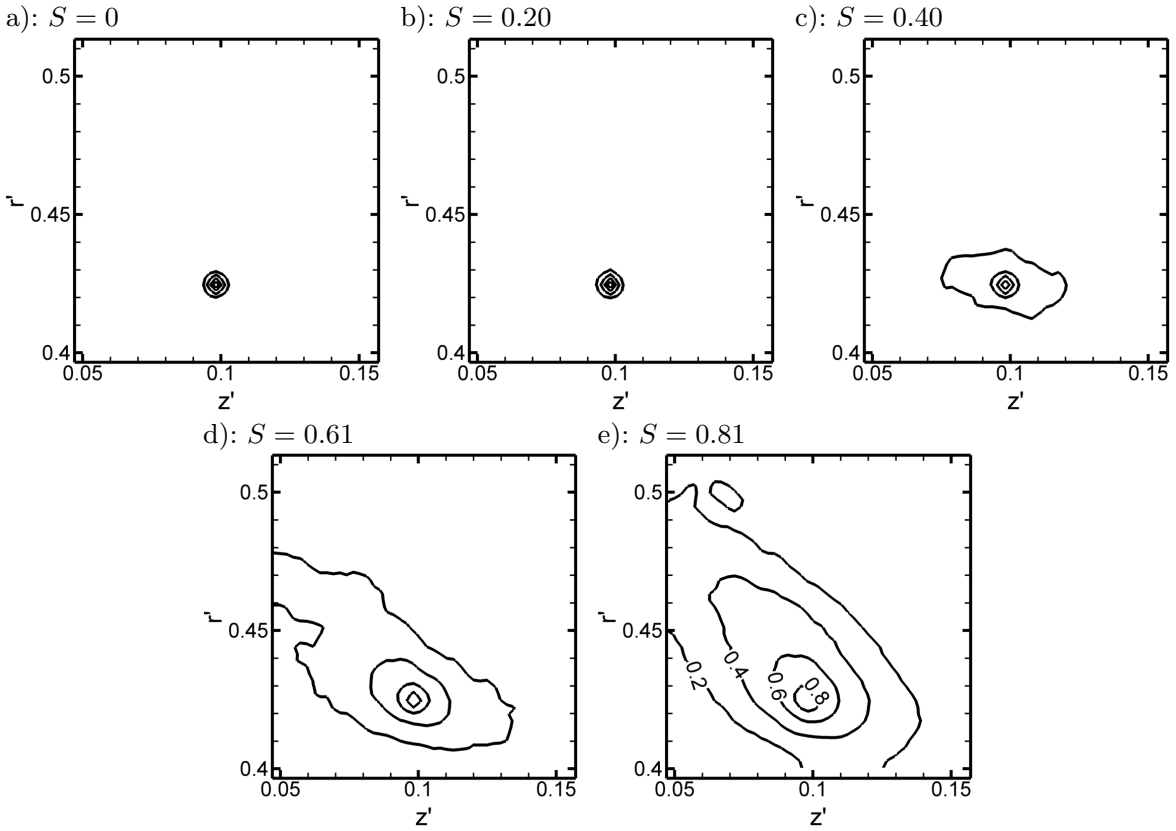

FIGURE 7. Evolution with S of the contours of the two-point correlation of azimuthal velocity $C_{u_\theta u_\theta}(r', z')_{(0.425,0.1)}$ defined in eq. (2.8). As shown in subfigure (e), contours are spaced by 0.2 starting from 0.2.

associated to a higher spatial growth rate and higher turbulent kinetic energy levels in the mixing layer. This will be further described in section 3.3. Focusing on the jet centerline, one can witness that adding swirl leads to an earlier decrease of the axial and angular velocity, together with stronger turbulence. This is described in section 3.2. Downstream of $z = 5$, diffusion of the angular momentum has led to a situation where the azimuthal component of velocity becomes negligible compared to its axial counterpart. This is in accordance with the similarity analysis of Ewing (1999), which shows that considering a fully developed swirling jet in a self-similar growth regime, conservation of axial momentum imposes a $1/z$ decay of the axial velocity while conservation of angular momentum leads to a $1/z^2$ decay for the azimuthal velocity. This is also in agreement with the experimental results presented by Shiri *et al.* (2008), where, in the far field, the overall effect of initially adding swirl reduces to a shift in the virtual origin of the self-similar jet model.

3.2. *Centerline quantities*

The axial velocity rms on the centerline is plotted in figure 9 (a). The initial rms value $< u_z'^2 >^{1/2} = 1.5\%$ corresponds to the PIV measurement noise (see section 2.2.3), the actual axial velocity fluctuation level in the core of the jet being 0.5% at the exit (hot-wire measurement, see section 2.1.1). The rise of the axial velocity rms on the axis starts near $z = 1.5$ and remains globally the same up to $S = 0.40$. A faster rise is obtained for $S = 0.61$ and a saturation is felt after $z = 6$. For $S = 0.81$, saturation of $\langle u_z'^2 \rangle^{1/2}$ to a level of 16% occurs beyond $z = 4.5$. A 'fully developed' turbulent regime is therefore attained earlier at these values of S.

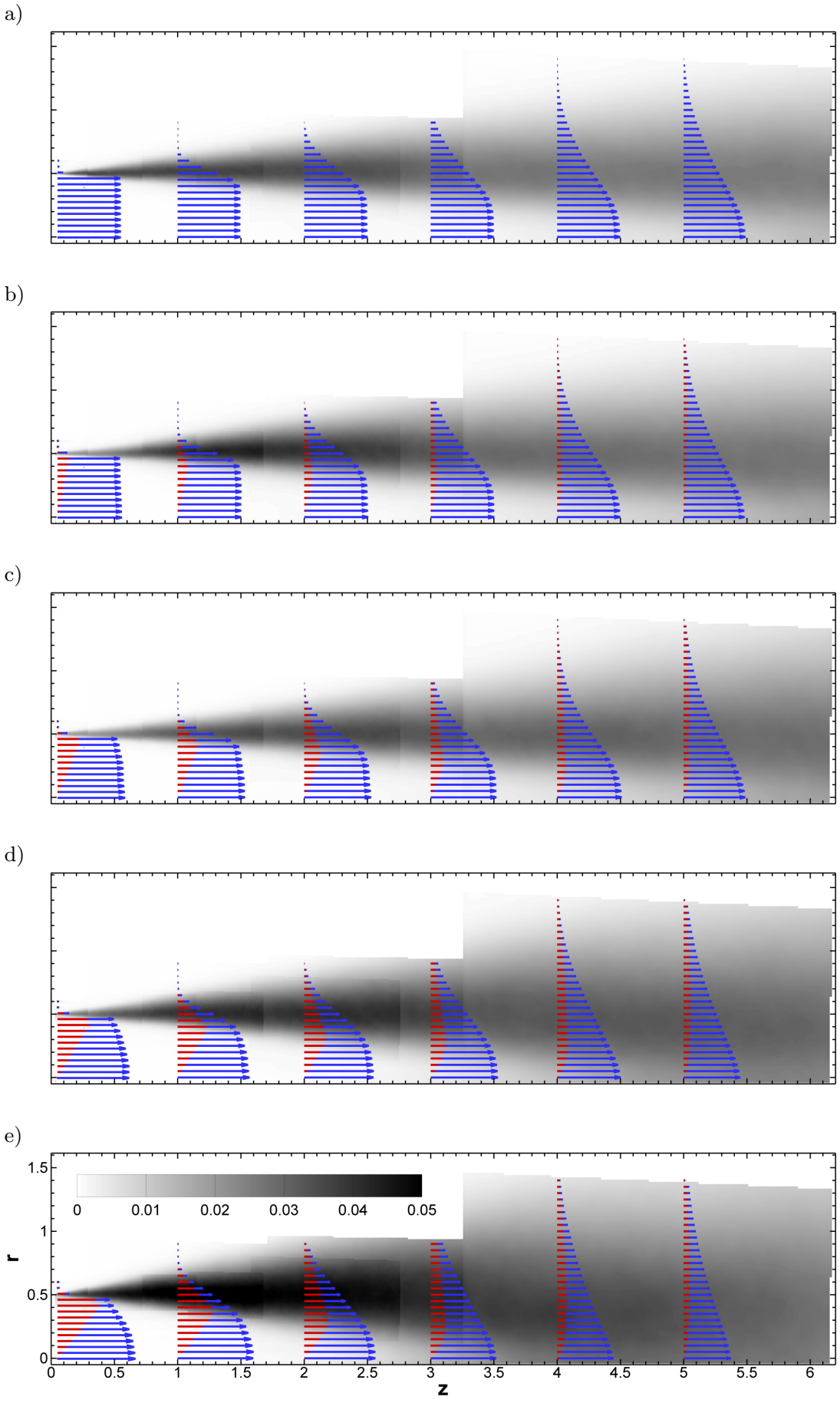

FIGURE 8. Turbulent kinetic energy contours (grey color map), axial velocity profile (blue vectors) and azimuthal velocity profiles (red bars) at $z = 0.07$, $z = 1$, $z = 2$, $z = 3$, $z = 4$, and $z = 5$. $u_z = 1$ ($u_\theta = 1$) corresponds to a segment of length $z = 0.5$. From top to bottom: $S = 0$ to $S = 0.81$.

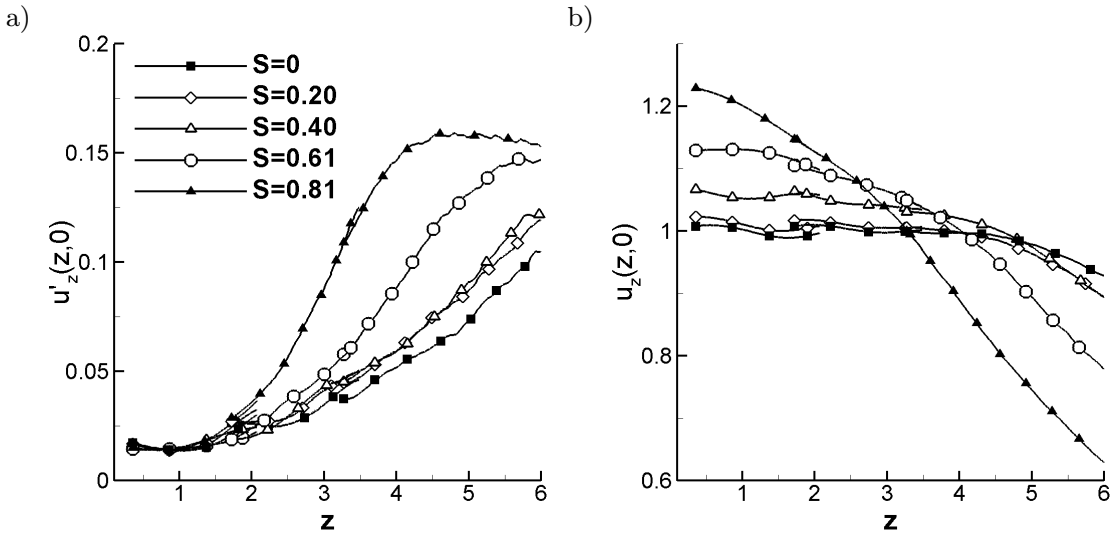

FIGURE 9. Downstream evolution of axial velocity rms (a) and mean axial velocity (b) on the jet axis, from longitudinal PIV planes $J1$ to $J4$ (figure 2).

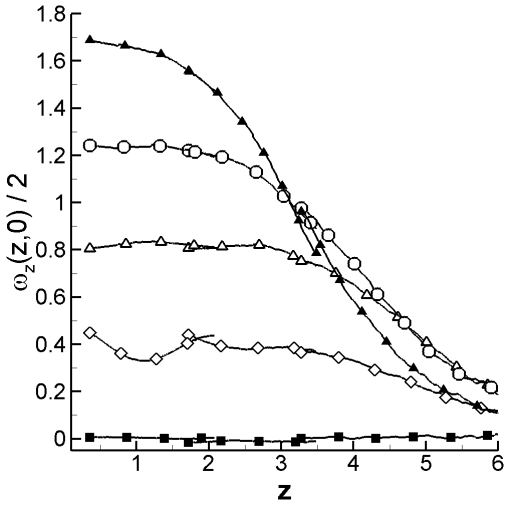

FIGURE 10. Downstream evolution of angular velocity on the jet axis $\frac{1}{2}\omega_z(0,z)$, same legend as figure 9.

The evolution of $u_z(0,z)$ is now plotted in figure 9 (b). For $S=0$ and $S=0.20$, one can see that the decay starts near $z=4.5$. This is consistent with previous observations on jets (see Iqbal & Thomas 2007). An earlier decay, near $z=3$, is obtained for $S=0.40$. Note also the rise of $u_z(0,0)$, which is due to the parabolization of the axial velocity profile at the exit (see section 2.3.1). For $S=0.61$ and 0.81, the centerline axial velocity decrease starts even closer to the jet exit. As shown in figure 9 (a), this is not due to turbulence which has not yet increased in the jet core, as will be explained in the next paragraph. The angular velocity on the jet axis, $\frac{1}{2}\omega_z(0,z)$, follows a similar behavior see figure 10. Note that the latter was here computed on a rather large $0 \leqslant r \leqslant 0.25$ stencil. As expected, its initial level near the exit plane is roughly $2S$. The location of its decrease coincides with that of the axial velocity on the centerline. In particular, for $S=0.81$, we observe a continuous decrease of $\frac{1}{2}\omega_z(0,z)$, starting from $z=0$.

The above mentioned decrease in $u_z(0,z)$ in the absence of turbulent diffusion should be attributed to pressure. This can be understood by the following arguments. On the centerline, a decrease of the axial velocity is equivalent to an adverse pressure gradient.

We will now show that this is indeed linked to the growth of the mixing layer. Neglecting the second order moments in the radial projection of the Reynolds averaged Navier-Stokes equations gives:

$$\frac{\partial p}{\partial r} \approx \frac{u_\theta^2}{r}, \tag{3.1}$$

where the physical pressure P has been normalized by ρU_0^2. In the core of the jet, one has $u_\theta = 2Sr$, and supposing that the mixing layer has a negligible thickness at $z = 0$, one obtains the value of the pressure on the jet centerline for $z = 0$ by integrating eq. (3.1) from 0 to infinity:

$$p(r = 0, z = 0) \approx p_\infty - \frac{1}{2}S^2. \tag{3.2}$$

A rough model for the mixing layer growth is now used to provide the downstream evolution of the centerline pressure. This model supposes that as a consequence of the growth of the mixing layer of thickness $\delta(z)$, the solid body rotation core of the flow extends only up to $r = 0.5 - \delta/2$, and that beyond, the contribution to the integration of the pressure using eq. (3.1) is negligible. This provides:

$$p(r = 0, z) \approx p_\infty - \frac{1}{2}S^2(1 - \delta(z))^2. \tag{3.3}$$

This links an adverse pressure gradient to the growth of the mixing layer and to the value of S. Conservation of the total pressure along the centerline then leads to the following law for the axial velocity on the centerline:

$$u_z(r = 0, z) \approx \sqrt{u_z^2(0, 0) - S^2\delta(z)}. \tag{3.4}$$

In this last equation, we have assumed that $\delta << 1$. The centerline velocity decrease thus also depends both on the value of S and on the growth rate. In a different configuration, Grabowski & Berger (1976) have also attributed an adverse streamwise pressure gradient due to the growth of an external shear layer. This is contrary to the hypothesis of a favorable pressure gradient by Mehta *et al.* (1991). At higher swirl than those considered in the present study, an adverse pressure gradient may trigger vortex breakdown (Sarpkaya 1974). This may be an additional motivation to study the effect of swirl on the growth of the mixing layer, as will now be done.

3.3. *Spatial growth and turbulence intensity*

Figure 11 (a) shows the downstream evolution of the axial shear thickness δ_ω for different values of S. This thickness does not increase significantly until $S = 0.61$, and it even slightly decreases for $S = 0.40$. This non-monotonic behavior of mixing with a decrease of the growth rate for $S = 0.40$ is not comparable to the monotonic variations measured by Mehta *et al.* (1991) and is a matter of interrogation.

The downstream evolution of the radial maximum of the turbulent kinetic energy k_m (in the mixing layer) is shown in figure 11 (b) for different swirl levels. In this figure, it seems that swirl produces two conflicting effects. First, it delays transition from the boundary layer to the mixing layer turbulence. Second it leads to a more energetic mixing layer. For $S = 0$, the evolution of k_m is consistent with the well described development of a turbulent mixing layer from a turbulent boundary layer, see e.g. Bradshaw (1966). Here, k_m rises from the initial level of 0.20 and stabilizes to a 0.35 plateau as early as $z = 0.5$, which is roughly equal to 215 initial boundary layer momentum thickness θ from the exit plane. This maximum level slightly decreases past $z = 1.5$, which may indicate the departure from a thin axisymmetric mixing layer as the potential core reduces. As S is increased, a larger distance is needed for stabilizing k_m. We note that this effect

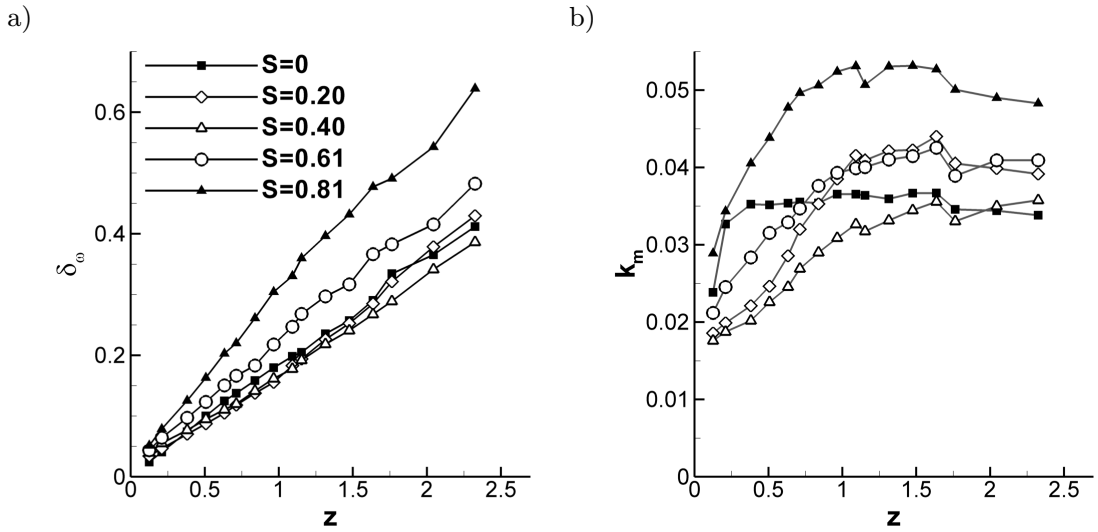

FIGURE 11. Downstream evolution of vorticity thickness δ_ω, (a), and radial maximum of turbulent kinetic energy k_m, (b).

is especially strong at $S = 0.40$, where the leveling to a plateau of k_m only occurs near $z = 2$. Note that for $S = 0.40$, the initial vorticity thickness inherited from the exit boundary layer has nearly doubled from $S = 0$, see figure 6 (b). This can explain the larger stabilization distance which scales with the exit boundary layer thickness. In addition, as was shown in section 2.3.2, the boundary layer that develops inside the jet exit nozzle is altered by spatially coherent structures that appear for $S = 0.40$. If the alignment of turbulent with the mean flow is altered, this may delay the stabilization even further.

For all swirl parameters, k_m has reached an asymptotic level for $z \geqslant 2$ close to $k_m = 0.4$ for $S = 0.20$ and $S = 0.61$, while k_m is near 0.5 for $S = 0.81$. We therefore expect that swirl introduces new turbulence production mechanisms. These should lead to a faster spatial growth of the mixing layer, but the swirl varying initial exit conditions may also play an important role. The next section describes the structure of the Reynolds stress tensor and that of the production terms of the turbulent kinetic energy in the mixing layer, with a special care to separate the new swirl-induced production mechanisms from the effects inherited from the initial conditions.

4. The kinematics of the Reynolds stress tensor

Swirl changes the production of turbulent kinetic energy by different means, in a simplified framework. We will restrict ourselves to the center of the mixing layer. As shown below, we must try to compare situations as free from the initial conditions effects as possible, in regions which are located downstream enough for the structure of turbulence to have reached a quasi-equilibrium.

4.1. *Downstream evolution of the Reynolds stress tensor*

In figure 12 (a) to (f), we represent the downstream evolution of the six Reynolds stress components $\langle u_i u_j \rangle$ at the center of the mixing layer, i.e. at radius r_m such that k is maximum, $k(r_m) = k_m$. Incidentally, the dispersion of the data leads to an experimental estimation of the statistical and measurement uncertainty, since some points come from independent overlapping PIV planes (labeled $M1$ to $M5$ in figure 2). Roughly, this comparison provides a $\pm 2 \times 10^{-3}$ rms uncertainty estimation on the normal stresses, which

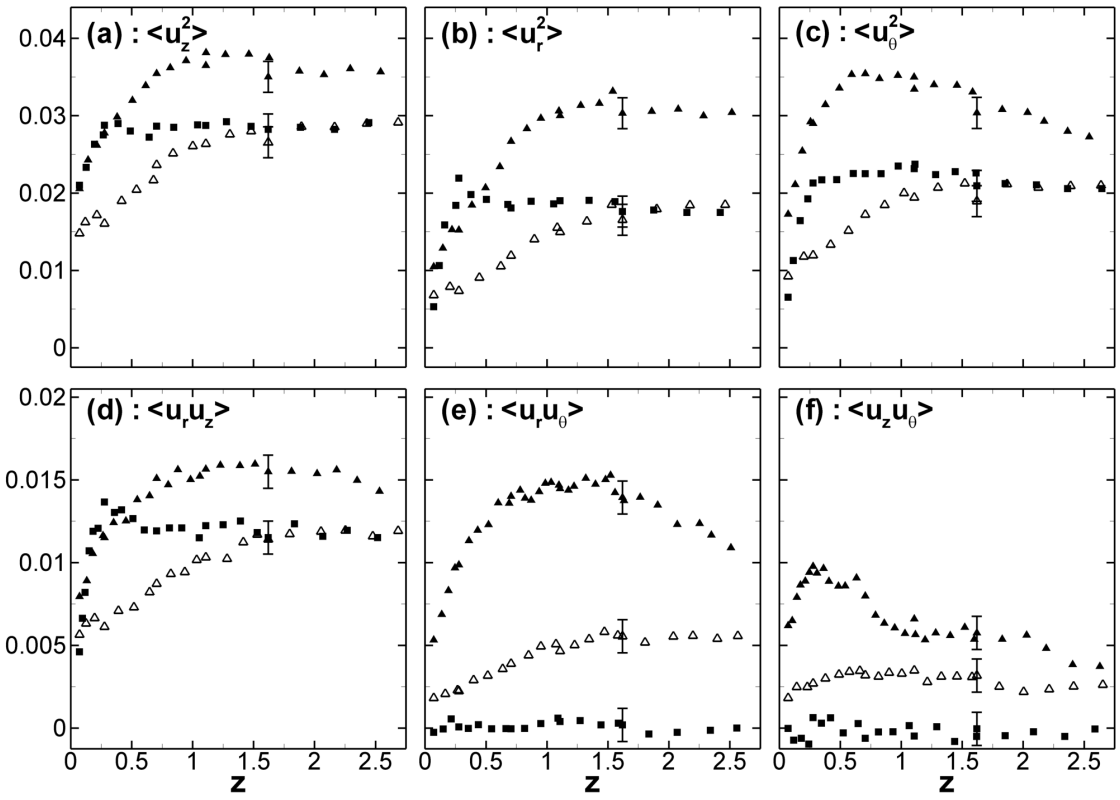

FIGURE 12. Downstream evolution of Reynolds stresses at the radial location r_m of the maximum turbulent kinetic energy k_m. (a): $\langle u_z^2 \rangle$, (b): $\langle u_r^2 \rangle$, (c) $\langle u_\theta^2 \rangle$, (d): $\langle u_r u_z \rangle$, (e): $\langle u_r u_\theta \rangle$, (f): $\langle u_z u_\theta \rangle$ for $S = 0$ (■), $S = 0.40$ (△) and $S = 0.81$ (▲). The error bars indicate the uncertainty estimated from overlapping PIV planes (see the text for more details).

is consistent with the estimation proposed in sub-section 2.2.3. The uncertainty on the shear stresses, which can also be recovered from the dispersion of $\langle u_r u_\theta \rangle$ and $\langle u_z u_\theta \rangle$ for $S = 0$, seems approximately two times smaller.

The $S = 0$ stabilized levels of the $\langle u_i^2 \rangle$ normal stresses and $\langle u_r u_z \rangle$ are similar to those reported in numerous mixing-layer studies (see, e.g. Bradshaw *et al.* 1964; Hussain & Husain 1980). When swirl is added, the increase of $\langle u_r^2 \rangle$ and $\langle u_\theta^2 \rangle$ is more important than that of $\langle u_z^2 \rangle$. Also, the level of $\langle u_r u_\theta \rangle$ increases strongly with swirl, and that of $\langle u_z u_\theta \rangle$ is significant.

As can be seen in figures 12 (a) to (c), the stabilization of $\langle u_i^2 \rangle$ is complete by $z = 2$ for all the values of S, except for $\langle u_\theta^2 \rangle$, which is observed to decrease beyond a maximum reached near $z = 1$ for $S = 0.81$. As for the turbulent kinetic energy, plotted in figure 11, the stabilization distance appears to be the longest for $S = 0.40$. Stabilization of the three shear stresses is also obtained by $z = 2$, as seen in figures 12 (d) to (f), except for a decrease of $\langle u_r u_\theta \rangle$ for $S = 0.81$. Despite of this, the Reynolds stress tensor globally achieves a stabilization from the initial boundary layer has been reached by $z = 2$.

4.2. *Turbulent kinetic energy budget*

We now make a focus on the $z = 2$ location to describe the production of turbulent kinetic energy. Turbulent kinetic energy k is governed by the convection $\frac{Dk}{Dt}$, the turbulent transport T, the production P and the dissipation ϵ:

$$\frac{Dk}{Dt} + T = P - \epsilon. \tag{4.1}$$

Referring to Bradshaw (1973), under the cylindrical statistical invariance ($\frac{\partial}{\partial\theta}=0$), and upon excluding ϵ and neglecting transport due to viscous stresses, these terms write:

$$\frac{Dk}{Dt} = u_z\frac{\partial k}{\partial z} + u_r\frac{\partial k}{\partial r}, \tag{4.2}$$

$$T = \frac{\partial}{\partial z}\left[\frac{\langle pu_z\rangle}{\rho} + \langle u_z k\rangle\right] + \frac{1}{r}\frac{\partial}{\partial r}\left[r\left(\frac{\langle pu_r\rangle}{\rho} + \langle u_r k\rangle\right)\right], \tag{4.3}$$

$$P = -\langle u_i u_j\rangle d_{ij}. \tag{4.4}$$

The quantities under brackets are fluctuations, and d_{ij} is the strain tensor, which writes:

$$d_{ij} = \begin{pmatrix} \frac{\partial u_r}{\partial r} & \frac{1}{2}r\frac{\partial}{\partial r}(\frac{u_\theta}{r}) & \frac{1}{2}\frac{\partial u_z}{\partial r} + \frac{1}{2}\frac{\partial u_r}{\partial z} \\ d_{\theta r} = d_{r\theta} & \frac{u_r}{r} & \frac{1}{2}\frac{\partial u_\theta}{\partial z} \\ d_{zr} = d_{rz} & d_{z\theta} = d_{\theta z} & \frac{\partial u_z}{\partial z} \end{pmatrix}. \tag{4.5}$$

Figure 13 gives a global view on the terms of eqs. (4.3) and (4.4) at $z = 2$ for $S = 0$, 0.40 and 0.81. Figures 13 (a) to (c) show the corresponding mean velocity profiles. The mean flow displays a constant shear for both the mean axial and azimuthal velocity components in a large portion of the mixing layer. The mean radial velocity is negligible. It is clear that at the same $z = 2$ downstream station, the shear thickness is increased for $S = 0.81$. The components of the Reynolds stress tensor are given in figures 13 (d) to (f). The hierarchy between the different components was described in the analysis of figure 12, see the above section. In the present figure, we can note that the maximum of each of the Reynolds stress tensor components occurs at the center of the mixing layer, and that the width of the peak scales with the shear thickness.

Finally, figures 13 (g) to (i) present the profiles of the production term P defined in eq. (4.4), along with the dominant term of radial transport noted $\tilde{T}''$, which is the $\frac{1}{r}\frac{\partial}{\partial r}(r\langle u_r' k'\rangle)$ term of eq. (4.3). In this equation, the second bracket is expected to be dominant since in this free shear flow, one may suppose that the streamwise derivatives, associated to a length scale l, are negligible compared to radial derivatives, associated to δ. Now in the second bracket, the pressure diffusion term cannot be measured, but direct Navier-Stokes simulations results show that it is not dominant at the center of a non-swirling mixing layer, where it typically scales as $\tilde{T}' \approx -\rho\frac{1}{5}\tilde{T}''$, see Pope (2008). We will suppose that this remains the case in the swirling mixing layer. An estimated rms uncertainty was obtained for P and $\tilde{T}''$ for each radial position by computing the variations from $z = 2 - \delta_\omega/4$ to $z = 2 + \delta_\omega/4$. Production and turbulent transport reach a maximum and a minimum located roughly at the center of the mixing layer. The ratio of $\tilde{T}''$ to P is almost conserved at the center of the mixing layer, whatever the swirl levels. It is therefore legitimate to suppose that the turbulent kinetic energy is driven by production, and that turbulent transport adapts. In the center of the mixing layer, the mean shear is constant and the Reynolds stresses, the TKE production and transport terms all reach a maximum. This leads us to analyze the flow here as if it were quasi-homogeneous in order to detail how the effect of swirl may enhance production of turbulence.

4.3. *Analysis of the production term*

4.3.1. *Tensor analysis*

According to eq. (4.4), production results from the alignment of the Reynolds stress tensor $\langle u_i u_j\rangle$ with the strain tensor d_{ij}. In order to analyze the effect of swirl on production in a general manner, we must consider the structure of these two symmetric tensors. One then considers their reduction to their eigenvectors and eigenvalues. We note these

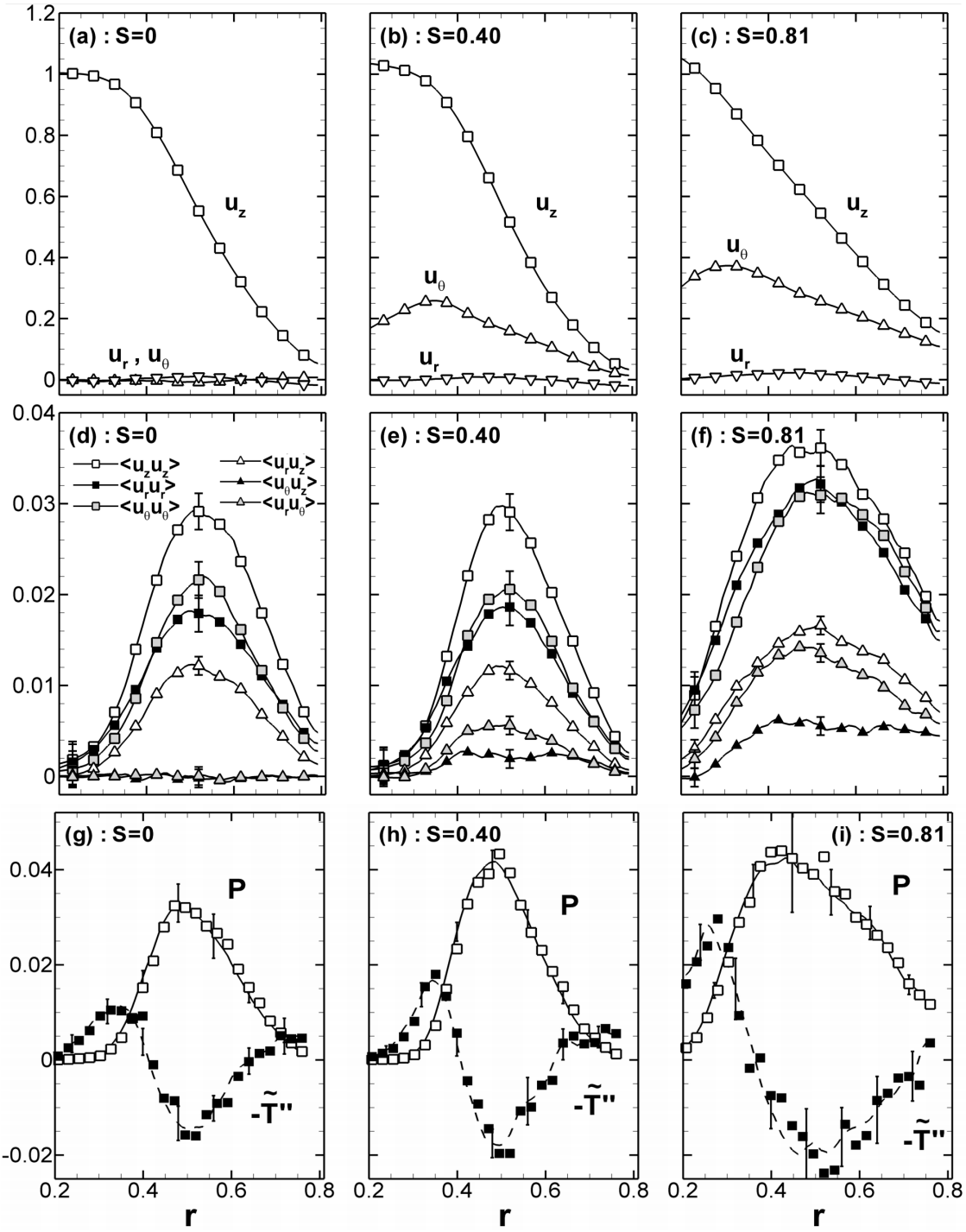

FIGURE 13. Mean velocity u_i at $z = 2$ for $S = 0$ (a) $S = 0.40$ (b) and $S = 0.81$ (c). Reynolds stresses $\langle u_i u_j \rangle$ for $S = 0$ (d) $S = 0.40$ (e) and $S = 0.81$ (f): same error bars as in figure 12. TKE production P eq. (4.4) and transport term $\tilde{T}'' = \frac{1}{r}\frac{\partial}{\partial r}(r\langle u'_r k' \rangle)$ of eq. (4.3) for $S = 0$ (g), $S = 0.40$ (h) and $S = 0.81$. The symbols are the measurements, and the lines are obtained with a $z = 2 \pm \delta_\omega/4$ spatial average. The error bars correspond to the dispersion rms (see the text for more detail).

quantities $(\vec{r}_i, \lambda_i^r)$ for the Reynolds stress tensor and by $(\vec{d}_i, \lambda_i^d)$ for the strain tensor, with $(1 \leqslant i \leqslant 3)$. In the following, unless specified otherwise, we will focus on $(r = r_m, z = 2)$. In order to take advantage of the locally spatially homogeneous nature of the statistics, statistical convergence is increased by using a spatial average over a $(r_m \pm \delta_\omega/8, z \pm \delta_\omega/4)$

S^u	$=$	$\frac{u_\theta(r_m,z)}{u_z(r_m,z)}$	: Ratio of azimuthal to axial velocities
S^d	$=$	$r\frac{\partial}{\partial r}(\frac{u_\theta}{r})/\frac{\partial u_z}{\partial r}$	: Ratio of azimuthal to axial shear
S_i^a	$=$	$(\vec{a}_i \cdot \vec{e}_\theta) \,/\, (\vec{a}_i \cdot \vec{e}_z)$	: Orientation of the eigenvectors $\vec{a}_i$, $i = 1$ and 2
S_3^a	$=$	$(-\vec{a}_i \cdot \vec{e}_z) \,/\, (\vec{a}_i \cdot \vec{e}_\theta)$	: Orientation of the eigenvector $\vec{a}_3$
β_i^a	$=$	$\arctan(\frac{\vec{a}_i \cdot \vec{e}_r}{\sqrt{(\vec{a}_i \cdot \vec{e}_z)^2+(\vec{a}_i \cdot \vec{e}_\theta)^2}})$	: Inclination angle of the eigenvector $\vec{a}_i$

TABLE 3. Summary of the definitions characterizing the mean flow, and an eigenvector $\vec{a}_i$, which can correspond to either the strain ($a = d$) or the Reynolds stress ($a = r$) tensors. A geometrical representation of S_i^a and β_i^a is given in figure 14.

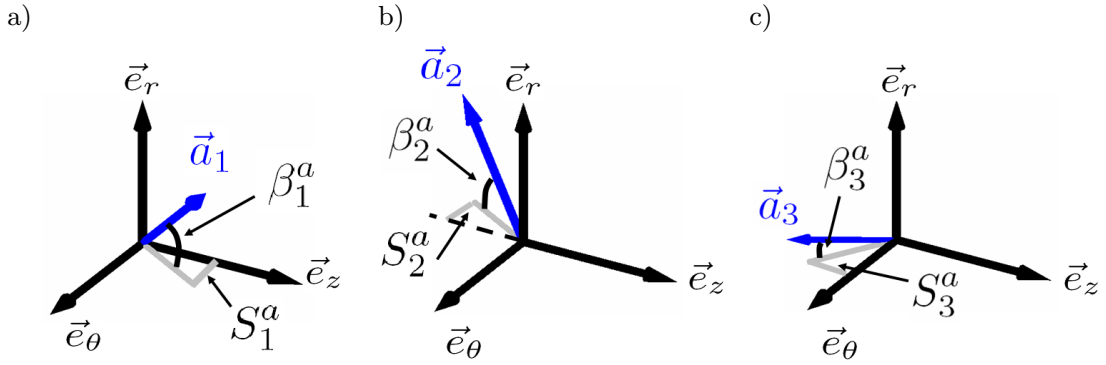

FIGURE 14. Orientation S_i^a and inclination β_i^a of the eigenvector $\vec{a}_i$, for $i = 1$ (a), $i = 2$ (b) and $i = 3$ (c). $\vec{a}_i$ stands for $\vec{d}_i$ or $\vec{r}_i$. Note: the different definition for S_3^a in (c).

area. Statistical convergence of the following results was checked by reducing the size of this spatial average or reducing the number of statistically independent PIV snapshots from $N = 5000$ to $N = 500$. This increased the relative uncertainties but did not quantitatively change the following results. The smoothness of the variations of the following quantities with consecutive 0.1 increases in S is one supplementary indication that a correct convergence is reached.

Table 3 summarizes the definitions introduced to describe the geometry of the eigenvectors of each tensor. These definitions rely on a representation in spherical coordinates, as defined in figure 14, and are exemplified using a generic unit vector noted $\vec{a}_i$. It is convenient to characterize the orientation of this vector by a first parameter noted S_i^a, which quantifies the rotation around $\vec{e}_r$ similarly to a swirl parameter. This leads to define a specific orientation of S_3^a, see table 3, since the third eigenvector is aligned with $\vec{e}_\theta$ for $S = 0$. The inclination of the eigenvectors above the $(\vec{e}_\theta, \vec{e}_z)$ plane is then expressed as the angle β_i^a. The evolution with S of these quantities will now be analyzed, for both the strain tensor (section 4.3.2) and the Reynolds stress tensor (section 4.3.3).

4.3.2. *Strain tensor*

This analysis is now performed on the strain tensor. The evolution with S of the orientation and inclination parameter of the eigenvectors along with the eigenvalues of the strain tensor is described in figures 15 (a) to (c). For $S = 0$, the structure of the strain tensor is characteristic of shear flow turbulence (see e.g. Townsend 1980). More specifically, as seen in figures 15 (a) and (b), the angles fulfill $\beta_1^d = \beta_2^d \approx 45°$ and

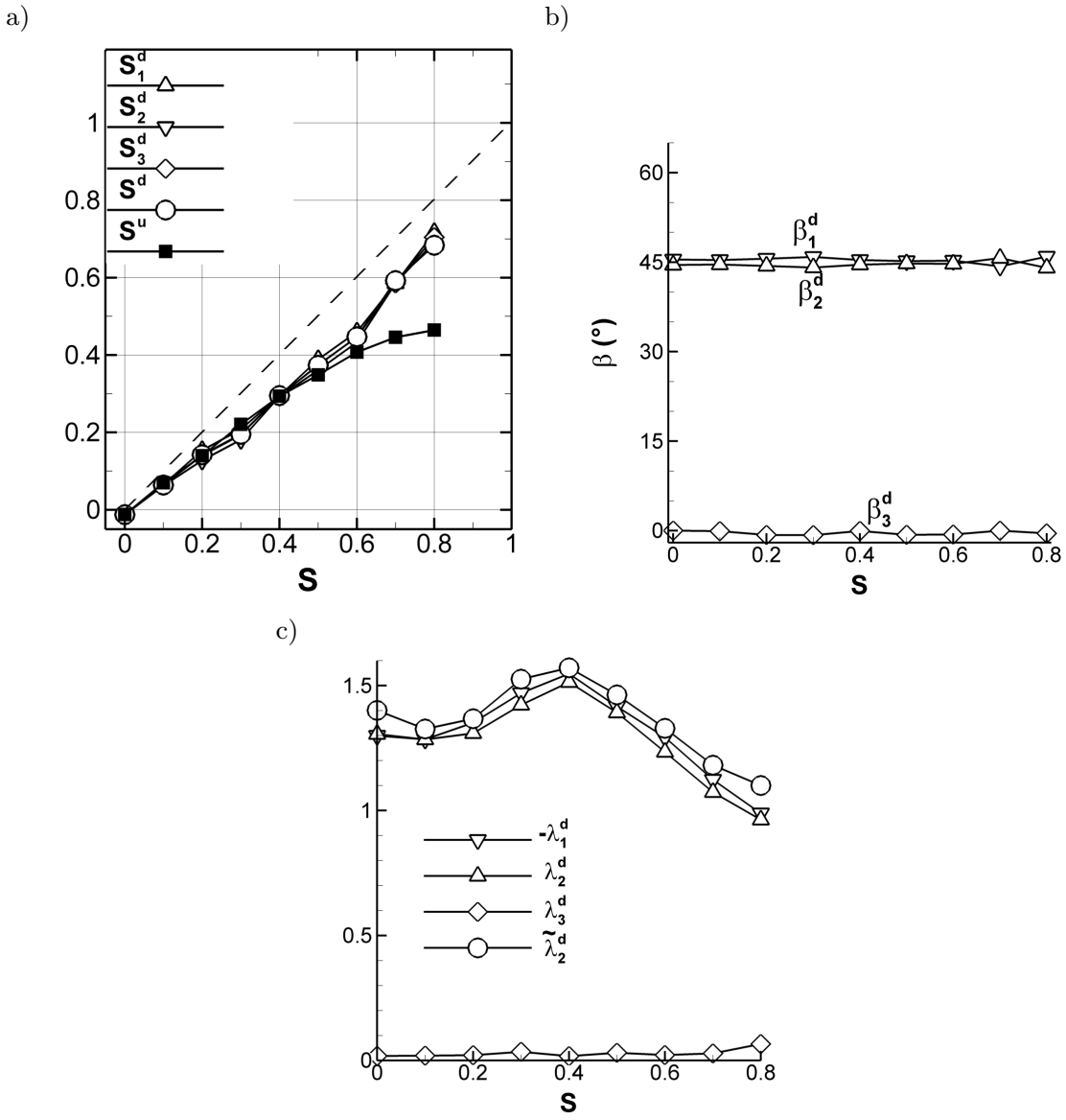

FIGURE 15. (a) and (b): Evolution of the orientation and inclination parameters describing the eigenvectors of the strain tensor, as defined in table 3. In (a), the dashed line has a unity slope. (c): Evolution with swirl of the eigenvalues of the strain tensor at $r = r_m, z = 2$. $\tilde{\lambda}_d^{(2)}$ is the eigenvalue of the approximated tensor defined by eq. (4.6).

$\beta_3^d = 0°$, and the orientation is such that $S_1^d = S_2^d = S_3^d = 0$. When swirl is added, it may be observed in these figures than its effect amount to a rigid clockwise rotation of the stress tensor around the radial unit vector $\vec{e}_r$. Indeed, S_1^d, S_2^d and S_3^d evolve in the same linear manner with a slope close to 0.8, which we can see is a similar evolution until $S \geqslant 0.61$ to the swirl parameter S^u which characterizes the local helix of the mean flow. The inclination angles keep their $\beta_i^d = 45°$ $S = 0$ structure. The eigenvalues, plotted in figure 15 (c) remain such that $\lambda_2^d \approx -\lambda_1^d \geqslant 0$ and $\lambda_3^d \approx 0$. This evolution can be justified theoretically by considering the approximate expression of the strain tensor under the thin free shear flow hypothesis:

$$d_{ij} \approx \tilde{d}_{ij} = \frac{1}{2}\frac{\partial u_z}{\partial r}\begin{pmatrix} 0 & S^d & 1 \\ S^d & 0 & 0 \\ 1 & 0 & 0 \end{pmatrix}, \tag{4.6}$$

where $S^d = r\frac{\partial}{\partial r}(\frac{u_\theta}{r})/\frac{\partial u_z}{\partial r}$ represents a swirl parameter based on the ratio of azimuthal to axial shear. It is straightforward to show that the eigenvectors of the approximated strain tensor $\tilde{d}_{ij}$ have an orientation which is precisely S^d. The validity of the approximation of d_{ij} by $\tilde{d}_{ij}$ is confirmed by the fact that S^d is identical to S_1^d and S_2^d, as can be seen in figure 15 (b). Supposing that $\frac{\partial u_z}{\partial r} \approx \frac{1}{\delta_\omega}$ for $r = r_m$, the positive and negative eigenvalues of the approximated tensor $\tilde{d}_{ij}$ defined in eq. (4.6) are simply

$$\tilde{\lambda}_1^d = -\frac{1}{2}\frac{\sqrt{1+S^{d^2}}}{\delta_\omega}, \tag{4.7}$$

$$\tilde{\lambda}_2^d = -\tilde{\lambda}_1^d = \frac{1}{2}\frac{\sqrt{1+S^{d^2}}}{\delta_\omega}. \tag{4.8}$$

In figure 15 (a), $\tilde{\lambda}_2^d$ is also close to eigenvalue λ_2^d. The full tensor therefore keeps the same structure and may be characterized by a single eigenvalue, say λ_2^d, and one orientation parameter, such as S_1^d. According to eqs. (4.7) and (4.8), the thickness representing the total shear distortion may be characterized by $\delta_\lambda = \frac{\delta_\omega}{\sqrt{1+S^{d^2}}}$. Also, as may be seen in figure 15 (b), the orientation of the mean flow, defined by S^u in table 3, follows the same rotation as the strain up to $S = 0.61$. Above $S \geqslant 0.61$ a misalignment between the mean shear and the mean flow is observed for $z = 2$, but note that it does not occur upstream, at $z = 1$. This leads us to conclude that at $S \geqslant 0.61$, the swirling mixing layer shear structure departs from that of a simple shear layer, possibly due the fact that δ_ω becomes significant compared to the jet width (see figure 11). To sum up, the behavior of the strain tensor shows that for $S \leqslant 0.61$, the shear flow structure at the center of the swirling mixing layer is similar to that obtained for $S = 0$, expect that it is aligned along the swirling mean flow. This is no longer the case for $S \geqslant 0.61$, although the same shear flow structure remains.

4.3.3. *Reynolds stress tensor*

The same method of analysis is now applied to the Reynolds stress tensor. The evolution of the orientation and inclination of the eigenvectors and of the eigenvalues of this tensor is given in figures 16 (a), (b) and (c). The eigenvectors have been ordered in a consistent manner with the directions of the strain tensor. For $S = 0$, the third eigenvector is in the azimuthal direction, which is transverse to the mean flow. The first and second eigenvector lie in the orthogonal plane defined by $(\vec{e}_z, \vec{e}_r)$, and their inclinations are $\beta_1^r = 33°$ and $\beta_2^r = 90 - 33 = 57°$, which is typical of turbulent free shear flow anisotropy. Similarly to the strain tensor, swirl also rotates the Reynolds stress tensor about the radial direction. Figure 16 (a) shows that the orientation S_1^r of the first eigenvector evolves in a similar manner to that of S_1^d in figure 15 (a). This is however not the case for the orientation of the second eigenvector, which is subjected to a larger rotation with $S_2^r > S_2^d$ and $S_2^r \approx 1.55S$. At the same time, as seen in figure 16 (b), the inclination of the first eigenvector increases from 33° to 40°, remaining almost constant for $0.20 \leqslant S \leqslant 0.61$. The second eigenvector evolves symmetrically as $\beta_2^r = 90° - \beta_1^r$. The evolution of the third eigenvector $\vec{r}_3$ is imposed by the orthogonally condition $\vec{r}_3 \cdot \vec{r}_1 = \vec{r}_3 \cdot \vec{r}_2 = 0$. Its orientation S_3^r, see figure 16 (a), evolves in between S_1^r and S_2^r. Its inclination β_3^d reaches 8° for $S = 0.40$ and then remains unchanged.

Figure 16 (c) presents the evolution of the Reynolds stress tensor eigenvalues normalized by $2k_m$. λ_1^r, the eigenvalue corresponding to the first eigenvector is the strongest. It is followed by λ_3^r, that of third eigenvector which is directed in the direction transverse to the flow for $S = 0$ which represents the intensity of turbulent fluctuation in a direction

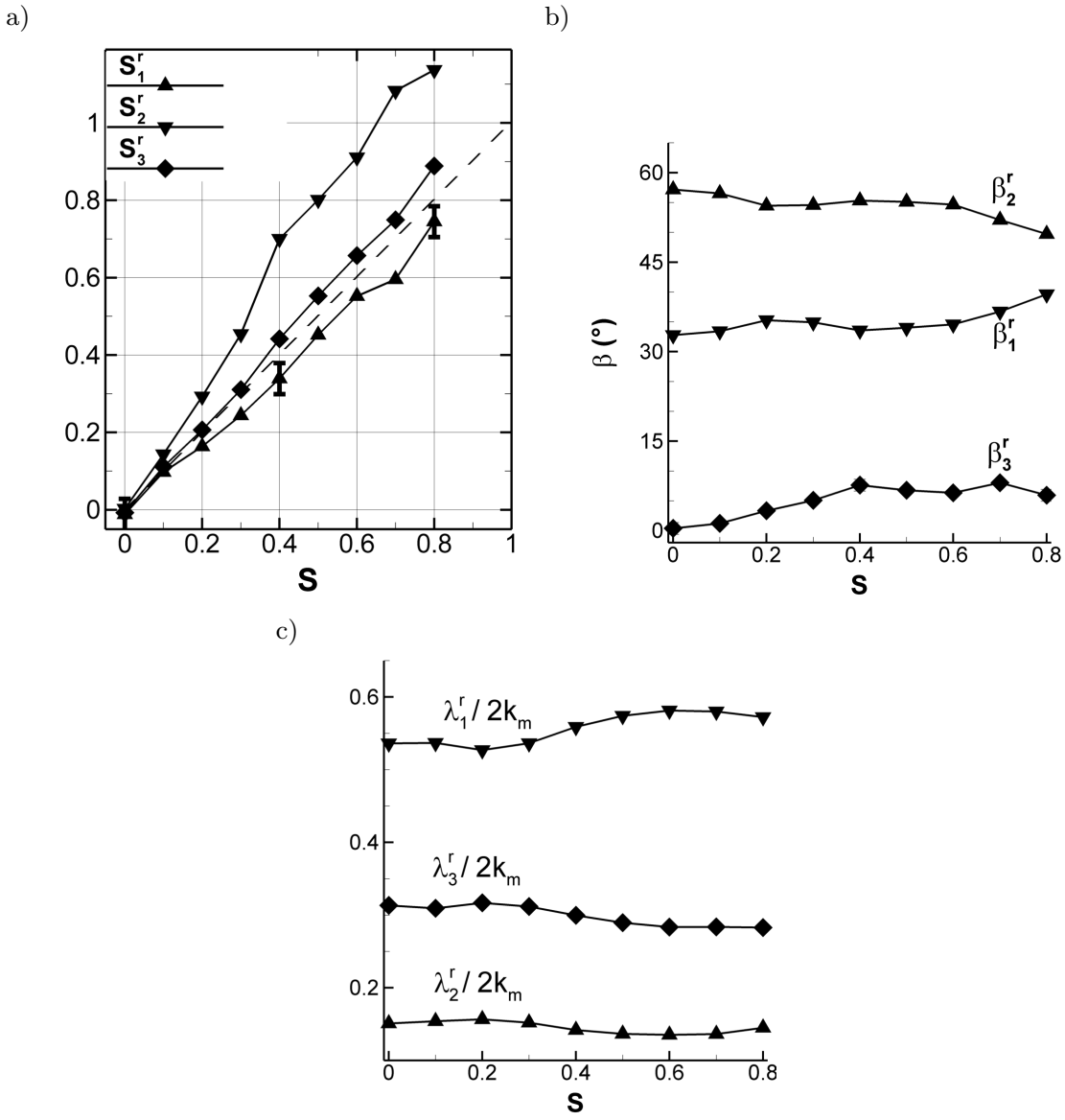

FIGURE 16. (a) and (b): Evolution of the orientation and inclination parameters describing the eigenvectors of the Reynolds stress tensor, as defined in table 3. In (a), the dashed line is the unity slope. (c): Evolution with swirl of the eigenvalues of the Reynolds stress tensor normalized by $2k_m$ at $r = r_m, z = 2$.

transverse to the local flow. This form of anisotropy is common in shear flow turbulence, see Pope (2008). The anisotropy globally increases with S. It is characterized by an overall increase of the first normalized eigenvalue, mainly to the detriment of the third. The decrease of this third normalized eigenvalue starts above $S = 0.20$ and is continuous until $S = 0.61$ where it stabilizes. We will now consider how do these changes in the individual tensors $\langle u_i u_j \rangle$ and d_{ij} affect the TKE production.

4.3.4. *Production in intrinsic coordinates*

To sum up, figure 17 gives an overview of the evolution with swirl of the eigenvectors of both the Reynolds stress tensor and the strain tensor for $S = 0$, 0.40 and 0.81. As described above, the global effect of swirl is to rotate clockwise both tensors around the radial unit vector $\vec{e}_r$, so as to follow the change in the mean flow direction. We can also see that the evolution of the relative orientation and inclination of the two tensors varies.

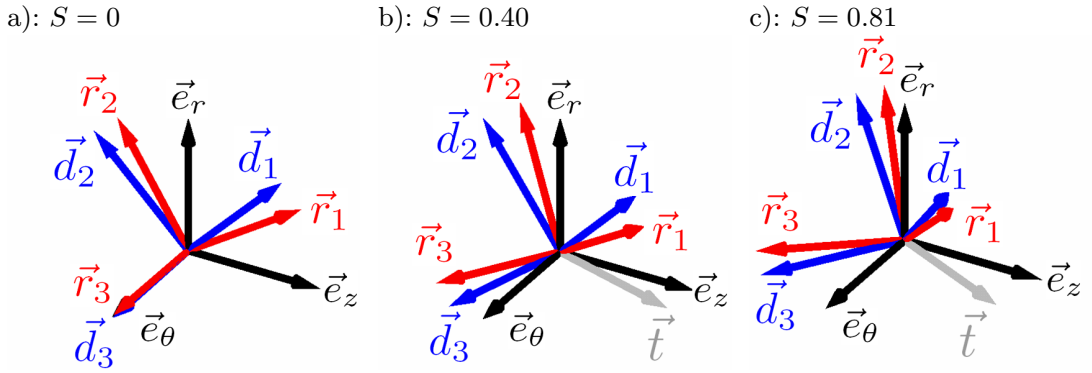

FIGURE 17. Perspective view of the orientation of the eigenvectors of the strain tensor ($\vec{d}_i$ for $i = 1, 2, 3$) and of the Reynolds stress tensor ($\vec{r}_i$ for $i = 1, 2, 3$) for $S = 0$ (a), $S = 0.40$ (b) and $S = 0.81$ (c). This structure is obtained at $(r_m, z = 2)$. The unit vector labeled $\vec{t}$ in grey represents the direction of the mean flow.

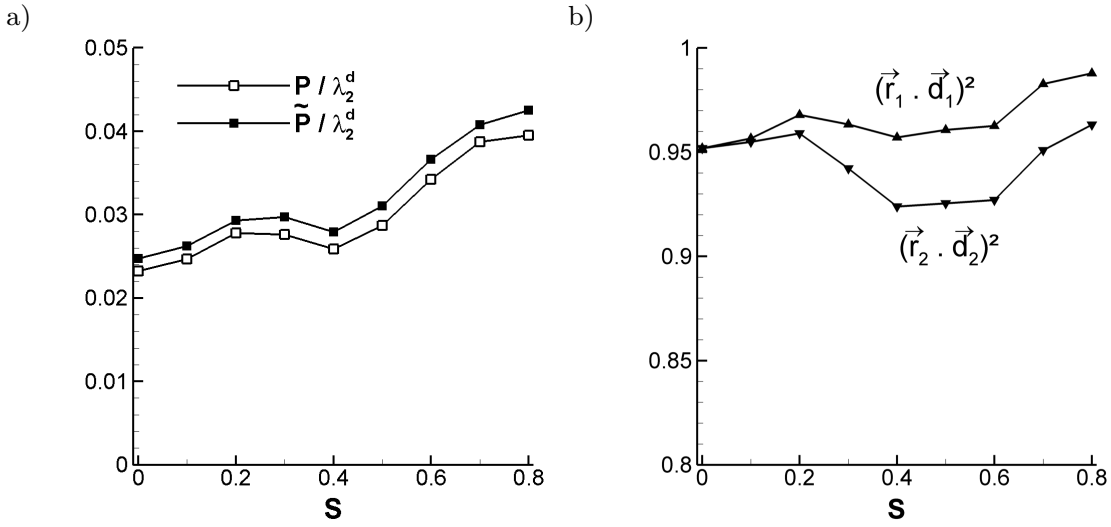

FIGURE 18. (a): Evolution with swirl S of the production of turbulent kinetic energy P at $(r_m, z = 2)$ along with approximated production $\tilde{P}$ (see the text for the definition). λ_2^d is used to normalize the results. (b): Evolution of $(\vec{r}_1 \cdot \vec{d}_1)^2$ and $(\vec{r}_2 \cdot \vec{d}_2)^2$ as a function of S for $z = 2$.

This tends to increase the alignment between the first eigenvectors of the Reynolds stress tensor $\vec{r}_1$ and of the strain tensor $\vec{d}_1$ from $S = 0$ to $S = 0.81$. As detailed in this section, this is one of the reasons why production of turbulent kinetic energy increases readily.

So, we consider now the product of the two tensors, which leads to the production of turbulent kinetic energy:

$$P = -\langle u_i u_j \rangle d_{ij} = -\sum_{i=1}^{i=3}\sum_{j=1}^{j=3} (\vec{r}_i \cdot \vec{d}_j)^2 \lambda_i^r \lambda_j^d. \tag{4.9}$$

This last expression shows that increase in the production could be either due to a better alignment (through an increase in the scalar product of the eigenvectors), or to a change in the magnitude of the eigenvalues. As shown in figure 15 (a) one has $\lambda_3^d = 0$ and $\lambda_2^d = -\lambda_1^d \geqslant 0$, which leads to

$$\frac{P}{\lambda_2^d} = (\vec{r}_1 \cdot \vec{d}_1)^2 \lambda_1^r - (\vec{r}_2 \cdot \vec{d}_2)^2 \lambda_2^r - (\vec{r}_1 \cdot \vec{d}_2)^2 \lambda_1^r + (\vec{r}_2 \cdot \vec{d}_1)^2 \lambda_1^r. \tag{4.10}$$

Note that production has been normalized by the strength of the shear λ_2^d, in order to account for the variation in the shear thickness with S. As suggested by figure 17, $(\vec{r}_1 \cdot \vec{d}_2)^2$ and $(\vec{r}_2 \cdot \vec{d}_1)^2$ are negligible. This is confirmed by a quantitative computation of these quantities (not shown here for conciseness). Neglecting these terms, one can therefore approximate $\frac{P}{\lambda_2^d}$ by:

$$\frac{\tilde{P}}{\lambda_2^d} = (\vec{r}_1 \cdot \vec{d}_1)^2 \lambda_1^r - (\vec{r}_2 \cdot \vec{d}_2)^2 \lambda_2^r. \tag{4.11}$$

The first term is a positive production resulting from the alignment of the eigenvector of the largest eigenvalue of the Reynolds stress tensor with that of the negative eigenvalue of the strain tensor. Production is increased when these two eigenvectors become more aligned (if $(\vec{r}_1 \cdot \vec{d}_1)^2$ increases), and when anisotropy increases (if λ_1^r increases). We expect this to be the case in the swirling mixing layer, since we have shown that swirl increased anisotropy and the inclination angle β_1^r corresponding to the first eigenvector of the Reynolds stress. The second term in eq. (4.11) is negative, and results from the work of the second eigenvector of both the Reynolds stress and the strain tensor. Production is therefore enhanced when these two eigenvectors become less aligned (if $(\vec{r}_2 \cdot \vec{d}_2)^2$ decreases), and also when anisotropy increases (if λ_2^r decreases). Figure 18 plots the evolution of $\frac{P}{\lambda_2^d}$ as a function of S. Note that $\tilde{P} \approx P$ whatever S, which justifies considering only the production terms of eq. (4.11). This normalized production globally increases with swirl but exhibits an unexpected local minimum near $S = 0.40$, which is consistent with the evolution of k_m in figure 11 (b). This phenomenon is now investigated. From the previous section, according to figure 16 (a), anisotropy is such that $\lambda_1^r \geqslant 3\lambda_2^r$. The alignment terms $(\vec{r}_1 \cdot \vec{d}_1)^2$ and $(\vec{r}_2 \cdot \vec{d}_2)^2$ are compared in figure 18 (b). Even if the alignment globally increases with swirl, these two terms participating in the production (4.11) remain of the same order. Therefore the contribution of the first term in the right hand side of eq. (4.11) is dominant. For this reason, it appears legitimate to make a focus on the first direction of the Reynolds stress to investigate the origin of the $S = 0.40$ accident. As we will show now the latter should be due to the boundary layer condition at the jet exit.

4.3.5. *Effects of initial conditions on production*

In figure 19 (a), we represent the downstream evolution of $(\vec{r}_1 \cdot \vec{d}_1)^2$, the term which represents the alignment of the first direction of the Reynolds stress tensor with that of strain tensor in eq. (4.11). For $S = 0$, $(\vec{r}_1 \cdot \vec{d}_1)^2$ almost does not depend on z. This agrees with the observation made in section 3.3 that for $S = 0$, the transition from the boundary layer to the mixing layer is complete by $z = 0.5$. When swirl is added, this is no longer the case. We observe that the alignment term is reduced by 10% at $z = 0.5$ for $S \geqslant 0.20$. A recovery occurs from $z = 0.5$ to 2 which is more pronounced for high values of swirl, e.g. $S = 0.81$, than for moderate values, e.g. $S = 0.40$. Cumulative effects of that kind then lead to lower intensity of the turbulence and smaller shear thickness at $z = 2$ for $S = 0.40$, as show figure 11.

The origin of this misalignment is not attributed to changes in the strain tensor, since we found that the shear flow structure is unchanged from $z = 0.5$ to $z = 2$ (we checked that the strain tensor follows the direction of the mean flow, except for $S \geqslant 0.61$ at $z = 2$, see section 4.3.2). Therefore, the reduction in the alignment between the principal directions of the strain tensor and the Reynolds stress tensor is due to the Reynolds stress tensor itself. Firstly we observe a reduction of the inclination angle β_1^r, see figure 19 (b), which is found to be minimum for $z = 0.5$, $S = 0.40 - 0.51$. Secondly, the

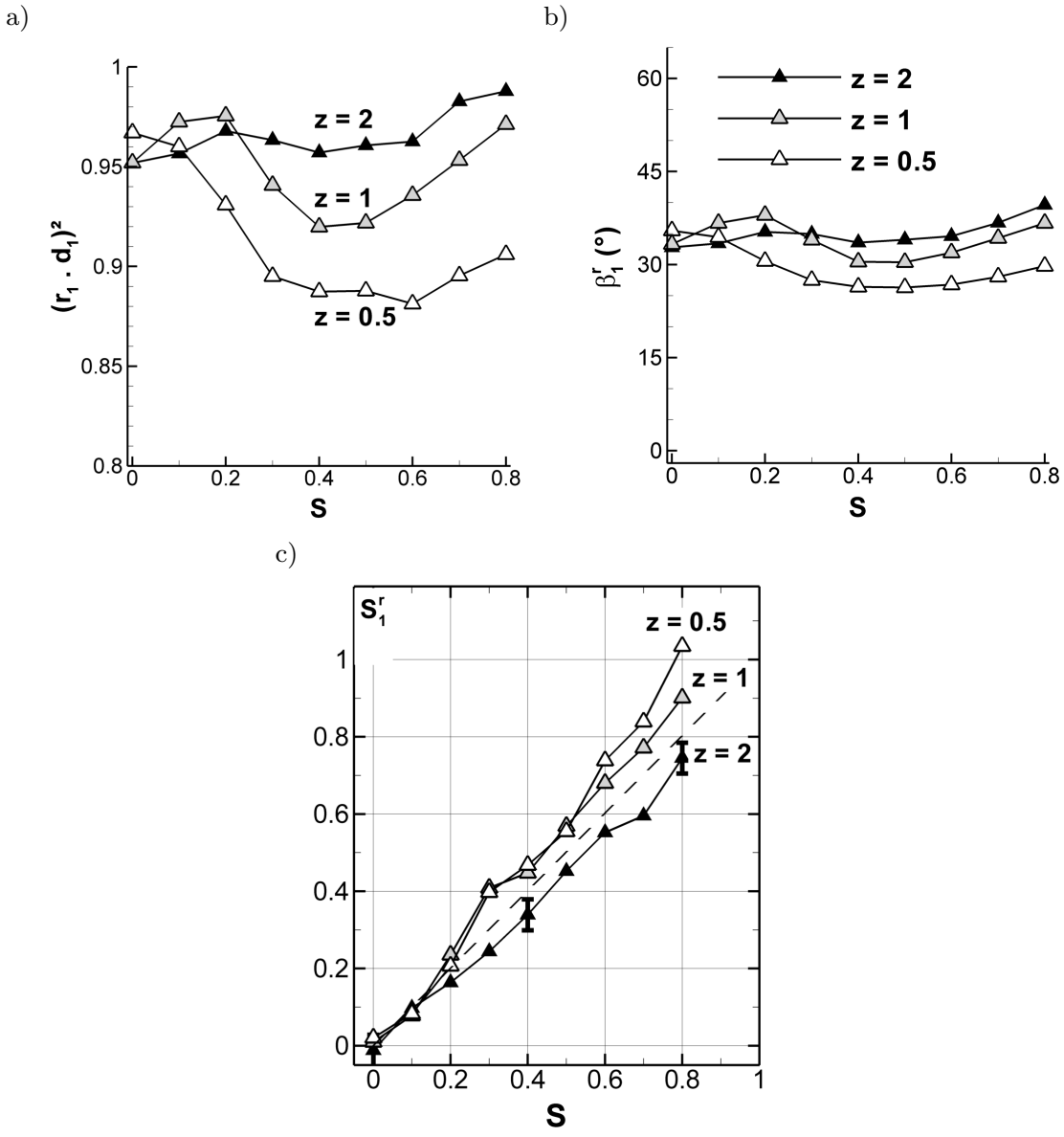

FIGURE 19. (a): $(\vec{r}_1 \cdot \vec{d}_1)^2$ as a function of S for $z = 0.5$, 1 and 2. (b): β_1^r for $z = 0.5$, 1 and 2. (c): S_1^r for $z = 0.5$, 1 and 2.

Reynolds stress tensor is misaligned compared with mean flow direction: the orientation S_1^r plotted in figure 19 (c) is larger than the $0.8S$ direction of the strain (see section 4.3.2) for $S \geqslant 0.30$, thus reducing alignment. A possible explanation for this large rotation comes from the nature of the distortion imposed by the pipe contraction on the swirling boundary layer. As explained in section 2.1, the contraction decreases the local swirl. If the turbulence does not adapt immediately to these variable conditions, one can expect that the Reynolds stress will keep its orientation prior to the contraction. In figures 19 (a) to (c), one can see that the return to equilibrium from the initial conditions is long, taking nearly 2 jet diameters whereas the initial shear thickness is much smaller. We have described in section 2.3.2 the appearance of large, but weak, spatially coherent structure in the outer part of the swirling exit boundary layer. Since these large structures carry a memory of the state of turbulence, this can qualitatively explain a longer relaxation time of the swirling boundary layer compared to the non-swirling one. The fact that turbulence equilibrium is recovered faster at high swirl, see figure 19 (a), may be due to

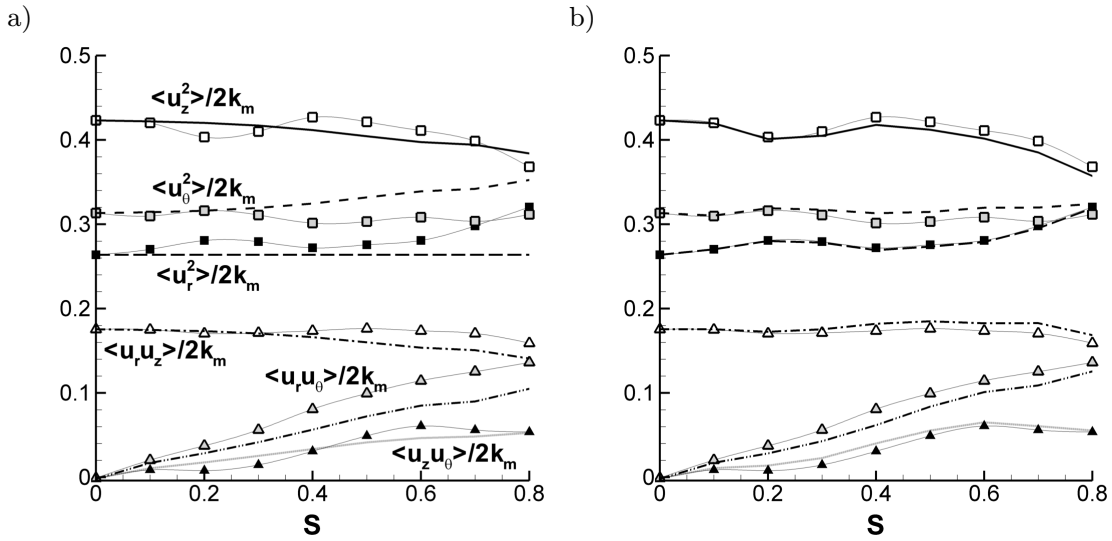

FIGURE 20. Evolution with swirl of the normalized components of the Reynolds stress tensor, which are the symbols which are labeled. In (a), the lines represent an approximation of the tensor described in section 4.4.1, while those in (b) are from section 4.4.2.

the stronger swirl induced production mechanism, which counterbalances the initial lag in the alignment of the two tensors.

4.4. *Approximation of the effects of swirl on the Reynolds stress*

In this last section, we investigate up to what extent may simplified geometrical approximations of the Reynolds stress tensor account for the experimental observations at the $r_m, z = 2$ station where the tensor has almost recovered from out of equilibrium initial conditions. We will show that the effect of swirl on the Reynolds stresses in the cylindrical coordinates can be decomposed into a geometric projection, a shear stress increase due to curvature, and an additional effect that should be accounted for.

4.4.1. *Change of coordinates for the $S = 0$ mixing layer structure*

We here attempt to reproduce the Reynolds stresses by considering a projection after a change of coordinate frame of the $S = 0$ structure, without including any of the physical effects of the swirl on the mixing layer. We introduce a local curvilinear basis $(\vec{s}, \vec{n}, \vec{b})$ attached to the principal direction of the Reynolds stress tensor, such that:

$$\vec{s} = \begin{pmatrix} \cos(\theta_1^r) \\ 0 \\ \sin(\theta_1^r) \end{pmatrix}, \tag{4.12}$$

$$\vec{n} = \vec{e}_r, \tag{4.13}$$

$$\vec{b} = \vec{s} \times \vec{n}. \tag{4.14}$$

Here, $\theta_1^r = \arctan(S_1^r)$ represents the rotation of the first eigenvector of the Reynolds stress with respect to the $\vec{e}_r = \vec{n}$ direction, see figure 14 (a). In this coordinate system, we denote the components of velocity fluctuations as u_i', with $i = s, n, b$. Let us suppose that in this coordinate system, the Reynolds stress tensor has the same structure than that of the $S = 0$ non-swirling mixing layer in which the principal direction is z. Under

this assumption,

$$\langle u_s^2 \rangle = \langle u_z^2 \rangle_{S=0}, \tag{4.15}$$

$$\langle u_n^2 \rangle = \langle u_r^2 \rangle_{S=0}, \tag{4.16}$$

$$\langle u_b^2 \rangle = \langle u_\theta^2 \rangle_{S=0}, \tag{4.17}$$

$$\langle u_n u_s \rangle = \langle u_r u_z \rangle_{S=0}, \tag{4.18}$$

$$\langle u_n u_b \rangle = \langle u_s u_b \rangle = \langle u_r u_\theta \rangle_{S=0} = \langle u_z u_\theta \rangle_{S=0} = 0. \tag{4.19}$$

The projection back to the (r, θ, z) cylindrical coordinates by means of a rotation of a $-\theta_1^r$ angle (see appendix A) provides a first approximation of the Reynolds stresses. The functions $\langle u_i u_j \rangle / 2k_m$, for $(r = r_m, z = 2)$ obtained with this model are shown in figure 20 (a). As one can see, this basic approximation correctly accounts for the decrease in $\langle u_z^2 \rangle$, but to the benefit of $\langle u_\theta^2 \rangle$, which increases, incorrectly. The increase of $\langle u_r^2 \rangle$ is not captured. Also, the projection of $\langle u_r u_z \rangle_{S=0}$ generates insufficient $\langle u_r u_\theta \rangle$ and leads to a too large decrease of $\langle u_r u_z \rangle$. Nevertheless, the $\langle u_z u_\theta \rangle$ stress is fairly reproduced.

4.4.2. *Effect of symmetric anisotropy evolution*

We now introduce in the model the changes in anisotropy described in section 4.3.3, which should improve the reconstruction. Here, we will restrict to the dominant changes, namely those that are symmetric about the $(\vec{s}, \vec{n})$ plane. In order to do so, we modify the $S = 0$ structure of the approximated Reynolds stress tensor to take into account the evolution with S of the Reynolds stress eigenvalues λ_i^r, and that of the inclination β_1^r of the principal direction in the $(\vec{s}, \vec{n})$ plane, the rest of the tensor rotating rigidly. In this model, we also suppose that $\vec{r}_3$ remains collinear to $\vec{b}$. This reconstruction should be exact for a flow which is invariant in the transverse $\vec{b}$ direction, such as a shear flow in the $(\vec{s}, \vec{n})$ plane subjected to curvature along $\vec{n}$. This leads to the following relations:

$$\langle u_s^2 \rangle = \lambda_1^r \cos^2(\beta_1^r) + \lambda_2^r \sin^2(\beta_1^r), \tag{4.20}$$

$$\langle u_n^2 \rangle = \lambda_1^r \sin^2(\beta_1^r) + \lambda_2^r \cos^2(\beta_1^r), \tag{4.21}$$

$$\langle u_b^2 \rangle = \lambda_3^r, \tag{4.22}$$

$$\langle u_n u_s \rangle = (\lambda_1^r - \lambda_2^r) \sin(\beta_1^r) \cos(\beta_1^r), \tag{4.23}$$

$$\langle u_n u_b \rangle = \langle u_s u_b \rangle = 0. \tag{4.24}$$

It is interesting to detail the evolution of $\langle u_n u_s \rangle / 2k_m$ as a function of δ_λ / r_c, the ratio of the shear thickness to the radius of curvature. The local radius of curvature r_c of the helical streamline is a simple function of S^u, the local ratio of azimuthal to axial mean velocity defined in table 3:

$$r_c = \frac{1}{2} \frac{1 + S^{u\,2}}{S^{u\,2}}. \tag{4.25}$$

In figure 21, we plot $\langle u_n u_s \rangle / 2k_m$ defined in eq. (4.23) as a function of δ_λ / r_c, and several corresponding values of S have also been marked. We can see that this anisotropy factor does not evolve until $\delta_\lambda / r_c = 0.075$. It then increases steadily until $\delta_\lambda / r_c = 0.15$, but does not rise above 0.21. This is in contrast with the linear fit of experimental results on the evolution of this anisotropy factor as a function of the curvature ratio obtained in a homogeneous shear by Holloway & Tavoularis (1992), even if a portion of our data points seems to agree with their observations. Note that Holloway & Tavoularis (1998) then proposed a geometrical interpretation of the turbulence anisotropy due to curvature, which allowed them to obtain a prediction consistent with their experimental linear fit. Their model supposes that the anisotropy increases because the Reynolds stress retains a mem-

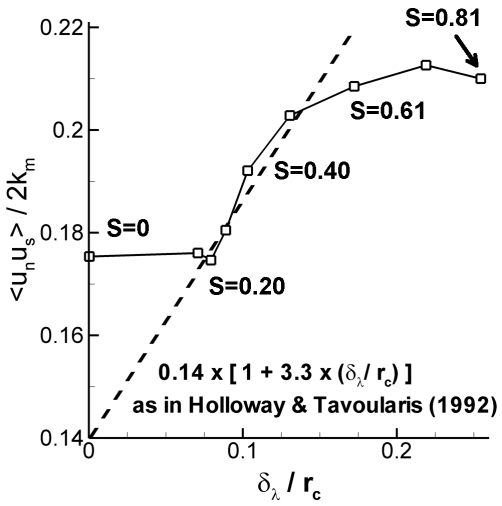

FIGURE 21. Anisotropy factor $\langle u_n u_s \rangle / 2k_m$, see eq. (4.23), as a function of the curvature parameter $\frac{\delta_\lambda}{r_c}$. The dashed line represents a fit of the experimental results gathered by Holloway & Tavoularis (1992).

ory of upstream anisotropy in fixed coordinates, while being convected along curvilinear coordinates. The present results show that such a curvature effect is not enough to fully account for the variation of $\langle u_n u_s \rangle / 2k_m$. From $S = 0$ to $S = 0.20$, it seems as if curvature was not sufficient to increase anisotropy, which is higher ($\langle u_n u_s \rangle / 2k_m = 0.175$) in the present free-shear flow than in the homogeneous shear of Holloway & Tavoularis (1992) ($\langle u_n u_s \rangle / 2k_m = 0.14$). It is only when the homogeneous shear flow anisotropy reaches the $S = 0$ value of 0.175 that anisotropy of the free-shear flow starts to increase along the experimental linear fit of Holloway & Tavoularis (1992), and no accident is observed for $S = 0.40$. Finally, there is a deviation from the linear fit beyond $\delta_\lambda / r_c = 0.15$.

Now, upon transforming the curvilinear coordinate Reynolds stresses of eqs. (4.20) to (4.24) back in cylindrical coordinates as in the above sub-section, one obtains the truncated contribution to the Reynolds stress structure shown in figure 20 (b). As can be seen, this approximation strongly improves the agreement with the full structure. Only the $\langle u_r u_\theta \rangle$ shear stress seems still significantly under-predicted. This indicates that symmetric curvature effects with respect to the transverse curvilinear direction $\vec{b}$, such as those observed in the experiment of Holloway & Tavoularis (1992), cannot explain all of the turbulent production increase. In the present case, curvature along the helical streamlines is accompanied by torsion, which represents the tendency of the flow to rotate around the streamline. The next section investigates the effect of rotation on the streamwise oriented vortices.

5. Effect of swirl on the streamwise oriented vortices

In this part, turbulence is studied from the point of view of its vortical organization. Streamwise oriented vortices will be especially considered as they are important dynamical features of shear flows where they contribute actively to entrainment (Liepmann & Gharib 1992) and to Reynolds stresses (Nickels & Marusic 2001). Their role has been evidenced in fully turbulent axisymmetric mixing layers by Citriniti & George (2000) and by Davoust *et al.* (2011). This section describes how does swirl influences streamwise vorticity. This will lead us to propose some dynamical interpretations of the Reynolds stress kinematics described in section 4.

5.1. *Diagnosis tools*

As noted by Rogers & Moin (1987), the two-point correlation of fluctuating vorticity components provides information on large scale vortical structures, while the vorticity fluctuation tensor $\langle \omega_i \omega_j \rangle$ describes small dissipative scales which dominate in the vorticity spectrum. Our objective here is to provide a dynamical interpretation of the Reynolds stresses by investigating the role of the largest vortical structures. This investigation is therefore based on the analysis of two point correlations of vorticity. Note that the Reynolds stresses can be theoretically recovered from the two point correlation of vorticity in spectral space, see Batchelor (1982). This means that the behavior of the Reynolds stress should be at least qualitatively described by that of the two-point correlation of vorticity.

Using a method described in Davoust & Jacquin (2011) we have established (Davoust 2011) that the validity of Taylor's hypothesis was degraded in the swirling jet, mainly because of the increased turbulence levels and because the azimuthal component of the convection velocity could not be determined from the HS-SPIV measurement plane. We therefore consider only the streamwise vorticity. For moderate swirl numbers, the large scale vorticity structures must remain fairly well described by this function, so let us consider the two-point correlation of the streamwise component of vorticity:

$$C_{\omega_z\omega_z}(r, r', \theta', t') = \frac{\langle \omega'_z(r, \theta, t)\omega'_z(r', \theta + \theta', t + t')\rangle_\theta}{\langle \omega'^2_z(r, \theta, t)\rangle_\theta}. \tag{5.1}$$

This function has been computed using a statistical average noted $\langle\rangle_\theta$ which includes 210 independent data blocks and all the 128 azimuthal positions θ. At $r = 0.52$ the azimuthal integral angular scale is typically 20°, so that the $\langle\rangle_\theta$ average is equivalent to nearly 2000 statistically independent samples. This provides a 95% confidence interval of ± 0.04 with a normal distribution assumption (see Benedict & Gould 1996) upon estimating this $0 \leqslant C_{\omega_z\omega_z} \leqslant 1$ function. However, an investigation of the statistical symmetries that this function should verify for $S = 0$, leads to lower 95% confidence interval, which is rather ± 0.004.

We restrict ourselves to the study of the statistical shape of vortical structures in the region where k is maximum, i.e. setting $r = 0.52$ in eq. (5.1). An example of iso-contours of $C_{\omega_z\omega_z}$ for $S = 0.6$ is plotted in figure 22. Note that the time separation t' has been replaced by a streamwise separation constructed with Taylor's hypothesis such as $z'_c = -u_c t'$, where $u_c = 0.6$ is a constant convection velocity as determined from Davoust & Jacquin (2011). No azimuthal convection convection velocity was used. As can be seen, the $C_{\omega_z\omega_z} = 0.1$ iso-contour has an ellipsoidal shape elongated in the streamwise direction and slightly inclined with a small angle (typically 20°) in the radial direction. A slight orientation in the azimuthal direction is also observed.

5.2. *Orientation and inclination angles of the vortices*

In figure 23, $C_{\omega_z\omega_z}$ is characterized by three-dimensional plots of its isovalues (figures (a) and (c)) together with streamwise-radial and streamwise azimuthal cuts (figures (b) and (d)). The presence of significant zones of negative correlation is noteworthy and will be described in the section below. Here we focus on the orientation and inclination of the positive contours. As summarized by Townsend (1980), the dynamics of vortical structures in a shear flow involves the production of vorticity in the positive eigen-direction of the symmetric part of the mean velocity gradient (strain tensor), and a tilting of the structure away from this maximum production direction due to the antisymmetric part of the mean velocity gradient (rotation tensor).

We define the inclination angle β^ω in figure 23 (b) as the angle made by positive

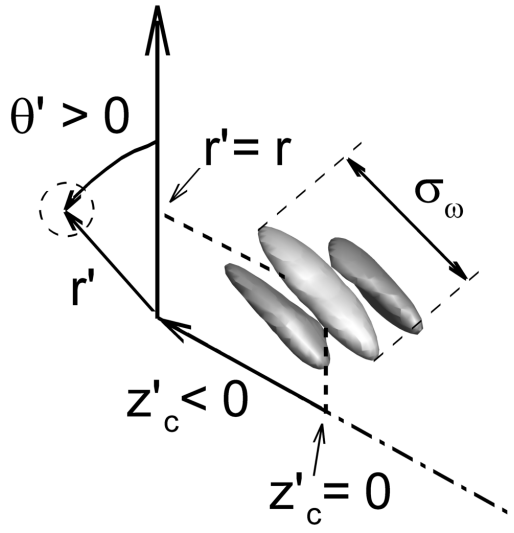

FIGURE 22. Sketch of the coordinate system used to describe the two-point correlation $C_{\omega_z\omega_z}$ as defined in eq. (5.1). The reference probing point lies at $(r' = r, \theta' = 0, z'_c = 0)$, and here $r = 0.52$. The function is then statistically constructed with the (r', θ', z'_c) separation (location of the dashed circle). The iso-contours that are represented correspond to $S = 0.6$, $C_{\omega_z\omega_z} = 0.1$ (light gray) and $C_{\omega_z\omega_z} = -0.1$ (dark gray). A characteristic spatial coherence length scale σ_ω is also introduced.

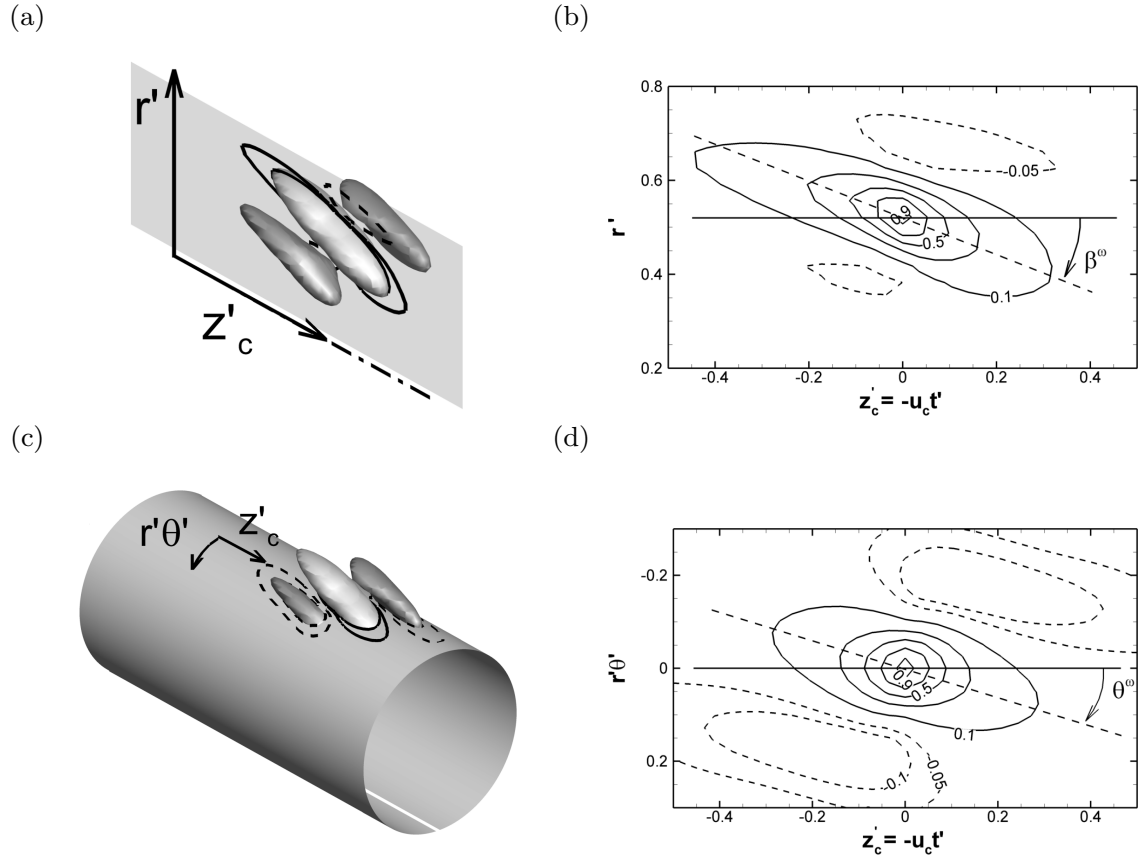

FIGURE 23. Cuts of the streamwise vorticity auto-correlation $C_{\omega_z\omega_z}$ defined in eq. (5.1). (a): Sketch of a cut in (r', z'_c) cross-sections for $\theta' = 0$. (b): Contours in this plane for $S = 0.6$. Note the definition of the projected inclination angle β^p_ω. (c): Sketch of a cut in $(r'\theta', z'_c)$ cross-sections for $r' = r$. (d): Contours in this plane for $S = 0.6$. Note the definition of the orientation angle θ_ω.

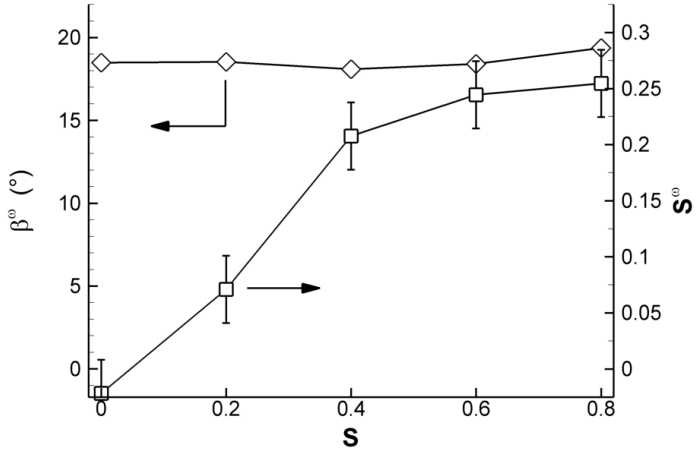

FIGURE 24. Evolution with swirl of the inclination angles β_ω (left scale) and the orientation parameter S_ω (right scale) defined in the text.

contours of the two point correlation in the streamwise-radial plane with respect to the streamwise axis. We also define the tilting angle θ^ω of the correlation ellipsoid in the streamwise-azimuthal plane in figure 23 (d). Note that $\beta^\omega = 45°$ would correspond to vortical structures aligned with the principal direction of strain tensor. As can be seen in figure 24, the value of β^ω corresponding to $S = 0$ is slightly smaller than 20°. Rogers & Moin (1987) found a similar value in their DNS of homogeneous shear flow. Following these authors, this corresponds to an equilibrium between production of new structures along the 45° direction and the accumulated rotation of older structures. Figure 24 proves that swirl leaves this inclination angle almost unaffected. Thus, surprisingly, streamline curvature, which imposes a rotation rate in the opposite direction to that of the mean shear when following a streamline, has a poor impact on the inclination angle. This means that the increased production of turbulence with swirl in not attributable to a better alignment of the vortical structures with the strain tensor, as could have been expected.

From the orientation angle θ^ω (figure 23(d)), we construct the orientation parameter $S^\omega = \tan(\theta^\omega)$. This parameter, plotted in figure 24 is analogous to a swirl number and it describes the tendency of vortical structures to follow the mean flow. However its interpretation must account for the absence of azimuthal convection velocity in the spatial reconstruction. Suppose that the streamwise vortices are aligned in the direction of the mean flow and are convected in the same direction, the present spatial reconstruction would give $S^\omega = 0$ since the structures would intersect the $z = 2$ measurement plane in a single point. Therefore, in figure 24, the fact that S^ω increases with S indicates that the streamwise vortices are not statistically aligned in the direction of the convection velocity and that they tend to be more rotated by swirl than the latter. This does not lead to an increase alignment between the strain and the Reynolds stress tensors, therefore, we can see that inclination and the orientation of the streamwise vortices does not account for the evolution of the Reynolds stresses. The next section which analyses the organization of negative contours of $C_{\omega_z\omega_z}$ allows us to propose an alternative explanation.

5.3. *Organization into contra-rotating pairs*

In the iso-contours presented in figure 22, and in the successive cuts presented in figure 23, one notes the presence of negative correlation values. These appear as two additional ellipsoidal shapes placed besides the ellipsoidal positive iso-contours. It is convenient to describe these negative correlation by considering the $(r', r'\theta')$ planes. This is shown in

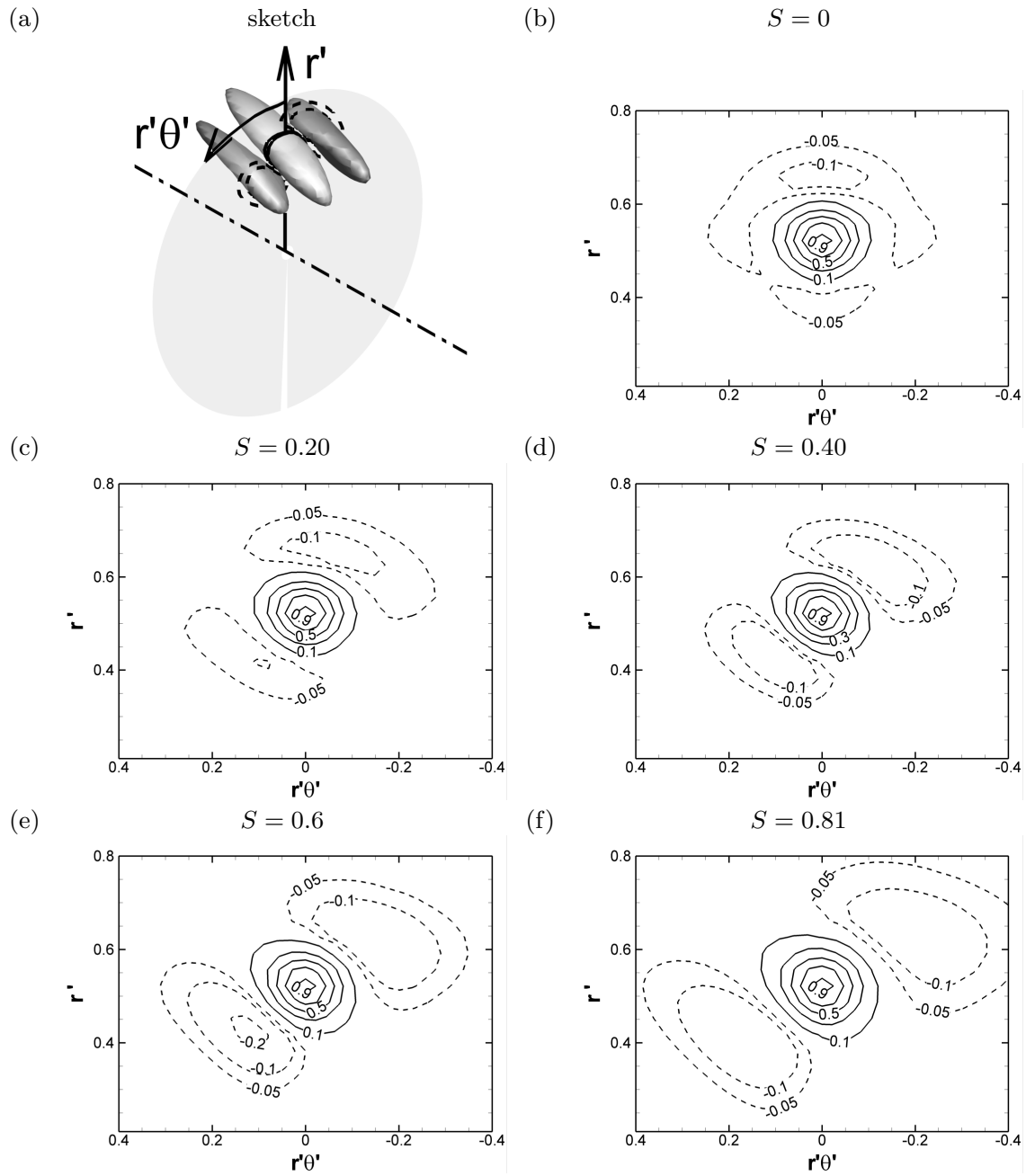

FIGURE 25. Streamwise vorticity auto-correlation $C_{\omega_z\omega_z}$ defined in eq. (5.1). (a): Three-dimensional representation with a cut in $(r', r'\theta')$ cross-sections for $t' = 0$ and $S = 0.6$. In this plane, contours are shown for $S = 0$ (b), $S = 0.20$ (c), $S = 0.40$ (d), $S = 0.61$ (e) and $S = 0.81$ (f).

figure 25 for various values of S. The zones of negative correlation represent the statistical organization of opposite vorticity.

The organization of the zones of negative correlation for $S = 0$ was explained in Davoust *et al.* (2011). In a non-swirling jet, the trace of azimuthally arranged vortex pairs separated by a distance Δ, such as those described by Martin & Meiburg (1991); Liepmann & Gharib (1992), among others, would imply that the zones of negative correlation be located symmetrically around the probing point at $(r'\theta' = \pm\Delta, r' = r)$ in figure 25 (b). However, we observe that the zones of negative correlation are rather radially located above and below the probing location. In this study, the mechanism which produces this organization was shown to result from an interaction between streamwise

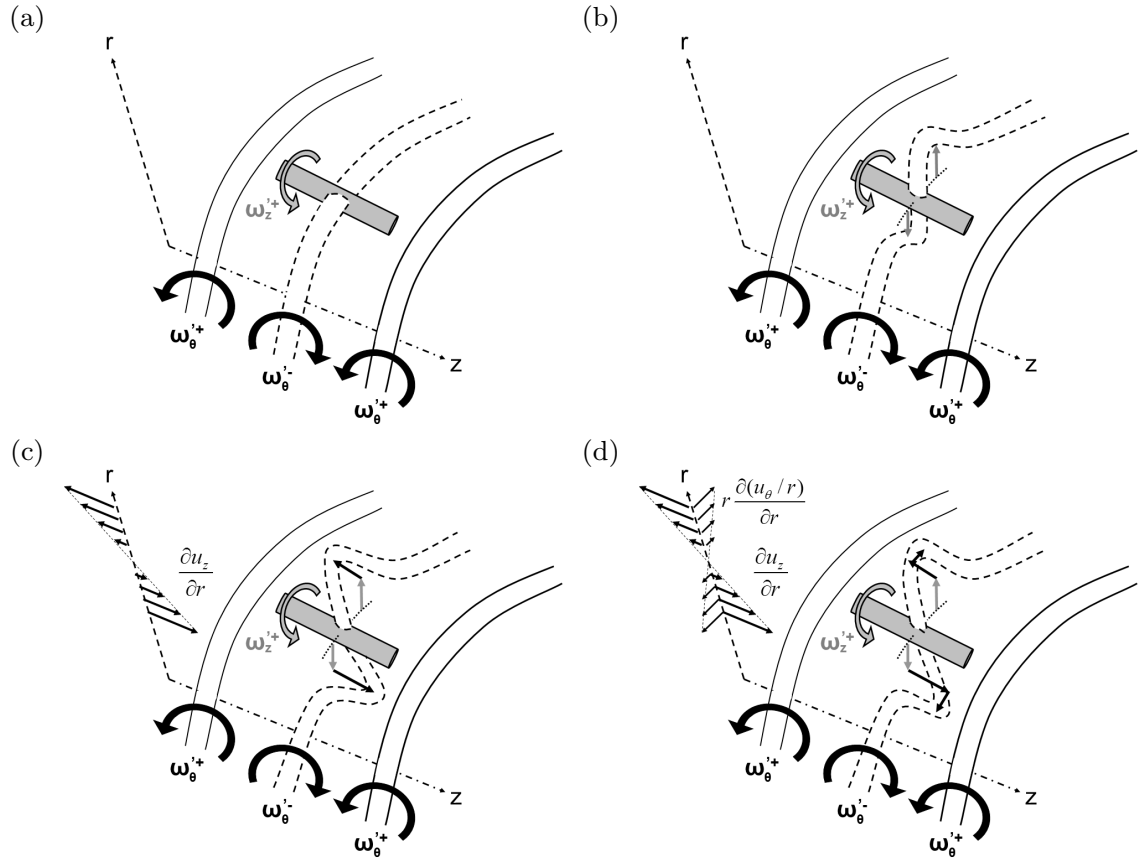

FIGURE 26. Mechanism accounting for the generation of opposite sign streamwise vorticity as proposed in Davoust *et al.* (2011) for $S = 0$. (a): initial most probable position of a streamwise vortex with respect to an $m = 0$ mode. (b): tilting of the negative azimuthal vorticity of the $m = 0$ mode by the streamwise vortex. (c) tilting and stretching of the deformed ring by the shear from the axial velocity for $S = 0$. Adding swirl: (d) tilting and stretching of the deformed ring by the mean shear including shear from the azimuthal velocity for $S \neq 0$.

vortices and large scale $m = 0$ and $m = \pm 1$ fluctuations. Streamwise vortices are preferentially known to be located in the braid region (see, e.g. Citriniti & George 2000), which is the zone located between two consecutive vorticity $m = 0$ rings, see figure 26 (a). In this region the vorticity perturbation corresponding to the $m = 0$ mode is azimuthal (rings) and negative. For $S = 0$, the magnitude of vorticity which corresponds to streamwise vortices ($\omega'_z \approx 2.5$) is well above the azimuthal vorticity perturbations linked to the $m = 0$ rings ($\omega'_{\theta,m=0} \approx 0.6$). In the braid region, the streamwise vortex therefore tilts the negative $m = 0$ vorticity and produces radial vorticity fluctuations, see figure 26 (b). This radial vorticity is then tilted and stretched by the mean shear the streamwise vortex, which produces streamwise vorticity of opposite sign located below and above, as in figure 26 (c). This mechanism accounts for the position of contours of negative correlation in figure 25 for $S = 0$. As can be seen in figure 25, for the swirling jet, the radial organization of the negative contours is rotated. This is attributed to a last mechanism depicted in figure 26 (d), which is introduced by the swirl, namely the differential convection by the mean azimuthal velocity. The tilting of the radial vorticity into streamwise vorticity occurs in the azimuthal direction, as depicted in 26 (d), which explains the increasing tilting.

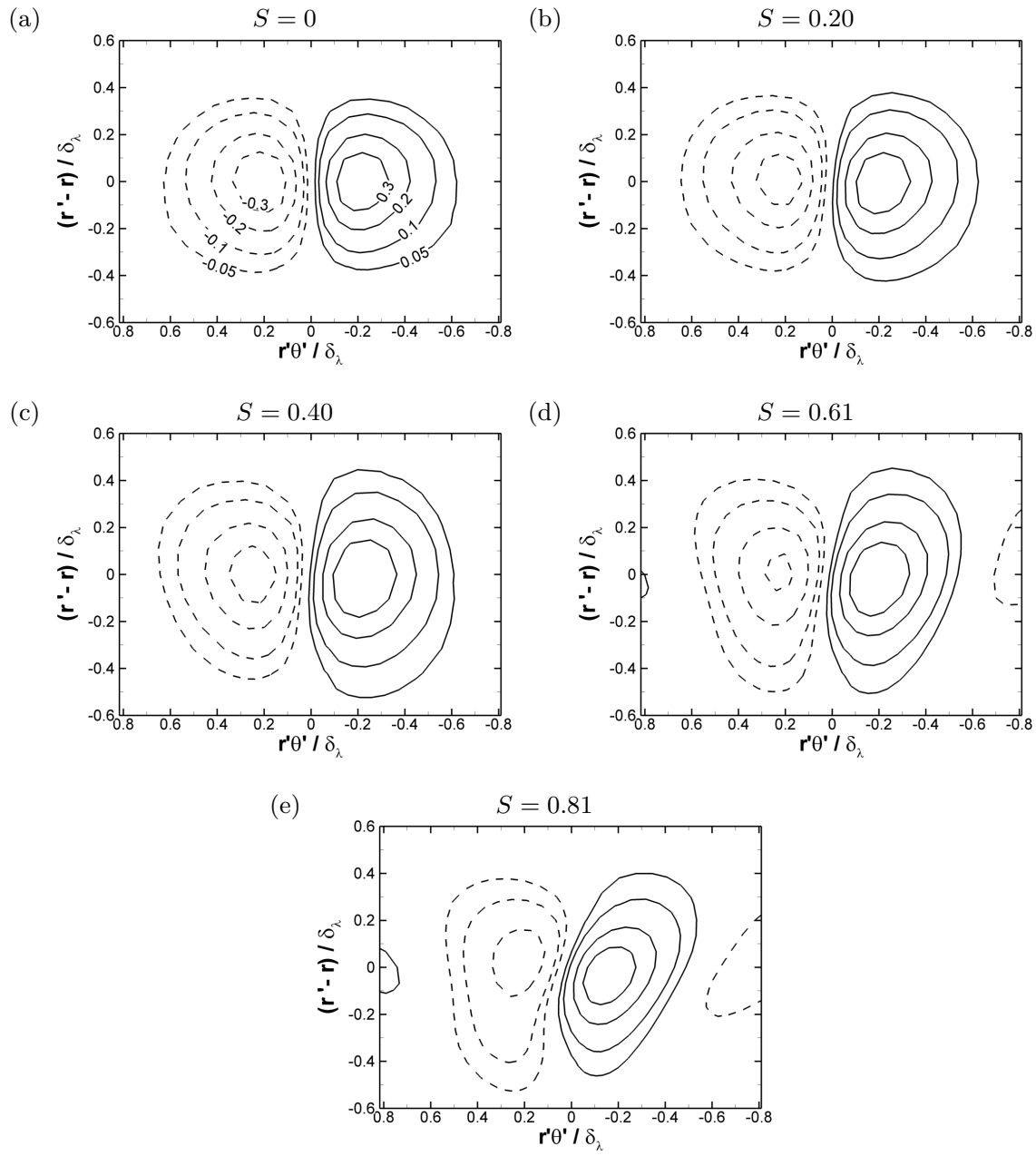

FIGURE 27. Cuts of the streamwise vorticity auto-correlation $C_{\omega_z u_z}$ defined in eq. (5.2), in $(r', r'\theta')$ cross-sections for $t' = 0$. In this plane, contours are shown for $S = 0$ (a), $S = 0.20$ (b), $S = 0.40$ (c), $S = 0.61$ (d) and $S = 0.81$ (e).

5.4. *Effect of swirl on the mixing capacity of streamwise vortices*

As discussed in the beginning of this section 5.1, the increased turbulence production capacity (disregarding initial condition effects) of the swirling mixing layer is expected to result from modifications in the vortical organization, here described with two-point statistics. However the orientation of the positive contours of the two-point correlations of streamwise vorticity investigated in section 5.2, did not reveal a mechanism that explained the increase in production. This led us to study the negative correlations. We have then observed in figure 25 how does swirl rotates the orientation of this vortex "triplet". We will now show that it is this last mechanism which is responsible for an increase in the capacity to produce mixing between the core and the exterior, through of a more favorable orientation. For this purpose, we consider the two-point correlations between

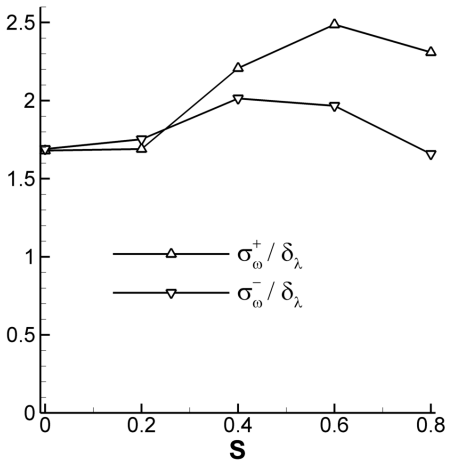

FIGURE 28. Evolution with swirl of the spatial coherence scale of the positive (σ_ω^+) and negative (σ_ω^-) streamwise vorticity fluctuations.

streamwise vorticity and streamwise velocity fluctuations:

$$C_{\omega_z u_z}(r, r', \theta', t') = \frac{\langle \omega_z'(r, \theta, t) u_z'(r', \theta + \theta', t + t') \rangle_\theta}{\langle \omega_z'^2(r, \theta, t) \rangle_\theta^{1/2} \langle u_z'^2(r, \theta, t) \rangle_\theta^{1/2}}. \tag{5.2}$$

The function is shown in figure 27 for different values of S, and the coordinates have been normalized by the thickness δ_λ. Its contours give a measure of the mixing capacity of the vortical organization. Indeed, the negative and positive contours of the figure represent negative and positive streamwise velocity fluctuations being transported inside and outside the mixing layer by the vortex. As can be noted in the evolution from figure 27 (a) to (d), the correlation contours have a greater radial extent as swirl is increased, and this holds for $S = 0.40$. This allows the streamwise vortices to radially transport fluid which is located deeper in the jet core. We attribute this to the increase in the rotation of the vortex array with swirl away from the radial direction, as observed in figure 26, since it leads to a greater contribution to mixing from the opposite signed vortices. If mixing is increased, so should be the Reynolds shear stresses. Also, the tilting angle β_3^r of the third eigenvalue of the Reynolds stress tensor described in section 4.3.3 may result from transverse fluctuation in a tilted direction resulting from the tilted positive/negative vortex organization. Note that the tilting angle evolves in a similar manner as β_3^r, increasing with swirl until $S \approx 0.4$. The tilting of the vortex pair therefore accounts for changes in the Reynolds stresses.

5.5. *Evolution of the spatial coherence*

The spatial length of iso-contours sketched in figure 22 may be characterized by the distance σ_ω between two points lying on the surface defined as an iso-contour of the correlation function. Here, this scale is based on the 0.1 iso-contour. Also, the correlation function is now conditioned with the sign of streamwise vorticity fluctuations, so that σ_ω^+ and σ_ω^- are length scales which characterize positive and negative streamwise vorticity fluctuations. Figure 28 shows the evolution of σ_ω^+ and σ_ω^- as a function of swirl. Note that they have been normalized by the total shear thickness δ_λ, defined in section 4.3.2. As can be seen in figure 28, on the whole the length scales increase from 1.5 to 2 from $S = 0.20$ to $S = 0.61$, and slightly decrease for $S = 0.81$. Note that saturation of a quantity that initially increases with swirl above $S = 0.61$ is a common feature in this experiment: it has been observed for the local swirl S^u (section 4.3.2) and for the local anisotropy of the Reynolds stress $\langle u_n u_s \rangle$ (figure 21). This is characteristic of the

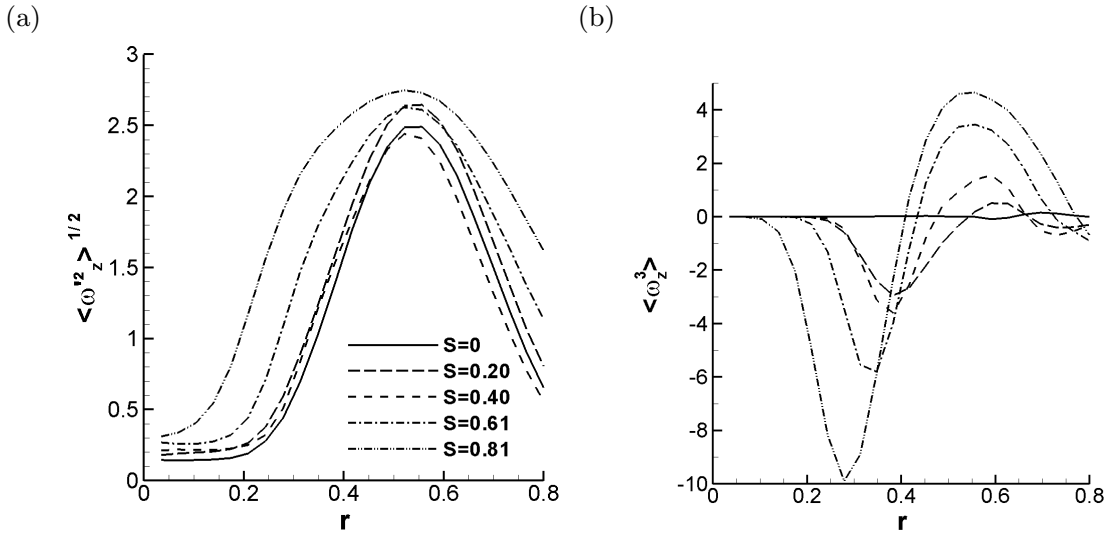

FIGURE 29. (a): Radial profile of $\langle\omega_z^2\rangle^{1/2}$ at $z = 2$ for different values of S. (c): Profile of $\langle\omega_z^3\rangle$

transition from a thin axisymmetric mixing-layer to a fully developed flow, here observed at a fixed position $z = 2$ as S increases. More importantly, one can observe that swirl breaks the symmetry between σ_ω^+ and σ_ω^-. This is consistent with the promotion of long cyclonic structures (positive streamwise vorticity) to the detriment of anticyclonic ones (negative streamwise vorticity), which is commonly observed in rotating systems, such as rotating homogeneous turbulence experiments (Hopfinger *et al.* 1982). Here, it means that the increased coherence of streamwise vortices, which can also account for the increased anisotropy of the Reynolds stress tensor, is mostly carried by positive streamwise vortices. The next section presents an investigation of this symmetry breaking.

5.6. *Second and third order moments of streamwise vorticity*

5.6.1. *Observations*

First, let us consider the streamwise vorticity fluctuation rms. Figure 29 shows radial profiles of second and third order moments obtained with the HS-SPIV data. The statistical average includes $N_b = 210$ blocks and $N_{\text{ech}} = 256$ samples in each bloc as well as a 2π azimuthal integral. An estimation of the azimuthal and temporal integral length scales shows that this represents nearly 40000 statistically independent samples. We have performed a convergence study to be sure that the statistical quantities that are presented in this section are fully converged. In figure 29 (a), the peak rms of streamwise vorticity varies slightly with the swirl number, and the radial extent of the profile increases for $S \geqslant 0.61$, which is consistent with the profiles of Reynolds stresses shown in figure 13. We now investigate the occurrence of positive versus negative streamwise vortices through the one-point triple correlation of streamwise vorticity $\langle\omega_z^3\rangle$. This is a key quantity in many studies on rotating homogeneous turbulence, where the balance between cyclonic and anticyclonic vortices if of particular importance regarding the transition from fully 3D to nearly 2D turbulence (see, e.g. Bartello *et al.* 1994; Staplehurst *et al.* 2008; Moisy *et al.* 2010). The radial profile of $\langle\omega_z^3\rangle$ and its evolution with swirl is reported in figure 29 (b). One can notice that for all values of swirl, the center of the mixing layer promotes positive streamwise vortices, as could be expected. The skewness factor $\langle\omega_z^3\rangle/\langle\omega_z^2\rangle^{3/2}$, which increases with swirl, reaches nearly 0.25 for $S = 0.81$ at $r = 0.52$. Even higher values may be reached in decaying rotating turbulence experiments (Moisy *et al.* 2010). In contrast, the strong skewness negative levels that may be observed near $r = 0.35$, in

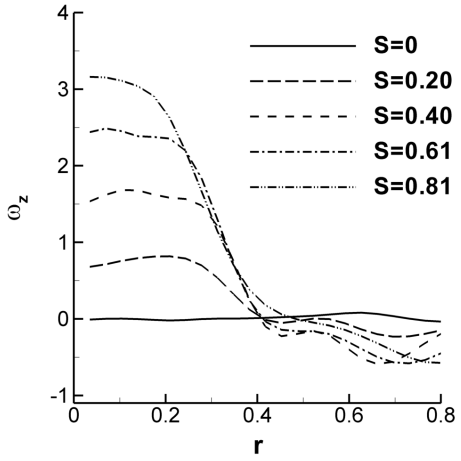

FIGURE 30. Mean streamwise vorticity ω_z as a function of S.

the intermediate region between the jet core and the mixing layer, cannot be explained by a promotion of cyclonic streamwise vorticity. The object of the next sub-section is to provide an interpretation of this phenomenon.

5.6.2. *Production of $\langle\omega_z^3\rangle$ in the presence of rotation*

The governing equation for $\langle\omega_z'^3\rangle$ which is derived in appendix B writes:

$$\frac{D}{Dt}\langle\omega_z'^3\rangle = \underbrace{-3\frac{u_\theta}{r}\langle\frac{\partial}{r\partial\theta}u_\theta'\omega_z'^2\rangle}_{T_1}\underbrace{-3\langle\omega_z'^2u_r'\rangle\frac{\partial}{\partial r}\omega_z}_{T_2}\underbrace{+3\omega_\theta\langle\omega_z'^2\frac{\partial}{\partial z}u_\theta'\rangle}_{T_3}\underbrace{+3\omega_z\langle\omega_z'^2\frac{\partial}{\partial z}u_z'\rangle}_{T_4}+T_{\omega_z'^3}. \tag{5.3}$$

We here made a focus on the production terms noted T_1 to T_4 which include the dominant mean flow gradients. The term noted $T_{\omega_z'^3}$ contains higher order terms. Unfortunately, because of the indetermination in the Taylor's hypothesis discussed in section 5.1, we could not compute all the terms of eq. 5.3 except T_2. We now show that this term which can be considered as the work of a radial transport of streamwise enstrophy against a mean vorticity gradient, may account for the negative peak of $\langle\omega_z^3\rangle$ near $r = 0.35$. As can be seen in eq. (5.3), this term is the product of a radial velocity fluctuation-streamwise enstrophy correlation with a mean vorticity gradient. The mean streamwise vorticity is plotted in figure 30. One can see that the mean streamwise vorticity is a constant $\omega_z \approx 4S$ in the jet core and decreases quickly towards slightly negative values at the center of the mixing layer: thus $\partial\omega_z/\partial r < 0$ near $r = 0.35$. The streamwise entrophy-radial velocity fluctuation correlation $\langle u_r'\omega_z'^2\rangle$ is plotted in figure 31 (a). This profile has a general form similar to other radial transport terms in free shear layers such as radial transport of kinetic energy fluctuations (Pope 2008): $\langle u_r'\omega_z'^2\rangle < 0$ near $r = 0.35$. Therefore, one can see that T_2, defined in eq. (5.3) should be negative in a region between the jet core and the center of the mixing layer, thereby producing negative $\langle\omega_z^3\rangle$. Although the other production terms must be considered, the similar location of strong negative production by T_2 with the strong negative peak of $\langle\omega_z^3\rangle$ profile displayed in figure 31 (b) is an indication that T_2 could be at the origin of this negative skewness. This can be interpreted as a consequence of the radial transport of streamwise enstrophy fluctuations away from the center of the mixing layer. Indeed, using a Langragian approach, one can show that when a streamwise vortex is displaced by δ_r to a zone where the angular velocity is different, conservation of total angular momentum imposes ω_z' to vary by $-\delta_r\frac{\partial\omega_z}{\partial r}$. Because of the

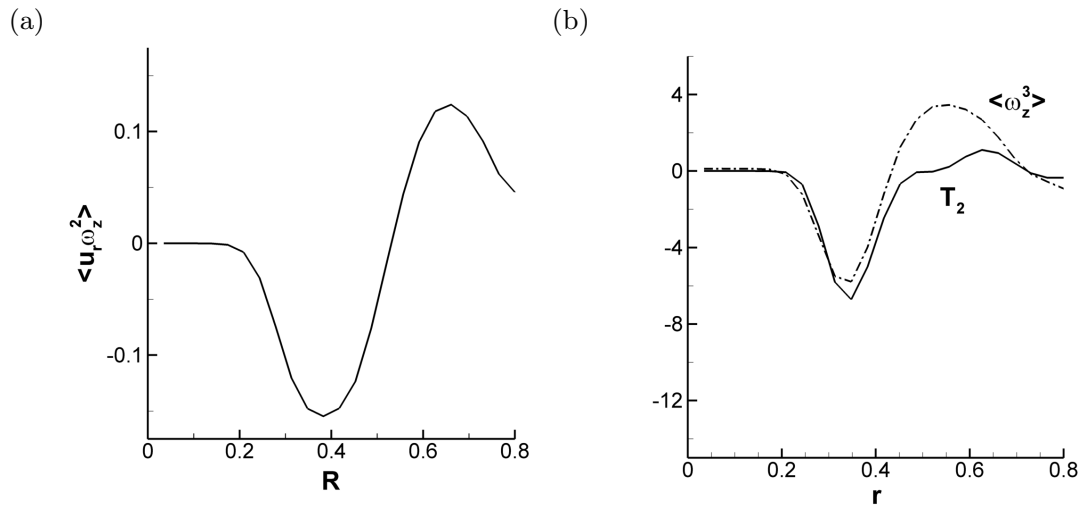

FIGURE 31. (a): Radial velocity fluctuation-streamwise enstrophy correlation $\langle u_r' \omega_z'^2 \rangle$ for $S = 0.61$. (b): Production terms T_2 in eq. (5.3) of the triple correlation of streamwise vorticity $\langle \omega_z'^3 \rangle$, compared to the profile of $\langle \omega_z'^3 \rangle$ itself for $S = 0.61$.

inhomogeneous character of the flow, radial transport of streamwise vorticity therefore favors stronger negative streamwise vorticity fluctuation.

We now seek to identify the terms responsible for positive $\langle \omega_z^3 \rangle$ at the center of the mixing-layer. The term labeled $T_4 = 3\omega_z \langle \omega_z'^2 \frac{\partial}{\partial z} u_z' \rangle$ in eq. (5.3) is analogous to a term obtained by Gence & Frick (2001) in the analysis of the evolution of third order moments of vorticity fluctuations in an initially homogeneous turbulent flow, set in solid body rotation. Since streamwise stretching is a production term for streamwise vorticity, the correlation $\langle \omega_z^2 \frac{\partial u_z'}{\partial z} \rangle$ should be positive. These authors concluded that while one point second order moments were initially unaffected, third order moments are subjected to a linear vortex stretching mechanism induced by rotation. The present laboratory reference frame is non-rotating, but we can see that the rotating mean flow plays a similar role. However in the present flow, since $\omega_z < 0$ at the center of the mixing layer, the T_4 term should produce anticyclonic vorticity. Therefore in this region, the production of cyclonic vorticity remains to be explained.

6. Conclusions

The near field of a turbulent swirling jet has been described using stereo PIV monitoring the growth of the axisymmetric mixing layer along with a cross-sectional high-speed stereo PIV plane located two jet diameters downstream of the jet exit. The swirl number has been varied in the range $0 \leqslant S \leqslant 0.81$. The growth rate and the intensity of turbulence increase with swirl, except for a profound accident centered around $S = 0.40$. Production of turbulent kinetic energy has been analyzed by considering the alignment between the strain tensor and the Reynolds stress tensor, which increases with swirl. We have detailed how the initial conditions arising from the boundary layer in the exit plane were responsible for the $S = 0.40$ accident. This effect was isolated by considering the evolution of a local curvilinear primary shear stress anisotropy factor, which was found to be monotonous with swirl. This means that the lower intensity of turbulence observed at $z = 2$ for $S = 0.40$ is a consequence of the recovery from a perturbed initial condition, and not due to the structure of turbulence at $z = 2$ itself. A supplementary curvilinear secondary shear stress should also be considered to account for full behavior of the Reynolds stress tensor.

The structure of the two-point correlations of streamwise vorticity has been studied in an effort to explain the behavior of the Reynolds stresses. We have identified a characteristic organization of opposite signed vorticity which is rotated by swirl and this tends to increase transport of axial momentum and thus explains the additional Reynolds stresses. Again, no sign of a specific behavior for $S = 0.40$ was observed in the structure of two-points correlations. The sign of streamwise vorticity fluctuations has been investigated through sign conditioned statistics such as $\langle \omega_z^3 \rangle$. The predominance of positive skewness at the center of the mixing layer could not be explained, but a mechanism to account for the strong negative skewness observed in the region between the mixing layer and the jet core has been proposed. Further studies, using high-speed Volumetric PIV or detailed numerical simulations, would be necessary to verify this mechanism and identify the production terms of $\langle \omega_z^3 \rangle$ responsible for the positive skewness at the center of the mixing layer.

Appendix A. Change of coordinates for Reynolds stress tensor

The following transformation is used to determine the correspondance between Reynolds stres tensor components expressed in the cylindrical (r, θ, z) coordinate frame and in the (s, n, b) coordinates frame. This is obtained by a $-\theta$ rotation about the r-axis of the cylindrical coordinates. In the article, the particular value of θ is set to $\theta = \theta_1^r = \arctan(S_1^r)$ (section 4.3.1, table 3 and section 4.3.4).

$$\langle u_z^2 \rangle = \langle u_s^2 \rangle \cos^2(\theta) + \langle u_b^2 \rangle \sin^2(\theta) - 2\langle u_s u_b \rangle \sin(\theta)\cos(\theta) \tag{A 1}$$

$$\langle u_r^2 \rangle = \langle u_n^2 \rangle \tag{A 2}$$

$$\langle u_\theta^2 \rangle = \langle u_s^2 \rangle \sin^2(\theta) + \langle u_b^2 \rangle \cos^2(\theta) + 2\langle u_s u_b \rangle \sin(\theta)\cos(\theta) \tag{A 3}$$

$$\langle u_r u_z \rangle = \langle u_n u_s \rangle \cos(\theta) + \langle u_n u_b \rangle \sin(\theta) \tag{A 4}$$

$$\langle u_r u_\theta \rangle = \langle u_n u_s \rangle \sin(\theta) + \langle u_n u_b \rangle \cos(\theta) \tag{A 5}$$

$$\langle u_\theta u_z \rangle = (\langle u_s^2 \rangle - \langle u_n^2 \rangle) \sin(\theta)\cos(\theta) \tag{A 6}$$

Appendix B. Governing equation for $\langle \omega_z'^3 \rangle$

In the following, the instantaneous value of a quantity is noted $\tilde{a}$, the statistical average is noted $a = \langle \tilde{a} \rangle$, and the instantaneous fluctuation is note $a' = \tilde{a} - a$. The equation governing evolution of the instantaneous streamwise vorticity $\tilde{\omega}_z$ in cylindrical coordinates writes:

$$\frac{\partial}{\partial t}\tilde{\omega}_z + \tilde{u}_z \frac{\partial}{\partial z}\tilde{\omega}_z + \tilde{u}_r \frac{\partial}{\partial r}\tilde{\omega}_z + \frac{\tilde{u}_\theta}{r}\frac{\partial}{\partial \theta}\left(\tilde{\omega}_z + \frac{\tilde{u}_\theta}{r}\right) = \tilde{\omega}_r \frac{\partial}{\partial r}\tilde{u}_z + \frac{\tilde{\omega}_\theta}{r}\frac{\partial}{\partial \theta}\tilde{u}_z + \tilde{\omega}_z \frac{\partial}{\partial z}\tilde{u}_z. \tag{B 1}$$

Note that the viscous diffusion term has been omitted. The equation governing the mean streamwise vorticity ω_z is obtained by applying the $\langle\rangle$ ensemble average to eq. (B 1). Making use of the statistical axisymmetry, one obtains:

$$\begin{aligned} &u_z \frac{\partial}{\partial z}\omega_z + u_r \frac{\partial}{\partial r}\omega_z + \langle u_z' \frac{\partial}{\partial z}\omega_z' \rangle + \langle u_r' \frac{\partial}{\partial r}\omega_z' \rangle + \langle \frac{u_\theta'}{r}\frac{\partial}{\partial \theta}\left(\omega_z' + \frac{u_\theta'}{r}\right) \rangle = \\ &\omega_r \frac{\partial}{\partial r}u_z + \omega_z \frac{\partial}{\partial z}u_z + \langle \omega_r' \frac{\partial}{\partial r}u_z' \rangle + \langle \frac{\omega_\theta'}{r}\frac{\partial}{\partial \theta}u_z' \rangle + \langle \omega_z' \frac{\partial}{\partial z}u_z' \rangle. \end{aligned} \tag{B 2}$$

Subtacting eq. (B 2) from eq. (B 1) gives the evolution equation for the streamwise vorticity fluctuation ω_z':

$$\begin{aligned}
&\frac{\partial}{\partial t}\omega_z' + u_z\frac{\partial}{\partial z}\omega_z' + u_r\frac{\partial}{\partial r}\omega_z' + \frac{u_\theta}{r}\frac{\partial}{\partial\theta}\left(\omega_z' + \frac{u_\theta'}{r}\right) + u_z'\frac{\partial}{\partial z}\omega_z + u_r'\frac{\partial}{\partial r}\omega_z + \\
&u_z'\frac{\partial}{\partial z}\omega_z' + u_r'\frac{\partial}{\partial r}\omega_z' + \frac{u_\theta{}'}{r}\frac{\partial}{\partial\theta}\left(\omega_z' + \frac{u_\theta'}{r}\right) - \\
&\left(\langle u_z'\frac{\partial}{\partial z}\omega_z'\rangle + \langle u_r\frac{\partial}{\partial r}\omega_z\rangle + \langle\frac{u_\theta'}{r}\frac{\partial}{\partial\theta}\left(\omega_z' + \frac{u_\theta'}{r}\right)\rangle\right) \\
=\ &\\
&\omega_r\frac{\partial}{\partial r}u_z' + \frac{\omega_\theta}{r}\frac{\partial}{\partial\theta}u_z' + \omega_z\frac{\partial}{\partial z}u_z' + \omega_r'\frac{\partial}{\partial r}u_z + \omega_z'\frac{\partial}{\partial z}u_z + \\
&\omega_r'\frac{\partial}{\partial r}u_z' + \frac{\omega_\theta'}{r}\frac{\partial}{\partial\theta}u_z' + \omega_z'\frac{\partial}{\partial z}u_z' - \\
&\left(\langle\omega_r'\frac{\partial}{\partial r}u_z'\rangle + \langle\frac{\omega_\theta'}{r}\frac{\partial}{\partial\theta}u_z'\rangle + \langle\omega_z'\frac{\partial}{\partial z}u_z'\rangle\right).
\end{aligned} \tag{B 3}$$

The equation governing $\langle\omega_z'^3\rangle$ is obtained by multiplying eq. (B 3) by $3\omega_z'^2$ before ensemble averaging. Denoting $\frac{D}{Dt} = u_z\frac{\partial}{\partial z} + u_r\frac{\partial}{\partial r}$, one gets:

$$\begin{aligned}
&\frac{D}{Dt}\langle\omega_z'^3\rangle + 3\frac{u_\theta}{r}\langle\frac{\partial}{\partial\theta}\left(\frac{u_\theta'}{r}\right)\omega_z'^2\rangle + 3\langle\omega_z'^2u_z'\rangle\frac{\partial}{\partial z}\omega_z + 3\langle\omega_z'^2u_r'\rangle\frac{\partial}{\partial r}\omega_z + \\
&3\langle\omega_z'^2u_z'\frac{\partial}{\partial z}\omega_z\rangle + 3\langle\omega_z'^2u_r'\frac{\partial}{\partial r}\omega_z'\rangle + 3\langle\omega_z'^2\frac{u_\theta}{r}\frac{\partial}{\partial\theta}\left(\omega_z' + \frac{u_\theta'}{r}\right)\rangle - \\
&3\langle\omega_z'^2\rangle\left(\langle u_z'\frac{\partial}{\partial z}\omega_z'\rangle + \langle u_r'\frac{\partial}{\partial r}\omega_z'\rangle + \langle\frac{u_\theta'}{r}\frac{\partial}{\partial\theta}\left(\omega_z' + \frac{u_\theta'}{r}\right)\rangle\right) \\
=\ &\\
&3\omega_r\langle\omega_z'^2\frac{\partial}{\partial r}u_z'\rangle + 3\frac{\omega_\theta}{r}\langle\omega_z'^2\frac{\partial}{\partial\theta}u_z'\rangle + 3\omega_z\langle\omega_z'^2\frac{\partial}{\partial z}u_z'\rangle + 3\langle\omega_z'^2\omega_r'\rangle\frac{\partial}{\partial r}u_z + 3\langle\omega_z'^3\rangle\frac{\partial}{\partial z}u_z + \\
&3\langle\omega_z'^2\omega_r'\frac{\partial}{\partial r}u_z'\rangle + 3\langle\omega_z'^2\frac{\omega_\theta'}{r}\frac{\partial}{\partial\theta}u_z'\rangle + 3\langle\omega_z'^3\frac{\partial}{\partial z}u_z'\rangle - \\
&3\langle\omega_z'^2\rangle\left(\langle\omega_r'\frac{\partial}{\partial r}u_z'\rangle + \langle\frac{\omega_\theta'}{r}\frac{\partial}{\partial\theta}u_z'\rangle + \langle\omega_z'\frac{\partial}{\partial z}u_z'\rangle\right).
\end{aligned} \tag{B 4}$$

We now denote by $T_{\omega_z'^3}$ the terms comprising the fourth order moments and the product of second order moments, and focus on the production terms involving the mean flow. Also, we suppose that the flow spreads slowly in the z direction so that $\omega_r << \omega_z \approx \omega_\theta$, $\frac{\partial u_z}{\partial z} << \frac{\partial u_z}{\partial r}$ and $\frac{\partial\omega_z}{\partial z} << \frac{\partial\omega_z}{\partial r}$. This reduces eq. (B 4) to:

$$\begin{aligned}
\frac{D}{Dt}\langle\omega_z'^3\rangle = &-3\frac{u_\theta}{r}\langle\frac{\partial}{\partial\theta}\left(\frac{u_\theta'}{r}\right)\omega_z'^2\rangle - 3\langle\omega_z'^2u_r'\rangle\frac{\partial}{\partial r}\omega_z \\
&+ 3\frac{\omega_\theta}{r}\langle\omega_z'^2\frac{\partial}{\partial\theta}u_z'\rangle + 3\omega_z\langle\omega_z'^2\frac{\partial}{\partial z}u_z'\rangle + 3\langle\omega_z'^2\omega_r'\rangle\frac{\partial}{\partial r}u_z \\
&+ T_{\omega_z'^3},
\end{aligned} \tag{B 5}$$

which may be re-arranged into:

$$\frac{D}{Dt}\langle\omega_z'^3\rangle = -3\frac{u_\theta}{r}\langle\frac{\partial}{\partial\theta}\left(\frac{u_\theta'}{r}\right)\omega_z'^2\rangle - 3\langle\omega_z'^2 u_r'\rangle\frac{\partial}{\partial r}\omega_z + 3\omega_\theta\langle\omega_z'^2\frac{\partial}{\partial z}u_\theta'\rangle + 3\omega_z\langle\omega_z'^2\frac{\partial}{\partial z}u_z'\rangle + T_{\omega_z'^3}. \quad \text{(B 6)}$$

REFERENCES

Bandyopadhyay, P.R. & Ahmed, A. 1993 Turbulent boundary layers subjected to multiple curvatures and pressure gradients. *Journal of Fluid Mechanics* **246**, 503–527.

Barlow, R.S. & Johnston, J.P. 1988 Structure of a turbulent boundary layer on a concave surface. *Journal of Fluid Mechanics* **191**, 137–176.

Bartello, P., Métais, O. & Lesieur, M. 1994 Coherent structures in rotating three-dimensional turbulence. *Journal of Fluid Mechanics* **273**, 1–29.

Batchelor, G.K. 1967 *An introduction to fluid dynamics*. Cambridge Univ Pr.

Batchelor, G.K. 1982 *The theory of homogeneous turbulence*. Cambridge University Press.

Benedict, L.H. & Gould, R.D. 1996 Towards better uncertainty estimates for turbulence statistics. *Experiments in Fluids* **22** (2), 129–136.

Bernal, L.P. & Roshko, A. 1986 Streamwise vortex structure in plane mixing layers. *Journal of Fluid Mechanics* **170**, 499–525.

Billant, P., Chomaz, J.M. & Huerre, P. 1998 Experimental study of vortex breakdown in swirling jets. *Journal of Fluid Mechanics* **376**, 183–219.

Bradshaw, P. 1966 The effect of initial conditions on the development of a free shear layer. *Journal of Fluid Mechanics* **26** (02), 225–236.

Bradshaw, P. 1973 Effects of streamline curvature on turbulent flow. *Tech. Rep.*.

Bradshaw, P., Ferriss, D.H. & Johnson, R.F. 1964 Turbulence in the noise-producing region of a circular jet. *Journal of Fluid Mechanics* **1964** (04), 591–624.

Castro, I.P. & Bradshaw, P. 1976 The turbulence structure of a highly curved mixing layer. *Journal of Fluid Mechanics* **73** (02), 265–304.

Champagnat, F., Plyer, A., Le Besnerais, G., Leclaire, B., Davoust, S. & Le Sant, Y. 2011 Fast and accurate PIV computation using highly parallel iterative correlation maximization. *Experiments in Fluids* **50**, 11691182.

Chigier, N.A. & Chervinsky, A. 1967 Experimental investigation of swirling vortex motion in jets. *Journal of Applied Mechanics* **34** (1967), 443–451.

Citriniti, J.H. & George, W.K. 2000 Reconstruction of the global velocity field in the axisymmetric mixing layer utilizing the proper orthogonal decomposition. *Journal of Fluid Mechanics* **418**, 137–166.

Davoust, S. 2011 Dynamics of large scale structures in turbulent jets with or without the effect of swirl. PhD thesis, ONERA, Ecole Polytechnique.

Davoust, S. & Jacquin, L. 2011 Taylor's hypothesis convection velocities from mass conservation equation. *Physics of Fluids* **23** (5).

Davoust, S., Jacquin, L. & Leclaire, B. 2011 Dynamics of $m = 0$ and $m = 1$ modes and of streamwise vortices in a turbulent axisymmetric mixing layer. *Submitted to Journal of Fluid Mechanics* .

Ewing, D. 1999 Decay of round turbulent jets with swirl. In *Engineering Turbulence Modelling and Experiments 4: Proceedings of the 4th International Symposium on Engineering Turbulence Modelling and Measurements, Ajaccio, Corsica, France, 24-26 May, 1999*. Elsevier Science.

Facciolo, L., Tillmark, N., Talamelli, A. & Alfredsson, P.H. 2007 A study of swirling turbulent pipe and jet flows. *Physics of Fluids* **19**, 035105.

Farokhi, S., Taghavi, R. & Rice, E.J. 1988 Effect of initial swirl distribution on the evolution of a turbulent jet. *AIAA Journal* **27** (6), 700–706.

Fernholz, H.H. & Warnack, D. 1998 The effects of a favourable pressure gradient and of the

reynolds number on an incompressible axisymmetric turbulent boundary layer. part 1. the turbulent boundary layer. *Journal of Fluid Mechanics* **359**, 329–356.

Foucaut, J.M., Carlier, J. & Stanislas, M. 2004 PIV optimization for the study of turbulent flow using spectral analysis. *Measurement Science and Technology* **15**, 1046–1058.

Gallaire, F. & Chomaz, J.M. 2003 Instability mechanisms in swirling flows. *Physics of Fluids* **15**, 2622.

Gence, J.N. & Frick, C. 2001 Birth of the triple correlations of vorticity in an homogenous turbulence submitted to a solid body rotation. *Comptes Rendus de l'Academie des Sciences Series IIB Mechanics* **329** (5), 351–356.

Gilchrist, R. T. & Naughton, J. W. 2005 Experimental study of incompressible jets with different initial swirl distributions: Mean results. *AIAA Journal* **43** (4).

Gillis, J.C. & Johnston, J.P. 1983 Turbulent boundary-layer flow and structure on a convex wall and its redevelopment on a flat wall. *Journal of Fluid Mechanics* **135**, 123–153.

Grabowski, W.J. & Berger, S.A. 1976 Solutions of the navier-stokes equations for vortex breakdown. *Journal of Fluid Mechanics* **75** (03), 525–544.

Hoffmann, P.H., Muck, K.C. & Bradshaw, P. 1985 The effect of concave surface curvature on turbulent boundary layers. *Journal of Fluid mechanics* **161**, 371–403.

Holloway, A.G.L. & Tavoularis, S. 1992 The effects of curvature on sheared turbulence. *Journal of Fluid Mechanics* **237**, 569–603.

Holloway, A.G.L. & Tavoularis, S. 1998 A geometric explanation of the effects of mild streamline curvature on the turbulence anisotropy. *Physics of Fluids* **10**, 1733.

Hopfinger, E.J., Browand, F.K. & Gagne, Y. 1982 Turbulence and waves in a rotating tank. *Journal of Fluid Mechanics* **125**, 505–534.

Hussain, A.K.M.F. & Husain, Z. D. 1980 Turbulence structure in the axisymmetric free mixing layer. *AIAA Journal* **18**, 12.

Iqbal, M.O. & Thomas, F.O. 2007 Coherent structure in a turbulent jet via a vector implementation of the proper orthogonal decomposition. *Journal of Fluid Mechanics* **571**, 281–326.

Jacquin, L., Leuchter, O., Cambon, C. & Mathieu, J. 1990 Homogeneous turbulence in the presence of rotation. *Journal of Fluid Mechanics* **220**, 1–52.

Leclaire, B. & Jacquin, L. 2011 On the generation of swirling jets: High Reynolds number rotating flow in a pipe with final contraction. *submitted to Journal of Fluid Mechanics* .

Leclaire, B., Jaubert, B., Champagnat, F., Le Besnerais, G. & Le Sant, Y. 2009 FOLKI-3C: a simple, fast and direct algorithm for stereo PIV. In *Proceedings of 8th International Symposium on Particle Image Velocimetry - PIV09*. Melbourne.

Liang, H. & Maxworthy, T. 2005 An experimental investigation of swirling jets. *Journal of Fluid Mechanics* **525**, 115–159.

Liepmann, D. & Gharib, M. 1992 The role of streamwise vorticity in the near-field entrainment of round jets. *Journal of Fluid Mechanics* **245**, 643–668.

Loiseleux, T. & Chomaz, J.M. 2003 Breaking of rotational symmetry in a swirling jet experiment. *Physics of Fluids* **15**, 511.

Martin, J.E. & Meiburg, E. 1991 Numerical investigation of three-dimensionally evolving jets subject to axisymmetric and azimuthal perturbations. *Journal of Fluid Mechanics* **230**, 271–318.

McIlwain, S. & Pollard, A. 2002 Large eddy simulation of the effects of mild swirl on the near field of a round free jet. *Physics of Fluids* **14**, 653.

Mehta, R.D., Wood, D.H. & Clausen, P.D. 1991 Some effects of swirl on turbulent mixing layer development. *Physics of Fluids* **3**, 2716.

Moisy, F., Morize, C., Rabaud, M. & Sommeria, J. 2010 Decay laws, anisotropy and cyclone–anticyclone asymmetry in decaying rotating turbulence. *J. Fluid Mech* **666**, 5–35.

Naughton, J.W., Cattafesta III, L.N. & Settles, G.S. 1997 An experimental study of compressible turbulent mixing enhancement in swirling jets. *Journal of Fluid Mechanics* **330**, 271–305.

Nickels, T.B. & Marusic, I. 2001 On the different contributions of coherent structures to the spectra of a turbulent round jet and a turbulent boundary layer. *Journal of Fluid Mechanics* **448**, 367–385.

Panda, J. & McLaughlin, D.K. 1994 Experiments on the instabilities of a swirling jet. *Physics of Fluids* **6**, 263.

Plesniak, M.W., Mehta, R.D. & Johnston, J.P. 1994 Curved two-stream turbulent mixing layers: Three-dimensional structure and streamwise evolution. *Journal of Fluid Mechanics* **270**, 1–50.

Pope, S.B. 2008 *Turbulent flows*. Cambridge Univ. Press.

Raffel, M., Willert, C., Wereley, C. & Kompenhans, J. 2007 *Particle Image Velocimetry. A Practical Guide*, 2nd edn. Springer Verlag, Berlin.

Rogers, M.M. & Moin, P. 1987 The structure of the vorticity field in homogeneous turbulent flows. *Journal of Fluid Mechanics* **176**, 33–66.

Rose, WG 1962 A swirling round turbulent jet, part 1: Mean flow measurements. *Journal of Applied Mechanics* **29**, 615–625.

Salhi, A. & Cambon, C. 1997 An analysis of rotating shear flow using linear theory and dns and les results. *Journal of Fluid Mechanics* **347**, 171–195.

Sarpkaya, T. 1974 Effect of the adverse pressure gradient on vortex breakdown. *AIAA Journal* **12**, 602–607.

Scarano, F. 2003 Theory of non-isotropic spatial resolution in piv. *Experiments in Fluids* **35** (3), 268–277.

Shiri, A., George, W. K. & Naughton, J. W. 2008 Experimental study of the far field of incompressible swirling jets. *AIAA Journal* **46** (8), 2002–2009.

Speziale, C.G., Gatski, T.B. & Mhuiris, N.M.G. 1990 A critical comparison of turbulence models for homogeneous shear flows in a rotating frame. *Physics of Fluids A: Fluid Dynamics* **2**, 1678.

Staplehurst, P.J., Davidson, P.A. & Dalziel, S.B. 2008 Structure formation in homogeneous freely decaying rotating turbulence. *Journal of Fluid Mechanics* **598**, 81–105.

Townsend, A.A.R. 1980 *The structure of turbulent shear flow*. Cambridge Univ Press.

Warnack, D. & Fernholz, H.H. 1998 The effects of a favourable pressure gradient and of the reynolds number on an incompressible axisymmetric turbulent boundary layer. part 2. the boundary layer with relaminarization. *Journal of Fluid Mechanics* **359**, 357–381.

Wieneke, B. 2005 Stereo-PIV using self-calibration on particle images. *Experiments in Fluids* **39** (2), 267–280.

Conclusion

5.1 Synthèse des principaux résultats

Une configuration expérimentale permettant d'étudier les effets du swirl sur la dynamique d'une couche de mélange axisymétrique a été réalisée. Plusieurs campagnes de mesures PIV ont étés menées afin de caractériser l'écoulement de jet tournant. Nous avons pris part à un projet visant à mettre en place un nouvel algorithme de PIV baptisé FOLKI-SPIV. Nous avons alors évalué certaines de ses caractéristiques comme sa réponse au bruit et sa résolution spatiale et nous avons participé à son adaptation au contexte expérimental lors de nos campagnes de mesure de PIV stéréoscopique. L'utilisation avancée de cet algorithme nous a poussé à porter un regard critique sur nos mesures. Pour chaque configuration PIV utilisée, une démarche visant à optimiser la qualité des mesures nous a permis d'obtenir des résultats dont la validité a été démontrée par une étude des incertitudes. Une méthode nouvelle permettant de déterminer la validité de l'hypothèse de Taylor ainsi que la vitesse de convection associée aux fluctuations de vitesse axiale d'une fréquence f a été proposée. Cette méthode, qui utilise seulement un plan de mesure transverse à l'écoulement, a été appliquée à l'écoulement de jet, avec ou sans rotation. Cette étude a montré que l'hypothèse de Taylor pouvait s'appliquer dans le jet non-tournant pour les grandes échelles énergétiques de la turbulence, excepté celles de très basse fréquence temporelle. Les petites échelles tendent à être filtrées par la faible résolution spatiale de la PIV et ne représentent pas des déplacements suffisants pour se distinguer du bruit de la mesure PIV, et donc ne peuvent pas être considérées dans l'analyse. Dans le cas du jet tournant, l'hypothèse de Taylor semble se dégrader à cause de l'augmentation du taux de turbulence et à cause de l'apparition d'une composante azimutale dans la vitesse de convection qui n'est pas prise en compte par la méthode.

La dynamique des structures cohérentes dans une couche de mélange axisymétrique turbulente a été détaillée dans un plan transverse situé à deux diamètres à la sortie du jet sans rotation. Une POD a d'abord été utilisée pour décrire les modes $m = 0$ et $m = 1$. La dynamique du mode $m = 1$ a été statistiquement décrite comme étant plus proche d'un battement que d'une hélice. Ensuite, nous avons étudié l'organisation spatiale des tourbillons longitudinaux. Nous avons mis en évidence une organisation caractéristique de ces structures sous forme de paires de signe opposé qui sont disposées selon la direction radiale, et non pas selon l'azimut. La localisation statistique de ces structures par rapport aux modes $m = 0$ et $m = 1$ a alors été déterminée par une analyse des corrélations triples enstrophie-vitesse. Cette démarche montre que les tourbillons longitudinaux, qui sont majoritairement produits par le cisaillement moyen, sont statistiquement localisés entre deux anneaux de Kelvin-Helmholtz par un phénomène de forçage faible dû à l'étirement instationnaire provoqué par les modes $m = 0$ et $m = 1$. Enfin, un mécanisme d'interaction entre les modes $m = 0$, les tourbillons longitudinaux et le cisaillement moyen qui permet

de rendre compte de l'organisation radiale des tourbillons longitudinaux de signe opposés a été proposé.

Nous avons ensuite étudié l'effet de la rotation sur une couche de mélange axisymétrique. Le nombre de swirl a été varié de manière paramétrique de $S = 0$ à $S = 0.81$. Nous avons montré que le taux de croissance de la couche de mélange et que l'intensité de la turbulence étaient accrus par la rotation, à l'exception d'une diminution anormale se produisant autour de $S = 0.40$. La production de l'énergie cinétique turbulente a alors été analysée en considérant la structure individuelle des tenseurs des déformations et de Reynolds, ainsi que leur alignement. Ceci a permis d'attribuer la baisse autour de $S = 0.40$ à un effet de désalignement initial de la turbulence lié au dispositif expérimental de génération du jet tournant. Mis à part cet effet, l'augmentation de la production turbulente a pu être attribuée à l'anisotropie accrue du tenseur de Reynolds ainsi qu'à un meilleur alignement avec le tenseur des déformations. Nous avons alors tenté de relier le comportement du tenseur de Reynolds à la dynamique des structures tourbillonnaires longitudinales. Ceci nous a amené à constater que la modification avec le nombre de swirl de l'orientation des paires de tourbillons de signe opposé qui sont disposées selon la direction radiale qui ont été mises en évidence dans le jet non tournant, pouvait expliquer le comportement du tenseur de Reynolds. Pour finir, l'étude de la brisure de la symétrie entre les tourbillons longitudinaux positifs et négatifs a révélé que les tourbillons négatifs, anticycloniques, dominaient dans une région intermédiaire entre le coeur du jet et la couche de mélange. Nous avons proposé un mécanisme de transport des fluctuations de vorticité axiale contre le gradient de vorticité axiale moyenne pour expliquer cet effet. La présence de tourbillons positifs, cycloniques, au centre de la couche de mélange n'a pas pu être expliquée.

5.2 Perspectives

Tout d'abord, il serait utile de poursuivre l'étude des tourbillons longitudinaux dans les jets tournants, afin de déterminer par quel mécanisme les tourbillons cycloniques sont promus au centre de la couche de mélange. Ceci peut nécessiter d'employer des moyens expérimentaux nouveaux comme la PIV volumétrique, ou des simulations avancées, afin de déterminer tous les termes de l'équation gouvernant le moment d'ordre trois de la vorticité axiale. Aussi, dans le cas du jet non-tournant, nous avons postulé que le scénario d'interaction dynamique entre les modes $m = 0$ et $m = 1$ et les tourbillons longitudinaux pouvait être général et robuste. En particulier, selon ce scénario, des conditions initiales différentes pourraient donner lieu à des comportements moyens différents, de par l'importance des tourbillons longitudinaux dans la dynamique du jet. Il parait donc nécessaire de vérifier ceci en étudiant l'effet des conditions initiales sur le scénario, et cela pourra éventuellement conduire à des stratégies de contrôle de l'écoulement. Pour finir, il reste à aborder l'éclatement tourbillonnaire à haut nombre de Reynolds. Seule une configuration expérimentale sans buse de contraction ($\chi = 1$) permettra de réaliser une étude satisfaisante avec la soufflerie R4Ch, et ceci imposera l'utilisation de champs de mesure PIV de taille supérieure à $0.5m$. Dans le cas où cela se révèle techniquement difficile, il sera nécessaire de concevoir une installation plus petite.

Troisième partie

Annexes

A Calculs PIV rapides et précis utilisant une maximisation massivement parallèle et itérative de la corrélation

Cet article, publié dans Experiments in Fluids [17], est le fruit d'un travail collectif entre les département DAFE et DTIM de l'ONERA. Il porte sur l'adaptation au contexte de la mesure par PIV de l'algorithme FOLKI, initialement destiné à des applications d'estimation de mouvements dans les séquences vidéo [66]. De par sa structure, cet algorithme a pu être porté sur des cartes graphiques (GPU) ce qui le rend très rapide.

Le transfert de l'algorithme FOLKI vers le logiciel FOLKI-SPIV était déjà en cours lors du début de cette thèse. Le traitement des images PIV a demandé des fonctionnalités nouvelles telles que l'égalisation dynamique des niveaux, la gestion des bords, et la symétrisation du critère de minimisation. Mon travail a porté sur l'étude de la résolution spatiale de l'algorithme, une question qui se pose naturellement lors d'une mesure expérimentale. Dans ce but, j'ai simulé des images PIV de synthèse avec des déplacements connus à l'aide du générateur SIG [72], puis j'ai analysé la réponse de l'algorithme. J'ai donc été en charge de rédiger la section 5 de cet article. Nous avons montré que l'algorithme se comportait quasiment comme une moyenne spatiale sur la fenêtre d'interrogation, ce qui constitue une limite pour ce type de méthode. Cette étude m'a permis aussi d'aborder le compromis résolution spatiale/bruit : diminuer la taille de la fenêtre d'interrogation améliore la résolution spatiale, au détriment de l'incertitude de la mesure. Nous avons trouvé que le compromis qui est atteint par FOLKI-SPIV est légèrement meilleur que celui d'un code de PIV classique.

Cette étude et cette maitrise de l'algorithme de dépouillement FOLKI-SPIV par le DAFE se sont révélées être des atouts pour mener et analyser les campagnes d'essai PIV. A cela, il faut ajouter que le fait de pouvoir traiter les données PIV rapidement (quelques minutes au lieu de quelques heures) permet d'envisager la PIV différemment. Par exemple, il est possible d'optimiser de manière itérative chaque réglage expérimental plus aisément.

Cette collaboration entre le DAFE et le DTIM de l'ONERA continue et se tourne à présent vers de nouvelles problématiques comme la conception de nouveaux algorithmes performants pour la PIV volumétrique, et l'amélioration du compromis résolution/bruit en PIV plane à l'aide de méthodes combinées locales/globales [34].

Exp Fluids (2011) 50:1169–1182
DOI 10.1007/s00348-011-1054-x

RESEARCH ARTICLE

Fast and accurate PIV computation using highly parallel iterative correlation maximization

F. Champagnat · A. Plyer · G. Le Besnerais · B. Leclaire · S. Davoust · Y. Le Sant

Received: 31 December 2009 / Revised: 26 January 2011 / Accepted: 1 February 2011 / Published online: 17 March 2011

Abstract Our contribution deals with fast computation of dense two-component (2C) PIV vector fields using Graphics Processing Units (GPUs). We show that iterative gradient-based cross-correlation optimization is an accurate and efficient alternative to multi-pass processing with FFT-based cross-correlation. Density is meant here from the sampling point of view (we obtain one vector per pixel), since the presented algorithm, FOLKI, naturally performs fast correlation optimization over interrogation windows with maximal overlap. The processing of 5 image pairs (1,376 × 1,040 each) is achieved in less than a second on a NVIDIA Tesla C1060 GPU. Various tests on synthetic and experimental images, including a dataset of the 2nd PIV challenge, show that the accuracy of FOLKI is found comparable to that of state-of-the-art FFT-based commercial softwares, while being 50 times faster.

1 Introduction

Particle Image Velocimetry (PIV) has become an essential tool for flow diagnosis and is therefore widely used in industrial as well as academic situations. Its current limitation is however, the time necessary to compute the vector fields from the images, which often imposes specific constraints in the schedule of test campaigns. In that respect, the important development of high-speed PIV systems over the last decade appears even more challenging. We propose a solution to shorten dramatically this processing time, based on an algorithm that computes dense 2C vector fields using Graphics Processing Units (GPUs).

GPU has already been compared to other architectures for PIV processing in previous works (Schiwietz and Westermann 2004; Venugopal et al. 2009). These studies concentrated on cross-correlation using FFT, but the speed-up factor for FFT using GPU versus CPU architecture does not exceed three. In this context, real-time computation therefore requires large PC clusters with a GPU at each node (Venugopal et al. 2009). Former real-time realizations also involve parallelization on Field-Programmable Gate Arrays (FPGA) (Iriarte Munoz et al. 2009; Yu et al. 2006). Although efficient and convenient for embedded systems, this solution is far more expensive than GPU to implement, both in terms of hardware cost and software development effort. Interestingly, these architectures get rid of FFT in favor of direct correlation, which is better suited to FPGA architectures. In contrast to these works, the approach proposed hereafter relies on a technique for cross-correlation maximization that departs from the classical FFT method or from direct correlation. Its structure is ideally matched to massively parallel architectures and therefore allows a 50 times speed-up using a single GPU.

The algorithm FOLKI (French acronym for Iterative Lucas–Kanade Optical Flow, Le Besnerais and Champagnat 2005) was originally designed in the context of computer vision for motion estimation in video sequences. But FOLKI proved also very robust and adaptive to many other kinds of images such as those obtained in photomechanics and PIV. It is based on the classical interrogation window

F. Champagnat (✉) · A. Plyer · G. Le Besnerais
Modeling and Information Processing Department,
French Aerospace Lab (ONERA), Chemin de la Hunière,
91761 Palaiseau Cedex, France
e-mail: fchamp@onera.fr

B. Leclaire · S. Davoust · Y. Le Sant
Fundamental and Experimental Aerodynamics Department,
French Aerospace Lab (ONERA), 8 rue des Vertugadins,
92190 Meudon, France

paradigm, but belongs to the family of Lucas–Kanade (LK) algorithms (see Baker and Matthews 2004, for a review). The basic LK method is already known in the PIV community but it is most often associated with Particle Tracking Velocimetry (Miozzi 2004; Stanislas et al. 2008), i.e., low-seeding densities and sparse estimation of displacements. In contrast, the improvement from the basic LK approach implemented in FOLKI naturally relies on the computation of dense fields, i.e., a displacement vector for each image pixel. This leads to a highly regular and parallel algorithm which is much more efficient than previous sparse LK techniques and furthermore specially suited to GPU architectures. Of course, the fact that one vector per pixel be obtained should not be confused with the spatial resolution of the method, which is tightly linked with the window size, as for any other window-based PIV technique.

The principle of FOLKI is the following: around each pixel, a fixed size interrogation window (IW) is defined, and a cross-correlation measure is defined as a Sum of Squared Differences (SSD) between the IW and a displaced window in the consecutive image. In contrast to mainstream PIV algorithms that perform extensive search over discrete pixel grid with a FFT correlation, this SSD is minimized using an iterative Gauss–Newton (GN) descent. On a general point of view, when initialized not too far (say 3 pixels) from the true displacement, it is known that the convergence of GN is fast, reaching a precision of the order of a tenth of a pixel in typically less than 5 iterations. As PIV images may often be characterized by larger displacements, a multiresolution scheme is used to avoid local minima. An image pyramid is built, starting from the acquired images, which correspond to the ground level. This is done by successively performing low-pass filtering and decimation, leading to successively smaller images. As each step also divides the displacements by two, this has to be done until the top-level images have displacements compatible with GN iterations initialized with a displacement equal to zero. This leads to first rough estimates, whose values are successively refined by descending the pyramid levels (whereby the spatial resolution is also refined). Such a coarse-to-fine multiresolution scheme has proven very efficient in optical flow methods in computer vision (Bergen et al. 1992) and is also used in PIV (see for instance Ruhnau et al. 2005). As will be shown in Sect. 2, an iterative image deformation technique (Lecordier and Trinite 2003; Stanislas et al. 2008) is implicitly embedded in the descent iteration.

Multiresolution, gradient descent and a dense velocity output are more often encountered in so-called "optical flow" methods (Corpetti et al. 2006; Ruhnau et al. 2005). However, FOLKI is a window-based method, with no spatial regularization such as a Horn & Schunk-like term (Corpetti et al. 2006). It should be compared to classical FFT correlators, which we will do in the assessment part of this paper.

The paper is organized as follows: Sects. 2 and 3 are devoted to a description of the basic FOLKI algorithm and to the principle of its GPU implementation. They consist in a more detailed version of the material presented in PIV'09 (Champagnat et al. 2009). Section 4 then describes specific improvements which were added to address situations typically encountered in PIV, the corresponding GPU implementation is then referred to as FOLKI-PIV. A detailed performance assessment follows, where FOLKI-PIV is characterized and benchmarked against a state-of-the-art commercial PIV software using FFT-based cross-correlation. First, synthetic images are specifically generated in order to determine its spatial resolution and its sensitivity to low-seeding densities and to noise. This is done in Sect. 5. Then, the comparative assessment is extended to experimental images, in Sect. 6. The level of peak-locking bias and sensitivity to actual measurement noise are explored by considering case A of the second PIV challenge (Stanislas et al. 2005), and results from a test campaign recorded at ONERA are introduced to show the advantages of dense sampling and illustrate how FOLKI-PIV deals with solid walls thanks to the use of masks. Finally, conclusive remarks and perspectives on future work are gathered in Sect. 7.

2 Basic FOLKI algorithm

2.1 Multiresolution setting and notations

The notations for the following derivations are illustrated in Fig. 1: observed image intensity at discrete positions $\boldsymbol{k} = [k, l]^t \in \mathcal{G} = \{0, \ldots, K-1\} \times \{0, \ldots, L-1\}$ and time indexes $t \in \{0, dt\}$ is denoted $I(\boldsymbol{k}, t)$. In the sequel, all summations $\sum_{\boldsymbol{k}}$ refer to summation on $\mathcal{G}$. We will sometimes use the notation $I(\cdot, t)$ for the function $\boldsymbol{k} \mapsto I(\boldsymbol{k}, t)$.

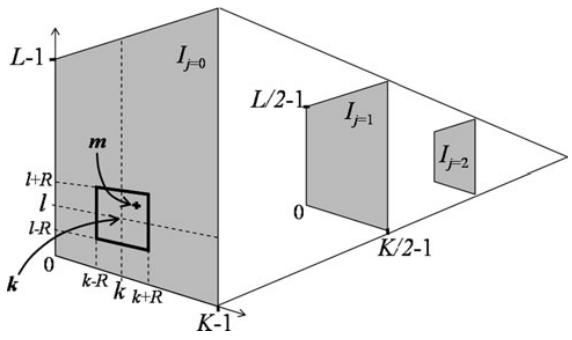

Fig. 1 Notations for image intensities within image pyramid and interrogation window

Exp Fluids (2011) 50:1169–1182 1171

We use a multiresolution framework (Bergen et al. 1992): image intensity $I_j(\boldsymbol{x},t)$ at any real position $\boldsymbol{x}=[x,y]^t$, and any resolution level $j>0$ is computed by means of a Gaussian pyramid (Burt and Adelson 1983): starting from a level j, the image of level $j+1$ is obtained by applying a low-pass filter on the intensity $I_j(.,t)$ and then retaining one pixel out of a square of 2×2 pixels. Thus, image $j+1$ is four times smaller than image j, while displacements are divided by two. For each level, the spatial image gradient $\nabla I_j(\boldsymbol{x},t)$ is computed by a first-order centered difference scheme.

In this framework, displacements of the initially recorded image (level $j=0$) are thus divided by 2^j at level j. This allows to settle the question of the first estimate for the Gauss–Newton iterations: indeed, initialization at the highest level $J-1$ (where J is the total number of levels) can be done with zero displacement, as long as J is chosen so that displacements to find at level $J-1$ are sufficiently small in the whole image. In practice, for standard PIV images with an 8 pixel dynamic range, $J=3$ is enough for this process to work successfully, without being trapped in local minima.

2.2 A Lucas–Kanade algorithmic core

FOLKI relies on a Lucas–Kanade paradigm (Baker and Matthews 2004), which has been extended in Le Besnerais and Champagnat (2005) so as to provide a convergent iterative estimation of the dense displacement field $\boldsymbol{u}$.

In a majority of current PIV algorithms, the displacement of a given IW is found by first calculating the cross-correlation score of all possible displacements, then finding the maximum correlation peak, and finally refining its position by sub-pixel fit or interpolation. Usually, this process is repeated iteratively with decreasing window sizes, and at each step, the IWs are shifted using the previous estimation of displacement. The LK algorithm is also a window matching technique, but differs on both the objective criterion and on the way to obtain sub-pixel displacements. Cross-correlation maximization is in fact achieved by minimizing a Sum of Squared Differences (SSD), in which the displacement to be found appears directly as a real-valued (and not integer-valued) quantity. This is achieved thanks to a Gauss–Newton iterative descent. The SSD criterion around pixel $\boldsymbol{k}$ at level j writes

$$\sum_{\boldsymbol{m}} w(\boldsymbol{m}-\boldsymbol{k})\big(I_j(\boldsymbol{m},0)-I_j(\boldsymbol{m}-\boldsymbol{u}(\boldsymbol{k}),dt)\big)^2 \tag{1}$$

where w is a weight function whose support defines the interrogation window $\mathcal{W}(\boldsymbol{k})$:

$$\mathcal{W}(\boldsymbol{k})=\{\boldsymbol{m}\in\mathcal{G}\mid w(\boldsymbol{m}-\boldsymbol{k})>0\}. \tag{2}$$

The following derivations are valid for any kind of weight function. Popular choices are rectangular and Gaussian weights. All the experimental results presented in this paper use a standard rectangular IW ($w_{\mathrm{f}}(\boldsymbol{m})=1/(2R+1)^2$ for $\boldsymbol{m}\in\{-R,\ldots,R\}\times\{-R,\ldots,R\}$). For convenience of coding, we use only odd IW dimensions.

Now addressing the minimization process, let us assume that an initial guess $\boldsymbol{u}_0(\boldsymbol{k})$ of the displacement is available and is a good approximation of the sought displacement $\boldsymbol{u}(\boldsymbol{k})$, i.e., $\boldsymbol{u}(\boldsymbol{k})-\boldsymbol{u}_0(\boldsymbol{k})\approx 0$. The Gauss–Newton iteration derives from the following first-order expansion of Eq. 1 around $\boldsymbol{u}_0(\boldsymbol{k})$, with $\boldsymbol{u}(\boldsymbol{k})-\boldsymbol{u}_0(\boldsymbol{k})$ as a small parameter:

$$\sum_{\boldsymbol{m}} w(\boldsymbol{m}-\boldsymbol{k})\big(I_j(\boldsymbol{m},0)-I_j(\boldsymbol{m}-\boldsymbol{u}_0(\boldsymbol{k}),dt) + \nabla I_j(\boldsymbol{m}-\boldsymbol{u}_0(\boldsymbol{k}),dt)^t(\boldsymbol{u}(\boldsymbol{k})-\boldsymbol{u}_0(\boldsymbol{k}))\big)^2. \tag{3}$$

Equation 3 is a linear least-squares criterion, which can already be optimized to yield $\boldsymbol{u}(\boldsymbol{k})$ by solving a 2×2 linear system.

In Bouguet (2000), a faster scheme was proposed. It relies on a slightly different form of Eq. 1:

$$\sum_{\boldsymbol{n}} w(\boldsymbol{m}-\boldsymbol{k})\big(I_j(\boldsymbol{m}+\boldsymbol{u}(\boldsymbol{k})-\boldsymbol{u}_0(\boldsymbol{k}),0) -I_j(\boldsymbol{m}-\boldsymbol{u}_0(\boldsymbol{k}),dt)\big)^2. \tag{4}$$

In this criterion, instead of searching $\boldsymbol{u}(\boldsymbol{k})$ in the image at time dt as in Eq. 1, image at time dt is shifted by the estimate $\boldsymbol{u}_0(\boldsymbol{k})$ and the increment $\boldsymbol{u}(\boldsymbol{k})-\boldsymbol{u}_0(\boldsymbol{k})$ is applied to the image at time 0. A Taylor expansion of $I_j(\cdot,0)$ around $\boldsymbol{m}$ then yields

$$\sum_{\boldsymbol{m}} w(\boldsymbol{m}-\boldsymbol{k})\big(I_j(\boldsymbol{m},0)-I_j(\boldsymbol{m}-\boldsymbol{u}_0(\boldsymbol{k}),dt) + \nabla I_j(\boldsymbol{m},0)^t(\boldsymbol{u}(\boldsymbol{k})-\boldsymbol{u}_0(\boldsymbol{k}))\big)^2. \tag{5}$$

The advantage of this "inverse additive" approach (Baker and Matthews 2004) is that the spatial intensity gradient $\nabla I_j(\boldsymbol{m},0)$ is computed only once for each resolution level j, while in Eq. 3 the spatial gradient, $\nabla I_j(\boldsymbol{m}-\boldsymbol{u}_0(\boldsymbol{k}),dt)$ has to be computed at each iteration.

2.3 Dense LK algorithm

As shown in Le Besnerais and Champagnat (2005), if one wants to apply iterative techniques based on expansions (3) or (5) *at each pixel*—which is the usual goal in computer vision—the overall cost is prohibitive, because, for each iteration, it requires $(2R+1)^2$ interpolations per pixel due to the $I_j(\boldsymbol{m}-\boldsymbol{u}_0(\boldsymbol{k}),dt)$ term (and also because of the gradient $\nabla I_j(\boldsymbol{m}-\boldsymbol{u}_0(\boldsymbol{k}),dt)$ which appears in Eq. 3). Faster schemes can in fact be obtained by using only one interpolated image per iteration. To do so, we introduce the following notation:

$$I_j^{\boldsymbol{u}_0}(\boldsymbol{m},dt) \triangleq I_j(\boldsymbol{m}-\boldsymbol{u}_0(\boldsymbol{m}),dt). \quad (6)$$

As this expression shows, image $I^{\boldsymbol{u}_0}$ is "warped" according to the current displacement field estimate $\boldsymbol{u}_0$ *evaluated at each pixel* $\boldsymbol{m}$, as opposed to a warping with one value of $\boldsymbol{u}_0$ per IW. In order to obtain a convergent scheme based on the unique warped image (6), FOLKI thus uses the approximation proposed in Le Besnerais and Champagnat (2005):

$$\boldsymbol{u}(\boldsymbol{k})-\boldsymbol{u}_0(\boldsymbol{m}) \approx 0, \quad \forall \boldsymbol{m} \in \mathcal{W}(\boldsymbol{k}) \quad (7)$$

Using Eq. 7, one then derives a first-order expansion of Eq. 1:

$$\sum_{\boldsymbol{m}} w(\boldsymbol{m}-\boldsymbol{k})\Big(I_j(\boldsymbol{m},0)-I_j^{\boldsymbol{u}_0}(\boldsymbol{m},dt) + \nabla I_j(\boldsymbol{m},0)^t(\boldsymbol{u}(\boldsymbol{k})-\boldsymbol{u}_0(\boldsymbol{m}))\Big)^2. \quad (8)$$

Minimization of Eq. 8 finally amounts to solving a 2×2 local system

$$\boldsymbol{H}(\boldsymbol{k})\boldsymbol{u}(\boldsymbol{k}) = \boldsymbol{c}(\boldsymbol{k}). \quad (9)$$

Let us detail the computation of the matrices $\boldsymbol{H}(\boldsymbol{k})$ for all pixel index $\boldsymbol{k}$. While searching for the stationary point which minimizes Eq. 8, one obtains:

$$\boldsymbol{H}(\boldsymbol{k}) = \sum_{\boldsymbol{m}} w(\boldsymbol{m}-\boldsymbol{k})\big(\nabla I_j(\boldsymbol{m},0)\nabla I_j(\boldsymbol{m},0)^t\big). \quad (10)$$

If $\boldsymbol{H}$ denotes the matrix valued function $\boldsymbol{k} \mapsto \boldsymbol{H}(\boldsymbol{k})$ of the pixel index, Eq. 10 for all pixels $\boldsymbol{k}$ can be globally written as a convolution:

$$\boldsymbol{H} = w * \big(\nabla I_j(\cdot,0)\nabla I_j(\cdot,0)^t\big), \quad (11)$$

where $*$ stands for the convolution of the scalar weight function w with each component of the matrix valued function which is inside the parenthesis. In the same way, the right-hand side vectors $\boldsymbol{c}(\boldsymbol{k})$ of Eq. 9 can be all computed by convolutions as follows

$$\boldsymbol{c} = w * (\epsilon \nabla I_j(\cdot,0)) \quad (12)$$

$$\epsilon = I_j(\cdot,0) - I_j^{\boldsymbol{u}_0}(\cdot,dt) - \nabla I_j(\cdot,0)^t \boldsymbol{u}_0 \quad (13)$$

As a result, at each iteration, local systems (9) for all pixels can be constructed *simultaneously* by Eqs. (6–11–13)—note however, that Eq. 11 can be computed once for all iterations, as already mentioned.

2.4 Overall algorithm and general comments

The global structure of the algorithm, summarized in Table 1, is a coarse-to-fine multiresolution scheme over J levels, with a fixed number N of Gauss–Newton iterations per level. As mentioned above, J should be chosen depending on the expected displacements in the image, and N may depend on the quality of the images and on the radius R of the IWs. More details on the way to choose these parameters will be given in Sects. 5 and 6. Also, note that the current version of FOLKI at use in ONERA gathers additional features specially adapted to PIV, which will be described in Sect. 4. Here, we simply comment on some specificities of the algorithm which are already contained in the above derivation.

A first remark is that, as shown in Table 1, each iteration begins with an image warp (6). Hence, FOLKI can be related to *image deformation techniques* (Lecordier and Trinite 2003; Stanislas et al. 2008). But, as FOLKI computes a dense vector field, the deformation is available at each pixel without velocity interpolation.

The dense character of the vector field also deserves further comment. First, it should be mentioned that it is an unavoidable building block of the algorithm: solving Eq. 9 for a restricted ensemble of spatial locations cannot be envisaged here, since computations (12, 13) require the availability of velocities at a much larger number of locations. Viewed in the PIV context, this by-product of the computer vision origin of FOLKI may however, appear useless, or even detrimental in terms of computational time. Indeed, as will be shown in Sect. 5, similarly to other PIV approaches based on window matching, FOLKI's spatial resolution remains related to the window size. A first important remark which justifies our choice is that this density is not an overload to the computational time: tests performed on a CPU implementation showed that the

Table 1 Pseudo GPU code of FOLKI

input: $I(\cdot,0)$ and $I(\cdot,dt)$
output: $\boldsymbol{u} = (u,v)$
begin
send $I(\cdot,0)$, $I(\cdot,dt)$ from CPU memory to GPU global memory
GPU: compute Burt pyramids *(SC)*
for $j = J-1 : -1 : 0$
  GPU: compute $\nabla I_j(\cdot,0)$ *(SC)*
  GPU: compute $\boldsymbol{H}$ *(PW)*
  for $n = 1 : N$, **iterate:**
    GPU: compute $I_j^{\boldsymbol{u}_0}(\cdot,dt)$ *(II)*
    GPU: compute ϵ *(PW)*
    GPU: compute $\boldsymbol{c}$ *(PW+SC)*
    GPU: solve local systems (9) *(PW)*
  GPU: upsample $\boldsymbol{u}$ vector fields *(SC)*
(option 1) GPU: compute output image result and transfer it into GPU visualization memory
(option 2) send $\boldsymbol{u} = (u,v)$ result from GPU to CPU
end

GPU: GPU functions, *II*: image interpolation, *SC*: separable convolution, *PW*: pixelwise operation

computational time of a dense vector field with FOLKI was comparable to that of a classical sparse computation with a commercial PIV software. This is due to the high degree of optimization of FOLKI. Besides, and paradoxically, it is in fact this dense character that leads to a highly regular and parallel algorithm which precisely allows the considerable speed-up provided by the GPU. In addition, density provides an appreciable degree of freedom of result sampling, e.g., to finely evidence vortex cores or investigate flows close to walls, see Sect. 6.2 for an example.

3 Implementation on a GPU

An implementation has been developed in C++ and CUDA language for NVIDIA GPU and tested on different hardwares (generic graphic unit of a laptop, and a dedicated GPU on a PC workstation) with Linux and Windows OS.

Different packages of FOLKI are freely available on the ONERA website, at the address: http://www.onera.fr/dtim-en/gpu-for-image/index.php. Note that the open source Linux package strictly corresponds to the algorithm described in Sect. 2, whereas the Windows packages include the additional features described in Sect. 4.

The efficiency of the GPU implementation stems from the fact that FOLKI relies mainly on three types of computations, image interpolation (II), pixelwise operations (PW) and separable convolution (SC), see Table 1. These computations are performed very efficiently on a GPU, see Champagnat et al. (2009) for a more detailed account on GPU architecture and how to make profit of it. Two main features can be highlighted:

1. Image bilinear interpolation is hardwired on a GPU, it is thus performed at a cost which is negligible compared to a CPU.
   Higher order interpolation can also be performed very efficiently thanks to the algorithm of Ruijters et al. (2008) that combines multiple bilinear interpolations to perform one bicubic B-spline interpolation.
2. It is fundamental to limit the number of CPU-GPU transfer which are particularly time-consuming. The GPU pseudo-code presented in Table 1 is designed to minimize the number of CPU-GPU image transfers. Note the optional steps at the end of Table 1: if the code is used only to visualize an output image which depends on the computed velocity field (for instance an image of the vorticity field), it is much faster to compute this image with the GPU and then to transfer it directly into the visualization memory of the GPU. This mode can be very useful for fast parameter tuning of an experiment.

4 Adapting FOLKI to PIV context

We now discuss some extensions of FOLKI, directly dictated by the typical constraints of PIV experiments. These developments principally aim at increasing the accuracy, properly handling boundaries and giving the user a quality criterion on the obtained vector fields. Results using this improved version, which we call FOLKI-PIV, are presented in Sects. 5 and 6.

4.1 Third-order B-spline interpolator

As mentioned in Sect. 4, the user may choose whether the image interpolation is performed via simple bilinear interpolation, or using third-order B-splines. Having such a choice may prove relevant in order to adapt to the image characteristics, as will be shown for instance in Sect. 6.1.

4.2 Symmetric matching cost

Following symmetric SSD criteria like

$$\sum_{\boldsymbol{m}} w(\boldsymbol{m}-\boldsymbol{k})\left(I_j\left(\boldsymbol{m}+\frac{\boldsymbol{u}(\boldsymbol{k})}{2},0\right)-I_j\left(\boldsymbol{m}-\frac{\boldsymbol{u}(\boldsymbol{k})}{2},dt\right)\right)^2, \tag{14}$$

have been proposed by many authors (Keller and Averbuch 2004; Zhao and Sawhney 2002), in order to suppress the dissymmetry of classical SSD costs, increase precision and robustness against occlusions. When upgrading toward FOLKI-PIV, we chose to implement this approach rather than the simple original SSD criterion (1).

In practice, Eq. 14 can be handled in a very similar manner as Eq. 1. Replace $u(\boldsymbol{k})$ by $u_0(\boldsymbol{m})+(u(\boldsymbol{k})-u_0(\boldsymbol{m}))$ in Eq. 14, then take first-order approximation for both images based on Eq. 7. Finally, one gets modified expressions for Eqs. 11, 12 and 13. For instance, the 2×2 matrix $\boldsymbol{H}(\boldsymbol{k})$ associated to pixel $\boldsymbol{k}$ now writes:

$$\sum_{\boldsymbol{m}} w(\boldsymbol{m}-\boldsymbol{k})\left(\nabla I_j\left(\boldsymbol{m}-\frac{\boldsymbol{u}_0(\boldsymbol{m})}{2}\right)\nabla I_j\left(\boldsymbol{m}-\frac{\boldsymbol{u}_0(\boldsymbol{m})}{2}\right)^t + \nabla I_j\left(\boldsymbol{m}+\frac{\boldsymbol{u}_0(\boldsymbol{m})}{2},dt\right)\nabla I_j\left(\boldsymbol{m}+\frac{\boldsymbol{u}_0(\boldsymbol{m})}{2},dt\right)^t\right), \tag{15}$$

(the '0' in $\nabla I_j(.,0)$ has been omitted for concision). The overall structure of the symmetric algorithm remains similar to the one in Table 1, except that expression (15) has to be recomputed at each iteration using spatial gradients and interpolations of both images. In this process, the computational time is multiplied by 2 compared to the basic algorithm of Sect. 2.

4.3 Robustness to varying illumination

In contrast to a zero-normalized cross-correlation (ZNCC) maximization objective, which is classically used in PIV, objectives defined by SSD minimization such as Eq. 14 are less robust to varying illumination conditions. Of course, global illumination changes can easily be handled by equalization using image gain and offset adjustment before feeding the algorithm with the corrected image pairs. But this approach will not work when, for instance, the lighting difference varies across the field of view, a situation which is encountered in PIV, see for instance both examples of Sect. 6. In this case, some kind of local equalization is required.

We follow hereafter the logic of mean and standard deviation normalization; note that the min–max normalization of Westerweel (1993) could also be implemented cheaply on a GPU. The principle of such a local equalization is to replace the image intensity values $I(\cdot,t)$ ($t = \{0, dt\}$) by normalized intensities $\widetilde{I}(\cdot,t)$. For an IW centered on a pixel $\boldsymbol{k}$, the vector of normalized intensities of pixels $\boldsymbol{m}$ inside the IW, $\{\widetilde{I}(\boldsymbol{m},t)\}_{\boldsymbol{m}\in\mathcal{W}(\boldsymbol{k})}$, should have approximately zero mean and unit standard deviation. If the displacement field is zero, such a normalization simply writes

$$\widetilde{I}(\boldsymbol{m},t) = (I(\boldsymbol{m},t) - M(\boldsymbol{k},t))/\sigma(\boldsymbol{k},t), \quad t = \{0, dt\},$$

where the local empirical mean $M(\cdot,t)$ and standard deviation $\sigma(\cdot,t)$ are computed simultaneously for all pixels by pixelwise operations and separable convolution.

For each iteration of FOLKI-PIV, the current displacement field is not zero anymore and local means and standard deviation should be computed on the warped images $I^{-\boldsymbol{u}_0/2}(\cdot,0)$ and $I^{\boldsymbol{u}_0/2}(\cdot,dt)$ (using the notation from Eq. 6), in order to write a normalized symmetric criterion from Eq. 14. A fast approximation is to perform the normalization only once, at the beginning of each level, and then performing the GN iterations on these images. With such a strategy, there is nearly no extra cost and empirical comparisons of both schemes—exact or approximate—show their equal effectiveness.

4.4 Boundary handling

This problem should be adequately addressed not only to process pixels located near the boundary of the field of view but also to take masks into account. A mask is a binary image aimed at excluding some pixels from the estimation process, because they belong to some rigid object (wing, measurement device, etc.) present in the field of view; see for instance the real dataset of Sect. 6.2. In the sequel, the image support refers to the set of non-masked pixels.

It is quite delicate to find an optimal way to handle boundaries in window-based displacement estimation. Indeed the *support of the estimation*, i.e., the pixels for which the system (9) can be constructed and inverted, varies with the estimate: if the displacement field locally tends to escape from the image, the support of the estimation consequently "moves back" away from the boundary. Such effect is even more pronounced in FOLKI, because of the dense estimation and also of the multiresolution process.

The proposed solution retained in FOLKI-PIV relies on dynamic masks which are updated at each iteration. Excluded pixels are (*i*) those whose current displacement vector falls outside of the image support (in the symmetric case, the displacement fields which are used are either $\boldsymbol{u}_0/2$ or $-\boldsymbol{u}_0/2$); (*ii*) those whose IW contains more than 80% of already excluded pixels. Displacement vectors are computed for the remaining pixels, then the holes are filled with nearest valid vectors before the next iteration.

4.5 Correlation quality

When analyzing PIV images, imperfect lighting, particle loss, and CCD noise will impact the quality of the correlation and thus increase the uncertainty of a computed vector. To yield a quality criterion to the user, we included in FOLKI-PIV a computation of the correlation peak height, as is traditionally done in PIV. This is done by first warping the images by the final displacement, so as to get images $I^{-\boldsymbol{u}/2}(\cdot,0)$ and $I^{\boldsymbol{u}/2}(\cdot,dt)$. Then, mean and standard deviation normalization is applied on these images, yielding $\widetilde{I}^{-\boldsymbol{u}/2}(\cdot,0)$ and $\widetilde{I}^{\boldsymbol{u}/2}(\cdot,dt)$. As a preliminary step, the ZNSSD score S_{ZNSSD} is then computed. This quantity is simply the residual of the symmetric SSD criterion (14) applied to these zero- normalized images:

$$S_{\text{ZNSSD}} = \sum_{\boldsymbol{m}} w(\boldsymbol{m}-\boldsymbol{k})\left(\widetilde{I}_0^{-\boldsymbol{u}/2}(\boldsymbol{m},0) - \widetilde{I}_0^{\boldsymbol{u}/2}(\boldsymbol{m},dt)\right)^2. \tag{16}$$

It finally turns out that S_{ZNSSD} is directly related to the classical correlation score S_{ZNCC}, or height of the correlation peak, which is defined as

$$S_{\text{ZNCC}} = \sum_{\boldsymbol{m}} w(\boldsymbol{m}-\boldsymbol{k})\widetilde{I}_0^{-\boldsymbol{u}/2}(\boldsymbol{m},0)\widetilde{I}_0^{\boldsymbol{u}/2}(\boldsymbol{m},dt). \tag{17}$$

Simple algebra, see for instance Pan et al. (2007, Appendix A), indeed shows that one has

$$S_{\text{ZNCC}} = 1 - \frac{S_{\text{ZNSSD}}}{2}. \tag{18}$$

Consequently, even though FOLKI-PIV's objective is formulated differently as in classical PIV, the quality of its results

Exp Fluids (2011) 50:1169–1182 1175

may be assessed—and vectors validated or not—in the same way, using S_{ZNCC}. $S_{ZNCC} = 1$ will indicate a perfect matching, while $S_{ZNCC} = 0$ is the theoretical limit of no correlation. Further elements on the way we use this score in practice will be given in Sects. 5 and 6.

5 Performance assessment: synthetic data

In the following, we use synthetic PIV images to study FOLKI-PIV's spatial frequency response, along with the effects of low seeding and noise on the reliability of the results. In order to determine whether the computation choices underlying FOLKI-PIV result in a different behavior as traditional PIV algorithms, we first present simple test cases for which the behavior of these algorithms is already documented. Then, we provide comparison of FOLKI-PIV's result to that of a state-of-the-art commercial software, hereafter denoted CPIV.

In the following, CPIV's estimation of an IW's displacement relies on the FFT-based computation of the cross-correlation map, followed by a Gaussian sub-pixel interpolation of the correlation peak. This process is embedded in an adaptive multi-pass scheme, in which the displacements are progressively refined from their previous estimates; this can be done with IWs of gradually decreasing size. Between each pass, rejection of spurious vectors is performed using a median filter, outliers being replaced either by other correlation maxima or by local interpolation, and the vector field is filtered with a 3×3 pixels Gaussian.

5.1 Parameters for the tests

The synthetic images used in the present work were generated with the EUROPIV Synthetic Image Generator (S.I.G.) which is described in Lecordier and Westerweel (2003). Keeping physical units in pixels, we use $1{,}025 \times 1{,}025$ images with a fully covered 8 bit range. Particles show as 2 pixels diameter Gaussian intensity distribution. The intensity level of a given particle depends on its out-of-plane position with respect to the $l_w = 2$ pixels width Gaussian-shaped light sheet that illuminates the scene. If N_p is the total number of particles in a volume V illuminated by the laser sheet, then particle density seen in the image is $N_d = \frac{N_p l_w}{V}$. Unless specified otherwise, particle density is set to $N_d = 0.02$ and no CCD noise is added, yielding sample images such as shown in Fig. 2. Displacement fields are applied symmetrically forward and backward to an initial cloud of randomly located particles. For each test case, identical displacement patterns are repeated in different zones of a given image pair, so that 25 image pairs are sufficient to achieve statistical convergence of the results.

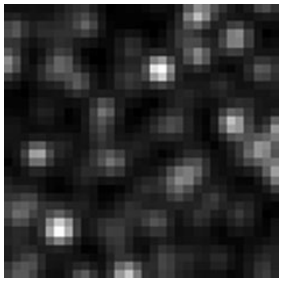

Fig. 2 32×32 pixel close-up at a S.I.G. image with $N_d = 0.02$

FOLKI-PIV's window radius R is varied from 5 to 31 pixels, and the interrogation window has a standard rectangular weight. We use $J = 1$ level because the pixel displacements in these tests are less than 2 pixels. Convergence is reached for $N = 3$ iterations. The interpolation is performed with a third-order B-spline.

CPIV is also used with various IW sizes (8×8, 16×16, 32×32 and 64×64 pixels) with rectangular weight. For a given result, the calculation is done thanks to a multi-pass scheme composed of 4 passes with the same IW size. We use a Whittaker pixel interpolation method and overlap is set to 75%.

5.2 Spatial frequency response

Following Scarano and Riethmuller (2000), the frequency response of a PIV algorithm can be evaluated using a sinusoidal shear displacement test:

$$(U, V) = \left(A \sin\left(2\pi \frac{Y}{\lambda}\right), 0\right) \tag{19}$$

where X and Y are the horizontal and vertical coordinates and U and V the associated displacement components.

We here reproduce this displacement field with amplitude A set to 2 pixel, and the wavelength λ varied from 20 to 400 pixels. Figure 3 compares the ground truth and the average value found by FOLKI-PIV for the U component, for case $\lambda = 200$ processed with $R = 10$ IWs. For each image corresponding to a given (λ, R) couple, we computed the ratio between the estimated amplitude of the sinusoid $A_{\text{FOLKI-PIV}}$ and the ground truth value $A = 2$ pixel. The evolution of this ratio as a function of the normalized IW size $2R/\lambda$ is plotted in Fig. 4. Although we used IW radii ranging from $R = 5$ to $R = 31$, all values of $A_{\text{FOLKI-PIV}}/A$ nearly collapse on a cardinal sine curve, which is the frequency response of a $[-R, R]$ sliding average. In comparison, as shown by Scarano and Riethmuller (2000), iterative multigrid methods with isotropically weighted

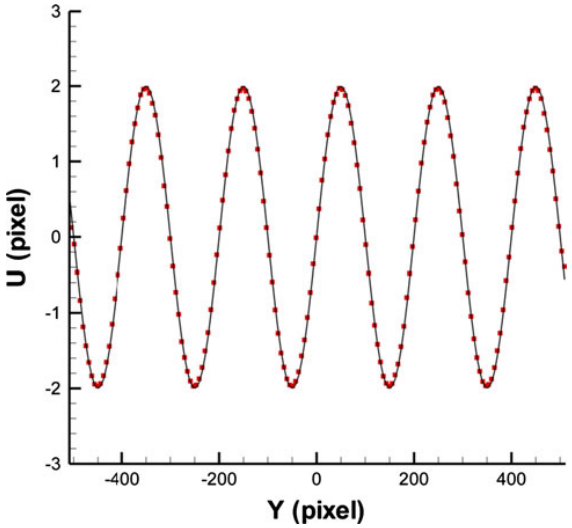

Fig. 3 Sinusoidal shear displacement with $A = 2$ pixels and $\lambda = 200$ pixels. Ground truth (*black curve*) and average displacement found by FOLKI-PIV with $R = 10$ IWs, downsampled every 6 pixels

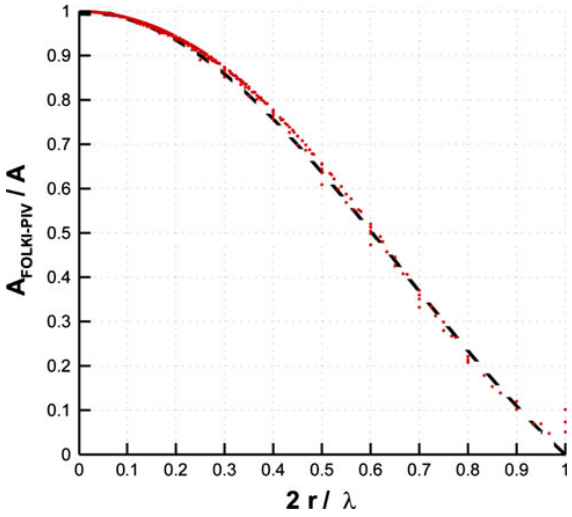

Fig. 4 Sinusoidal shear displacement with $A = 2$ pixels: amplitude ratio $A_{\text{FOLKI-PIV}}/A$ as a function of the normalized window size $2R/\lambda$ (*red symbols*), for IW radii R ranging from 5 to 31. The *dashed line* is the response of a $[-R, R]$ sliding average (cardinal sine function)

IWs follow a similar trend, but with an amplitude damping compared to the ideal sliding average, which we do not observe with FOLKI-PIV.

5.3 Resolution versus noise

One other way to evaluate the effective spatial resolution is to recover the response of the algorithm to a sharp spatial

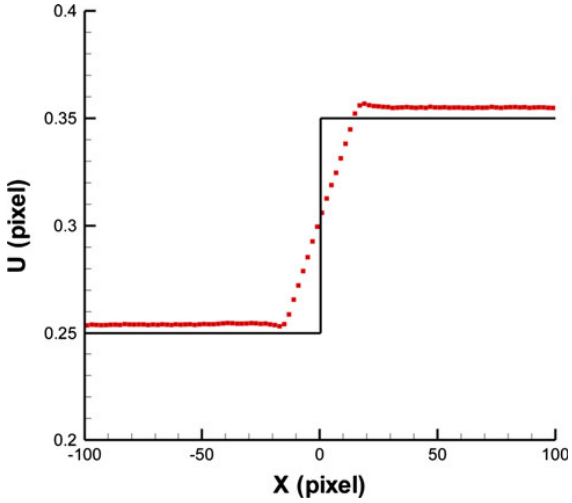

Fig. 5 Sharp horizontal step: displacement estimated by FOLKI-PIV with $R = 15$ (*red dots*, downsampling every 2 pixels) and ground truth (*black curve*). Note that the displacement error for FOLKI-PIV which appears from this figure (roughly 0.005 pixel) remains well below the usual PIV uncertainty

step in the displacement field, similar to the high velocity gradient that can be found across a shock wave. The following test was suggested to us by B. Wieneke (private communication): the displacement field is a sudden step from a $U = 0.25$ to a $U = 0.35$ pixel horizontal translation. Figure 5 compares the average result found for U by FOLKI-PIV with $R = 15$ to the ground truth. For a given window radius R, we determine the effective spatial resolution by measuring the width over which the PIV algorithm integrates the sharp edge. In practice, this width can be recovered as the inverse of the slope of the estimated $U(X)$ at the center of the step. Figure 6, in which this quantity is plotted against R, shows that FOLKI-PIV integrates the step exactly like the $[-R, R]$ moving average, which has a $2R$ effective spatial resolution.

An experimentalist seeking a better spatial resolution will be tempted to use smaller window sizes, but the drawback is an increased measurement uncertainty. Previous studies have shown that this resolution versus uncertainty trade-off also depends on the quality of the images (Raffel et al. 2007, pp. 174–176). To show how FOLKI-PIV behaves in that respect, we have considered three test cases keeping the same sudden step displacement, each of them characterized with a different type of image degradation or added noise compared to the above ideal situation. For each of them, we compute the rms displacement error U_{RMS} of both FOLKI-PIV and CPIV, for various IW sizes.

First, we have added an out-of-plane displacement $W = 0.5$ pixels so that some particles are lost (case I). W is to be compared to the Gaussian light sheet width $l_w = 2$

Exp Fluids (2011) 50:1169–1182 1177

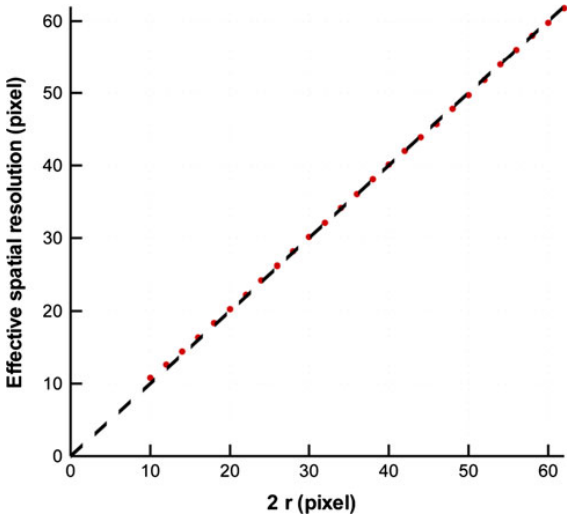

Fig. 6 Effective spatial resolution of FOLKI-PIV as a function of the total IW width $2r$ (*red symbols*) computed from the sharp horizontal step test case, compared with the effective spatial resolution of the $[-R, R]$ sliding average (*dashed black curve*)

pixels. Second, we have added to the images a Gaussian CCD noise with 20 gray level standard deviation, while reducing the 8 bit dynamic range down to 7 bit, thus reducing the signal to noise ratio (case II). Finally, using the same CCD noise as in case II, we have reduced the seeding density from $N_d = 0.02$ down to $N_d = 0.005$ (case III). In Fig. 7, FOLKI-PIV's rms displacement error U_{RMS} is compared to CPIV's for different IW sizes. For all these

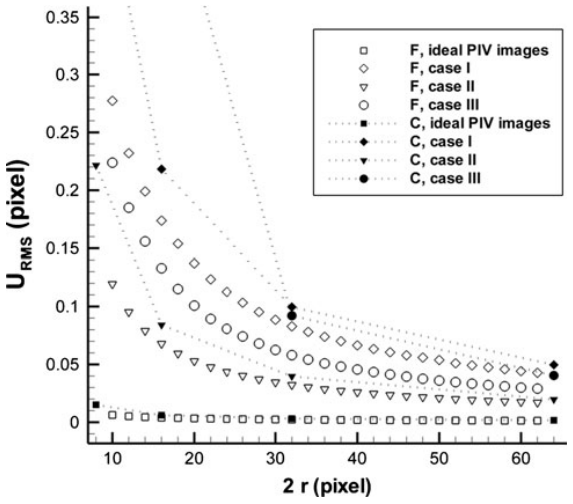

Fig. 7 Rms displacement error U_{RMS} against IW size $2R$ for three test cases of sharp horizontal step displacement (see the text for their exact characteristics). FOLKI-PIV (F) and CPIV (C) results in open and filled symbols, respectively. For clarity, CPIV results are linked by *dotted lines*

cases, FOLKI-PIV and CPIV have a similar behavior, the rms error rising as the IW size decreases. But remarkably, it turns out that FOLKI-PIV performs equally or better than CPIV depending on the cases, whereas it does not involve any data post-processing between two successive iterations, as CPIV does. This is especially true for small windows sizes.

The results presented in this section show a reassuring behavior of FOLKI-PIV with respect to noise and resolution, in other terms FOLKI-PIV does not sacrifice measurement accuracy for speed.

6 Performance assessment: real data

In the following, we provide results on two experimental PIV datasets using FOLKI-PIV with the improvements described in previous sections. The main purposes of these tests are to refine the assessment of FOLKI-PIV's rms displacement error for difficult experimental conditions, as well as its peak-locking bias error, to show how FOLKI-PIV deals with solid boundaries and illustrates the advantages of density for result sampling.

6.1 Case A of the second PIV challenge

Our first real dataset is case A of the second PIV challenge (Stanislas et al. 2005). In this experiment, a round turbulent jet is imaged at a distance from its exhaust large enough for the flow to be self-similar there. This way, a quantitative performance assessment is made possible, by comparison with canonical self-similar turbulent jets, even though the data are extracted from a real experiment with typically encountered difficulties. The sample retained in the 2003 PIV challenge consists of 100 images of resolution 992 × 1,004 pixels, in which the particles images have a diameter estimated to 1 pixel. As described by Stanislas et al. (2005), the main goals of proposing this test case were to assess the ability of PIV algorithms to deal with strongly turbulent flows, as well as to evaluate their rms displacement error and their peak-locking error.

6.1.1 Choice of the vector computation parameters

In the following, as done in the previous paragraph, we compare the results obtained by both FOLKI-PIV and CPIV on these data. For the former, we use $J = 3$ levels, $N = 7$ iterations and $R = 15$ IWs, and for the latter, a multi-pass iterative scheme composed of 2 passes with 64 × 64 IWs followed by 4 passes with 32 × 32 IWs (50% overlap at each pass), with the same intermediate spurious vector rejection and data processing between passes as described in Sect. 5. After the last pass of CPIV, this post-processing is applied once again to yield the final vector fields. For both

algorithms, local zero normalization of the image intensities is applied, and a bilinear interpolator is used, instead of the more accurate interpolators used in the previous paragraph. It is indeed known that for data having a low signal to noise ratio, bilinear interpolation yields optimal performance, especially regarding peak-locking (Lecordier and Trinité 2006; Yamamoto and Uemura 2009). Our tests (not shown here for conciseness) confirmed this conclusion for the present dataset.

Concerning FOLKI-PIV's settings, the choice $N = 7$ stems from a convergence study performed on two image pairs, labeled 1 and 5 in the dataset. We processed these images with N increasing from 1 to 20, keeping all other parameters constant. For each value of $N \geq 2$, we here compute at each image point (X, Y) the norm $\Delta(X, Y)$ of the difference between the displacement vectors found at iterations N and $N - 1$. The optimal choice for the iteration number then results from the fact that for $N \geq 7$, Δ is observed to be inferior to 0.1 pixel in the whole field, this limit being a traditional estimate of PIV accuracy on experimental images. Figure 8 below yields an illustration of this convergence, by showing the evolution with N of Δ, together with the correlation score S_{ZNCC} at $(X, Y) = (497, 502)$. As can be observed, at this location, an accurate result is reached for N well below 7. More importantly, the correlation score convergence is seen to be similar to that of Δ. This shows that the user may tune the parameters of FOLKI-PIV by a visual diagnosis of either the velocity fields or the correlation score S_{ZNCC}, by monitoring when the fields cease to change as N is increased. In practice, this quick preliminary convergence study should be led bearing the following typical values in mind: good quality images usually yield converged results for N as low as 3 (as was the case for the synthetic images of Sect. 5), whereas experimental images of poor quality may require values of N reaching up to 10.

6.1.2 *Comparative results*

To compare FOLKI-PIV's and CPIV's results, we downsample the dense vector fields of FOLKI-PIV every 15 × 15 pixels. Upon applying for both datasets the same a posteriori detection of outliers as in Stanislas et al. (2005), which amounts to keeping vectors lying in the inside of a given ellipse in a (U, V) scatter plot, we found 5 outliers with FOLKI-PIV, over a total of 442,200 vectors. In comparison, 87 vectors were found outside of the ellipse with CPIV, over a total of 390,600. It is worth noticing that FOLKI-PIV yields a remarkably small number of outliers despite the fact that it does not include any spurious vector rejection step between iterations—whereas CPIV does.

Results for the peak-locking bias are shown in Figs. 9 and 10, where the global histogram for U and the histogram for the fractional part of U are plotted, respectively. These curves show that for images with particles of small size, FOLKI-PIV displays a level of peak-locking bias comparable with that of CPIV, with a slightly higher level for even values of the displacement. To date, we have no explanation for this difference, as both algorithms use a symmetrical window shift before each iteration or pass. Overall, both figures thus show that, even though it does not involve any interpolation of the correlation peak, FOLKI-PIV performs comparably to algorithms based on multi-pass schemes involving a three-point Gaussian

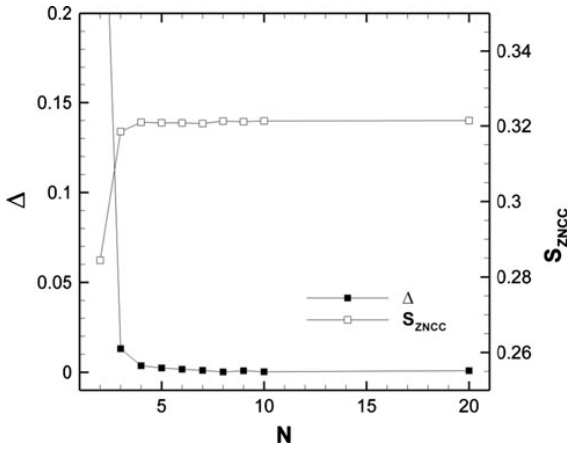

Fig. 8 Convergence with N of the displacement found by FOLKI-PIV at $X = 497$, $Y = 502$, image 1 of PIV challenge 2003 A's dataset. Plotted quantities are the correlation score S_{ZNCC} and the norm $\Delta(X, Y)$ of the difference between the displacement vector at iterations N and $N - 1$

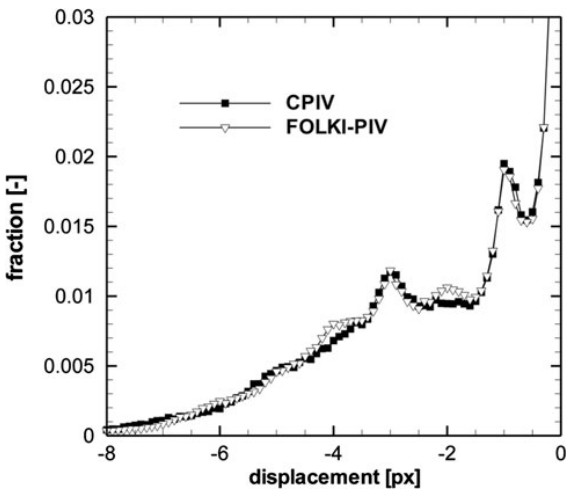

Fig. 9 Histograms of the U displacement

Exp Fluids (2011) 50:1169–1182 1179

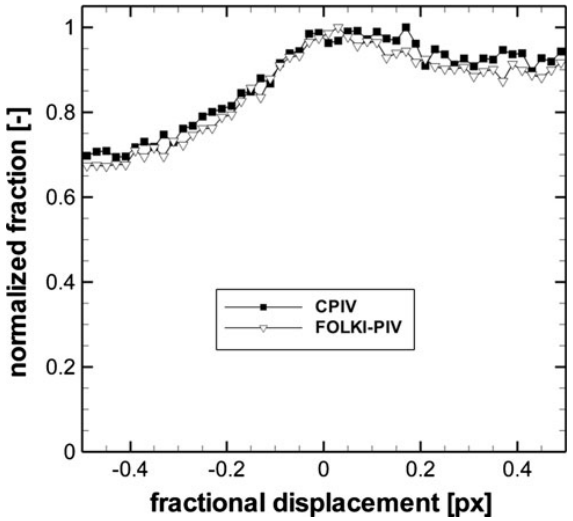

Fig. 10 Fractional part of the U displacement

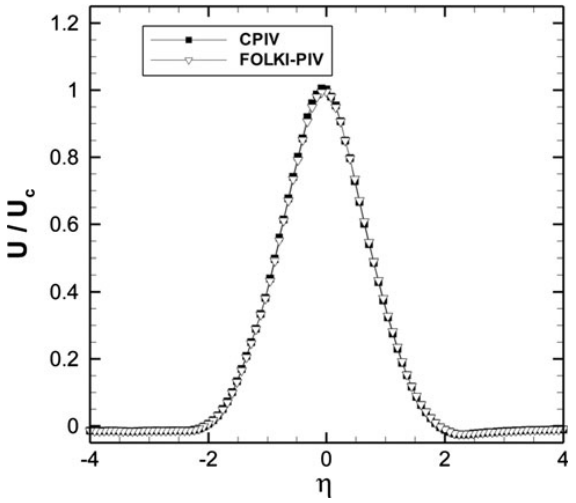

Fig. 11 Normalized mean horizontal displacement U/U_c as a function of the self-similar variable η

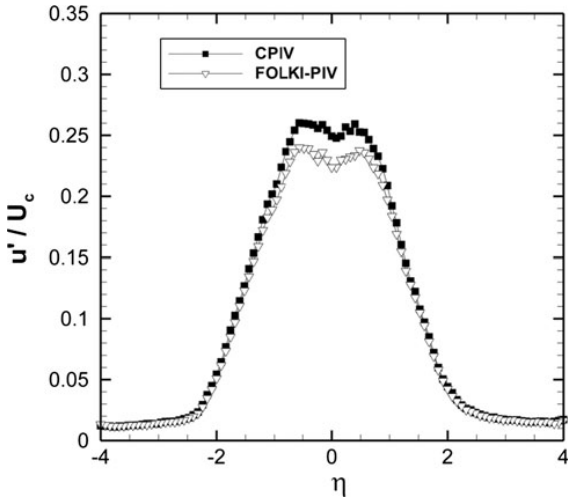

Fig. 12 Normalized rms horizontal displacement u'/U_c as a function of the self-similar variable η

sub-pixel interpolation (Westerweel 2000a, b; Westerweel et al. 1997).

Still following Stanislas et al. (2005), we now represent the mean and rms axial velocities U and u' as single one-dimensional profiles. This can be achieved by taking advantage of the jet self-similarity: first, the ensemble averaged axial velocity U must be fitted to

$$U(x-x_0, y-y_0) = U_c(x)\exp(-\eta^2) = U_c(x)\exp\left(-\frac{y^2}{l(x)^2}\right) \quad (20)$$

with

$$U_c(x) = \frac{A}{x-x_0} \quad \text{and} \quad l(x) = B(x-x_0), \quad (21)$$

using parameters B (jet spreading rate), x_0 and y_0 (jet virtual origin), and A. Then, values of U/U_c and u'/U_c from each profile at a given x may be gathered so as to represent one single profile depending on η. This is done in Figs. 11 and 12, respectively.

Concerning the mean velocity, an excellent agreement is found between CPIV and FOLKI-PIV. Both curves collapse almost perfectly, both in the jet itself and in the outer flow. The same remark also holds for the rms u' in the outer flow and in the jet shear layers (see Fig. 12). In the middle of the jet, for $-1.5 \le \eta \le 1.5$, discrepancies between both softwares are however observed, which are maximal in the plateau region, for $-0.6 \le \eta \le 0.6$. The average plateau value found by CPIV is of roughly 0.255, while that found by FOLKI-PIV is of roughly 0.235. Note that discrepancies of the same order of magnitude were found between algorithms tested during the second PIV challenge. To us, this is not surprising, since the present test case corresponds to difficult experimental conditions (seeding inhomogeneities in the individual images, differences in light intensity between two images in a pair, small particles). In practice, we find quite low values of the correlation score S_{ZNCC} close to the jet centerline, especially near the right edge of the images (typically, between 0.1 and 0.3). This may explain why algorithms may perform differently there.

As a last quality assessment from this test case, we consider the level of u'/U_c obtained in the outer flow region, where turbulence should progressively return to zero when $|\eta|$ increases. Similarly to the analysis performed

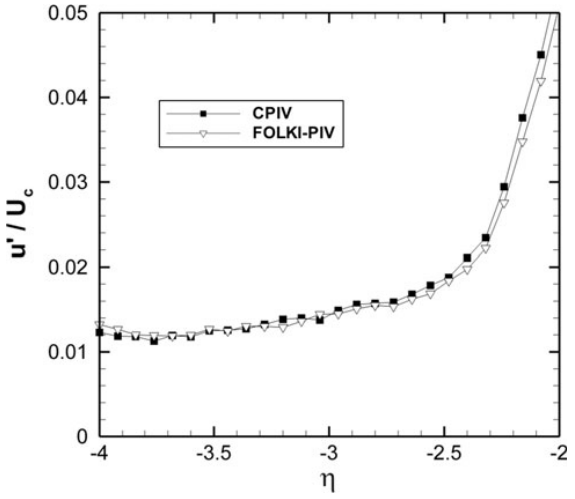

Fig. 13 Normalized rms horizontal displacement u'/U_c as a function of η, close-up

Table 2 Per image average computational time (in s), PIV challenge 2003 A dataset

FOLKI-PIV	CPIV standard	CPIV-high accuracy
0.2	9.4	19.4

All computations were performed on a PC with an Intel Core2 CPU at 3.16 *GHz*, 3 *Go* RAM and a NVIDIA Tesla C1060 GPU. See the text for more details on the settings used for each algorithm

by Stanislas et al. (2005), we plot in Fig. 13 a close-up of u'/U_c in the region $-4 \leq \eta \leq -2$. For $-4 \leq \eta \leq -3.5$, both codes reach approximately the same asymptotic limit of $u'/U_c \approx 0.012-0.013$. There as well, it appears that FOLKI-PIV performs nearly identically to a state-of-the-art PIV software using a FFT-based cross-correlation and a three-point Gaussian sub-pixel interpolation (Westerweel 2000a, b; Westerweel et al. 1997).

Finally, we compare in Table 2 the average time of computation of one vector field of this dataset for each algorithm. For CPIV, we also performed a simpler computation, composed of 1 pass with 64 × 64 IWs followed by 2 passes with 32 × 32 IWs, still with 50% overlap. Such a setting is usually a standard for a majority of PIV images, leading to a high enough accuracy. In Table 2, it is denoted by "CPIV-standard", as opposed to the setting used for the above comparisons, which is denoted by "CPIV-high accuracy". All these computations were performed on a machine equipped with an Intel Core2 CPU at 3.16 *GHz*, 3 *Go* RAM and a NVIDIA Tesla C1060 GPU.

As shown by Table 2, the high level of optimization of FOLKI together with the GPU implementation leads to computational gains ranging from 50 to 100 compared to a state-of-the-art traditional PIV approach, with a similar accuracy of the results.

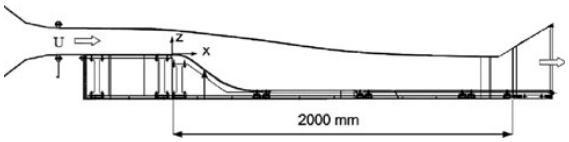

Fig. 14 Principle sketch of the ONERA S19Ch wind-tunnel

6.2 Massive flow separation over a rounded ramp (ONERA data, Gardarin et al. 2008)

The data considered in this paragraph are extracted a from High-Speed PIV (HS-PIV) test campaign on massive boundary layer separation and its control Gardarin et al. (2008), performed in the S19Ch wind-tunnel of ONERA Meudon center (see Fig. 14). In this closed-loop wind-tunnel, the test section is 300 mm wide and 2 m long and allows convenient optical access thanks to transparent lateral walls. As seen in Fig. 14, the flow enters the test section with a horizontal velocity $U = 30$ m s^{-1}. Separation then occurs due to the strong adverse pressure gradient created by the rounded ramp. While the purpose of the global test campaign has been to evaluate the efficiency of several control devices [in particular mechanical and fluidic vortex generators, Gardarin et al. (2008)], we here present the reference case, where the unforced separation occurs.

Figure 15 shows a sample image obtained with a HS-PIV system composed of a Litron LDY 303HE25 Nd:YLF laser and a Phantom V12.1 camera (1,280 × 800 pixels CCD). The generated laser sheet is 1 mm thick, and the flow is seeded using DiEthylHexyl Sebacate (DEHS) droplets. The repetition rate of the laser is set to 3 kHz, and the time interval between two images in a pair is 60 μs. The zone of interest is a rectangular field located near the

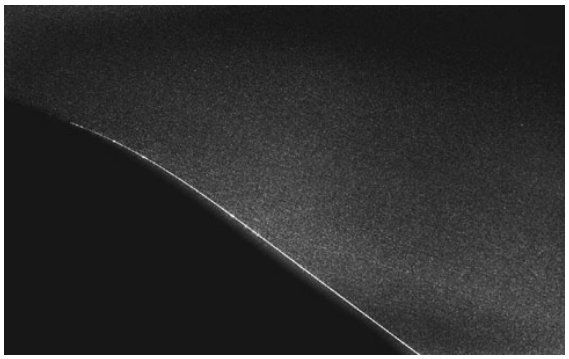

Fig. 15 PIV image sample of ONERA S19Ch HS-PIV experimental dataset

Exp Fluids (2011) 50:1169–1182

beginning of the rounded ramp, where boundary layer separation occurs. As mentioned above, this test case is specially interesting in that it combines several common experimental difficulties: a solid wall (the rounded ramp) is included inside the field of view so that a light reflection occurs on it, and the light intensity is not homogeneous in the bulk of the image, with in particular irregularities in the light sheet.

We have processed this PIV image pair with FOLKI-PIV using mean and standard deviation local normalization, and a mask following the contour of the rounded ramp. We used the following parameters: $R = 16$ IWs, $N = 6$ iterations, $J = 3$ pyramid levels. The value of N was chosen after a qualitative convergence study in the same way as described in Sect. 6.1.1. Results are shown in Figs. 16 and 17, which represent the obtained velocity field, together with vorticity iso-contours post-processed from this velocity field. To compute the velocity gradients involved in the vorticity, we used a 5×5 Gaussian filter before applying a traditional second-order finite difference scheme. Note that in both figures, the velocity field has been downsampled, respectively, to every 32×32 and 6×6 pixels.

Figure 16 shows that despite the difficult configuration, the flow physics is fully retrieved, since the boundary layer separation is precisely captured (here it is visible at around $x = -0.055$), as well as the various vortical structures which develop on the downstream mixing layer. Figure 17 confirms that FOLKI-PIV and its improvements described in Sect. 4 yield physically sound results even close to the wall, as seen from the various recirculation vortices which are captured until the mask edge. In this respect, it is important to emphasize that the dense result provided by the improved FOLKI-PIV is a real advantage, since it allows to sample the vector field even very close to obstacles.

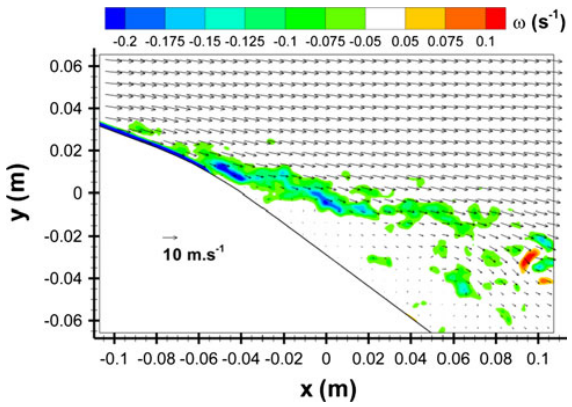

Fig. 16 Instantaneous velocity field obtained with FOLKI-PIV, together with iso-contours of vorticity post-processed from the velocity field by using a 5×5 pixels Gaussian filter. Vectors are displayed every 32×32 pixels

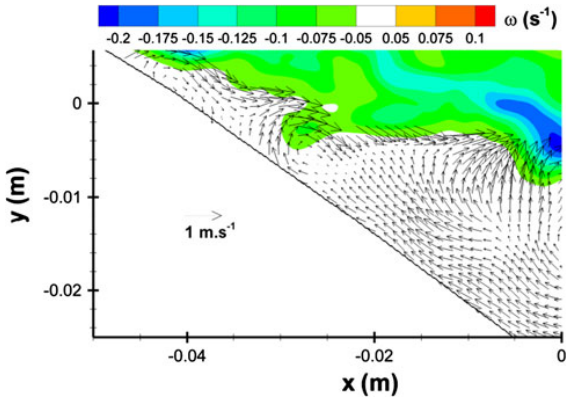

Fig. 17 Instantaneous velocity and vorticity field, close-up on the recirculation region. For clarity, we only plot velocity vectors which have a modulus inferior to 1 m s^{-1}. These vectors are displayed every 6×6 pixels

7 Conclusions

We have presented FOLKI-PIV an algorithm that performs fast computation of dense two-component (2C) PIV vector fields using Graphics Processing Units. Tested on both synthetic and real images, FOLKI-PIV proved as accurate as a state-of-the-art standard PIV software, while being 50 times faster and allowing a convenient degree of freedom for result sampling due to its dense character.

Our simulation study confirms that the behavior of FOLKI-PIV is that of a moving average filter—with $1/(2R)$ bandwidth, R being the window's radius. Robustness to noise is equal or better than state-of-the-art PIV software, without the need for any spurious vector rejection process between iterations. As a result, FOLKI-PIV appears very simple to tune for the practitioner.

To date, these features of FOLKI-PIV already offer to the experimentalists at ONERA a precious help in the way to conduct their PIV experiments, by allowing faster diagnosis on their experimental settings. Indeed, the accuracy of optical parameter tunings may now in particular be assessed also by investigating the mean and rms of the flows. This is especially precious when dealing with turbulent flows, which require a large number of image pairs for the turbulent statistics to converge. More generally, we believe that such a fast PIV code opens the way to significant changes in the way to perform experiments in fluids with PIV, allowing a much faster flow diagnosis and extending considerably possibilities of trial-and-error in the optimization phasis of experimental campaigns.

The basic rationale of the algorithm is furthermore generic enough to enable various extensions. On-going work considers Stereo PIV [see Leclaire et al. (2010)] and 3D velocity estimation for tomographic PIV, both settings which can be cast into the FOLKI-PIV scheme, so as to derive fast GPU implementation in the near future.

Acknowledgments Benoît Gardarin, Laurent Jacquin and Gilles Losfeld are gratefully acknowledged for providing their experimental TR-PIV dataset. Moreover the authors salute the helpful comments of the referees.

References

Baker S, Matthews I (2004) Lucas-Kanade 20 years on: a unifying framework. Int J Comput Vis 56(3):221–255

Bergen JR, Anandan P, Hanna KJ, Hingorani R (1992) Hierarchical model-based motion estimation. In: ECCV 92, Proceedings of the second European conference on computer vision, pp 237–252

Bouguet JY (2000) Pyramidal implementation of the Lucas-Kanade feature tracker: description of the algorithm. Tech. rep., Open CV Documentation

Burt P, Adelson E (1983) The Laplacian image pyramid as a compact image code. IEEE Trans Commun 31:532–540

Champagnat F, Plyer A, Le Besnerais G, Leclaire B, Le Sant Y (2009) How to calculate dense PIV vector fields at video rates. In: Proceedings of 8th international symposium on particle image velocimetry—PIV09, Melbourne

Corpetti T, Heitz D, Arroyo G, Mémin E, Santa-Cruz A (2006) Fluid experimental flow estimation based on an optical-flow scheme. Exp Fluids 40(1):80–97

Gardarin B, Jacquin L, Geffroy P (2008) Flow separation control with vortex generators. In: AIAA 4th flow control conference, Seattle, WA, 23–26 June

Iriarte Munoz J, Dellavale D, Sonnaillon M, Bonetto F (2009) Real-time particle image velocimetry based on FPGA technology. In: Programmable logic, 2009. SPL. 5th Southern conference on, pp 147–152

Keller Y, Averbuch A (2004) Fast motion estimation using bi-directional gradient methods. IEEE Trans Image Process 13(8):1042–1054

Le Besnerais G, Champagnat F (2005) Dense optical flow by iterative local window registration. In: ICIP'05, Proceedings of the IEEE international conference on image processing, vol I, pp 137–140

Leclaire B, Le Sant Y, Davoust S, Le Besnerais G, Champagnat F (2010) FOLKI-SPIV: a new, ultra-fast approach for stereo PIV. submitted to Experiments in Fluids

Lecordier B, Trinite M (2003) Advanced PIV algorithms with image distortion validation and comparison using synthetic images of turbulent flow. In: Stanislas M, Westerweel J, Kompenhans J (eds) Particle image velocimetry: recent improvements. Proceedings of the EUROPIV 2 workshop, Springer, pp 115–132

Lecordier B, Trinité M (2006) Accuracy assessment of image interpolation schemes for PIV from real images of particle. In: Proc. 13th int. symp. on appl. of laser techn. to fluid mechanics, Lisbon, Portugal

Lecordier B, Westerweel J (2003) The EUROPIV Synthetic Image Generator (SIG). In: Stanislas M, Westerweel J, Kompenhans J (eds) Particle image velocimetry: recent improvements. EUROPIV 2 workshop, Springer

Miozzi M (2004) Particle image velocimetry using feature tracking and Delaunay Tessellation. In: Proceedings of the XII international symposium on application of laser technique to fluid mechanics, Lisbon

Pan B, Xie H, Guo Z, Hua T (2007) Full-field strain measurement using a two-dimensional Savitzky-Golay digital differentiator in digital image correlation. Opt Eng 46(3):1–10

Raffel M, Willert C, Wereley C, Kompenhans J (2007) Particle image velocimetry. A practical guide, 2nd edn. Springer, Heidelberg

Ruhnau P, Kohlberger T, Schnörr C, Nobach H (2005) Variational optical flow estimation for particle image velocimetry. Exp Fluids 38:21–32

Ruijters D, ter Haar Romeny BM, Suetens P (2008) Efficient GPU-based texture interpolation using uniform B-splines. J Graphics GPU Game Tools 13(4):61–69

Scarano F, Riethmuller M (2000) Advances in iterative multigrid PIV image processing. Exp Fluids 29:51–60

Schiwietz T, Westermann R (2004) GPU-PIV. In: Girod B, Magnor MA, Seidel HP (eds) Proceedings of the vision, modeling, and visualization conference, Aka GmbH, Stanford, CA, pp 151–158

Stanislas M, Okamoto K, Kähler CJ, Westerweel J (2005) Main results of the second international PIV challenge. Exp Fluids 39:170–191

Stanislas M, Okamoto K, Käler CJ, Westerweel J, Scarano F (2008) Main results of the third international PIV challenge. Exp Fluids 45:27–71

Venugopal V, Patterson C, Shinpaugh K (2009) Accelerating particle image velocimetry using hybrid architectures. In: Proceedings of symposium on application accelerators in high performance computing (SAAHPC'09), Urbana, Illinois

Westerweel J (1993) Digital particle image velocimetry—theory and application. PhD thesis, University Press, Delft

Westerweel J (2000a) Effect of sensor geometry on the performance of PIV interrogation. Laser techniques applied to fluid mechanics. Springer, Berlin, pp 37–55

Westerweel J (2000b) Theoretical analysis of the measurement precision in particle image velocimetry. Exp Fluids 29:3–12

Westerweel J, Dabiri D, Gharib M (1997) The effect of a discrete window offset on the accuracy of cross-correlation analysis of digital PIV recordings. Exp Fluids 23(1):20–28

Yamamoto Y, Uemura T (2009) Robust particle image velocimetry using gradient method with upstream difference and downstream difference. Exp Fluids 46(4):659–670

Yu H, Leeser M, Tadmor G, Siegel S (2006) Real-time particle image velocimetry for feedback loops using FPGA implementation. J Aerosp Comput Inf Commun 3(2):52–62

Zhao W, Sawhney H (2002) Is super-resolution with optical flow possible? In: ECCV02, Proceedings of the European conference on computer vision, pp 153–162

B Etude des incertitudes des mesures PIV

B.1 Sources d'erreurs

Comme rappelé dans Raffel et al. [99], l'erreur totale qui affecte chaque vecteur vitesse se décompose en une série de biais à laquelle s'ajoute une erreur aléatoire de mesure.

B.1.1 Erreur aléatoire de mesure

Une erreur aléatoire affecte l'estimation du déplacement par algorithme de dépouillement. En guise d'exemple, la position du pic de corrélation de la sous-section 2.3.1 est déterminée avec une certaine incertitude. Comme le montre la figure 7 de l'annexe A, cette incertitude dépend de la taille de la fenêtre d'interrogation et de la qualité des images. Dans les conditions expérimentales, on admet qu'une incertitude de 0.1 pixel affecte l'estimation du déplacement. Dans notre cas, cela équivaut à une incertitude relative de 1.5% sur la vitesse car notre dynamique moyenne représente à environ 7 pixel de déplacement. Il est possible de vérifier cette estimation en comparant la rms de la vitesse axiale mesurée par PIV à celle d'un fil-chaud au centre du jet. On obtient 2% pour la PIV et alors que le fil-chaud indique 0.5%. Ceci confirme que l'incertitude due à cette erreur aléatoire de mesure PIV est de l'ordre de 1.5%.

B.1.2 Erreur de positionnement

Une erreur de positionnement est inhérente à toute mesure d'un champ dans l'espace. Grâce à un laser en autocolimation avec le plan de sortie du jet qui définit l'axe du jet, nous estimons avoir atteint une précision de $0.5mm$ sur la position de la mire de calibration par rapport au repère soufflerie. Mais, l'épaisseur de la nappe, qui peut atteindre 3 mm, introduit une première incertitude quant à la position réelle du plan de mesure.

B.1.3 Erreur de reconstruction stéréoscopique

La qualité de la reconstruction stéréoscopique dépend de la calibration des caméra. Lors des étalonnages, on peut définir une erreur d'étalonnage moyenne définie comme l'écart entre la position réelle des marqueurs de la mire de calibration sur l'image, et leur position estimée par la fonction pin-hole de calibration qui projette la géométrie de la mire sur le capteur de la caméra. Cette écart moyen est de l'ordre de 0.1 px, pour chaque marqueur. Il est néanmoins difficile d'estimer l'impact de cet écart moyen, car il résulte de facteurs qui sont parfois indépendants de la calibration elle-même, notamment la qualité de l'éclairage de la mire. Dans la sous-section suivante, nous proposons

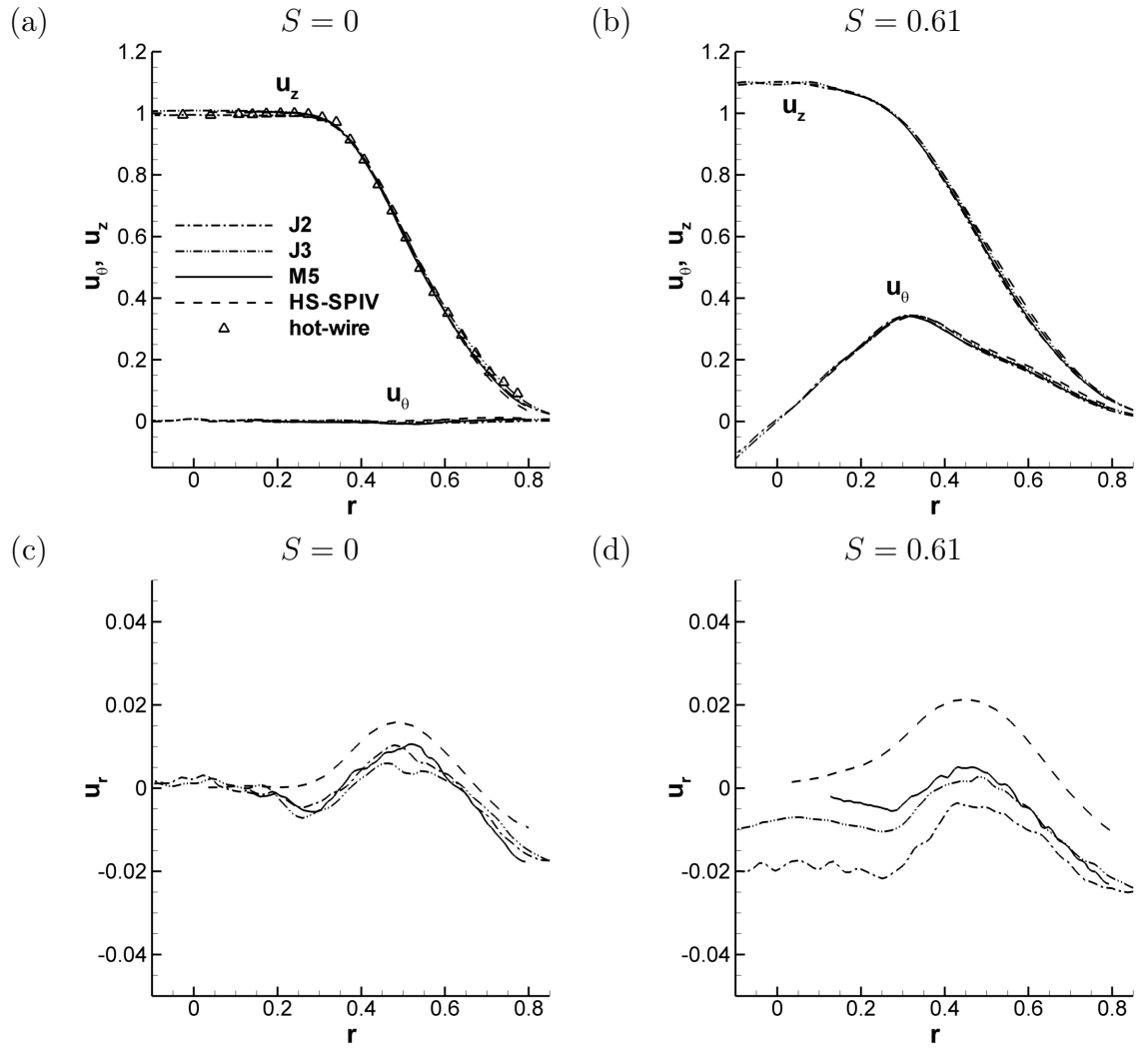

FIGURE B.1 – Comparaison entre des mesures réalisées à $z = 2$ par différents sondages PIV ainsi que par fil-chaud (seulement pour la vitesse axiale). Vitesses moyenne axiale et azimutale pour $S = 0$ (a) et $S = 0.61$ (b). Vitesse moyenne radiale pour $S = 0$ (c) et $S = 0.61$ (d). La légende de toutes les courbes est donnée sur la figure (a).

donc d'estimer l'erreur de positionnement et l'erreur de reconstruction stéréoscopique de manière simultanée.

B.1.4 Incertitude résultante des erreurs de positionnement et de reconstruction

L'intersection en $z = 2$ des plans PIV libellés J2, J3, M5 et HS-SPIV (voir sous-section 2.2.3) permet d'obtenir une estimation des incertitudes qui résultent des erreurs de positionnement et de reconstruction stéréoscopique, en comparant les vitesses moyennes obtenues par ces mesures comme dans la figure B.1. Les figures B.1 (a) et (b) révèlent que l'écart entre les vitesses moyennes axiales et azimutales mesurées par les différents plans PIV est inférieur à 1% pour $S = 0$ et pour $S = 0.61$. Pour $S = 0$, figure B.1 (a), une validation supplémentaire est apportée par une mesure de la vitesse axiale par un fil chaud. On note aussi que la condition $u_\theta = 0$ est bien respectée, à 1% près, ce qui confirme que les plans longitudinaux sont parallèles à l'axe du jet. Pour $S = 0.61$, figure B.1 (b),

le profil de vitesse azimutale moyenne de rotation solide vérifie bien $u_\theta(r=0)=0$, ce qui indique a minima que l'origine verticale des plans de mesures longitudinaux SPIV correspond bien à l'axe du jet. La composante radiale de la vitesse moyenne est ensuite comparée dans les figures B.1 (c) et (d). Pour $S=0$ (c) l'écart entre les différentes mesures est consistant avec la dispersion de 1% observé sur les autres composantes. On note les faibles valeurs de cette composante, conformément à la nature de type couche de mélange mince de cet écoulement. On observe aussi que $u_r(r=0)=0$, ce qui confirme alors que le plan de mesure PIV est bien orienté dans la direction de l'écoulement (sinon la composante de vitesse axiale affecterait la composante radiale mesurée). D'ailleurs, pour $S=0.61$ (figure B.1 (d)), on constate une nette dispersion des mesures, de l'ordre de 2%, avec notamment $u_r(r=0)\neq 0$. Nous avons noté que ce phénomène était la manifestation d'un léger décalage du plan de mesure par rapport à l'axe du jet (de l'ordre de la demi épaisseur de nappe, soit 1.5 mm). La composante de vitesse azimutale pollue alors la composante radiale mesurée à hauteur de $2S\frac{1.5\text{mm}}{D_0}\approx 1.6\%$ pour $S=0.61$. Cette erreur n'est alors pas visible pour $S=0$. Pour conclure, on peut donc dire qu'en ce qui concerne les champs moyens, les erreurs de positionnement et de reconstruction stéréoscopique se traduisent par une incertitude de l'ordre de 1% sur les vitesses moyennes axiale et azimutale, et de l'ordre de 2% pour la vitesse radiale. On peut s'attendre à retrouver des incertitudes similaires sur les champs instantanés.

B.1.5 Biais de filtrage spatial

Taille physique de la fenêtre d'interrogation (FI)

Comme nous l'avons montré dans l'annexe A, la mesure par PIV entraine une intégration spatiale du champ des vitesses instantanées sur la fenêtre d'interrogation (FI). Nous avons montré (voir figure 4, annexe A) que la fréquence spatiale de coupure à $-3dB$ notée K_{-3dB} s'écrit

$$K_{-3dB}=0.45/(L_{\text{FI}}), \tag{B.1}$$

ici L_{FI} est la largeur correspondant à la FI dans l'espace physique. D'après Foucaut et al. [35], ce filtrage spatial a pour effet d'atténuer le contenu énergétique des petites échelles d'un spectre unidirectionnel des fluctuations, alors que l'énergie contenue dans les grandes échelles est fidèlement reproduite. On peut donc constater une différence avec les conclusions de l'étude de l'intégration spatiale par un long fil-chaud menée par Citriniti and George [21], qui montre que l'intégration spatiale du signal selon une direction privilégiée conduit à un abaissement des niveaux de l'ensemble du spectre unidirectionnel.

La largeur de la FI dans l'espace physique est donnée par

$$L_{\text{FI}}=\frac{\mathcal{L}_{\text{FI}}L_{\text{PIV}}}{M}, \tag{B.2}$$

où $\mathcal{L}_{\text{FI}}$ est la taille de la FI en pixel, L_{PIV} la taille physique d'un pixel, et M le rapport de grandissement entre le plan objet et le plan image. Notons que cette échelle caractérise la taille de la FI dans la direction verticale Y commune aux deux caméras, voir figure 2.3. Le tableau B.1 résume l'estimation de L_{FI} par la relation (B.2) pour chacun des plans réalisés. Le filtrage spatial qui va s'opérer constitue alors un biais qui peut affecter la détermination des variations spatiales des champs des vitesses instantanées ou moyennes.

	J1	J2	J3	J4	M1	M2	M3	M4	M5	HS-SPIV
L_{FI} (mm)	2.89	4.60	4.59	7.05	0.87	1.29	1.30	1.66	2.88	6.14

TABLE B.1 – Largeur de la fenêtre d'interrogation (FI) L_{FI} dans l'espace physique pour chaque plan PIV réalisé (voir figure 2.4).

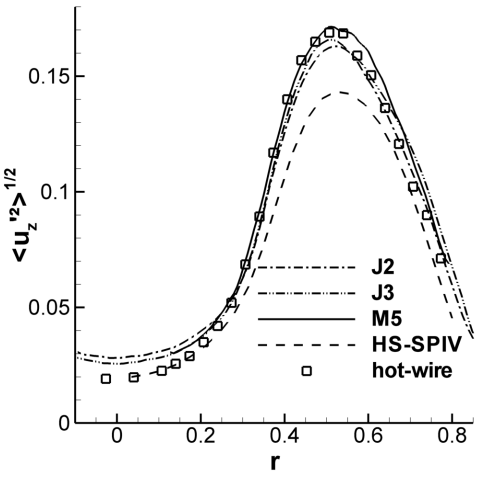

FIGURE B.2 – Comparaison entre des rms de la vitesse axiale mesurées à $z = 2$ par différents plans PIV ainsi que par un sondage fil-chaud.

Impact sur les rms

L'impact d'un tel filtrage peut être observé sur les rms des composantes des vitesses. La figure B.2 compare les profils de rms de vitesse axiale donné par le fil-chaud avec ceux des plans PIV. Mis à part dans la zone du coeur du jet, nous observons un bon accord de la mesure issue du plan SPIV M5 avec celle du fil-chaud. La résolution spatiale du plan M5 pour $L_{\mathrm{FI}} = 2.88$ mm, cf. tableau B.1, semble suffisante pour capturer toutes les échelles énergétiques. Par ailleurs, on constate que les mesures issues des plans J2 et J3 qui sont moins spatialement résolues, affichent une légère dégradation du maximum de rms. Pour une mesure en $z = 2$, cette taille de fenêtre d'interrogation $L_{FI} \approx 3$ mm représente donc une limite inférieure. Nous pouvons associer à cette échelle une taille de FI adimensionnée par l'épaisseur de la couche de mélange en posant :

$$l_{\mathrm{FI}} = \frac{L^{\mathrm{FI}}}{D_0 \delta_\omega} \approx 0.1. \tag{B.3}$$

Comme l'écoulement de couche de mélange est auto-semblable il suffit de conserver $l^z_{\mathrm{FI}} \leq 0.1$ pour ne pas filtrer les échelles énergétiques. Comme le montre la table B.1, la taille physique de FI diminue des plans M4 vers M1, alors que l'épaisseur de la couche de mélange diminue linéairement vers l'amont (voir la figure 11 du chapitre 5). Cette analyse permet alors de prévoir que le filtrage des échelles énergétiques ne pourra plus être négligé en deçà de $z \leq 0.1$ dans le plan M1, ce qui valide donc le choix de la taille des plans PIV. Les rms mesurées seront alors baisées par ce filtrage.

Bénéfice pour la HS-SPIV

Ce filtrage spatial est cependant utile lors de l'acquisition haute-cadence de HS-SPIV. En effet, lorsque l'on échantillonne un signal à la fréquence F_{acq}, il est impératif de filtrer

les fréquences supérieures à $F_{\text{acq}}/2$ (fréquence de Nyquist) si l'on veut éviter le repliement spectral des hautes fréquences [93]. Lors d'une acquisition fil-chaud, on effectue donc un filtrage analogique du signal avant l'échantillonnage. Or, il n'existe pas de moyen de réaliser cela avec la HS-SPIV. Dans ce cas le filtrage des petites échelles par la résolution spatiale limitée s'avère utile. Si l'on dénote F_{-3dB} la fréquence de coupure à $-3dB$ de la HS-SPIV, pour limiter le repliement, il est souhaitable d'imposer une condition du type :

$$F_{-3dB} \leq F_{\text{acq}}/2 \tag{B.4}$$

Il est possible d'estimer F_{-3dB} en utilisant la taille physique de la FI L^{FI} (voir table B.1), ainsi que la relation (B.1) suivie d'une hypothèse de Taylor pour déterminer la fréquence. On obtient alors la condition

$$F_{-3dB} \approx u_c U_0 K_{-3dB} \approx u_c U_0 \times 0.45/(L_{\text{FI}}) \approx 1kHz, \tag{B.5}$$

$u_c = 0.6$ est l'échelle de la vitesse de convection. Il est donc à priori nécessaire d'effectuer une acquisition pour $F_{\text{acq}} \geq 2kHz$ si l'on veut limiter le repliement spectral, ce qui conforte notre choix de $F_{acq} = 2.5kHz$.

B.2 Convergence statistique

B.2.1 Moyennes d'ensemble

Dans cette section, nous considérons les 3 moyennes d'ensemble que nous utilisons pour l'analyse des résultats PIV. On considère une variable aléatoire $a(r, \theta, z, t)$. La première moyenne que nous définissons concerne l'ensemble des $N = 5000$ clichés SPIV, et notée

$$\langle a \rangle = \frac{1}{N} \sum_{i=1}^{N} a(r, \theta = 0, z, t_i), \tag{B.6}$$

t_i représente l'instant de l'acquisition. Nous utilisons aussi une moyenne azimutale sur N_θ position des N_b blocs de N_{ech} échantillons de clichés HS-SPIV réalisés au plan $z = 2$:

$$\langle a \rangle_{\theta,t} = \frac{1}{N_b N_{\text{ech}} N_\theta} \sum_{i=1}^{N_b} \sum_{j=1}^{N_{\text{ech}}} \sum_{k=1}^{N_\theta} a_i(r, \theta_k, z = 2, t_j). \tag{B.7}$$

Une autre moyenne est utilisée pour déterminer les corrélations en deux points à partir des résultats d'acquisitions HS-SPIV. On définit alors une moyenne en sommant sur les blocs et l'azimut. Cette moyenne est définie par

$$\langle a(r', \theta + \theta', t + t') a(r, \theta, t) \rangle_\theta = \frac{1}{N_b N_\theta} \sum_{i=1}^{N_b} \sum_{k=1}^{N_\theta} a_i(r', \theta_k + \theta', 2, t + t') a_i(r, \theta_k, 2, t). \tag{B.8}$$

De manière générale, nous avons réorganisé les données HS-SPIV de manière à obtenir $N_b = 210$ blocs de $N_{\text{ech}} = 256$ échantillons.

B.2.2 Echelles intégrales

Pour estimer le nombre d'échantillons statistiquement indépendants équivalents lors du calcul des moyennes, il est nécessaire d'obtenir une approximation des échelles intégrales azimutales et temporelles notées θ_{int} et $\mathcal{T}_{\text{int}}$. Nous proposons d'utiliser une estimation basée sur la moitié de l'épaisseur de vorticité δ_ω, à la manière de Citriniti and

George [22] :

$$\theta_{\text{int}} \approx \frac{\frac{\delta_\omega}{2}}{2\pi 0.5} \approx 20^\circ \tag{B.9}$$

$$\mathcal{T}_{\text{int}} \approx \frac{\frac{\delta_\omega}{2} D_0}{u_c U_0} \approx 0.003s. \tag{B.10}$$

L'échantillonnage à $4Hz$ de la SPIV est suffisamment lent pour que les N échantillons soient statistiquement indépendants. Pour la HS-SPIV, le nombre d'échantillons statistiquement indépendants lors d'une moyenne sur l'azimut ou sur un nombre $N_{\text{ech}} = 256$ d'échantillons s'écrit alors [43] :

$$\tilde{N}_\theta = \frac{2\pi}{2\theta_{\text{int}}} \approx 10 \tag{B.11}$$

$$\tilde{N}_{\text{ech}} = \frac{N_{\text{ech}}}{f_{\text{acq}} 2\mathcal{T}_{\text{int}}} \approx 20. \tag{B.12}$$

La moyenne $\langle\rangle_{\theta,t}$ bénéficie donc d'un nombre échantillons statistiquement indépendants de $\tilde{N}_{\langle\rangle\theta,t} \approx 40000$ alors que la moyenne $\langle\rangle_\theta$ est réduite à $\tilde{N}_{\langle\rangle\theta} \approx 2000$ échantillons. Cette analyse, que nous avons mené pour $S = 0$, peut se généraliser aux autres nombres de swirl.

B.2.3 Estimation des incertitudes pour une distribution normale

La détermination de l'incertitude d'une grandeur statistique a estimée par une moyenne d'ensemble est abondamment décrite dans la littérature [7, 43, 117]. La variance de l'estimateur de la grandeur statistique est considérée afin de définir un intervalle de confiance. Par exemple, en ce qui concerne la valeur moyenne a de la variable aléatoire $a(r, 0, z, t_i)$, la variance de l'estimateur $a = \langle a(r, 0, z, t_i)\rangle$ basée sur les N échantillons indépendants s'exprime :

$$\text{var}(a) = \frac{\langle a'^2\rangle}{N} \tag{B.13}$$

L'intervalle $\pm 1.96\sqrt{\text{var}(a)}$ autour de la grandeur estimée a représente l'intervalle de confiance de 95%, c'est à dire qui contient la valeur réelle de la moyenne avec une probabilité supérieure à 95%. Nous faisons maintenant référence à l'analyse menée par Benedict and Gould [7]. Dans le cas des moments d'ordre 2, nous nous plaçons dans l'hypothèse d'une distribution normale pour estimer les variances des estimateurs. Dans cette analyse, conformément à nos observations expérimentales, nous avons fixé $u' = 0.2$ pour échelle des fluctuations de vitesse, et $\omega'_z = \frac{1}{\delta_\omega} = 2.8$ pour échelle des fluctuations de vorticité axiale. L'écart-type des estimateurs calculés correspond alors au cas le plus défavorable. Le tableau suivant B.2 regroupe l'écart attendu pour les estimateurs des principales grandeurs statistiques considérées dans nos travaux.

grandeur	valeur de référence	moyenne	écart type de l'estimateur
$u_i, (i = r, \theta, z)$	1	$\langle\rangle$	0.003
$\langle u_i' u_j' \rangle, (i, j = r, \theta, z)$	0.04	$\langle\rangle$	0.001
$C_{u_\theta u_\theta}$	1	$\langle\rangle$	0.015
$u_i, (i = r, \theta, z)$	1	$\langle\rangle_{\theta,t}$	0.001
ω_z	$2S$	$\langle\rangle_{\theta,t}$	0.04
$C_{\omega_z\omega_z}$, $C_{\omega_z u_z}$	1	$\langle\rangle_\theta$	0.02

TABLE B.2 – Ecart-type des différents estimateurs calculés dans nos travaux.

B.2.4 Utilisation des symétries

L'approche présentée ci-dessus donne une majoration des incertitudes des moments d'ordre 1 et 2. Les corrélations spatio-temporelles définies par

$$C_{\omega_z\omega_z}(r, r', \theta', t') = \frac{\langle \omega_z'(r, \theta, t)\omega_z'(r', \theta + \theta', t + t')\rangle_\theta}{\langle \omega_z'^2(r, \theta, t)\rangle_\theta}, \tag{B.14}$$

$$C_{\omega_z u_z}(r, r', \theta', t') = \frac{\langle \omega_z'(r, \theta, t)u_z'(r', \theta + \theta', t + t')\rangle_\theta}{\langle \omega_z'^2(r, \theta, t)\rangle_\theta^{1/2}\langle u_z'^2(r, \theta, t)\rangle_\theta^{1/2}}, \tag{B.15}$$

$$C_{\omega_z^2 u_z}(r, r', \theta', t') = \frac{< \omega_z'^2(r, \theta, t)u_z'(r', \theta + \theta', t + t') >_\theta}{< \omega_z'^2(r, \theta, t) >_\theta \sqrt{< u_z'^2(r, \theta, t) >_\theta}}, \tag{B.16}$$

sont utilisées dans les chapitres 4 et 5. Il est facile de montrer que pour $S = 0$, l'estimation des fonctions $C_{\omega_z\omega_z}$ et $C_{\omega_z^2 u_z}$ doit converger vers une fonction paire ($\theta' \to -\theta'$), alors que l'estimation de $C_{\omega_z u_z}$ doit converger vers une fonction impaire. Ces symétries sont effectivement observées, comme on peut le voir sur la figure 15 du chapitre 4 et sur la figure 27 du chapitre 5 pour $S = 0$. L'écart des estimateurs vis à vis de ces symétries permet alors d'estimer leur convergence. Nous définissons alors les variances suivantes :

$$\mathrm{Var}_{\omega_z\omega_z}(r) = \frac{1}{1.68\pi\Delta t}\int_{0.38}^{0.8}\int_{-\pi}^{\pi}\int_{-\Delta t}^{\Delta t}\left(C_{\omega_z\omega_z}(r, r', \theta', t') - C_{\omega_z\omega_z}(r, r', -\theta', t')\right)^2 \mathrm{d}t'\mathrm{d}\theta'\mathrm{d}r', \tag{B.17}$$

$$\mathrm{Var}_{\omega_z u_z}(r) = \frac{1}{1.68\pi\Delta t}\int_{0.38}^{0.8}\int_{-\pi}^{\pi}\int_{-\Delta t}^{\Delta t}\left(C_{\omega_z u_z}(r, r', \theta', t') + C_{\omega_z u_z}(r, r', -\theta', t')\right)^2 \mathrm{d}t'\mathrm{d}\theta'\mathrm{d}r', \tag{B.18}$$

$$\mathrm{Var}_{\omega_z^2 u_z}(r) = \frac{1}{4\pi\Delta t}\int_{-\pi}^{\pi}\int_{-\Delta t}^{\Delta t}\left(C_{\omega_z^2 u_z}(r, r' = 0.24, \theta', t') - C_{\omega_z^2 u_z}(r, r', -\theta', t')\right)^2 \mathrm{d}t'\mathrm{d}\theta'. \tag{B.19}$$

L'intervalle de temps $[-\Delta t, +\Delta t]$ couvre l'ensemble du domaine de définition des fonctions. Pour $C_{\omega_z\omega_z}$ et $C_{\omega_z u_z}$, nous n'avons pas intégré les erreurs pour $r \leq 0.38$ car nous n'étudions pas ces fonctions dans le coeur du jet. Pour $C_{\omega_z^2 u_z}$, nous nous limitons à $r' = 0.24$ car c'est le seul rayon que nous avons considéré. En utilisant alors $r = 0.38$, $r = 0.52$ et $r = 0.66$ à la manière des analyses des chapitres 4 et 5, nous obtenons alors les écarts types regroupés dans la table B.3. Pour $S = 0$, on peut donc majorer l'écart des estimateurs $C_{\omega_z\omega_z}$ et $C_{\omega_z^2 u_z}$ à 5×10^{-3}. Cette estimation est quatre fois inférieure à celle obtenue par l'analyse supposant une distribution normale donnée dans la table B.2,

et correspond ainsi mieux aux dissymétries que l'on observe. Enfin, l'écart type associé à l'estimation de $C_{\omega_z^2 u_z}$ dépend de r, de même que l'amplitude des oscillations de la fonction $C_{\omega_z^2 u_z}$ elle-même. Ceci permet d'obtenir un écart type constant, relativement à l'amplitude de ces oscillations.

estimateur	r	valeur de référence	écart type de symétrie $\sqrt{\text{Var}}$
$C_{\omega_z\omega_z}$	$r = 0.38$	1	3.5×10^{-3}
	$r = 0.52$	1	2.1×10^{-3}
	$r = 0.66$	1	3.7×10^{-3}
$C_{\omega_z u_z}$	$r = 0.38$	0.3	4.9×10^{-3}
	$r = 0.52$	0.3	3.1×10^{-3}
	$r = 0.66$	0.3	4.5×10^{-3}
$C_{\omega_z^2 u_z}$	$r = 0.38$	0.2	2.7×10^{-3}
	$r = 0.52$	0.02	9.8×10^{-4}
	$r = 0.66$	0.04	1.4×10^{-3}

TABLE B.3 – Tableau regroupant les écart types de symétrie des fonctions de corrélations en deux points calculés.

B.2.5 Autres méthodes

Dans le chapitre 5, section 4, nous avons introduit plusieurs autres grandeurs dérivées des estimateurs des tenseurs déformation et de Reynolds, comme des paramètres d'orientation, des angles d'inclinaison, et les valeurs propres des tenseurs considérés. Nous avons vérifié la convergence des estimateurs diminuant le nombre d'échantillons utilisés dans les estimateurs statistiques de $N = 5000$ à $N = 500$. Les résultats sont comparés aux résultats convergés dans les figures B.3 et B.4. Pour chaque grandeur, l'accord entre les deux statistiques permet d'aboutir aux mêmes conclusions que dans le chapitre 5. Les conclusions tirées des analyses statistiques des $N = 5000$ échantillons sont donc validées.

Cette approche qui consiste à diminuer le nombre d'échantillons pour vérifier la convergence a aussi été utilisée pour l'estimation de statistiques en un point de la vorticité de la section 5 du chapitre 5. La figure B.5 présente la convergence des estimateurs de ω_z (a), $\langle \omega_z^2 \rangle_{\theta,t}$ (b), $\langle \omega_z^3 \rangle_{\theta,t}$ (c) et $\langle u_r \omega_z^2 \rangle_{\theta,t}$ (d) pour un nombre de blocs de données HS-SPIV réduit. Grâce à la moyenne azimutale, la convergence est très bonne pour toutes ces grandeurs, même en ne gardant que $N_b = 7$ blocs sur l'ensemble des $N_b = 210$ blocs.

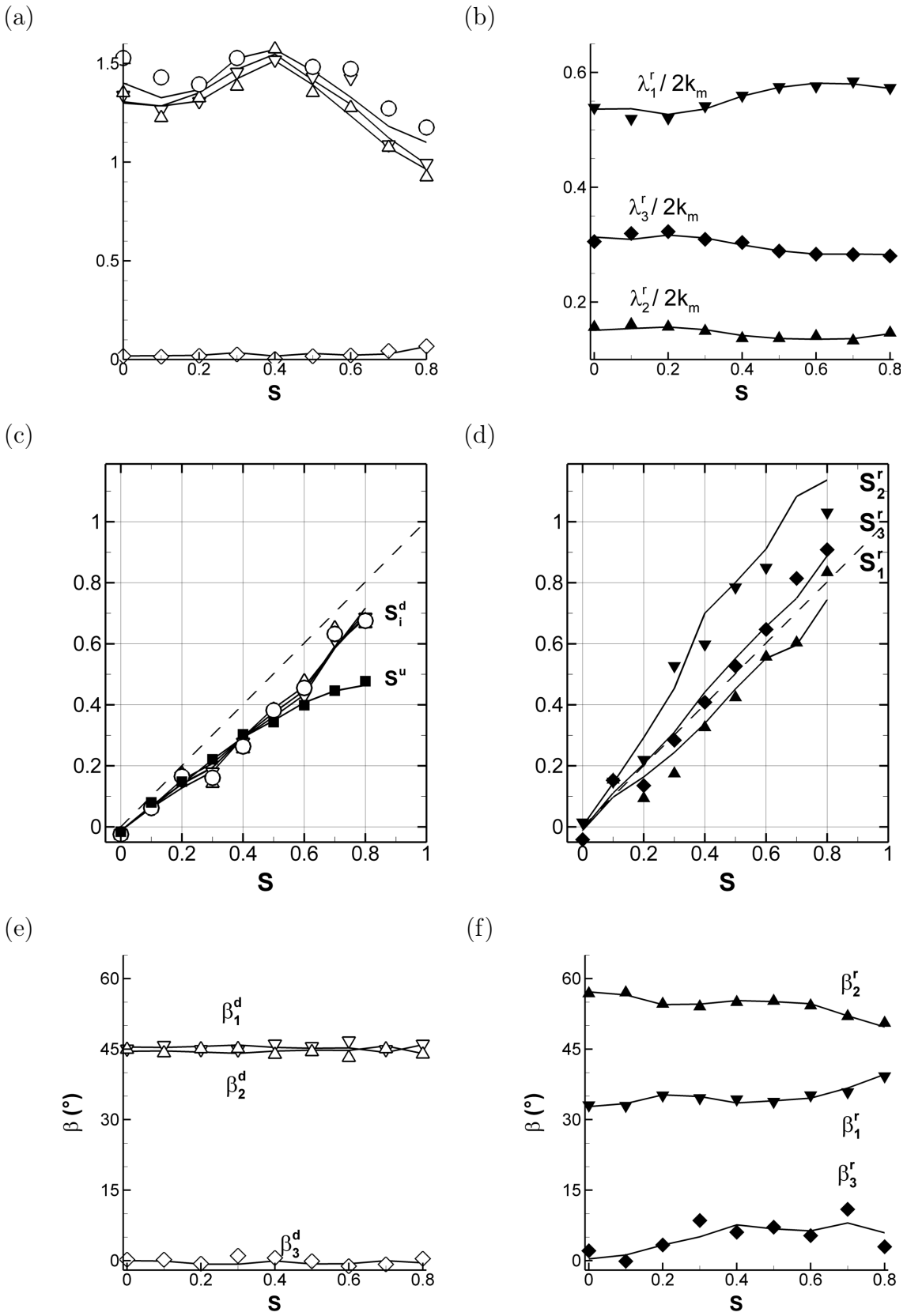

FIGURE B.3 – Convergence statistique correspondant aux figures 15 et 16 du chapitre 5. Les symboles correspondent aux estimations qui utilisent seulement $N = 500$ échantillons, alors que les lignes sont les estimations qui utilisent l'ensemble des $N = 5000$ échantillons, comme présenté dans les figures du chapitre 5.

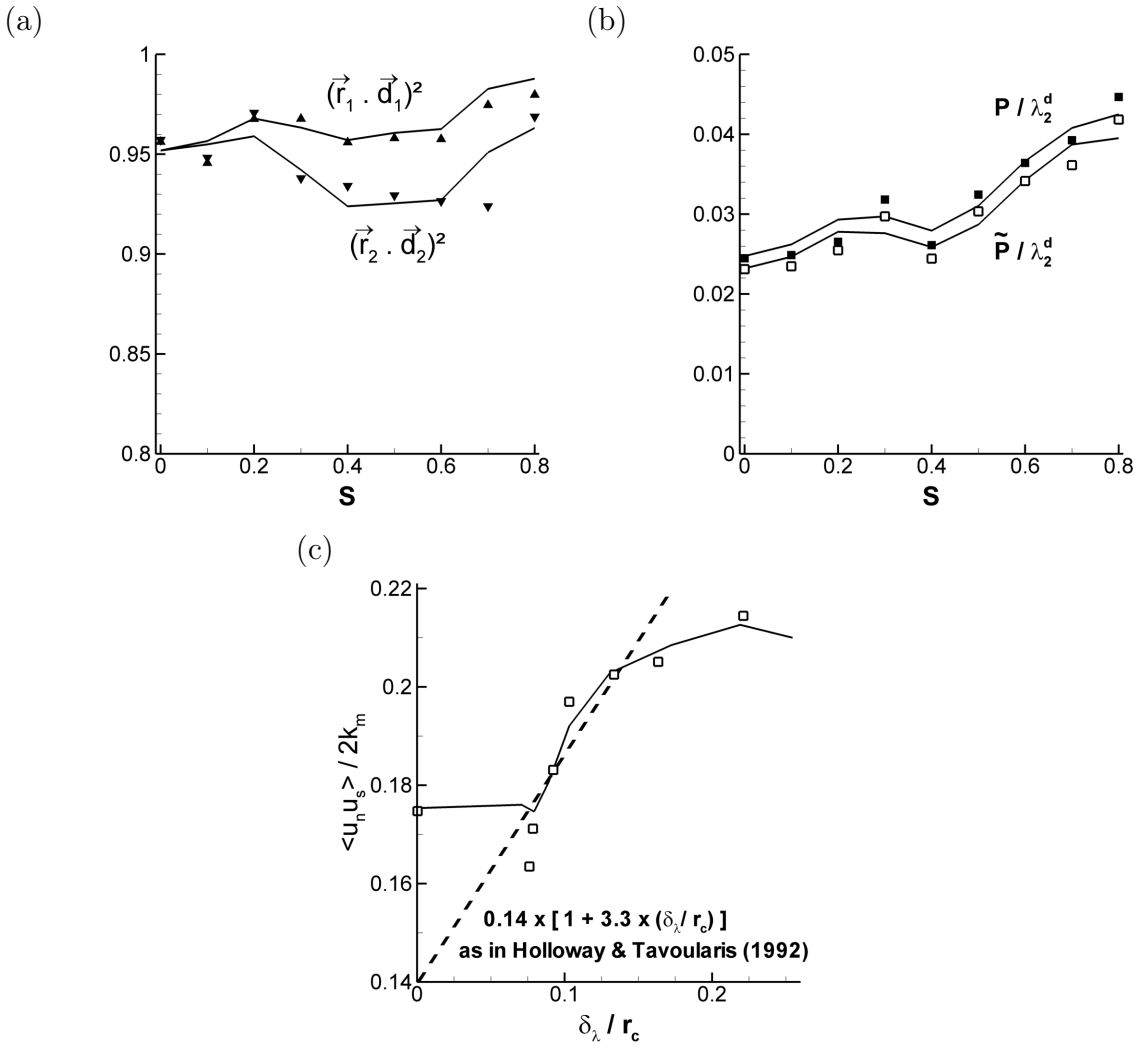

FIGURE B.4 – Convergence statistique correspondant aux figures 18 et 21 du chapitre 5. Les symboles correspondent aux estimations qui utilisent seulement $N = 500$ échantillons, alors que les lignes sont les estimations qui utilisent l'ensemble $N = 5000$ échantillons, comme présenté dans les figures du chapitre 5.

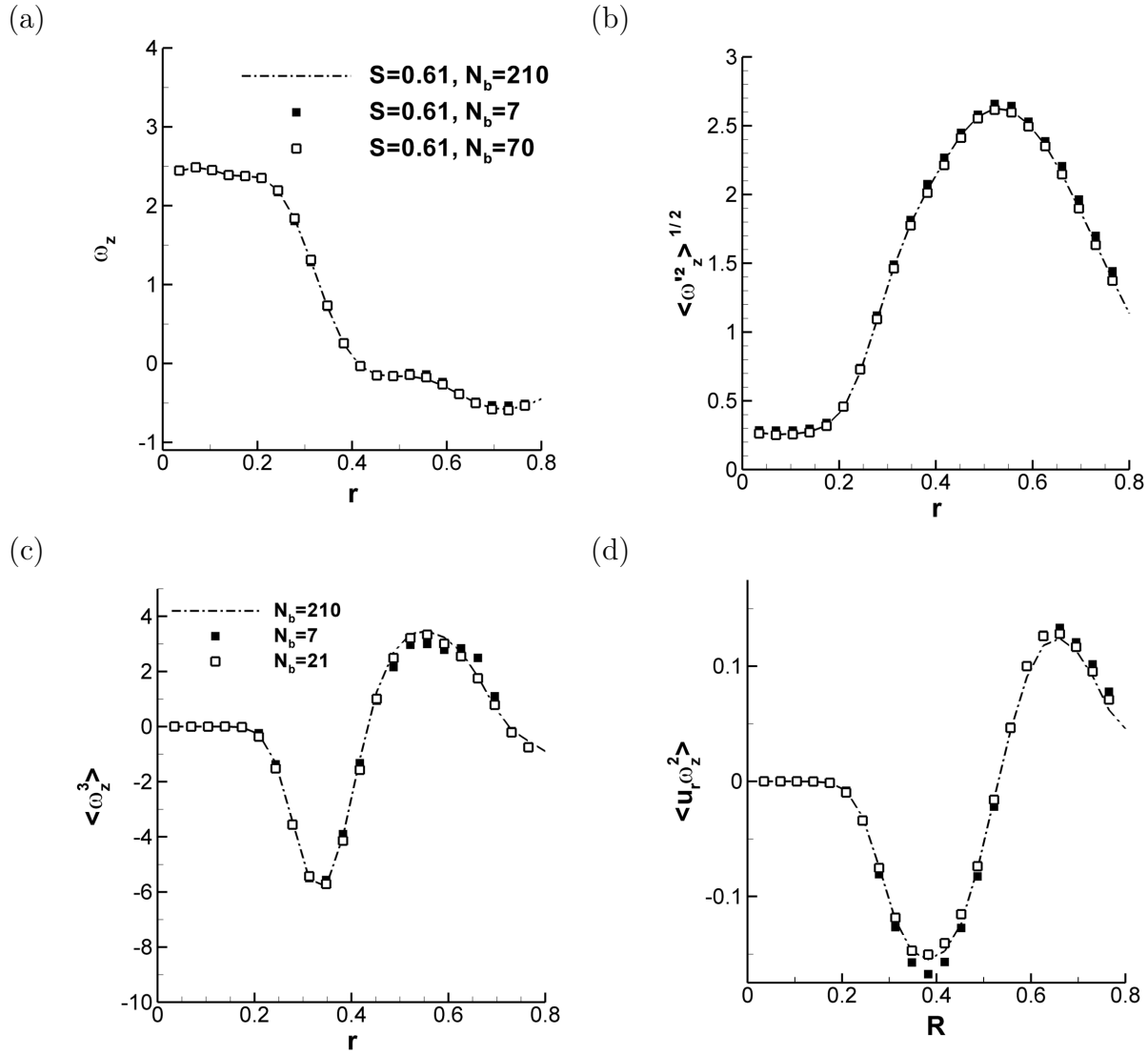

FIGURE B.5 – Convergence statistique correspondant aux figures 29,30 et 31 du chapitre 5. Les symboles correspondent aux estimations qui utilisent seulement $N_b = 7$ et $N_b = 70$ blocs de données, alors que les lignes sont les estimations qui utilisent l'ensemble des $N_b = 210$ blocs, comme présenté dans les figures du chapitre 5.

Bibliographie

[1] C. Bailly and G. Comte-Bellot. *Turbulence*. 2003.

[2] R.S. Barlow and J.P. Johnston. Structure of a turbulent boundary layer on a concave surface. *Journal of Fluid Mechanics*, 191 :137–176, 1988.

[3] G.K. Batchelor. *An introduction to fluid dynamics*. Cambridge Univ Pr, 1967. ISBN 0521663962.

[4] G.K. Batchelor. *The theory of homogeneous turbulence*. Cambridge University Press, 1982.

[5] J. Bell and R. Mehta. Development of a two-stream mixing layer from tripped and untripped boundary layers. *AIAA Journal*, 28(12) :2034–2042, 1990.

[6] J.H. Bell and R.D. Mehta. Measurements of the streamwise vortical structures in a plane mixing layer. *Journal of Fluid Mechanics*, 239 :213–248, 1992.

[7] L.H. Benedict and R.D. Gould. Towards better uncertainty estimates for turbulence statistics. *Experiments in Fluids*, 22(2) :129–136, 1996.

[8] T.B. Benjamin. Theory of the vortex breakdown phenomenon. *Journal of Fluid Mechanics*, 14(04) :593–629, 1962.

[9] L.P. Bernal and A. Roshko. Streamwise vortex structure in plane mixing layers. *Journal of Fluid Mechanics*, 170 :499–525, 1986.

[10] P. Billant, J.M. Chomaz, and P. Huerre. Experimental study of vortex breakdown in swirling jets. *Journal of Fluid Mechanics*, 376 :183–219, 1998.

[11] P. Bradshaw. The effect of initial conditions on the development of a free shear layer. *Journal of Fluid Mechanics*, 26(02) :225–236, 1966.

[12] P. Bradshaw. The analogy between streamline curvature and buoyancy in turbulent shear flow. *Journal of Fluid Mechanics*, 36(01) :177–191, 1969.

[13] P. Bradshaw. Effects of streamline curvature on turbulent flow. Technical report, 1973.

[14] P. Bradshaw, D.H. Ferriss, and R.F. Johnson. Turbulence in the noise-producing region of a circular jet. *Journal of Fluid Mechanics*, 1964(04) :591–624, 1964.

[15] C. Cambon and J.F. Scott. Linear and nonlinear models of anisotropic turbulence. *Annual review of fluid mechanics*, 31(1) :1–53, 1999.

[16] I.P. Castro and P. Bradshaw. The turbulence structure of a highly curved mixing layer. *Journal of Fluid Mechanics*, 73(02) :265–304, 1976. ISSN 1469-7645.

[17] F. Champagnat, A. Plyer, G. Le Besnerais, B. Leclaire, S. Davoust, and Y. Le Sant. Fast and accurate PIV computation using highly parallel iterative correlation maximization. *Experiments in Fluids*, 50 :1169–1182, 2011.

[18] F. Charru. *Instabilités hydrodynamiques*. EDP Sciences, 2007.

[19] N.A. Chigier and A. Chervinsky. Experimental investigation of swirling vortex motion in jets. *Journal of Applied Mechanics*, 34(1967) :443–451, 1967.

[20] M.S. Chong, A.E. Perry, and B.J. Cantwell. A general classification of three-dimensional flow fields. page 408, 1990.

[21] J.H. Citriniti and W.K. George. The reduction of spatial aliasing by long hot-wire anemometer probes. *Experiments in fluids*, 23(3) :217–224, 1997.

[22] J.H. Citriniti and W.K. George. Reconstruction of the global velocity field in the axisymmetric mixing layer utilizing the proper orthogonal decomposition. *Journal of Fluid Mechanics*, 418 :137–166, 2000.

[23] S.C. Crow and F.H. Champagne. Orderly structure in jet turbulence. *Journal of Fluid Mechanics*, 48(03) :547–591, 1971. ISSN 0022-1120.

[24] P. Davies, M.J. Fisher, and M.J. Barratt. The characteristics of the turbulence in the mixing region of a round jet. *Journal of Fluid Mechanics Digital Archive*, 15 (03) :337–367, 1962.

[25] S. Davoust and L. Jacquin. Taylor's hypothesis convection velocities from mass conservation equation. *Physics of Fluids*, 23(5), 2011.

[26] J.C. Del Alamo and J. Jiménez. Estimation of turbulent convection velocities and corrections to Taylor's approximation. *Journal of Fluid Mechanics*, 640 :5–26, 2009. ISSN 0022-1120.

[27] J. Delville, L. Ukeiley, L. Cordier, J.P. Bonnet, and M. Glauser. Examination of large-scale structures in a turbulent plane mixing layer. Part 1. Proper orthogonal decomposition. *Journal of Fluid Mechanics*, 391 :91–122, 1999.

[28] L.H. Dorey, L. Tessé, N. Bertier, and F. Dupoirieux. Modélisation de la formation des suies et du couplage avec le rayonnement dans les foyers aéronautiques. In *Présentation des journées des doctorants ONERA*. DEFA / ONERA, Janvier 2011.

[29] A. Dupeuble. *Etude d'une turbulence homogène soumise a des effets couplés de rotation et de contraction axisymétrique*. PhD thesis, ONERA, Université Claude Bernard (Lyon I), 1992.

[30] D. Ewing. Decay of round turbulent jets with swirl. In *Engineering Turbulence Modelling and Experiments 4 : Proceedings of the 4th International Symposium on Engineering Turbulence Modelling and Measurements, Ajaccio, Corsica, France, 24-26 May, 1999*. Elsevier Science, 1999.

[31] L. Facciolo, N. Tillmark, A. Talamelli, and P.H. Alfredsson. A study of swirling turbulent pipe and jet flows. *Physics of Fluids*, 19 :035105, 2007.

[32] S. Farokhi, R. Taghavi, and E.J. Rice. Effect of initial swirl distribution on the evolution of a turbulent jet. *AIAA Journal*, 27(6) :700–706, 1988.

[33] O. Faugeras. *Three-dimensional computer vision*, volume 11. MIT press Cambridge, MA, 2001.

[34] R. Fezzani, F. Champagnat, G. Le Besnerais, B. Leclaire, S. Davoust, and Y. Le Sant. Combined local-global approach in PIV processing : a better tradeoff between noise and resolution. In *9th International Symposium on Particle Image Velocimetry*, 2011.

[35] J.M. Foucaut, J. Carlier, and M. Stanislas. PIV optimization for the study of turbulent flow using spectral analysis. *Measurement Science and Technology*, 15 : 1046–1058, 2004.

[36] C. Gailledreau. Débitmètres à pression différentielle. Technical report, Techniques de l'Ingénieur, traité Mesures et Contrôle, 1999.

[37] F. Gallaire. *Instabilités dans les jets tournants et contrôle de l'éclatement tourbillonnaire*. PhD thesis, PhD thesis, LadHyX, Ecole Polytechnique, 2002.

[38] F. Gallaire and J.M. Chomaz. Instability mechanisms in swirling flows. *Physics of Fluids*, 15 :2622, 2003.

[39] F. Gallaire and J.M. Chomaz. Mode selection in swirling jet experiments : a linear stability analysis. *Journal of Fluid Mechanics*, 494(1) :223–253, 2003.

[40] M. Gaster, E. Kit, and I. Wygnanski. Large-scale structures in a forced turbulent mixing layer. *Journal of Fluid Mechanics*, 150 :23–39, 1985.

[41] J.N. Gence and C. Frick. Birth of the triple correlations of vorticity in an homogenous turbulence submitted to a solid body rotation. *Comptes Rendus de l'Academie des Sciences Series IIB Mechanics*, 329(5) :351–356, 2001. ISSN 1620-7742.

[42] W.K. George. The self-preservation of turbulent flows and its relation to initial conditions and coherent structures. *Advances in Turbulence*, pages 39–74, 1989.

[43] W.K. George, P.D. Beuther, and J.L. Lumley. Processing of random signals. In *Proceedings of the dynamic flow conference*, pages 757–800, 1978.

[44] R. T. Gilchrist and J. W. Naughton. Experimental study of incompressible jets with different initial swirl distributions : Mean results. *AIAA Journal*, 43(4), 2005.

[45] S.S. Girimaji. Pressure–strain correlation modelling of complex turbulent flows. *Journal of Fluid Mechanics*, 422 :91–123, 2000.

[46] H.P. Greenspan. *The theory of rotating fluids*. Cambridge University Press, 1968.

[47] C. Ho and P. Huerre. Perturbed free shear layers. *Annual Reviews in Fluid Mechanics*, 16(1) :365–422, 1984.

[48] P.H. Hoffmann, K.C. Muck, and P. Bradshaw. The effect of concave surface curvature on turbulent boundary layers. *Journal of Fluid mechanics*, 161 :371–403, 1985.

[49] A.G.L. Holloway and S. Tavoularis. The effects of curvature on sheared turbulence. *Journal of Fluid Mechanics*, 237 :569–603, 1992.

[50] E.J. Hopfinger, F.K. Browand, and Y. Gagne. Turbulence and waves in a rotating tank. *Journal of Fluid Mechanics*, 125 :505–534, 1982.

[51] B.K.P. Horn and B.G. Schunck. Determining optical flow. *Artificial intelligence*, 17(1-3) :185–203, 1981.

[52] P. Huerre and PA Monkewitz. Local and global instabilities in spatially developing flows. *Annual Reviews in Fluid Mechanics*, 22(1) :473–537, 1990.

[53] P. Huerre and M. Rossi. Hydrodynamic instabilities in open flows. pages 81–294. CAMBRIDGE UNIVERSITY PRESS, 1998.

[54] A.K.M.F. Hussain and A. Clark. Measurements of wavenumber-celerity spectrum in plane and axisymmetric jets. *AIAA Journal*, 19 :51–55, 1981. ISSN 0001-1452.

[55] A.K.M.F. Hussain and M.F. Zedan. Effects of the initial condition on the axisymmetric free shear layer : Effects of the initial momentum thickness. *Physics of Fluids*, 21(7) :1100–1112, 1978. doi : 10.1063/1.862349.

[56] A.K.M.F. Hussain and M.F. Zedan. Effects of the initial condition on the axisymmetric free shear layer : Effect of the initial fluctuation level. *Physics of Fluids*, 21 (9) :1475–1481, 1978. doi : 10.1063/1.862410.

[57] H.J. Hussein, S.P. Capp, and W.K. George. Velocity measurements in a high-reynolds-number, momentum-conserving, axisymmetric, turbulent jet. *Journal of Fluid Mechanics*, 258 :31–75, 1994.

[58] M.O. Iqbal and F.O. Thomas. Coherent structure in a turbulent jet via a vector implementation of the proper orthogonal decomposition. *Journal of Fluid Mechanics*, 571 :281–326, 2007.

[59] L. Jacquin. *Etude théorique et expérimentale de la turbulence homogène en rotation*. PhD thesis, ONERA, Université Claude Bernard (Lyon I), 1987.

[60] L. Jacquin, O. Leuchter, C. Cambon, and J. Mathieu. Homogeneous turbulence in the presence of rotation. *Journal of Fluid Mechanics*, 220 :1–52, 1990.

[61] J. Jeong and F. Hussain. On the identification of a vortex. *Journal of Fluid Mechanics*, 285 :69–94, 1995.

[62] J. Jeong, F. Hussain, W. Schoppa, and J. Kim. Coherent structures near the wall in a turbulent channel flow. *Journal of Fluid Mechanics*, 332 :185–214, 1997.

[63] J. Kim and H. Choi. Large eddy simulation of a circular jet : effect of inflow conditions on the near field. *Journal of Fluid Mechanics*, 620, 2009.

[64] S. Komori and H. Ueda. Turbulent flow structure in the near field of a swirling round free jet. *Physics of Fluids*, 28 :2075, 1985.

[65] B.E. Launder, G.J. Reece, and W. Rodi. Progress in the development of a reynolds-stress turbulence closure. *Journal of Fluid Mechanics*, 68(03) :537–566, 1975.

[66] G. Le Besnerais and F. Champagnat. Dense optical flow by iterative local window registration. In *Image Processing, 2005. ICIP 2005. IEEE International Conference on*, volume 1, pages I–137. IEEE, 2005.

[67] Y. Le Sant, B. Gardarin, B. Leclaire, P. Geffroy, and D. Soulevant. Polynomial calibration vs. pinhole calibration. In *7th International Symposium on Particle Image Velocimetry, Roma, Italy*, 2007.

[68] B. Leclaire. *Etude théorique et expérimentale d'un écoulement tournant dans une conduite*. PhD thesis, ONERA, Ecole Polytechnique, 2006.

[69] B. Leclaire and L. Jacquin. On the generation of swirling jets : High Reynolds number rotating flow in a pipe with final contraction. *Journal of Fluid Mechanics, in press*, 2012.

[70] B. Leclaire and D. Sipp. A sensitivity study of vortex breakdown onset to upstream boundary conditions. *Journal of Fluid Mechanics*, 645 :81–119, 2010.

[71] B. Leclaire, B. Jaubert, F. Champagnat, G. Le Besnerais, and Y. Le Sant. FOLKI-3C : a simple, fast and direct algorithm for stereo PIV. In *Proceedings of 8th International Symposium on Particle Image Velocimetry - PIV09*, Melbourne, 2009.

[72] B. Lecordier and J. Westerweel. The europiv synthetic image generator (sig). In M. Stanislas, J. Westerweel, and J. Kompenhans, editors, *Particle image velocimetry : recent improvements. EUROPIV 2 workshop.* Springer, 2003.

[73] S. Leibovich and K. Stewartson. A sufficient condition for the instability of columnar vortices. *Journal of Fluid Mechanics*, 126 :335–356, 1983.

[74] H. Liang and T. Maxworthy. An experimental investigation of swirling jets. *Journal of Fluid Mechanics*, 525 :115–159, 2005.

[75] D. Liepmann and M. Gharib. The role of streamwise vorticity in the near-field entrainment of round jets. *Journal of Fluid Mechanics*, 245 :643–668, 1992.

[76] S.J. Lin and G.M. Corcos. The mixing layer : deterministic models of a turbulent flow. Part 3. The effect of plane strain on the dynamics of streamwise vortices. *Journal of Fluid Mechanics*, 141 :139–178, 1984. ISSN 0022-1120.

[77] T. Loiseleux and J.M. Chomaz. Breaking of rotational symmetry in a swirling jet experiment. *Physics of Fluids*, 15 :511, 2003.

[78] J.L. Lumley. Interpretation of time spectra measured in high-intensity shear flows. *Physics of Fluids*, 8 :1056, 1965.

[79] D.P. Margolis and J.L. Lumley. Curved turbulent mixing layer. *Physics of Fluids*, 8 :1775, 1965.

[80] J.E. Martin and E. Meiburg. Numerical investigation of three-dimensionally evolving jets subject to axisymmetric and azimuthal perturbations. *Journal of Fluid Mechanics*, 230 :271–318, 1991.

[81] S. McIlwain and A. Pollard. Large eddy simulation of the effects of mild swirl on the near field of a round free jet. *Physics of Fluids*, 14 :653, 2002.

[82] R.D. Mehta, D.H. Wood, and P.D. Clausen. Some effects of swirl on turbulent mixing layer development. *Physics of Fluids*, 3 :2716, 1991.

[83] R.W. Metcalfe, S.A. Orszag, M.E. Brachet, S. Menon, and J.J. Riley. Secondary instability of a temporally growing mixing layer. *Journal of Fluid Mechanics*, 184 : 207–243, 1987. ISSN 1469-7645.

[84] A. Michalke. On spatially growing disturbances in an inviscid shear layer. *Journal of Fluid Mechanics*, 23(03) :521–544, 1965.

[85] A. Michalke. Survey on jet instability theory. *Progress in Aerospace Sciences*, 21 (3) :159–199, 1984.

[86] P. Moin. Revisiting Taylor's hypothesis. *Journal of Fluid Mechanics*, 640 :1–4, 2009.

[87] F. Moisy, C. Morize, M. Rabaud, and J. Sommeria. Decay laws, anisotropy and cyclone–anticyclone asymmetry in decaying rotating turbulence. *J. Fluid Mech*, 666 :5–35, 2010.

[88] S.C. Morris and J.F. Foss. Turbulent boundary layer to single-stream shear layer : the transition region. *Journal of Fluid Mechanics*, 494 :187–221, 2003.

[89] J.W. Naughton, L.N. Cattafesta III, and G.S. Settles. An experimental study of compressible turbulent mixing enhancement in swirling jets. *Journal of Fluid Mechanics*, 330 :271–305, 1997.

[90] J.C. Neu. The dynamics of stretched vortices. *Journal of Fluid Mechanics*, 143 : 253–276, 1984. ISSN 0022-1120.

[91] ONERA. Souffleries de recherches de la direction de l'aérodynamique et souffleries industrielles de la direction des grandes souffleries de Modane-Avrieux. Technical report, Office National d'Etudes et de Recherches Aérospatiales, 29, Avenue de la Division Leclerc, 92 Chatillon, France, 1969.

[92] J. Panda and D.K. McLaughlin. Experiments on the instabilities of a swirling jet. *Physics of Fluids*, 6 :263, 1994.

[93] A. Papoulis. The Fourier integral and its applications. 1962.

[94] M.W. Plesniak, R.D. Mehta, and J.P. Johnston. Curved two-stream turbulent mixing layers : Three-dimensional structure and streamwise evolution. *Journal of Fluid Mechanics*, 270 :1–50, 1994.

[95] S.B. Pope. *Turbulent flows*. Cambridge Univ. Press, 2008.

[96] S. Pouillard, L. Jacquin, and P. Geffroy. Etude expérimentale d'un jet tournant : qualification de la veine (première partie). Technical report, Office National d'Etudes et de Recherches Aérospatiales. Départment d'Aérodynamique Fondamentale et Expérimentale, 1999.

[97] A.K. Prasad and K. Jensen. Scheimpflug stereocamera for particle image velocimetry in liquid flows. *Applied optics*, 34(30) :7092–7099, 1995.

[98] B.D. Pratte and J.F. Keffer. The swirling turbulent jet. *ASME, Transactions, Series D-Journal of Basic Engineering*, 94 :739–747, 1972.

[99] M. Raffel, C. Willert, C. Wereley, and J. Kompenhans. *Particle Image Velocimetry. A Practical Guide*. Springer Verlag, Berlin, 2nd edition edition, 2007.

[100] L. Rayleigh. On the dynamics of revolving fluids. *Proceedings of the Royal Society of London. Series A, Containing Papers of a Mathematical and Physical Character*, 93(648) :148–154, 1917.

[101] M.M. Rogers and P. Moin. The structure of the vorticity field in homogeneous turbulent flows. *Journal of Fluid Mechanics*, 176 :33–66, 1987. ISSN 0022-1120.

[102] M.M. Rogers and R.D. Moser. Direct simulation of a self-similar turbulent mixing layer. *Physics of Fluids*, 6 :903, 1994.

[103] WG Rose. A swirling round turbulent jet, part 1 : Mean flow measurements. *Journal of Applied Mechanics*, 29 :615–625, 1962.

[104] M.R. Ruith, P. Chen, E. Meiburg, and T. Maxworthy. Three-dimensional vortex breakdown in swirling jets and wakes : direct numerical simulation. *Journal of Fluid Mechanics*, 486 :331–378, 2003.

[105] A. Salhi and C. Cambon. An analysis of rotating shear flow using linear theory and dns and les results. *Journal of Fluid Mechanics*, 347 :171–195, 1997.

[106] W.S. Saric. Gortler vortices. *Annual Review of Fluid Mechanics*, 26 :379–410, 1994.

[107] R. Seele, K. Obertleithner, C. O. Paschereit, and I. Wygnanski. Vortex breakdown in swing free jets. part 1. mean properties of the swirled flow. In *Int. Conf on Jets, Wakes and Separated Flows, ICJWSF-2008*, 2008.

[108] A. Shiri, W. K. George, and J. W. Naughton. Experimental study of the far field of incompressible swirling jets. *AIAA Journal*, 46(8) :2002–2009, 2008.

[109] D. Sipp, E. Lauga, and L. Jacquin. Vortices in rotating systems : Centrifugal, elliptic and hyperbolic type instabilities. *Physics of Fluids*, 11 :3716, 1999.

[110] SNECMA. URL `http://www.snecma.com/-gp7200`.

[111] C.G. Speziale, S. Sarkar, and T.B. Gatski. Modelling the pressure–strain correlation of turbulence : an invariant dynamical systems approach. *Journal of Fluid Mechanics*, 227 :245–272, 1991.

[112] P.J. Staplehurst, P.A. Davidson, and S.B. Dalziel. Structure formation in homogeneous freely decaying rotating turbulence. *Journal of Fluid Mechanics*, 598 : 81–105, 2008.

[113] G.I. Taylor. The spectrum of turbulence. *Proceedings of the Royal Society of London. Series A-Mathematical and Physical Sciences*, 164(919) :476, 1938.

[114] H. Tennekes and J.L. Lumley. *A first course in turbulence*. MIT press, 1999.

[115] F.O. Thomas. Structure of mixing layers and jets. *Applied Mechanics Reviews*, 44 :119, 1991.

[116] A.A.R. Townsend. *The structure of turbulent shear flow*. Cambridge Univ Press, 1980.

[117] C. Tropea, A.L. Yarin, and J.F. Foss. *Springer Handbook of Experimental Fluid Mechanics*. Springer Verlag, 2007.

[118] C.W.H. van Doorne and J. Westerweel. Measurement of laminar, transitional and turbulent pipe flow using stereoscopic PIV. *Experiments in Fluids*, 42 :259–279, 2007.

[119] J. Westerweel. Fundamentals of digital particle image velocimetry. *Measurement Science and Technology*, 8 :1379, 1997.

[120] B. Wieneke. Stereo-PIV using self-calibration on particle images. *Experiments in Fluids*, 39(2) :267–280, 2005.

[121] Wikipedia. URL `http://en.wikipedia.org/wiki/Kelvin-Helmholtz_instability`.

[122] I. Wygnanski and H. Fiedler. Some measurements in the self-preserving jet. *Journal of Fluid Mechanics*, 38(03) :577–612, 1969.

[123] A.J. Yule. Large-scale structure in the mixing layer of a round jet. *Journal of Fluid Mechanics*, 89(03) :413–432, 1978.

[124] K.B.M.Q. Zaman and A.K.M.F. Hussain. Taylor hypothesis and large-scale coherent structures. *Journal of Fluid Mechanics*, 112 :379–396, 1981.

[125] K.B.M.Q. Zaman and A.K.M.F. Hussain. Natural large-scale structures in the axisymmetric mixing layer. *Journal of Fluid Mechanics*, 138 :325–351, 1984.

Dynamique des grandes échelles dans les jets turbulents avec ou sans effets de rotation

Résumé : Cette thèse est une contribution à l'étude de la turbulence dans le champ proche de la sortie de jets, avec ou sans effets de rotation. Notre dispositif expérimental permet de générer un jet tournant qui se développe en formant une couche de mélange axisymétrique turbulente et dont le nombre de swirl peut être précisément fixé. L'écoulement est caractérisé par PIV stéréoscopique, avec un recours à des acquisitions à haute cadence de manière à résoudre la dynamique des grandes échelles de la turbulence. Nous avons proposé une méthode qui permet de déterminer la vitesse de convection des structures turbulentes et d'estimer la validité de l'approximation de Taylor. Cette étude démontre qu'il est ici légitime de décrire les structures spatiales de la turbulence à partir de mesures temporelle réalisées dans un plan transverse à l'écoulement.

Dans le coeur du jet non tournant, une POD confirme la prédominance de modes m=0 et m=1 décrite dans de précédentes études. Le mode m=1 prend plus souvent la forme d'un battement que d'une hélice. Dans la couche de mélange, les tourbillons longitudinaux sont les structures dominantes. Une organisation sous forme de paires de signe opposé orientées radialement est mise en évidence par l'analyse des corrélations doubles de vorticité. L'étude des corrélations vorticité-vitesse donne la position préférentielle de ces tourbillons par rapport aux modes m=0 et m=1. Nous avons alors proposé un scénario d'interaction entre les modes m=0 et m=1, les tourbillons longitudinaux et le champ moyen.

Lorsque le nombre de swirl augmente, le taux de croissance et l'énergie cinétique turbulente dans la couche de mélange du jet varient de manière non-monotone. Ceci est dû à des conditions initiales issues du mécanisme de mise en rotation, qui ont un effet contraire à celui de l'alignement du tenseur de Reynolds avec le tenseur des déformations. L'orientation des paires de tourbillons avec le swirl permet d'interpréter dynamiquement l'évolution du tenseur de Reynolds.

Mots-clés : Jet, Turbulence, Ecoulement cisaillé, Ecoulement tournant, Swirl, PIV, POD, Hypothèse de Taylor, Structures cohérentes, Tourbillons longitudinaux, Tenseur de Reynolds.

Dynamics of large scale structures in turbulent jets with or without the effects of swirl

Summary : This thesis is a contribution to the study of turbulence in the near field of a jet exit, with or without swirl. We use an experimental setup which has been validated to generate a thin axisymmetric mixing layer developing into a jet, and where the amount of swirl can be precisely set. The flow is characterized using stereoscopic PIV measurements, including high-speed acquisitions which resolve the dynamics of the large scale turbulent structures. We have proposed and tested a method which allows the estimate the convection velocities of these structures and to determine the validity of Taylor's hypothesis using the experimental dataset. This study shows that in the jet near field, it is legitimate to perform a pseudo spatial reconstruction using temporal PIV data.

In the jet core, without swirl, a POD confirms the predominance of m=0 and m=1 modes, in line with previous studies. A detailed statistical analysis brings to light that the motion of m=1 modes is closer to a flapping than to a helix. In the mixing layer, streamwise vortices are dominant. Radially oriented pairs are shown to be frequent by analyzing spatial correlation of streamwise vorticity. The relative organization of these vortices with m=0 and m=1 modes is quantitatively established using velocity and vorticity correlations. This leads us to propose an interaction scenario between m=0 and m=1 modes, streamwise vortices, and the mean flow.

When swirl is added, the growth rate and turbulent kinetic energy level in the mixing layer do not vary in a monotonous manner. This is due to specific initial conditions obtained from the swirl generation mechanism, which counter the effects arising from the increased alignment between the Reynolds stress and the strain tensor. On this last point, we show that the orientation of the initially radial vortex pair changes with swirl, and this provides a dynamical interpretation of evolution of the Reynolds stress tensor.

Keywords : Jet, Turbulence, Shear flow, Rotating flow, Swirl, PIV, POD, Taylor hypothesis, Coherent structures, Streamwise vortices, Reynolds stress.